

# Response of stochastic adhesion clusters to pulling and shearing forces

Inaugural-Dissertation

zur

Erlangung des Doktorgrades

der Mathematisch-Naturwissenschaftlichen Fakultät  
der Universität zu Köln



vorgelegt von

Andrea Bräutigam

aus Arnsberg, Deutschland

Jülich

2021



---

Berichterstatter: Prof. Dr. Gerhard Gompper  
Prof. Dr. Johannes Berg

Tag der mündlichen Prüfung: 10.12.2021



*“Working hard is important. But there’s something that matters even more.  
Believing in yourself.”*

J. K. Rowling. Harry Potter and the Order of the Phoenix.



# Zusammenfassung

Zellen haften an Oberflächen oder benachbarten Zellen über lokal aggregierte Proteinkomplexe, die auf transmembranen Zelladhäsionsmolekülen wie Cadherinen oder Integrinen basieren. Diese Komplexe sorgen nicht nur für strukturelle Stabilität, sie sind auch in zahlreiche zelluläre Prozesse involviert, die Zellentwicklung, -regulation und -migration betreffen. Die Fähigkeit, mechanische Signale in einem mehrschrittigen Prozess wahrzunehmen, wird als Mechanotransduktion bezeichnet. Ihr wird eine zentrale Rolle zugeschrieben, weil sie eine abgestimmte Reaktion und Anpassung auf Umgebungseinflüsse, wie zum Beispiel steigende mechanische Belastung, erlaubt.

Ein Musterbeispiel für die komplexe Reaktion auf steigende Spannung ist das Adaptorprotein Talin, welches mit seiner Kopfreion an Integrin und mit seiner Stabregion an F-Aktin bindet. Unter Kraftereinwirkung entfalten Regionen entlang der Stabregion sukzessive, wodurch Bindungsstellen für Vinculin geöffnet werden, die zuvor unzugänglich waren. Vinculinmoleküle werden somit in die Adhäsion eingezogen und verstärken die Verbindung durch das Binden an Talin und Aktin. Während die kollektiven Auswirkungen des Bindens und Reißens einzelner Verbindungen in Adhäsionsclustern bereits seit mehr als zwei Jahrzehnten modelliert werden, werden Adaptationsmechanismen wie die Konformationsänderungen von Talin erst seit Kurzem in theoretische Untersuchungen miteinbezogen.

In dieser Arbeit wird ein Minimalmodell für Adhäsionscluster vorgestellt und analysiert, um mögliche generische Mechanismen der Adhäsionsanpassung unter Kraftereinwirkung aufzudecken. Ein Adhäsionscluster besteht aus elastischen, stäbchenförmigen Molekülen, die zwei ebene Oberflächen, auf die eine äußere Kraft wirkt, verbinden. Moleküle durchlaufen reversible stochastische Übergänge zwischen ausgewählten Zuständen, die den Bindungszustand und die Konformation der Moleküle beschreiben. Zusätzlich werden Adhäsionscluster mit fixierter und variabler Molekülzahl verglichen. Alle Übergangsraten erfüllen die thermodynamischen Randbedingungen, sodass im Gleichgewicht, d.h. ohne äußere Kraftanwendung, mikroskopische Reversibilität gewährleistet wird. Der gesamte Cluster wird durch einen einschrittigen Markov-Prozess beschrieben, der analytisch und mithilfe kinetischer Monte-Carlo-Simulationen untersucht wird.

Die Ergebnisse zeigen, dass das Entfalten von Adhäsionsmolekülen qualitativ unter-

schiedliche Auswirkungen unter vornehmlich Zug- und Scherkräften hat. Bei reinem Zug sind Verbindungen orthogonal zu den Oberflächengrenzen angeordnet, sodass der Entfaltungsübergang die Distanz erhöht, die durch den Cluster überbrückt werden kann. Die Begrenzung durch die harten Oberflächen führt zu einer Konkurrenz zwischen gefalteter und entfalteter Konformation. Dadurch nimmt die Clustergröße mit steigender Kraft ab und die Wahrscheinlichkeit für eine vollständige Dissoziation des Clusters wächst. Wenn die beiden Oberflächen nicht auseinander gezogen werden, sondern Scherkräften ausgesetzt sind, kommt es zu einer breiten Verteilung an Dehnungen der Verbindungen. Das System wird mit kontinuierlichen Zyklen aus Binden, Entfalten und Reißen einzelner Verbindungen aus dem Gleichgewicht gebracht, was zu einer im Mittel konstanten Gleitgeschwindigkeit des Systems führt. Wenn der Cluster an ein Reservoir gekoppelt ist, ziehen die nicht im Gleichgewicht befindlichen Zustände neue Moleküle in die Adhäsion. In einer solchen Situation nimmt die Anzahl der gebundenen Moleküle trotz steigender Kraft zu. Die mittlere Lebensdauer des Clusters erreicht ihren höchsten Wert bei nicht verschwindenden Kräften. Dieser Selbststabilisierungsmechanismus ist das zentrale Ergebnis der Arbeit. Sie zeigt, dass die Anpassung an mechanische Belastung generisch mithilfe weniger Zutaten in einem vereinfachten, aber thermodynamisch konsistentem Modell erreicht werden kann. Mit diesem Beitrag zielt die Arbeit auf ein besseres Verständnis der zugrundeliegenden Mechanismen in zellulären Adhäsionen oder verwandten Systemen und dient möglicherweise als Inspiration für biomimetische Materialien.



# Abstract

Cells adhere to surfaces or neighbouring cells via locally aggregated multi-protein complexes that are based on transmembrane cellular adhesion molecules, such as cadherins or integrins. These complexes do not only provide structural stability, but are also involved in numerous cellular processes concerning development, regulation and migration. The ability to sense mechanical cues in a multi-step process is termed mechanotransduction and has been ascribed a crucial role, because it allows a tuned response and adaptation to environmental factors, such as increasing mechanical stress.

A paradigm for an intricate response to increased tension is the adaptor protein talin, which binds with its head region to integrin and with its rod domain to F-actin. Under force, domains along the talin rod successively unfold, thereby opening binding sites for vinculin that were previously inaccessible. Vinculin molecules are thus recruited to the adhesion and strengthen the linkage by binding both talin and actin. While the collective effects of binding and rupture of distinct bonds in adhesion clusters have already been modeled for more than two decades, adaptation mechanisms like the conformational changes of talin have only recently been included in theoretical studies.

In this thesis, a minimal model for adhesion clusters is introduced and analysed to uncover possible generic mechanism of adhesion adaptation under force. An adhesion cluster is composed of elastic rod-like molecules that connect two planar surfaces under an external force. Molecules undergo reversible stochastic transitions between selected states, which describe the molecules' binding state and conformation. Additionally, adhesion clusters with a fixed and variable number of molecules are compared. All transition rates fulfil the thermodynamic constraints, so that microscopic reversibility is guaranteed in equilibrium, i.e. without external force application. The whole cluster is described by a one-step Markov process, which is studied analytically and by means of kinetic Monte Carlo simulations.

The results demonstrate that unfolding of adhesion molecules has qualitatively different effects under predominantly pulling and shearing forces. In the case of pure pulling, bonds are aligned orthogonally to the surface boundaries, so that the unfolding transition increases the distance that can be bridged by the cluster. However, the confinement due to the rigid surfaces leads to a competition between the folded and unfolded conformation. As a

consequence, cluster size decreases with increasing force and the probability for complete cluster dissociation grows. When the two surfaces are not pulled apart, but are subject to shearing forces, a broad distribution of bond stretches results. The system is shifted out of equilibrium with continuous cycles of bond binding, unfolding, and rupture which lead to an on average constant sliding velocity of the system. If the cluster is coupled to a reservoir, non-equilibrated states draw new molecules into the adhesion. In such a situation, the number of bonds increases despite increasing forces. The average cluster lifetime exhibits a peak at non-vanishing forces. This self-stabilization mechanism is the central finding of the study. It demonstrates that adaptation to mechanical stress can be achieved generically with few ingredients in a simplified, but thermodynamically consistent model. With this contribution, the study aims at a better understanding of the underlying mechanisms in cellular adhesions or related systems and potentially serves as an inspiration for biomimetic materials.

# Contents

	Page
<b>Zusammenfassung</b>	<b>i</b>
<b>Abstract</b>	<b>iii</b>
<b>1 Introduction</b>	<b>1</b>
1.1 Motivation . . . . .	1
1.2 Adhesion science . . . . .	2
1.2.1 Adhesive interactions . . . . .	2
1.2.2 Biological Adhesions . . . . .	4
1.2.3 Biomimetic adhesives . . . . .	6
1.3 Mechanobiology of cells . . . . .	6
1.3.1 Mechanosensitive cell components and structures . . . . .	7
1.3.2 Mechanotransduction . . . . .	10
1.4 Outline of the thesis . . . . .	11
<b>2 Biological background: Cellular adhesions</b>	<b>13</b>
2.1 Overview . . . . .	14
2.1.1 Cell-cell contacts . . . . .	14
2.1.2 Cell-matrix contacts . . . . .	16
2.2 Adherens junctions . . . . .	17
2.2.1 Cadherin clustering . . . . .	18
2.2.2 Adaptor proteins . . . . .	19
2.2.3 Mechanotransduction . . . . .	19
2.3 Focal adhesions . . . . .	20
2.3.1 Integrin clustering . . . . .	20
2.3.2 Adaptor proteins . . . . .	22

2.3.3	Maturation steps and structure . . . . .	25
2.3.4	Mechanotransduction . . . . .	27
2.4	Experimental Methods . . . . .	29
2.4.1	Application of external force . . . . .	29
2.4.2	Observing forces generated by the cell . . . . .	30
2.5	Modelling approaches . . . . .	32
2.5.1	Modelling single bonds . . . . .	32
2.5.2	Bond clusters . . . . .	36
2.6	Open questions addressed in the thesis . . . . .	39
<b>3</b>	<b>Modelling an adhesion cluster under pulling forces</b>	<b>41</b>
3.1	Introduction . . . . .	42
3.1.1	Rates . . . . .	43
3.1.2	Units . . . . .	46
3.1.3	Simulation algorithm . . . . .	47
3.2	Binding and rupture model . . . . .	48
3.2.1	Constant number of molecules . . . . .	49
3.2.2	Variable adhesion size . . . . .	64
3.3	Extended model with conformational changes . . . . .	70
3.3.1	Constant number of molecules . . . . .	71
3.3.2	Variable adhesion size . . . . .	76
3.4	Extended model with conformational changes and adhesion molecule recruitment . . . . .	80
3.5	Summary . . . . .	82
3.6	Parameter values . . . . .	84
	<b>Preface to chapter 4</b>	<b>87</b>
	Declaration of individual contribution . . . . .	87
<b>4</b>	<b>A generic self-stabilization mechanism for biomolecular adhesions under load</b>	<b>89</b>
4.1	Abstract . . . . .	89
4.2	Introduction . . . . .	89
4.3	Results . . . . .	90
4.4	Discussion . . . . .	97

4.5	Model and Methods . . . . .	98
	Supplementary Information . . . . .	100
I	Parameters . . . . .	100
II	Stochastic simulations . . . . .	102
III	Adhesion model without unfolding . . . . .	103
IV	Adhesion model with unfolding . . . . .	104
V	Adhesion model with unfolding and catch bonds . . . . .	108
VI	Adhesion model with unfolding and cross-linking . . . . .	110
<b>5</b>	<b>Extension to two dimensions</b>	<b>113</b>
5.1	Modifications to the model . . . . .	114
5.1.1	Binding rate . . . . .	114
5.1.2	Restoring force balance . . . . .	116
5.2	Limiting cases of pure pulling and shearing . . . . .	117
5.2.1	Pulling force . . . . .	117
5.2.2	Shearing force . . . . .	119
5.3	Intermediate force directions . . . . .	120
5.4	Summary . . . . .	124
5.5	Parameter values . . . . .	127
<b>6</b>	<b>Conclusions and outlook</b>	<b>129</b>
6.1	Modelling an adhesion cluster . . . . .	129
6.2	Response to pulling forces . . . . .	131
6.3	Response to shearing forces . . . . .	132
6.4	Extension to arbitrary directions of force . . . . .	134
6.5	Outlook . . . . .	135
	<b>References</b>	<b>137</b>
	<b>Appendix</b>	<b>163</b>
<b>A</b>	<b>Mathematical background: Stochastic processes and applications</b>	<b>163</b>
A.1	Stochastic processes . . . . .	164
A.1.1	Definition . . . . .	164
A.1.2	Markov processes . . . . .	165
A.1.3	Master equation . . . . .	166

A.1.4	Macroscopic equations . . . . .	168
A.1.5	Fokker-Planck equation . . . . .	168
A.2	Stochastic chemical reaction kinetics . . . . .	169
A.2.1	Reactions and rates . . . . .	170
A.2.2	Chemical master equation . . . . .	171
A.2.3	Gillespie algorithm . . . . .	171
	<b>Acknowledgements</b>	<b>175</b>
	<b>Erklärung</b>	<b>177</b>
	<b>CV</b>	<b>179</b>

# Chapter 1

## Introduction

### 1.1 Motivation

A pioneer of cell biology, Edmund B. Wilson, wrote in 1925: “Long ago it became evident that the key to every biological problem must finally be sought in the cell; for every living organism is, or at some point has been, a cell” [341]. Indeed, cells were identified as a fundamental building block of life already in the 19th century. Since then, the field of cell biology has grown steadily and it attracts not only biologists, but also researchers from other natural sciences, such as physicists [343]. Understanding the physical principles that underlie the complex and intertwined processes inside the cell poses a difficult task, but at the same time a great opportunity for advances in the field and beyond. However, the cell is not a stand-alone unit; it is embedded in a complex surrounding, for instance in a fluid, on top of a surface or within a multicellular organism. Numerous vital processes depend on the cell’s ability to establish contact to its environment [170, 186, 283, 335]. Among the different structures that connect the intra- and extracellular world, cellular adhesion molecules have been attributed great importance [60, 132, 176, 191]. They typically assemble in clusters to connect a cell to its neighbour or the extracellular matrix. Most importantly, these contacts provide structural stability and tissue integrity. Additionally, they act as transmission pathways for the exchange of information. For both purposes, adhesion clusters need to respond and adapt to diverse mechanical cues [95, 117].

Experimental advances in the last decades allow the observation of structure and mechanoreponse of cellular adhesions on the molecular scale. Also, theoretical models have contributed to a better understanding of force transmission along adhesion molecules. The progress in the field shows that mechanical stress influences numerous cellular processes both locally within the cluster and globally – up to tissue architecture, function, and fate [69, 131]. To allow a robust force response, it is important that cellular adhesions are stable but also able to adapt to a changing environment. One striking finding in this context is the ability of adhesion clusters to grow under force [15, 272]. However, the

underlying mechanisms are not clarified yet.

The aim of this thesis is to deepen the understanding of general mechanisms in adhesion clusters under mechanical stress. For this purpose, a minimal model for a single adhesion cluster under force has been developed. The basic idea ties in with already existing models, but it is modified and extended to account for physical constraints and observations in the biological systems. One important question which accompanies the thesis concerns possible stabilization mechanisms: what are the necessary ingredients for biological adhesion clusters to grow or strengthen under force? Naturally, the full complexity of cellular adhesions cannot be included in the model. Yet, generalizations allow the study of mechanisms that are normally hidden or superimposed. Furthermore, the generic mechanism may serve as an inspiration for related systems since adhesive structures also appear in other biological systems, such as adhesive toes pads in animals, and in industrial products like rubber and glues.

This introductory chapter firstly provides an overview of adhesions in general, from the basic interactions to prominent examples. Secondly, a brief account on mechanobiology of cells is given, including main mechanosensitive structures in cells. Mechanotransduction, the process of turning a mechanical signal into a biochemical response, is also introduced. The chapter closes with an outline of the main part of the thesis.

## 1.2 Adhesion science

The word adhesion comes from the Latin noun *adhaesio* (linkage). The term describes the tendency of two, typically dissimilar materials to stick to each other. The associations with adhesions or adhesive systems differ between fields of science. In medicine, adhesions refer to bands of scar-like tissue that connect areas which are typically separated. They often form after injuries, surgeries, or other irritations in the abdomen or pelvis, at the shoulder, or between heart and sternum. Adhesions in this sense of the word can cause pain and severe complications [51]. In natural sciences, the term is used more generally for a broad range of mechanisms on very different length scales. These mechanisms share the common idea of an attractive energy that causes the linkage. In most cases, the adhesion can be disrupted again by application of energy. The strength of an adhesion is related to the amount of energy that is required for detachment.

### 1.2.1 Adhesive interactions

The interaction between adhesive and adherend is located either within the adhesive, within the adherend, or at their interface. Physical bonds are caused by Van der Waals forces, hydrogen bonds or dipole-dipole interactions. They are typically weaker than chemical interactions such as covalent or ionic bonds. Other linkages depend on mechanical



interlocking as in the case of entangled fibers. In many biological applications, these and other kinds of mechanisms are simultaneously present. Besides the type of interaction, important parameters typically comprise the geometry of the adhesive region, its surface area, and the material properties at the interface [222].

Adhesions can be classified as dry or wet. As the name suggests, wet adhesions typically include a liquid film. Hence they are based on surface tension and capillary effects, whereas dry adhesions originate from chemical bonds or Van der Waals attractions. A well-known example for wet adhesion is the stickiness of water to substrates. Water is highly polar and hence shows strong cohesion (an attraction between similar materials) and adhesion to other polar substances. In capillary tubes, the competition between adhesion and cohesion can be observed at the meniscus interface, see Fig. 1.1a. If adhesion to the charged surface is higher than cohesion, as in the case of water in glass, a concave meniscus forms. Alternatively, if the liquid-liquid attraction is stronger, the meniscus is convex. The resulting capillary repulsion can for example be observed for mercury [354]. Adhesive forces thus support spreading of liquids on substrates whereas cohesive forces tend to a lower degree of wetting. A measure for the wettability is given by the surface angle  $\theta$  [134], see Fig. 1.1b. In equilibrium between a flat, rigid solid  $S$ , a gas  $G$  and a liquid  $L$ , Young's equation connects  $\theta$  with the surface tensions  $\gamma_{SG}$ ,  $\gamma_{LG}$ , and  $\gamma_{SL}$  via [354]

$$0 = \gamma_{SG} - \gamma_{SL} - \gamma_{LG} \cos \theta. \quad (1.1)$$

The work per unit area  $W_a$  that is required to separate liquid and solid is described by the Dupré equation

$$W_a = \gamma_{SG} + \gamma_{LG} - \gamma_{SL}. \quad (1.2)$$

A large value of  $W_a$  corresponds to a strong liquid-solid bond. Combining (1.1) and (1.2) yields the Young-Dupré equation

$$W_a = \gamma_{LG}(1 + \cos \theta). \quad (1.3)$$

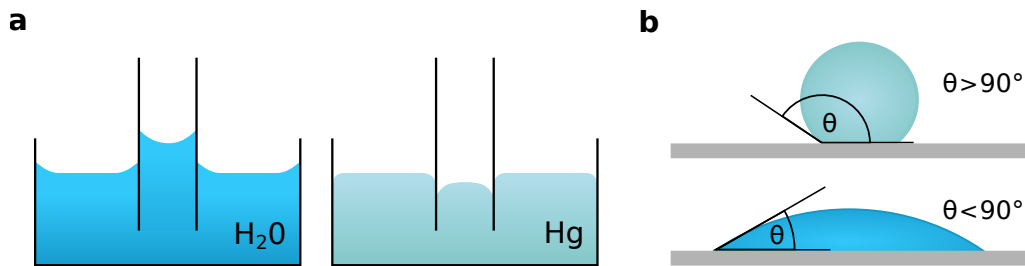


Figure 1.1. Capillary action and wettability. a) Demonstration of the competition between adhesion and cohesion with liquids in capillary tubes. While in the case of water adhesion dominates, mercury has stronger cohesion forces. b) In equilibrium, the contact angle  $\theta$  quantifies the wettability of a surface by a liquid.

Hence, complete wetting and the strongest adhesion is achieved for  $\theta = 0$ . For high values of the contact angle, i.e.  $\theta \gtrsim 160^\circ$ , wetting and adhesion is highly unfavourable. The latter situation is known from the so-called “lotus effect” [362].

### 1.2.2 Biological Adhesions

Animals and plants have developed different strategies for strong, but often reversible adhesion. A remarkable example for reversible dry adhesion is the gecko that clings to vertical and overhanging surfaces with its toe pads. The toe pads exhibit a complex, hierarchical structure of millimeter-sized lamellae, see Fig. 1.2a. The lamellae are made of setae, up to 100  $\mu\text{m}$  long, hair-like structures with a diameter of few micrometers [248]. Setae terminate in nanometer-sized plates called spatulae which provide the surface for attractive Van der Waals forces. Other debated interactions include electric charges and capillary effects [248]. Because every seta generates an adhesive force of tens of micronewton, the toe pad supports a multiple of the gecko’s body weight. Nevertheless, geckos can lift their toes and detach in tens of milliseconds with ease [12]. Next to the strong adhesion and low detachment forces, several other features are remarkable about gecko adhesion. The toe pads stick not only to dry, smooth, and clean, but also to dry, wet, and rough surfaces. Additionally, they exhibit both active and passive self-cleaning, so that dirt is removed from their toes while walking.

Other terrestrial animals, e.g. tree frogs, use adhesive toe pads as well, which allow them to climb on almost all surfaces. In contrast to the gecko, the surface of tree frog toes consists of hexagonal epidermal cells, each covered with thousands of nanopillars. The channels between the cells are filled with fluid and contain mucous glands. The frogs adhere via wet adhesion, i.e. by a combination of surface tension and viscous forces [21]. Many spiders, beetles and flies exhibit legs or feet with setae or similar structures as well. Smooth adhesive toe pads are found for example in ants, bees, grasshoppers and cockroaches [91]. The smooth surface adapts as a whole to the substrate surface, even if it is rough. Some hairy or smooth attachment pads additionally secrete a liquid for wet adhesion [93, 120].

Under water, many adhesion strategies involve interlocking, suction, and gluing. The abalone is a sea snail with a muscular pedal foot, which is covered with setae and fibrils [119]. An interplay of suction, Van der Waals forces, and capillary forces contribute to a strong normal adhesion force [207]. Marine mussels generate a strong adhesive glue by means of an external structure, the byssus, see Fig. 1.2b. The byssal threads end in a dense plaque with different adhesive proteins, but also metal [301]. The adhesive proteins allow a remarkably robust underwater attachment that persists even under strong sea currents. Permanent underwater adhesions are also found in tubeworms and barnacles [119].

Similar to animals, plants have developed several mechanisms to attach to their surrounding. Adhesion in plants is predominantly not reversible. The species of ivy climb other

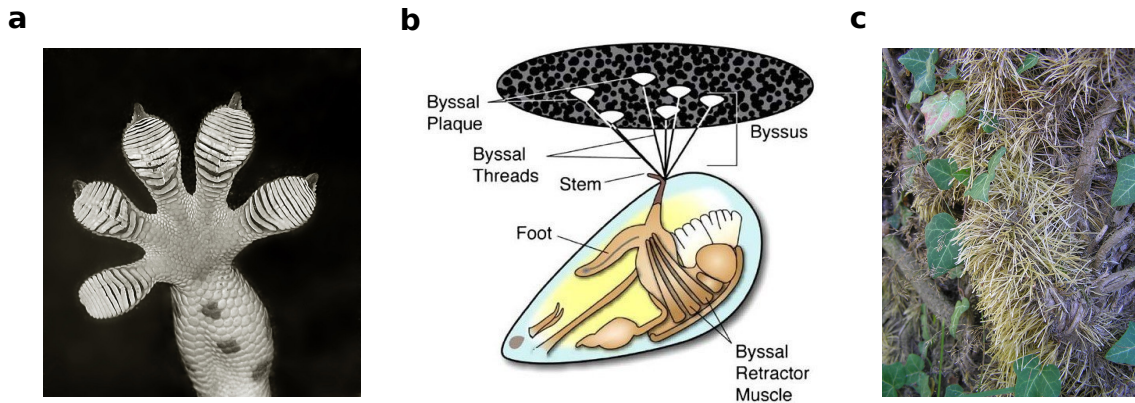


Figure 1.2. Examples for biological adhesion structures in animals and plants. a) Adhesive toe pads of a tokay gecko. Photograph by David Clements, 2006, public domain [78]. b) Anatomy and byssus structures in blue mussels [301]. Copyright 2007, CC-BY-NC, Springer Science Business Media, LLC. c) Stems of rootlets in *hederia helix* (common ivy). Photograph by Beentree, Copyright 2005, CC BY-SA 3.0 [26].

plants, but also rocks and other surfaces by means of small hair-like roots, see Fig. 1.2c. Algae are famous for their rapid and permanent attachment to other organisms and rocks. They establish a first contact via adhesive proteins and afterwards secrete extracellular polymeric substances for long-time adhesion [119]. Carnivorous plants use adhesive glues to capture and trap insects. Sundew, for instance, creates droplets of a sticky mucus on the surface of their leaves or tentacles [119].

Besides in animals and plants, adhesion also plays a major role on the level of individual cells. Bacteria that reach the surface of a substrate experience a sum of forces, which result from attractive Van der Waals, steric, electrostatic, and hydrophobic interactions. The microscopic interactions are hence the same as for climbing animals or strongly attaching mussels and plants. If the repulsive forces are not too strong, the bacterium can establish contact to the surface via several mechanisms [29]. Frequently, bacteria employ extracellular appendages, such as flagella, curli, or pili, with adhesive proteins for initial attachment. Subsequently, the contact can mature and strengthen to achieve permanent adhesion. This process typically involves a repositioning of the cell body to increase the contact area, the production of adhesin molecules or a rearrangement of the appendages. Irreversible attachment of bacteria to the substrate initiates colonization and biofilm formation, see Ref. [128] for a review.

In eukaryotic cells, the adhesion between two cells or a cell and a substrate involves non-covalent receptor-ligand bonds, which also depend on Van der Waals and electrostatic forces like hydrogen bonds [2, 114]. Different families of integral membrane proteins are specialized in forming the contact to adjacent cells, the extracellular matrix or other substrates. These cellular adhesions play a vital role in animals and are involved in

numerous biological processes, such as embryonic development, cell migration and wound healing [39, 186, 287]. As one major motivation for this thesis, they will be discussed separately in Chapter 2.

### 1.2.3 Biomimetic adhesives

Both reversible and permanent biological adhesions have fascinated scientists for decades. Observation and analysis of relevant components and their complex interplay inspire and guide the design of new biomimetic adhesives. Natural and ecofriendly materials experience a high demand in times of increasing environmental awareness. Furthermore the unique and outstanding features of biological adhesions drive the attempt to replicate them. Many applications are found in our every day life, such as glues, scotch tape and Velcro. Biological adhesions are interesting for numerous industrial products, e.g. rubber and coatings. Close to the original function of biological adhesions are systems for locomotion, drug delivery, tissue engineering and wound healing.

Reversible dry adhesions in animals are often implemented via complex hierarchical structures that end with nanometer sized objects like pillars or spatulae. Gecko toe pads motivate the design of climbing robots and self-cleaning, re-attachable adhesives based on arrays of nano- to micrometer-sized pillars [12, 133, 356]. For permanent adhesions, the adhesive glue produced by mussels is a role model because of its strength and durability. Additionally, mussel adhesion is suggested to depend on degradable proteins with low immunogenicity, an attractive feature for biomedical use [301]. However, many components of the mussel byssus and adhesion plaque are subject of current research and not well known. Recently, progress has been made on mimicking robust attachment under wet conditions, but the complex interactions at the interface are still a limiting factor [364].

Ongoing and future research will contribute to a better understanding of the intricate interplay between substrates and biological adhesives. So far, many artificial adhesives are motivated by large systems, like gecko and mussel adhesion. Technological progress from the last decades allows us now to study the underlying mechanisms on the nano- and micrometer scale. A comparison of the few examples presented here already uncovers that there are similar key principles of reversible adhesions, and these are also found on the cellular scale. Therefore not only the biological adhesions in animals and plants, but also cellular linkages offer promising model systems for future bio-inspired adhesives.

## 1.3 Mechanobiology of cells

Cells are the structural and functional units of living organisms. Their plasma membrane forms a protective and stabilizing border with the extracellular space. At the same time, the membrane functions as a contact zone at which permanent exchange of material and

information takes place. Since not only the cell but also its surrounding are highly dynamic systems, physical forces are constantly at play during a cell's life-cycle. These forces can be generated and act in the intracellular space, e.g. for purposes of transport or cell division. Alternatively, force can be transmitted across the plasma membrane inside-out or outside-in, as in the case of cell migration. The field of mechanobiology studies the response of cells and tissues to mechanical stimuli. There is growing evidence that most cellular processes are either crucially depending or at least influenced by force. Therefore research in this field is not an end in itself, but paves the way for advances in biomedicine and bioengineering [117, 170].

It is well known from basic laws of physics that the direct response to force, typically a deformation, depends on the mechanical properties of the deformed material. In this context, cells are often regarded as an elastic solid or as a liquid supported by an elastic cortex [157]. This assumption is reasonable, because water makes up approx. 70% of the cellular volume and structural stability is provided by macromolecular networks. Nevertheless, cell models inevitably simplify the anisotropy and heterogeneous composition of cells, which lead in general to a nonlinear mechanical response [253]. Additionally, environmental conditions and the origin of forces vary greatly. Externally generated stresses result from physical activity, e.g. breathing, muscle contraction and blood flow, but they are also present as tension and compression within tissues or take effect as hydrostatic pressure. In accidents, collisions cause large impacts.

Independently of how and where they are generated, natural cellular forces are typically on the order of pN or nN. The related lengths range from tens of nm for molecules to tens of  $\mu\text{m}$ , the typical size of an animal cell [2]. Therefore tensions are often measured in units of pN/nm or nN/ $\mu\text{m}$ . Stresses and pressures are expressed in pascal or kilopascal, since  $1 \text{ pN}/\mu\text{m}^2 = 1 \text{ Pa}$  and  $1 \text{ nN}/\mu\text{m}^2 = 1 \text{ kPa}$ . The Young's modulus describes the ratio of stress to strain and has the same dimension as stress. Typical stiffness values in the mammalian cellular environment range from 100 Pa in brain tissue to 10 kPa in muscles and reach 10 GPa in bones [92, 289]. Cancerous tissue typically exhibits a higher stiffness than its surrounding, which favours tumor growth [141].

Mechanical stimuli can act on the cell as a whole, for instance in the case of a hydrostatic pressure. However, there are many intricate force perception and transmission pathways along individual molecules and structures, which allow a precisely controlled and regulated response. In the following, the most important mechanosensitive components of eukaryotic cells are introduced.

### 1.3.1 Mechanosensitive cell components and structures

Despite the complexity and great diversity within living organisms, the building blocks for the mechanosensitive modules are largely preserved. In animal cells, two mesh works

## Introduction

contribute crucially to force transmission: the intracellular cytoskeleton and the extracellular matrix (ECM). The plasma membrane with its integral proteins and ion channels connects these two elements.

The cytoskeleton pervades the intracellular space and provides structural stability. The main components, filamentous actin, intermediate filaments and microtubules, are sketched in Fig. 1.3. Among these three, actin has a key role as an active building material [17]. Monomeric actin (G-actin) is constantly assembled at the barbed end of twisted filaments (F-actin) and is disassembled at the pointed end, leading to a treadmilling mechanism. In branched, bundled or disordered arrangements, actin filaments form different kinds of networks that span the cytosol. In many cell types, a thin, but dense actin network, the actin cortex, is located below the plasma membrane and controls cell morphogenesis [75]. Migrating cells often exhibit lamellipodia at the leading edge, in which chemical energy is used to push the membrane for spreading and migration. The lamellipodium is followed by

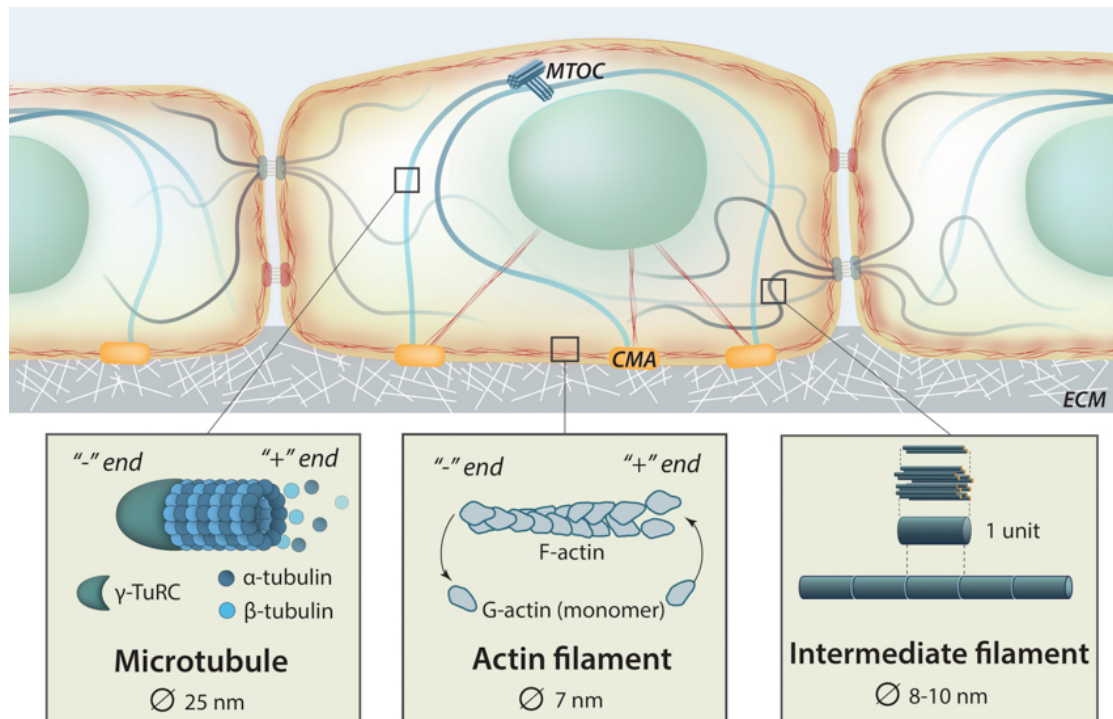


Figure 1.3. Main components of the cytoskeleton. Actin filaments are found close to the plasma membrane and pervade the cytosol, thereby connecting cellular matrix adhesion (CMA) sites with each other and with the nucleus. Microtubules are linked to the microtubule-organizing center (MTOC) and provide platforms for intracellular transport. Intermediate filaments connect adhesive structures at the surface with organelles. The cytoskeleton is influenced by the extracellular matrix (ECM) properties and contacts to neighbouring cells. Copyright 2009–2018, CC BY-NC 4.0, The National University of Singapore [229].

the lamellum, a contractile module with different actin structures, like bundles of stress fibers. These contractile bundles consist of crosslinked filaments and myosin II motor proteins and in many cases they terminate in cell-matrix adhesions. The motors slide filamentous actin of opposing polarity against each other and thus generate forces. This actomyosin network is the basis for cell contractility. The movement of actin from cell edges towards the center due to myosin activity is called retrograde flow [254].

Like actin, microtubules are polar filaments that can grow and shrink. They are stiff polymers in the shape of hollow tubes that offer tracks for motor proteins like kinesins and dyneins [117, 170]. Additionally, microtubules are the main components of the mitotic spindle, which is important for cell division [319]. Intermediate filaments are a diverse group of nonpolar proteins. Vimentin, keratin and lamin connect the nucleus with other organelles and adhesive structures and thus provide structural integrity. The protein family of plakins connects actin filaments, microtubules and intermediate filaments to a large network.

The second mesh work that crucially regulates force sensing and transmission is the ECM. The ECM is the natural environment of tissues and organs in animals. Therefore its composition and properties affect vital processes, such as cell shape, development and migration [95]. The matrix consists of typically long polysaccharides (glycosaminoglycans), fibrous proteins such as collagen, and various glycoproteins, e.g. laminin and fibronectin. A crosslinked network of elastin can provide high elasticity, but in general the biochemical and biophysical properties differ strongly within an organism [2].

Since mechanical signals need to be transmitted across cell boundaries, the plasma membrane contains several mechanosensitive structures. Among these are transmembrane channels and receptor proteins. The receptors are the basis of cellular adhesion sites and connect the cytoskeletons of adjacent cells or the cytoskeleton to ECM ligands. Cellular adhesions close an important gap in the force transmission pathway across cells and tissues. They will be discussed in detail in chapter 2.

In summary, the different mechanosensitive components of multicellular organisms, the cytoskeleton, the ECM, and the plasma membrane, are intricate structures with many different components. However, they can also be considered as one large mechanically sensitive machinery, because they are in direct contact. The contact is established by the surface of cells at all times. Additionally, integral adhesion proteins establish a specific, force sensitive linkage between cells and to the extracellular space. Along these pathways, force can be transmitted repeatedly and in a regulated manner, which is a prerequisite for the conversion of mechanical signals into a robust cellular response.

### 1.3.2 Mechanotransduction

The ability to turn a mechanical signal into a biochemical response is termed mechanotransduction [95, 191, 259]. Mechanotransduction starts with a mechanical stimulus and mechanosensing. Once a stress is perceived by a mechanosensitive element, it is transmitted along its mechanical linkages in microseconds. Since it is often required to transmit forces from or to the extracellular space or across multiple cells, mechanotransduction is often receptor-mediated [69]. The propagating signal causes modulations, such as changes in protein dynamics and conformation. Common examples are deformations, displacements, unfolding, cluster rearrangement, or opening of ion channels [69, 278, 335]. These modulations in turn alter binding affinities, regulate enzyme activities, or activate biochemical signalling pathways, which feed back into the mechanosensitive system or trigger other cellular mechanisms [335, 339]. Thereby, the fine-tuned response to mechanical signals affects manifold processes, locally and globally.

The forces that are generated or experienced by the cell directly regulate cytoskeletal structure and its polarization, and hence cell shape, organization, and adhesion. In many cases, the contractile activity of the cell is an important factor for a robust mechanoresponse. Some cells exploit the mechanical signals to collect information about their surrounding. In a process termed rigidity sensing, cells probe their environment mechanically by pulling on proteins or neighbouring cells [283]. Thereby, cells “measure” extracellular properties like matrix stiffness or the density of embedded ligands, which influences a variety of processes, e.g. cell growth, adhesion, and migration [335]. The motion of cells that is guided by stiffness gradients is termed durotaxis [214, 256]. Durotactic motion has not only been observed for single cells, but also for multicellular clusters [186, 313]. Furthermore, matrix elasticity and force influence genetic responses, such as cell proliferation and differentiation of stem cells [106]. Therefore, the proper transduction of mechanical signals is important at all stages of life, from embryogenesis to tissue homeostasis and apoptosis [95, 117]. Accordingly, perturbation of the mechanical pathways is associated with many pathological conditions and diseases, e.g. arthritis, osteoporosis, and deafness. Disruption or impaired cellular force response over a longer time period can cause atherosclerosis and promote cancer metastasis [95].

Despite progress in detecting the numerous force-dependent processes, many steps in mechanotransduction, especially on the microscopic level, are still poorly understood. A better understanding of cellular components and mechanisms may serve as a door-opener for new insights on mechanically regulated processes and shed light on healthy and pathological cell function.



## 1.4 Outline of the thesis

The thesis is organized as follows: Chapter 2 provides an account of different forms of cellular adhesions and of the current methods and models in adhesion research. It serves as background and basis for the models discussed in Chapters 3, 4 and 5. In Chapter 3, the one-dimensional model for a single cluster that is subject to pulling forces is introduced. The case of an adhesion cluster under shearing forces is treated in Chapter 4. The cluster model is generalized to arbitrary force directions in Chapter 5. Finally, Chapter 6 summarizes the main results and concludes the thesis with an outlook. Additional information on the mathematical background and a short introduction to the field of stochastic chemical reaction kinetics are given in the appendix sections A.1 and A.2.



# Chapter 2

## Biological background:

### Cellular adhesions

The discovery of cellular adhesion molecules dates back almost half a century. The contact areas between a cell and an underlying substrate were described first in the 1960s and 1970s [1, 84]. The transmembrane protein that acts as a surface receptor within these “dense plaques” [1] was given the descriptive name *integrin* in 1986 [316]. By the end of the 1980s, a whole family of integrins for different extracellular ligands had been discovered [167]. The full picture of a complex adhesion protein network started to emerge with the discovery of proteins like vinculin and talin, which assemble on the cytoplasmic site of cell-ECM connections [40–42, 130]. At around the same time, transmembrane proteins that establish cell-cell contacts were identified [314] and termed *cadherins* because of their calcium-dependent functioning [352, 353]. When related proteins were found, the previously discovered members got the name “classical cadherins” [45, 340]. Because they establish the connection between the intracellular space and the cell’s environment, integrins and cadherins are fundamental components of cellular adhesions. Other major superfamilies of cellular adhesion molecules are selectins and the immunoglobulin (Ig) superfamily.

The study of adhesions has expanded into an interdisciplinary research field. Advances in experimental methods, in particular single-molecule techniques, promote the progress of knowledge about cellular adhesions. Theoretical models and simulations further provide useful explanations and predictions, especially for cases in which *in vivo* or *in vitro* studies are unfeasible or limited. With this in mind, this chapter starts with the current understanding of cellular adhesions and their functions. Special attention is given to two adhesive structures, adherens junctions and focal adhesions, and their role in mechanotransduction. Afterwards, the experimental methods that led to today’s picture of adhesions are briefly presented. Finally, the focus turns to theoretical approaches that aim at the description and explanation of adhesive structures on the level of single connections or local clusters of bonds. The chapter closes with a discussion of the open questions addressed in this thesis.

## 2.1 Overview

Broadly, cellular adhesions can be divided into two categories; those that build structural connections between two cells or between a cell and the ECM. In both cases, it is typically not a single molecule that constitutes an adhesion. Instead, clusters of protein bonds, ranging from the nanometer to the micrometer scale, with potentially hundreds of different molecules, are observed at adhesion sites. Despite their complexity, a common feature of cellular adhesion clusters is their regular and organized structure [30, 174].

There are several benefits of cluster formation over relying on a single connective molecule. Since biological bonds rupture eventually, multiple bonds enable long-lasting networks with concurrent individual rupture and rebinding events. Weak binding affinities are therefore sufficient and sometimes even favorable, because they allow a rapid assembly and dissociation. Thereby, durable and yet flexible adhesions are established. Additionally, mechanical cues can be distributed among several bonds. A cluster can thus fine-tune its response via bond recruitment or dissociation and potentially withstand higher forces. Finally, the assembly of different molecules with distinct properties within a single cluster promotes diversity and specificity. Distribution of tasks and multiple pathways ensure robust functioning, even when single components may be impaired. On the other side, increased complexity requires highly regulated and coordinated mechanisms. Cellular adhesions are therefore not simple and static functional modules, but rather comparable to dynamic organelles.

### 2.1.1 Cell-cell contacts

Contacts between cells are important to maintain tissue integrity and to exchange molecules or signals. Multiple kinds of adhesive structures connect the plasma membranes of cells for these purposes. A few examples are shown for the case of an epithelial cell in Fig. 2.1a. The most prominent cell-cell adhesions are based on proteins from the cadherin family. The common motif of all cadherins is a repeating amino acid sequence: the extracellular cadherin domain. The 18 classical cadherins in vertebrates exhibit five of these domains and play an important role in cell-cell contacts [297]. Already at early stages of life, expression of different cadherins regulates cell sorting and morphogenesis [193]. The first adhesive contact is established by two cadherins that form a homophilic bond in the intercellular space. Cadherin clustering and the recruitment of adaptor proteins in the cytoplasm lead to large macromolecular complexes that connect the cytoskeletons of neighbouring cells. In adherens junctions (Fig. 2.1a), cadherins bind via adaptor proteins, like catenin and vinculin, to actin filaments. More than 160 different proteins have so far been identified as a part of this cytoplasmic molecular network, sometimes also referred to as the cadherin adhesome [357]. Adherens junctions appear in various kinds of tissue, e.g. the endothelium,

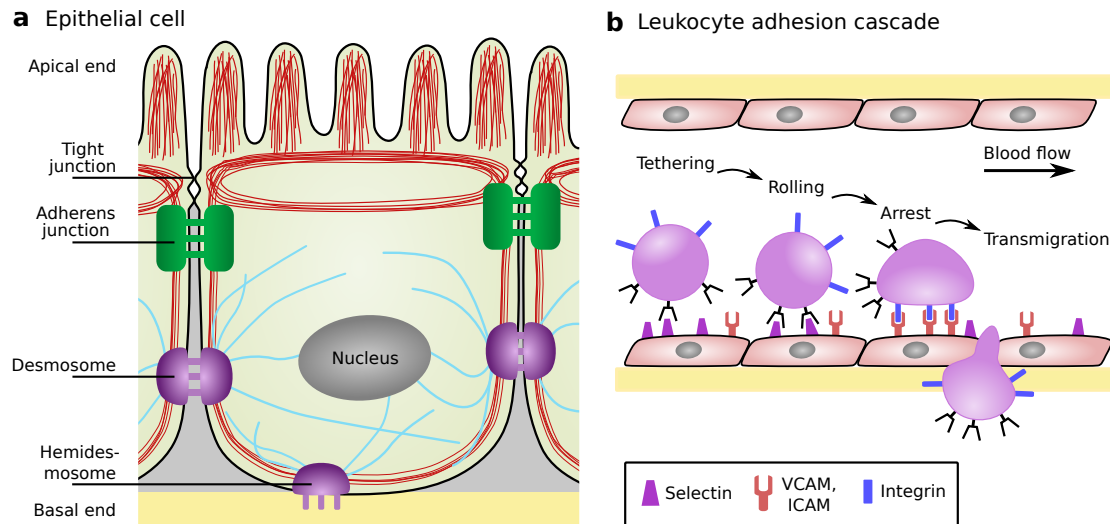


Figure 2.1. Forms of cell-cell adhesions. a) Epithelial cells establish contacts to their neighbours via adherens junctions, which are linked to the actin cytoskeleton, and desmosomes, which bind intermediate filaments. Tight junctions create a barrier between the apical and basal side. Based on a figure in [224], Copyright 2009–2018, CC BY-NC 4.0, The National University of Singapore. b) Leukocyte rolling on endothelial cells is mediated by selectins. They are slowed down and stopped by integrins, ICAMs and VCAMs, so that the leukocyte can enter the neighbouring tissue. Based on a figure in [242], Copyright 2018, CC-BY, Morikis and Simon.

epithelium, fibroblasts, muscle cells, neurons and astrocytes [191]. The multiple operation sites indicate their exceptional importance for cells. Therefore, adherens junctions and their functions are discussed separately in section 2.2.

Non-classical cadherins play a role in diverse tissues, e.g. in epithelial and inner hair cells, and in brain tissue. In many cases their function is not well understood [37]. One example for adhesion structures based on non-classical cadherins are desmosomes, see Fig. 2.1a [89]. The intracellular domains of desmoglein and desmocollin establish a connection to keratin intermediate filaments via desmosomal plaque proteins, such as plakoglobin and desmoplakin. Desmosomes allow a strong cell-cell coupling, which is why they appear in cells subject to large mechanical stresses. Examples are the epidermis and cardiac muscle tissue. In addition to strong adhesion, it is assumed that they also influence signalling processes in embryonic development, tissue homeostasis, and wound healing [329].

Cadherins provide the basis for several other adhesive structures. A special kind of adherens junction appears in epithelial cells close to the apical end. In these zonula adherens, cadherins circumscribe the whole cell and stabilize its shape [196]. Zonula adherens are closely connected to so-called tight or occluding junctions. In most vertebrates, tight junctions are found above zonula adherens at the apical end of epithelial cells, see Fig. 2.1a.

They are formed by claudin, occludin, and junctional adhesion molecules [77]. The junctions connect opposing plasma membranes tightly around the whole perimeter of each cell and restrict the passage of liquids, ions and molecules. The tight sealing thus creates a barrier between the basal and apical side of epithelial cells [57].

Among the superfamilies mentioned above, also selectins mediate cell-cell contacts and they depend, like cadherins, on the extracellular calcium concentration. The three known selectin family members E-, L-, and P-selectin are expressed in endothelial cells, leukocytes, and platelets, where they mediate mostly transient adhesions [202]. Selectins share a similar structure with a lectin domain on the extracellular side. In vertebrates, the main task of selectins is to regulate leukocyte movement in the bloodstream to lymphoid organs or inflamed tissue, see Fig. 2.1b. Selectin contacts can rapidly form and break in order to allow leukocyte rolling on vascular surfaces. The activation of integrins slows the process down and facilitates migration to the inflammatory tissue [231]. Therefore, selectin-based adhesions play a major role for the immune system and the response to inflammation. However, tumor cells can exploit the same mechanism, so that selectins are involved in cancer metastasis as well [71].

An example for calcium independent cellular adhesion molecules in cell-cell contacts are members of the immunoglobulin family. Proteins such as NCAM, ICAM-1, or VCAM-1 (neural, intercellular, or vascular cell adhesion protein) share an immunoglobulin domain in their extracellular structure. They are expressed in endothelial cells, where they also take part in leukocyte rolling and arrest by binding to leukocyte integrins, see Fig. 2.1b [231].

### 2.1.2 Cell-matrix contacts

Cell-matrix interactions play a similar structural role as cell-cell adhesions: they stabilize the cellular shape and position by anchoring them to their microenvironment. Cell shape and its control by adhesions is for instance an important factor in embryogenesis and cell division [318, 319]. Structural stability is however only one of many functions. Cell-matrix adhesions establish a bidirectional pathway for mechanical signals. Thereby, they allow communication with the outer world and a response to external stimuli. The process of cell migration combines many of these mechanisms [81]. To fulfil their function, adhesions need to provide a strong connection, but at the same time they need to stay dynamic for quick adaptation.

The most important examples for cell-matrix adhesions are based on integrin dimers. Some of them are depicted in Fig. 2.2. Nascent adhesions typically form at the lamellipodium, grow to focal complexes at the lamellum and later reach mature stages as focal or fibrillar adhesions in the central and rear regions of cells, see Fig. 2.2a. As a common motif, all of these adhesions connect the extracellular ligands to actin filaments. Their structure, the different maturation steps and their mechanosensitive response are discussed

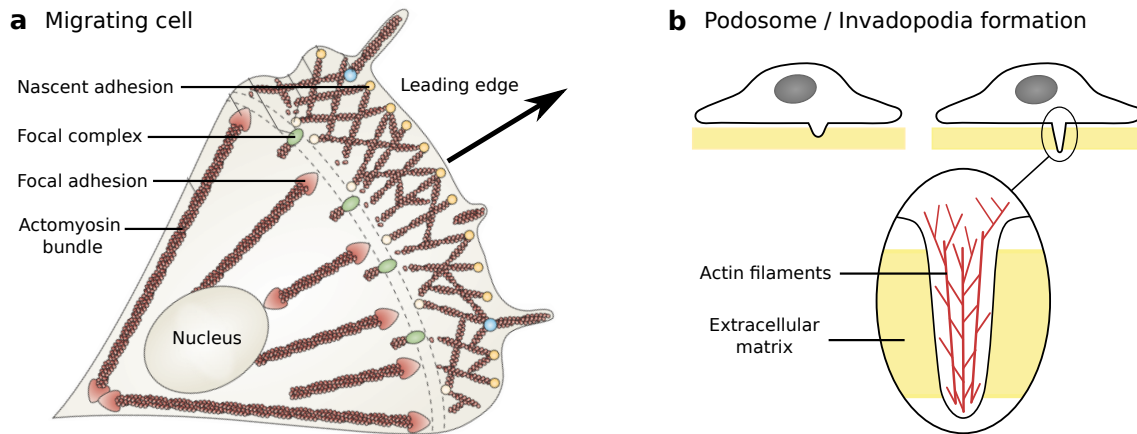


Figure 2.2. Forms of cell-matrix adhesions. a) In migrating cells, nascent adhesions rapidly form in the lamellipodium close to the leading edge. Few of them mature into focal complexes at the interface to the lamellum. Focal adhesions are associated with stress fibers in the central and rear regions of the cell. They can further elongate and mature into central fibrillar adhesions (not shown). Based on a figure in [254], Copyright 2010, Nature Publishing Group, adapted with permission. b) Podosomes and invadopodia are dynamic protrusions, which degrade the extracellular matrix. While the term podosome refers to normal cell types, invadopodia are characteristic for cancer cells. Based on a figure in [230], Copyright 2009–2018, CC BY-NC 4.0, The National University of Singapore.

in section 2.3. A different example for integrin-based adhesions are hemidesmosomes that establish a link to the keratin intermediate filament network. They are found in basal epithelial cells, where integrins bind to extracellular laminins in the basement membrane, see Fig. 2.1a [336]. Other cell-matrix adhesions in which integrin is involved include podosomes and invadopodia, actin-rich protrusions of the plasma membrane, see Fig. 2.2b. Podosomes occur, when migrating cells need to cross tissue boundaries. The term invadopodia is typically used to describe cancerous cells and tissue. One of their specific functions is the degradation of the ECM [212, 244].

## 2.2 Adherens junctions

Adherens junctions connect actin bundles of neighbouring cells. They are found in various cell types and regulate crucial functions, such as tissue integrity, remodelling and collective cell migration. The section starts with a description of cadherin dimerization and clustering. Afterwards, an overview of some important adaptor proteins and the mechanosensitive features of adherens junctions are given.

## 2.2.1 Cadherin clustering

Adherens junctions are mediated by classical cadherins. Their ectodomain consists of five extracellular cadherin domains that are rigidified by three calcium ions at each domain interspace [297]. As a result, the ectodomain has a characteristic bent shape as sketched in Fig. 2.3a. Two opposing cadherins of neighbouring cells can interact in the intermembrane space and form a homophilic bond. They bridge the distance between both plasma membranes which is typically less than 40 nm [37, 191]. In the longer bond conformation, a part of the membrane-distal extracellular domain EC1 interacts with the EC1 domain of the binding partner, creating a “strand-swap” dimer (Fig. 2.3b). However, since the binding pockets are symmetric, the energy difference between monomers and strand-swap dimers is small [63]. A shorter conformation in which two cadherins interact at the last linker region between EC1 and EC2 is called “X-dimer” (Fig. 2.3b). Via an intermediate state, cadherins interconvert between both conformations. In single bond pulling experiments the mean lifetime of a cadherin-cadherin dimer was found to be on the order of  $10^{-2}$  s to  $10^{-1}$  s, depending on the applied force [267]. Under tension the bond lifetime of strand-swap dimers decreases. For X-dimers however, lifetime first increases up to a pulling force of approx. 30 pN and then decreases for higher forces. In the intermediate state, lifetime is independent of force [219, 267]. The strength of a cell-cell connection is achieved through local clustering of cadherin dimers. Lateral cis-interactions between cadherins of the same cell result in a dense two-dimensional lattice, see Fig. 2.3c. Thermally induced membrane

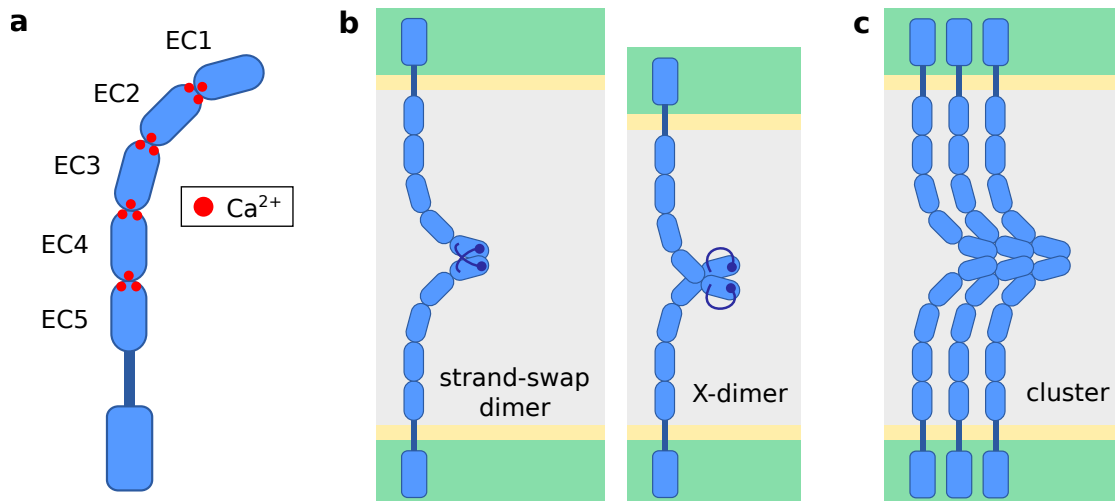


Figure 2.3. Cadherin dimerization and clustering. a) Classical cadherins consist of five extracellular domains, a transmembrane anchor and a short cytoplasmic domain. The structure is stabilized by twelve calcium ions. b) Two cadherins form a strand-swapped dimer or a X-dimer in the intercellular space. c) Lateral clustering strengthens the connection between both cells. Based on figures in. [225, 228], Copyright 2009–2018, CC BY-NC 4.0, The National University of Singapore.



fluctuations are shown to cause long-range, lateral cis-interactions and to regulate the trans-interaction to the neighbouring cell [121]. The resulting clusters can grow to diameters of approx. 50 nm. These nanoclusters assemble to larger, micrometer-sized complexes [348].

### 2.2.2 Adaptor proteins

On the intracellular site, cadherins interact with adaptor proteins to mechanically couple the cytoskeletons of adjacent cells. The short cytoplasmic tail binds to p120-catenin and  $\beta$ -catenin. It has been assumed that  $\alpha$ -catenin binds both  $\beta$ -catenin and actin simultaneously and thus establishes the connection to the cytoskeleton. In contrast to this classical view, experiments in 2005 suggested that only free  $\alpha$ -catenins bind F-actin, because  $\beta$ -catenin inhibits this bond [94, 344]. A few years ago, protein mapping by super resolution microscopy showed that the cadherin/catenin complex forms a layer that is connected to the actin cytoskeleton via an approx. 30 nm wide zone of mediator proteins [30]. Among the mediator proteins in the interface between cadherin/catenin and actin, vinculin has been ascribed an important role for adhesion strengthening [189, 328]. Vinculin can bind with its head domain to  $\alpha$ - and  $\beta$ -catenin and with its tail domain to actin.

The question how vinculin is recruited is not conclusively answered, but both  $\alpha$ - and  $\beta$ -catenin influence the process. Under tension,  $\alpha$ -catenin is suggested to undergo a conformational change in which certain molecular domains unfold. The unfolding step opens a previously buried vinculin binding site, thus triggering vinculin recruitment [345, 351]. This idea is supported by the finding of significantly lower vinculin levels in cells without  $\alpha$ -catenin [299]. Also cells that are lacking  $\beta$ -cadherin exhibit a weaker recruitment of vinculin [268]. In a system with vinculin mutants that do not bind  $\beta$ -catenin, cadherin expression is reduced and the adhesion fails [257]. Another factor that might contribute to vinculin recruitment is tyrosine phosphorylation [24, 30].

### 2.2.3 Mechanotransduction

The ability of adherens junctions to withstand mechanical stress is of vital importance for cell functioning. Together with other cadherin-based adhesions, they provide the physical link between cells and tissues. By stabilizing the cell-cell interface, they maintain tissue integrity and allow coordinated multi-cellular mechanisms. Yet, these adhesions do not simply constitute passive anchors, but instead they are dynamic macromolecular complexes. Cadherins couple actomyosin networks, so that they are involved in fundamental morphogenetic processes, such as cell sorting and remodelling, which affect embryonic development and cell turnover [217, 232, 259]. Adherens junctions also take part in collective migration and epithelial-mesenchymal transitions [25, 46, 80, 324]. Furthermore, adhesions act as signalling modules that probe their environment and adapt to the received cues.

In many of these functions, force plays a crucial role [191, 194, 332]. Under tension a positive feedback loop triggers adhesion strengthening and growth [189, 328]. The underlying mechanisms range from intrinsic properties of single adaptor proteins to the interplay of multiple molecules, e.g. in the case of vinculin recruitment. In epithelial tissues, remodelling processes under tension occur frequently and include cell intercalation, division, and delamination [259]. Additionally, when cells coordinate their movement by following leader cells with high traction forces, cell-cell junctions need to balance the tension to maintain tissue cohesion [39, 186].

## 2.3 Focal adhesions

Cell-matrix adhesions mediate the interaction between cells and the extracellular space. Hundreds of proteins aggregate into a complex network at the plasma membrane to connect ligands of the ECM to the cytoskeleton inside the cell. The family of receptor proteins that reach through the plasma membrane led to the name “integrin adhesome” [342, 358, 359]. These integrin-based adhesions are probably the best studied cell-matrix contacts [274].

In fact, there are many different types of integrin-based adhesions. Small and transient structures that mostly appear at the edge of spreading or migrating cells are called nascent adhesions or focal complexes. Under certain conditions they can mature into focal adhesions, which form more stable and regulated micrometer-sized clusters. Focal adhesions in turn can develop into fibrillar adhesions, more elongated structures that are located towards the cell center.

In this section, the focus lies on focal adhesions. After an introduction of single components such as integrin proteins and selected adaptor proteins, the different maturation stages and the structure of focal adhesions are described. Finally, the role of cell-matrix adhesions in the transduction of mechanical signals is discussed.

### 2.3.1 Integrin clustering

The integrin family of transmembrane adhesion receptors comprises 24 distinct members. All of them consist of two, non-covalently bound subunits. One of 18  $\alpha$ -subunits binds to one of eight  $\beta$ -subunits to form a heterodimeric protein [50]. Half of the identified integrins contain the  $\beta_1$ -subunit [164]. A common feature is a short cytoplasmic domain, a single-pass transmembrane helix and a long ectodomain, where the connection to the ECM or a substrate is established. On the extracellular side, integrins bind multiple ligands and vice versa. For instance,  $\alpha_4\beta_1$ - and  $\alpha_5\beta_1$ -integrin both bind to fibronectin, but  $\alpha_4\beta_1$  also binds to vascular cell adhesion protein-1 (VCAM-1). Other examples for ligands are laminin, fibrinogen, collagen, and the intercellular adhesion molecule 1 (ICAM-1) [164]. The cytoplasmic domain can be indirectly linked to the cytoskeleton via adaptor proteins

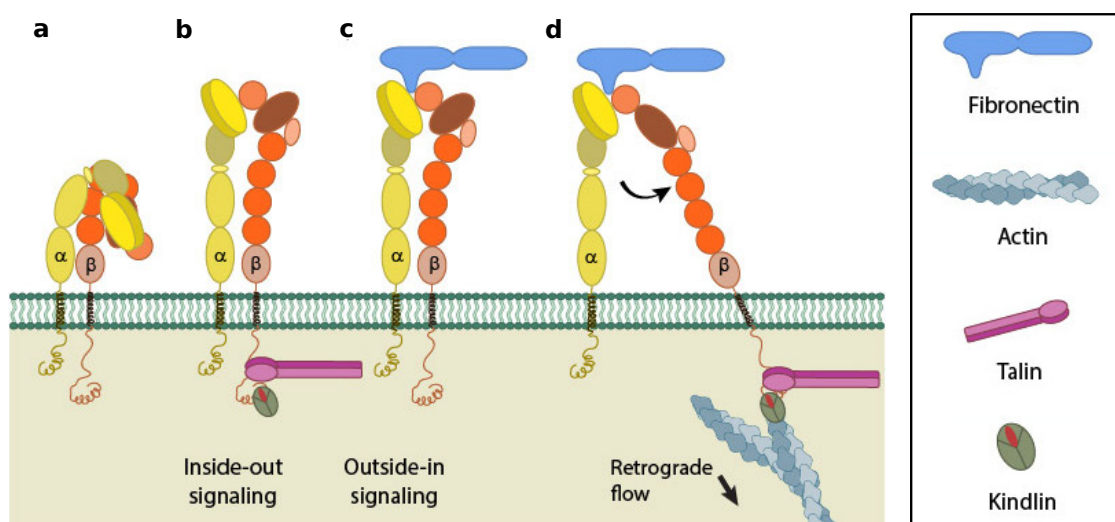


Figure 2.4. Steps of integrin activation. a) In the low affinity state, the  $\alpha$ - and  $\beta$ -subunit are in a bent-closed conformation. b) Activation via the adaptor proteins talin and kindlin tilts the integrin angle and separates the subunits. c) Activation via a thermally induced outside-in mechanism with ligand binding. d) In the high affinity state the link to actin is established. Force transmission stabilizes the connection. [226], Copyright 2009–2018 by The National University of Singapore, CC BY-NC 4.0

(see below).

Integrins are synthesized in the endoplasmic reticulum and transported to the cell surface in a bent conformation, see Fig. 2.4a [330]. In this inactive conformation, the transmembrane helices stay close and the extracellular domain extends only 11 nm from the surface [307, 349]. The shift to an extended-open conformation is termed integrin activation [311]. Possible intermediate states are shown in Fig. 2.4b,c. In the extended-open state, the cytoplasmic tails are separated and extend 19 nm from the cell, see Fig. 2.4d [349]. The upright conformation is associated with the high-affinity state, because the ligand binding site is open. In  $\alpha_5\beta_1$ -integrin, which is ubiquitously expressed, a 5000-fold increase in affinity has been measured [205]. Hence the process of integrin activation plays an important role for the onset of adhesions. A requirement for successful integrin activation is the presence of talin and kindlin [47]. In the classical inside-out scenario, talin competes with the  $\alpha$ -subunit for binding to the  $\beta$ -tail, see Fig. 2.4b. Binding of talin is regulated by kindlin and tilts the angle of the  $\beta$ -transmembrane domain. This process separates both subunits and enables ligand binding [298]. Alternatively, a thermodynamically regulated outside-in activation has been proposed, see Fig. 2.4c. Ligand binding occurs when integrins change from the bent-closed to the extended-open state due to thermal equilibrium fluctuations and bind immobilized ligands [311]. Successive transmission of force via talin stabilizes the active conformation [204, 205].

Activated integrins assemble into clusters. A simple energetic argument for clustering

is that it reduces the tension on single molecules [283, 311]. The tension along individual integrins is reported to lie in a range from few pN up to 40 pN [243, 338]. Clustering is regulated by the glycocalyx, which can be compressed by the cell to facilitate further integrin activation [311]. Findings suggest that already a small number of molecules are able to establish a cluster, as long as the ligand spacing is sufficiently small [14, 285, 294]. While a ligand spacing of less than 60 nm is required on rigid substrates, focal adhesions grow on soft substrates with a ligand spacing of 200 nm [56, 251]. Additionally, the availability of cytoplasmic proteins, lateral crosslinks, and probably other factors influence successive integrin binding [60, 298, 311].

### 2.3.2 Adaptor proteins

Adaptor proteins connect integrin receptors with the cytoskeleton. Together, they build a complex macromolecular network. From the hundreds of molecules involved, a core of 60 proteins has been identified as the “consensus adhesome” for cells connected to fibronectin [159, 160]. The observed components can be sorted according to their typical sequence between integrin and actin, or according to their interactions, which are often regulated in a switch-like manner [159, 358]. Although the reported network has grown immensely in the last decades, many mechanisms are still unknown. Here, only some of the most important adhesion proteins are introduced. Among those, talin and vinculin play an extraordinary role in force transduction.

Five proteins are reported to connect integrin and actin directly:  $\alpha$ -actinin, filamin, talin, tensin, and plectin [359]. In general, two or more proteins establish the connection. Other integrin-associated molecules include focal adhesion kinase (FAK), paxillin and integrin-linked-kinase (ILK), which are important for remodelling and signalling processes [149, 174]. Among the actin binding adaptor proteins are vasodilator-stimulated phosphoprotein (VASP), zyxin and vinculin [126, 132]. In Fig. 2.5a, a small integrin-fibronectin cluster is sketched. The different adaptor proteins connect the cluster to the actin cytoskeleton. Myosin motors generate contractile forces. The scaffold protein actinin crosslinks the filaments. The whole complex can be divided into functional layers. They are described in detail in 2.3.3.

#### Talin

Talin is an adaptor protein that directly links integrin to actin filaments. In mammals, two similar talin paralogues are expressed; while talin-1 is localized in diverse cell types, talin-2 is mostly found in muscle and neuronal cells [47]. Talin consists of a N-terminal, globular head domain and a C-terminal rod with 13 domains (R1-R13), see Fig. 2.5b. Head and tail domain are connected via a short and flexible linker.

Talin is recruited from the cytosol to the plasma membrane via RIAM (Rap1-interacting-

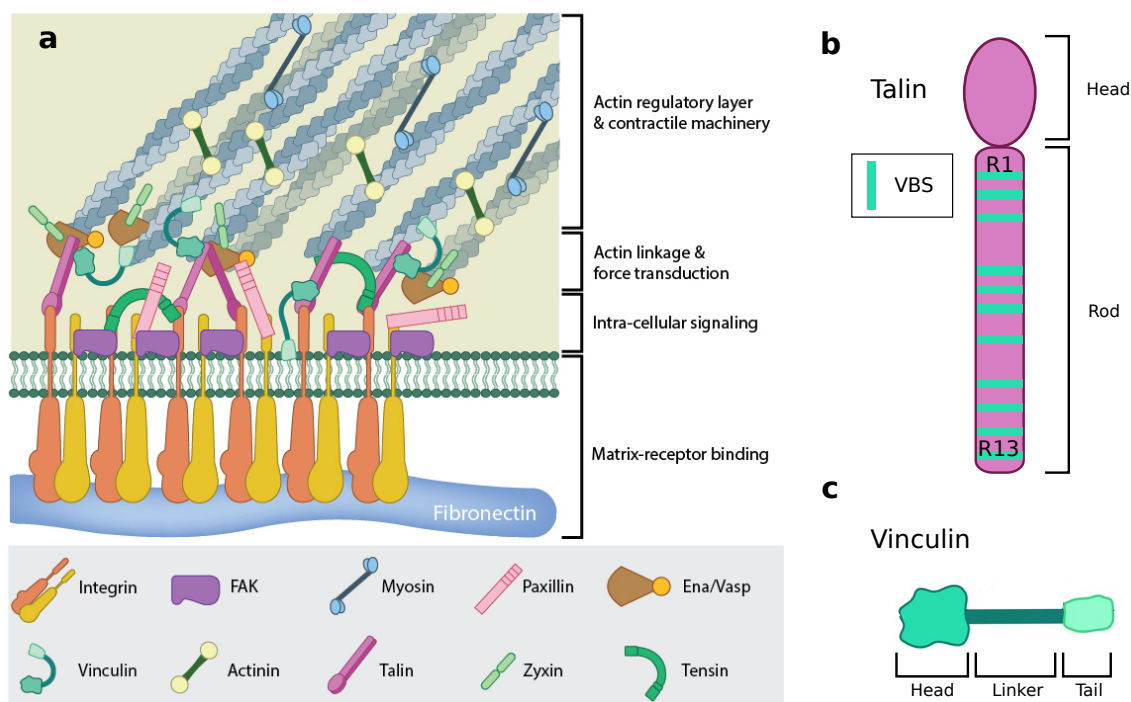


Figure 2.5. Sketch of a focal adhesion. a) The adhesion cluster connects extracellular fibronectin to the actin cytoskeleton via adaptor proteins. On the cytoplasmic side, it is organized in three functional layers. b) Structure of the adaptor protein talin with eleven vinculin binding sites (VBS). c) Structure of the adaptor protein vinculin, which binds talin and actin. [227], Copyright 2009–2018 by The National University of Singapore, CC BY-NC 4.0

adaptor-molecule) and needs to be activated before it can engage with integrins [47, 59]. Activation of talin enhances both integrin activation and actin binding. At an integrin binding site in the talin head domain, talin interacts with the cytoplasmic tail of the integrin  $\beta$ -subunit. However, a second integrin binding site is located at the talin R11 domain [140]. First experiments agree with the hypothesis that the additional integrin binding site promotes initial contact and further integrin clustering [61, 178]. The connection to the cytoskeleton can be established via three actin binding sites (ABS). Among these three, the C-terminal ABS3 in R13 is suggested to be most important for coupling to the cytoskeleton and assembling the adhesion. Subsequently, actin binding at ABS2 along R4 to R8 is triggered, so that the linkage is strengthened [8].

A critical step in adhesion maturation and strengthening is based on the mechanical response of talin. Under force, talin rod domains successively unfold and open previously buried vinculin binding sites (VBS). Thereby, stretching of talin leads to vinculin binding [156, 271]. The rod domain R3 exhibits the lowest mechanical stability and unfolds at a force of 5 pN [346, 347]. At forces around this value, rapid equilibrium unfolding and folding is observed, accompanied by a length change of approx. 20 nm [320, 346, 347].

Recent findings show that constant, linearly increasing, and also oscillatory signals induce unfolding. External noise passes however without effect. The R3 domain is hence compared to a fine-tuned frequency filter [321].

In the R3 domain, two of the eleven cryptic VBS along the talin rod are located. Experimental results suggest that, after unfolding of R3, two vinculin bind simultaneously, which is observed as a short contraction of 3 nm [320]. It has been shown that higher forces up to 40 pN lead *in vitro* to a progressive unfolding of all talin rod domains [148, 347]. Furthermore, vinculin recruitment locks the respective domain in its unfolded state, even after release of force [346]. Unfolding entails an increase in length, which agrees with the finding of 100 nm to 300 nm large extension fluctuations *in vivo* [220]. Reported values for the native, i.e. folded, length of talin vary between 50 nm and 80 nm [144, 220, 239, 347]. The length of wild-type talin in focal adhesions was determined as 97 nm, but with the possibility that talin is not completely folded [213]. Considering that talin spans a vertical distance between integrin and actin of around 30 nm only, a tilted orientation with an angle of approx. 15° relative to the plasma membrane is assumed [174, 213].

Talin orientation is likely to depend on the tension along the integrin-talin-actin link. During extension measurements as a response of unfolding, the tension across a single talin molecule is reported to stay below 10 pN [347]. This agrees with a different study, in which most talins are subject to forces from 7 pN to 10 pN and only a small fraction experiences forces higher than 10 pN [11]. Moreover, vinculin binding has been observed in a force range of 2 pN to 12 pN [271]. Tension along talin can vary within focal adhesions and further depends on substrate rigidity: lower tensions are measured on soft substrates and high tensions in regions of assembly [184, 185, 270].

In summary, several features of talin contribute to its unique role in cell-matrix adhesions. Talin is indispensable for integrin activation and cells lacking talin are not able to form mature adhesions [363]. Due to its long structure, it serves as a molecular ruler in the three dimensional organization of mature focal adhesions [174, 213]. Furthermore, its position between integrin and actin paves the way for its function as a mechanosensor.

## Vinculin

The adaptor protein vinculin is enriched in both cell-cell and cell-matrix adhesions. It consists of a head and a tail domain, connected by a linker region, see Fig. 2.5c. Vinculin has a high number of binding partners; vinculin head binds talin,  $\alpha$ -actenin, IpaA, and both  $\alpha$ - and  $\beta$ -catenins. The linker region offers binding sites for VASP, vinexin, ponsin, and Arp2/3. Vinculin tail binds for instance paxillin and F-actin [366]. However, all of these sites are masked in the closed, autoinhibited state, in which the tail is connected to both head and linker. Because of the strong interaction with an affinity of <1 nM it is assumed that more than one ligand is required for vinculin activation [79]. Several mechanisms for vinculin activation have been proposed which include a combined effect of talin and other

adhesion components, such as the phospholipid PIP<sub>2</sub>, actin, or phosphorylated paxillin [10, 55, 65, 72, 97, 255, 310]. A recent study suggests recruitment of talin-vinculin precomplexes to adhesion sites as an important step for adhesion maturation [152]. Accordingly, the ultimate pathways for vinculin activation are still under investigation.

In its activated state, the vinculin head binds to talin and the tail establishes a connection to F-actin. Therefore, vinculin plays an important role in the force transmission machinery of adhesions. The vinculin-talin connection drives integrin clustering and, as a result, adhesion growth and stabilization [97, 165]. Furthermore, it regulates recruitment and release of other adhesion components, such as paxillin and vinexin [53, 165]. In particular, vinculin binding to the talin R3 domain acts as an important switch [320, 346]. At the low force of 5 pN the domain unfolds and opens two cryptic VBS. Binding of vinculin enables a second talin-actin link at talin's ABS2, which reinforces the link and promotes maturation [8]. Recent experiments show that the stability of head-VBS interactions depends on the pulling geometry, suggesting that vinculin differentiates force directions and thus promotes maturation into a regularized shape [179]. Force transmission requires the interaction between vinculin tail and F-actin. However, vinculin does not act as a passive transmitter, but it regulates the organization and dynamics of F-actin [325]. In cell migration, vinculin is required for reducing retrograde flow and it promotes traction forces that pull the cell forward [53, 280, 325]. High forces along vinculin are measured at the leading edge of migrating cells, whereas lower forces are observed in sliding or disassembling adhesions. At stable focal adhesions, an average tension of 2.5 pN along vinculin is measured [145].

In summary, vinculin's position between actin and talin is the basis for its important role in cellular adhesions. Vinculin is already recruited to nascent adhesions where it promotes adhesion stabilization under force. It transmits mechanical signals between the actomyosin complex and ECM and regulates processes such as cell migration. Vinculin depletion leads to weaker adhesions with impaired cell spreading and migration [97].

### **2.3.3 Maturation steps and structure**

Activated integrin molecules aggregate into clusters in a hierarchical manner. The smallest adhesive cell-matrix structures are called nascent adhesions, which are shown in Figs. 2.2a and 2.6. They reach a consistent size of around 100 nm with a mean number of 50 integrins [61]. Their formation is independent of force, substrate rigidity, and contractility, but it involves adaptor proteins like talin, FAK, and paxillin. Additionally, actin polymerization is required [73, 282]. Nascent adhesions appear in the lamellipodium, close to the leading edge of migrating cells [73]. If they do not disassemble rapidly within tens of seconds or after few minutes, nascent adhesions grow to approximately 1  $\mu\text{m}$ -sized focal complexes at the interface of lamellipodium and lamellum [254], see Fig. 2.6. In contrast to nascent

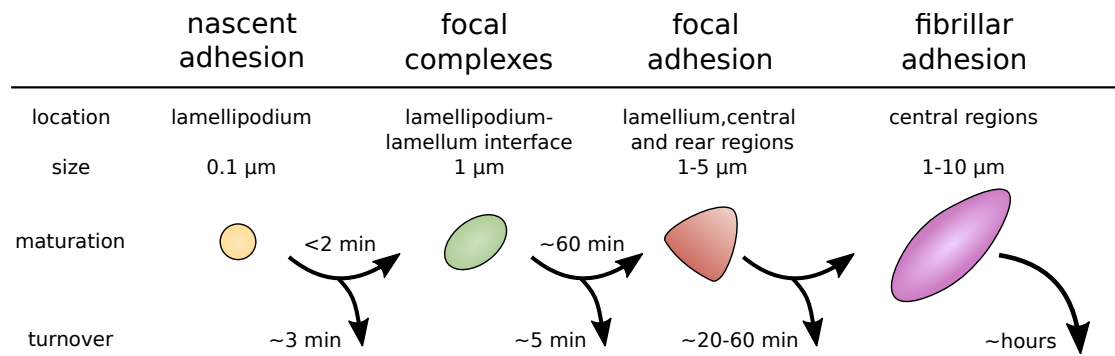


Figure 2.6. Stages of cell-matrix adhesions. The smallest adhesive structures are nascent adhesions. They mature to focal complexes and further to focal adhesions. Fibrillar adhesions are the largest and most durable structures along the maturation pathway. Values are taken from Refs. [61, 124, 126, 132, 289, 303, 333].

adhesions, focal complexes depend on myosin II activity [254]. Many focal complexes turn over within several minutes. Only a fraction matures from nascent to focal adhesions [73].

The maturation process is accompanied by the formation of short actin bundles along which the complex elongates [73, 249]. The actin bundles are crosslinked by myosin II and  $\alpha$ -catenin. Next to its role in regulating actin structure, myosin generates contractile forces that are transmitted to the developing adhesions. The resulting tension triggers strengthening of the molecular network in different ways. Adhesion bonds can be strengthened directly, whereas other molecules, e.g. talin, undergo conformational changes that lead to further recruitment and linkage reinforcement. The actomyosin contractility can be bypassed by an external pulling force, showing that tension per se plays a crucial role [272]. However, maturation is still observed, when myosin induced tension is reduced by 75% or more [249, 303, 334]. Therefore both the change in actin structure and the resulting force transmission are likely to influence adhesion maturation.

The transition to focal adhesions is further accompanied by an accumulation of adaptor proteins like VASP, zyxin, tensin, and vinculin. Thereby, the complex expands to a size of several micrometer [368]. Focal adhesions exhibit a high inner structural organization with at least three overlapping layers [174], see Fig. 2.5a. The integrin signalling layer close to the plasma membrane contains the cytoplasmic tail of integrins and several adaptors, such as FAK and paxillin. Talin and vinculin define the force transduction layer, because talin spans the gap of more than 30 nm between integrin and actin. The force transduction layer is followed by an actin-regulatory layer with VASP, zyxin,  $\alpha$ -actinin, and actin filaments.

The regulated structure of focal adhesions may create the false impression of a static entity. In fact, adhesions are subject to continuous changes and remodelling processes. Integrins undergo cycles of diffusion and immobilization within single clusters [276]. Accordingly, force transmission is not uniformly distributed along the cluster, but its maximum has been localized at the tip towards the cell's leading edge [261]. Furthermore, FRAP



experiments show that adhesion components dissociate and associate several times during the lifetime of a typical focal adhesion site of 20 min [211]. Talin is among the proteins with the longest residence time in focal adhesions, whereas FAK, paxillin, vinculin, and zyxin dissociate in tens of seconds [60, 199]. The residence time of vinculin has been shown to increase under force [97].

Eventually, the whole adhesion disassembles, but how this process is regulated remains poorly understood [166]. The turnover of focal adhesions occurs in central regions, or more often at the cell rear side, which allows effective cell migration. Associated steps are loss of traction and phosphorylation [88, 149]. Experiments also suggest that adaptor proteins are lost prior to actin-binding molecules and integrins [159]. The protein Kank2 for instance binds talin and thus uncouples integrin and actin [312]. This can result in an apparent sliding motion of the focal adhesion inwards, supported by the disassembly of integrins at the distal edge and integrin rebinding at the proximal edge [16].

Instead of disassembly at the cell rear, focal adhesions can also mature further into fibrillar adhesions, see Fig. 2.6. Fibrillar adhesions have an elongated structure and are located in the central regions and at the rear of cells. They specifically establish connections between fibronectin and  $\alpha_5\beta_1$  and show high levels of tensin [132]. With a lifetime on the order of hours, they belong to the most stable integrin-based adhesive structures [333].

### 2.3.4 Mechanotransduction

Cell-matrix adhesions are naturally positioned as force sensors and transducers. These forces can originate from intracellular processes, such as actomyosin contractility or actin polymerization, but they can also be applied externally, e.g. as shear stress from the blood flow or as tensile stress within tissues. Since tension is transmitted from actin via adaptor proteins to integrins and their ligands or vice versa, in principle every component within the adhesion complex can shape the response to mechanical cues. This response can take effect locally within a few seconds or minutes, but also globally and on a longer time scale of days, as in cell proliferation and differentiation [98, 106, 304]. Furthermore, the behaviour changes at different maturation stages. While nascent adhesions are suggested to form independent of force, the maturation steps to focal adhesions and fibrillar adhesions are mediated by tension [61, 249, 275]. Especially the activation of proteins like integrin, talin, or vinculin, and integrin clustering depend on force. Focal complexes and focal adhesions grow and strengthen under mechanical load [15, 272]. Recruitment of adaptor proteins to fibrillar adhesions is tension-independent, so that they, unlike focal adhesions, do not disassemble when tension is lost [15, 360]. Due to their complexity, only a few of the numerous molecular interactions and biochemical pathways that take part in mechanosensing are presented here; detailed reviews are given in Refs. [129, 156, 211, 312].

A common mechanism of mechanosensitivity is force-induced regulation of molecular

interactions, specifically binding dynamics. The most commonly observed bonds are weakened under force, resulting in a shorter lifetime. Several interactions in focal adhesions however show a strengthening up to certain force threshold. The lifetime decreases with force only after this initial regime. This “catch-slip” behaviour (see sec. 2.5) has been observed for instance in integrin-ligand interactions with  $\alpha_5\beta_1$ ,  $\alpha_L\beta_2$  and  $\alpha_V\beta_3$ , but also in adaptor proteins linkages, such as binding of vinculin to actin [66, 68, 161, 181]. Repeated stretching of  $\alpha_5\beta_1$ -fibronectin bonds results in greatly prolonged lifetimes. This effect is called cyclic mechanical reinforcement [182].

A second kind of mechanism is the recruitment of further cytoskeletal proteins to the adhesion. In thermodynamic models, it is proposed that force shifts the chemical potential or changes the local density of focal adhesions such, that free molecules enter the adhesion site [31, 247, 300]. The prominent path for protein recruitment however is paved by structural changes of proteins that open previously hidden binding sites or shift binding affinities. A paradigm for this process is vinculin recruitment after talin unfolding, as described above. But also other associated molecules, such as fibronectin and filamin, deform or undergo conformational changes in response to force [99, 198]. Instead of protein recruitment, protein stretching can also trigger phosphorylation events or whole signalling cascades [281, 315]. Downstream signalling molecules induce for instance delayed, orientation-specific focal adhesion disassembly, when cells experience sustained stretch perpendicularly to their long axis [67].

The response to forces that are applied to the adhesion site does not only depend on the number and type of cytoplasmic proteins, but also on the mechanical properties of the extracellular environment, i.e. the ECM or a substrate. Experiments with fibroblasts and endothelial cells show that traction force increases with substrate stiffness and spreading area [48, 214]. This dependency enables cells to indirectly measure substrate stiffness by mechanically probing their environment at adhesion sites, i.e. rigidity sensing [146, 240]. Rigidity sensing triggers a response that affects many processes, both at adhesion sites and at the full cell or tissue scale [92, 261]. Stiffness regulates the adhesion structure, dynamics, and its strength [74, 256, 331]. Furthermore, cell differentiation and proliferation are shown to depend on stiffness, promoting soft tissue types on soft substrates and rigid tissues on stiff substrates [105, 106]. However, response to stiffness is assumed to differ strongly with cell types and between single or adjacent cells [350].

In summary, focal adhesion assembly and functioning are strongly coupled to transmission and transduction of mechanical signals. Numerous mechanisms like protein activation, clustering, signalling, and sensing depend on externally or internally generated forces. A recurrent effect is tension-induced adhesion stabilization. Even though experiments by Riveline et al. and Balaban et al. observed this counterintuitive behaviour already twenty years ago, the molecular mechanisms are just starting to emerge [15, 272]. A major contribution is assigned to the adaptor proteins talin and vinculin which are recruited to

adhesion sites, stabilize them, and regulate further protein assembly [8, 145, 165, 185, 325]. Since strengthening depends on robust force transmission, an intact connection to the actin cytoskeleton is required. The retrograde flow generated by the actomyosin cytoskeleton regulates focal adhesions and reciprocally, adhesions model actin structure [125]. Further factors that influence adhesions and their stabilization are the properties of the extracellular matrix and ligands [28, 251, 293]. Finally, downstream signalling controls and affects both local and global dynamics [123, 305].

## 2.4 Experimental Methods

Experimental observations of cells and their response to mechanical cues have greatly improved our understanding of numerous biological processes. In turn, new findings feed back into the development of enhanced and refined experimental methods. A challenge lies in the fact that force cannot be measured directly, because it is obtained from other quantities, such as the deformation of a material with certain mechanical properties. These mechanical properties differ strongly for fluid, elastic or viscoelastic materials, so that methodology and analysis need to be carefully chosen. Cells behave in general as viscoelastic materials, so that time-dependent effects, e.g. relaxation, creep, and hysteresis need to be taken into account. The experimental methods for the study of cellular adhesions can be divided into two broad categories: active methods, in which external force is applied and passive methods, which observe the forces generated by the cell [22].

### 2.4.1 Application of external force

An extensively used technique with external force application is atomic force microscopy (AFM), reviewed for example in Ref. [175]. In this method, a sample is scanned by a soft cantilever with a sharp tip. In a distance of a few angstrom or nanometer, interactions between tip and sample result in a deflection of the tip. The deformation can be observed for instance with a laser. By precisely shifting the tip, the whole surface of the sample can be mapped with nanometer resolution, which is determined by the tip curvature radius. AFM offers high-resolution imaging of living cells, but also allows probing the sample mechanically. For this purpose, the cantilever is pushed into the sample to apply a precise force, which is controlled by the cantilever and tip properties. Force-distance curves record the deflection of the cantilever during approach and withdrawal, indicating interactions with the sample. From these curves, the Young's modulus and the elasticity of the sample can be inferred. Alternatively, the tip can be labelled with single molecules or whole cells for pulling experiments. Thus, the binding strength of receptors or whole adhesions can be measured [181, 219, 267, 304]. A detailed account of AFM in the field of cell mechanics and adhesions is given in [96]. AFM has the advantages that quantitative measurements

without a reference image are possible *in vivo* and in real time. However, scanning of a large surface might require hours. In this time, the assumption that sample and substrate behave like a homogeneous and well-defined system is in general inaccurate, especially for dynamic complexes like cells and their adhesion sites. Several modifications have been developed to overcome this drawback, see Refs. [22, 175].

There are several other methods in which pushing or pulling mechanisms are exploited to measure surface tension or other quantities. Micropipette aspiration belongs to the oldest techniques with a comparably simple set-up [157]. In the original procedure, pipettes with a radius in the micrometer range are used to locally aspirate portions of the sample. Aspiration pressure and surface tension determine the observed deformation. Due to the large pipette size, difficulties may arise from heterogeneous aspirated material. Additionally, the large invasion can interrupt cellular processes and morphology. Microindenter or microplates are available to compress or push whole samples or large fractions of it. Their large size is suited to study cells or aggregates of cells rather than intracellular components.

Tweezing methods allow probing samples contact-free with precise forces in the range from few to hundreds of piconewton and even nanonewton. Optical tweezers employ a focused laser beam to generate an optical trap. Close to the center, the trap behaves like a linear elastic spring. The calibration is complex, especially for *in vivo* studies, but highly localized and quantitative force measurements can be carried out. Next to the challenging setup, the focused laser beam can cause local heating and even sample damage. Nevertheless, optical tweezers are widely used for single molecule experiments [52, 245]. Magnetic tweezers trap magnetic particles in a gradient field generated by permanent magnets or electromagnets. The forces are typically larger than those generated by optical and tweezers, but also range from pico- to nanonewton. Moreover, also torques can be applied. Magnetic tweezers are used for molecules, cell and tissues, e.g. to pull on fibronectin coated beads that are attached to cells to study rupture kinetics [103] or to stretch single  $\alpha$ -catenin molecules to observe protein unfolding [345]. In a third tweezing method, so-called acoustic tweezers, sound waves are employed to manipulate cells. Due to their low intensity, acoustic tweezers are the most gentle option among the three tweezing methods presented here [22].

### 2.4.2 Observing forces generated by the cell

Passive methods, in which internally generated forces are measured, can be further divided into techniques with known material properties and unknown material properties [273]. A frequently used example from the first group is traction force microscopy (TFM) [291, 306]. In TFM, deformations of the cellular environment are measured that arise from forces exerted by the cell. This basic idea makes the method very suitable for the study of cellular adhesions, because the internally generated forces are transmitted via adhesion

sites to the surrounding. As a substrate, traditional TFM uses soft, but linear-elastic gels with a Young's modulus of few Pa to hundreds of kPa in which fluorescent beads can be inserted to visualize the elastic response [4, 125]. Surface traction stresses are calculated from displacements via inverse Fourier transformation or other approaches, e.g. finite element methods. Fine-tuned computational algorithms facilitate and improve the force reconstruction [151, 158, 163]. Since its first application, TFM has emerged as a versatile and thus powerful tool for the field of mechanobiology and cell adhesion [153, 262]. In the last decade, set-ups were developed to study cells embedded in three dimensional matrices to mimic a more natural environment [197]. A typical challenge of TFM experiments lies in the filtering and regulation of measurement noise. Since only linear elastic responses are desired, only small gel deformations are permitted. Additionally, the reconstruction typically poses an ill-conditioned mathematical problem, so that even a small noise can lead to large errors in the traction field [22]. In related methods, cellular traction is not observed on a continuous gel, but on microengineered platforms with deformable pillars [135, 280, 317]. Adhesion sites are restricted to grow on the array of posts, which brings advantages, like a simpler force reconstruction, but also drawbacks, like the artificial topological confinement and a smaller stiffness range compared to TFM on flat substrates [273].

While TFM is typically conducted *in vitro*, an *in vivo* method for the observation of cellular forces was recently developed by Campàs et al. [49]. In the study, stabilized biocompatible and fluorescent oil droplets coated with surface-receptor ligands were inserted into living embryonic tissue. Anisotropic stresses within the tissue cause a deformation of the droplet shape. The method can be employed for external force application, if the insert responds to a magnetic field [296]. On one side the technique makes real-time and local measurements in living cells with the option to specifically target surface receptors possible. On the other side, the data only allows reconstructing anisotropic stresses or stress variations, and the preparation of inserts requires special care [273, 308].

Since droplet inserts are typically on the size of cells, they are not suited to investigate single molecules. A smaller scale is accessible via molecular pN-force sensors that are coupled to the target. In Förster resonance energy transfer (FRET)-based experiments, the sensor is placed between donor and acceptor of the FRET system. Since the FRET efficiency changes with the distance between donor and acceptor, the force-extension curves are used to quantify the forces transmitted through the target, when the force sensor response is known. This method has been successfully used to determine the tension along vinculin, talin, and cadherin [11, 46, 145].

While the methods mentioned above rely on known material properties of the substrates, inserts or force sensors, there are also approaches where calibration is not necessary. In laser ablation experiments, a focused laser beam disrupts the sample, e.g. cell patches or tissues, partially. The subsequent recoil velocity of the surrounding cells scales with the force of ablated structures, as in the case of cutting a previously stretched rubber

band [369]. However, no absolute, but only relative forces are accessible. Despite its high invasivity, laser ablation has an established role for studying tissue mechanics *in vivo*.

A second example for a group of methods that allows relative tension measurement is the group of force inference techniques. Under several assumptions about the thermodynamic and mechanical nature of the system, the balance between intracellular pressure and cortical tension determine the cellular shape and contact points [273, 308]. Thus, angle measurements and the comparison to a configuration in equilibrium yield information about relative tensions. Such a procedure was used for instance by Maître et al. to investigate the different effects of cortex tension and adhesion strength in cell-cell contact formation [217].

## 2.5 Modelling approaches

In natural sciences, particularly in physics, there is a strong symbiotic relationship between experiments and theory. Experimental results are explained by theoretical models and theoretical models inspire the design of experiments. Before experimental methods even allowed studying the microscopic nature of cellular adhesions, researchers used theories to try to understand the underlying behaviour. One example for the strength of models is the concept of so-called “catch bonds”, non-covalent bonds that become longer lived under tension. This bond type was already proposed by Dembo et al. in 1988 [90], but it took until 2003 to observe the first catch bonds experimentally between P-selectin and its glycoprotein ligand PSGL-1 [221].

A challenge of modelling complex systems like cellular adhesions lies in the different time and length scales that are involved. The smallest lengths are defined by the molecular components of the adhesion site and the distances they need to bridge, typically tens of nanometer. However, when single bonds cluster to a macromolecular complex and additionally couple to the intracellular networks, such as the cytoskeleton, objects on the micrometer scale are involved. Similarly, times range from milliseconds for molecular conformation changes to minutes for the lifetime of adhesion junctions or even hours in the case of fibrillar adhesions.

The section starts with models that focus on the microscopic scale of single receptor-ligand bonds. Simple adhesion models are based on clusters of these bonds and their stochastic dynamics. They already show a rich behaviour concerning cluster size, stability, and lifetime. Additional elements are the mechanical properties of the extra- and intracellular surrounding, which further explain mechanosensitive features of cellular adhesions.

### 2.5.1 Modelling single bonds

The bond formed between a receptor and a ligand is typically weak with a strength on the order of  $10 \text{ kJ mol}^{-1}$  [2]. It results from a superposition of local interactions, such as

Van der Waals or electrostatic attractions, hydrogen bonds, or hydrophobic forces. Since the interactions are distributed over many atoms in the well-defined molecular structure, biomolecules exhibit a high specificity for binding.

Because of the weak nature of receptor-ligand interactions, thermal motion plays a key role in bond association and dissociation. The bound state corresponds to an energy minimum of a thermodynamic potential. In the simplest case, a single barrier separates bound and unbound state, but in general the energy landscape can be arbitrarily complex. For a two-state system in equilibrium, as sketched in Fig. 2.7, the probability to find the system in the bound state,  $p_1$ , is given by the Boltzmann distribution with the energy difference  $\Delta E^* = E_{12} - E_{21} > 0$  between unbound and bound state,

$$\frac{p_1}{1 - p_1} = \exp\left(\frac{\Delta E^*}{k_B T}\right), \quad (2.1)$$

where  $k_B$  is Boltzmann's constant and  $T$  is the temperature.

The binding strength or affinity between two molecules is often expressed via the equilibrium dissociation constant  $K_d$ . In analogy to a chemical reaction,  $K_d$  describes the ratio of the dissociation rate  $k_{\text{off}} = k_{12}^*$  and the association rate  $k_{\text{on}} = k_{21}^*$ . Since this ratio is proportional to the inverse left hand side of (2.1), the relation

$$K_d = \frac{k_{\text{off}}}{k_{\text{on}}} = c \exp\left(-\frac{\Delta E^*}{k_B T}\right) \quad (2.2)$$

holds with the free ligand concentration  $c$ . Higher affinity corresponds to a lower dissociation constant  $K_d$ . Reported  $K_d$  values for cadherin dimerization range from  $10^{-5}$  M to  $10^{-4}$  M [192]. Integrin-ligand binding depends strongly on the conformational state of integrin. In the case of  $\alpha_4\beta_1$  for example, the dissociation constant decreases from  $10^{-6}$  M in the bent-closed state to  $10^{-10}$  M –  $10^{-8}$  M in the extended-open state [206].

When a force acts on the bond, the energy landscape is shifted. As a result, the binding and rupture kinetics are altered. Therefore, the dissociation constant is in general a force-dependent quantity  $K_d(F)$  [339]. Different models for the force dependence of the dissociation rate  $k_{\text{off}}$  and association rate  $k_{\text{on}}$  have been developed in the last decades. Under the simple assumption that force shifts the thermodynamic potential linearly by  $-Fx$ , the new energy differences to the transition state are given by  $E_{12} - Fx_{12}$  and  $E_{21} - Fx_{12} + F(x_{12} + x_{21})$ , see Fig. 2.7.

## Bond dissociation

How force modulates the thermodynamic potential was already discussed by Bell in 1978 [27] and later refined by Evans et al. [114, 116]. In Bell's model it is assumed that the dissociation rate  $k_{\text{off}}$  grows exponentially with the applied force on the bond:

$$k_{\text{off}}(F) = k_{\text{off}}^* \exp\left(\frac{F}{F_0}\right). \quad (2.3)$$

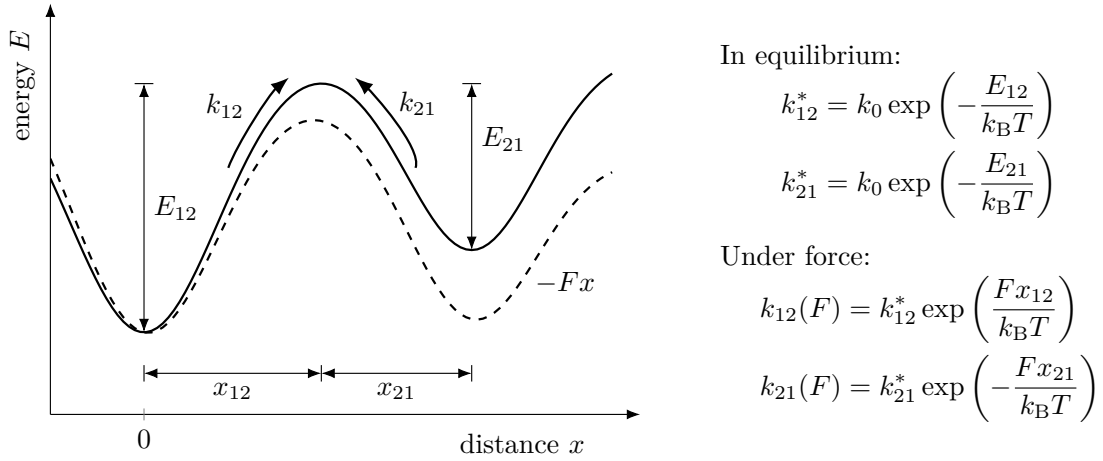


Figure 2.7. Energy landscape of a two-state system in equilibrium and under force. The global energy minimum at  $x = 0$  is separated by an energy barrier from a metastable second state at  $x = x_{12} + x_{21}$ . The energy differences  $E_{12}$  and  $E_{21}$  define the transition rates  $k_{12}^*$  and  $k_{21}^*$ . Under force, the potential shifts by  $-Fx$ . The transition rates  $k_{12}(F)$  and  $k_{21}(F)$  are functions of  $E_{12} - Fx_{12}$  and  $E_{12} + Fx_{21}$ , respectively.

Here,  $k_{\text{off}}^*$  denotes the equilibrium dissociation rate at  $F = 0$  and  $F_0 > 0$  is an intrinsic force scale. For biological systems like cellular adhesions with binding energies of several  $k_B T$  ( $1k_B T = 4.114 \text{ pN nm}$  at  $25^\circ \text{C}$ ) and a nm length scale, the intrinsic forces are expected to be on the pN scale. The exponential dependence results from the assumption that force shifts the thermodynamic potential linearly, see Fig. 2.7. Under this premise, both transition state theory and Kramer’s theory for the thermally assisted escape over the energy barrier lead to the expression (2.3) [118, 183, 235]. The relation (2.3) has been confirmed in different experiments, see e.g. Refs. [87, 215, 234, 345]. In traditional methods, either a constant force is applied, which yields a distribution of lifetimes and thus the dissociation rate  $k_{\text{off}}(F)$ , or the force is linearly increased in time with a loading rate  $r_F$ . In many cases a bond with stiffness  $\kappa$  is pulled with a constant velocity  $v$ , so that  $r_F = \kappa v$ . Evans and coworkers found that the bond strength, typically given by the most probable rupture force  $\hat{F}$ , depends logarithmically on the force ramp [116]

$$\hat{F} = F_0 \ln\left(\frac{r_F}{F_0 k_0}\right). \quad (2.4)$$

Therefore, the loading rate is an essential parameter in experiments with non-constant force application [87, 115, 309].

The rupture rate (2.3) describes a “slip bond”. In this model application of force leads to a higher rupture probability, because it is more likely that the bond slips out of the binding pocket. A characteristic feature of slip bonds is the decreasing bond lifetime under increasing tensile force. The mean lifetime of a single bond is given by



the inverse rupture rate  $k_{\text{off}}^{-1}$ . At adhesion sites, slip bonds were found for instance in fibronectin-integrin-talin-actin linkages and E-cadherin strand-swap dimers [171, 267].

However, some biological bonds exhibit a different and counterintuitive force response. Their lifetime initially increases with force and reaches a maximum under tension of the bond. Beyond this threshold, a slip regime starts and leads to shorter lifetimes with further increasing forces. This “catch-slip”-behaviour has been observed in many adhesion molecules [68, 104, 161, 181, 219, 221, 267]. Catch bonds were first proposed by Dembo et al. in 1988 [90], but the underlying mechanisms are still subject of current research [211]. In structural models, a sliding and rebinding mechanism or allosteric changes of the binding pocket are hypothesized [216, 326, 327]. This leads to multiple unbinding pathways within the energy landscape. The unbinding kinetics of selectin-ligand bonds can be described by a superposition of two exponentials [258]

$$k_{\text{off}}(F) = k_c \exp(F/F_c) + k_s \exp(F/F_s) , \quad (2.5)$$

where the catch-bond term with  $F_c < 0$  dominates for low forces and the slip-bond term with  $F_s > 0$  takes over at high forces.

### Bond association

In the Bell-Evans model, bond rupture is regarded as an irreversible process. As a result, the bond strength  $\hat{F}$  goes to zero or negative values for low forces or loading rates, see (2.4). Simulations and experiments suggest however nonzero strengths at vanishing loading rate, which are associated with rebinding events [203]. A reversible process of binding and unbinding was already studied in the model by Dembo et al. for adhesion bonds [90]. They argue that thermodynamic consistency requires that the ratio of binding and unbinding rate is given by a Boltzmann factor, which contains the energy differences between the states, see Eqs. (2.1)–(2.2). As soon as one of the rates is chosen or measured, the rate ratio ultimately determines the remaining one. Despite this constraint, the binding rate is assumed to be a constant in many models from the early 2000s [108, 111, 288, 292]. Under the assumption of a harmonic potential for the ligand, which confines the bond’s mobility, an association rate

$$k_{\text{on}} \propto \exp\left(-\frac{\kappa d^2}{2k_B T}\right) \quad (2.6)$$

was derived by Erdmann et al. [109, 112]. Here,  $d$  is the distance between ligand and receptor and  $\kappa$  describes the bond stiffness. This idea was adopted in later models [32, 264]. The quadratic dependence on the distance, which is related to the resulting stretch of the bond, makes it possible to fulfil the condition for local thermal equilibrium, as in the case of Dembo’s rate, see e.g. Refs. [32, 269]. The on-rate (2.6) naturally incorporates that binding is only possible when receptor and ligand are in a reasonable distance to each other, but all other membrane properties are neglected.

## Conformational changes

Proteins fold into a three dimensional, highly complex structure with a tight connection between shape and function. Four organizational levels are distinguished, from the amino acid sequence as the primary structure up to the arrangement of multiple subunits of polypeptide chains in the quaternary structure. Additionally, many proteins can be divided into different domains that are structurally connected by short, flexible chains, like the vinculin head and tail domain [2]. The final structure corresponds to the native conformation of the protein, which minimizes the free energy. Natural interactions with surrounding molecules or external perturbations can cause conformational changes of the protein. Conformational changes comprise reversible continuous shifts or transitions between different (metastable) states. Under large stress or in the presence of specific solvents, proteins are denatured, so that they lose structure and function. Even then, proteins can in general refold along the reverse pathway, unless they do not get stuck in local energy minima.

Transitions between two conformational states are often described by a two-state model. The multidimensional energy landscape is reduced to one dimension along which the transition occurs. In the case of unfolding events, the reaction coordinate is given by the protein length  $x$ . The native, folded state is separated from the unfolded state by an energy barrier, which determines the so-called transition state [169]. Application of force shifts the energy landscape by  $-Fx$ , so that the unfolding rate can be modeled by exactly the same formula that is used to describe bond dissociation

$$k_u(F) = k_u^* \exp(F/F_u) . \quad (2.7)$$

The force scale  $F_u = k_B T/x_u > 0$  is determined by the distance from the folded state to the transition state  $x_u$ . For the refolding process, the analogue expression

$$k_f(F) = k_f^* \exp(-F/F_f) \quad (2.8)$$

with  $F_f = k_B T/x_f > 0$  holds. This choice leads to the equilibrium constant at a constant force  $F$

$$K_u(F) = \frac{k_u(F)}{k_f(F)} = K_u^* \exp\left(\frac{F(x_u + x_f)}{k_B T}\right) . \quad (2.9)$$

The exponent equals the free energy difference for increasing the protein length by  $x_u + x_f$ . The unfolding and refolding rates (2.7) and (2.8) have successfully been applied to data from single molecule force spectroscopy experiments [209, 320]. Adaptations have been suggested for force-dependent transition state distances [64, 347].

## 2.5.2 Bond clusters

The kinetics of a parallel cluster of receptor-ligand bonds was already described by Bell for a constant force that is equally shared among all attached bonds [27]. This idea was extended

by Seifert to account for linear loading [292]. In these and other cases, a deterministic equation was used to describe the number of bonds [150]. A probabilistic approach was applied to receptor-ligand clusters for the first time in 1990 by Cozens-Roberts et al. [82]. Due to the stochastic nature of cellular adhesions it was soon adopted by others [70, 322]. These and other early adhesion models are reviewed in Ref. [365].

The stability and lifetime of simple adhesion clusters were studied rigorously on the basis of a one-step master equation by Erdmann et al. [108, 111]. In this model, the cluster consists of  $N_t$  open or closed bonds with a force-dependent rupture rate and a constant rebinding rate. The shared force promotes dissociation of the cluster, but this process can be balanced by rebinding. In their detailed analysis with stochastic and deterministic approaches, Erdmann et al. find a critical force  $f_c$  below which a stable solution exists. The critical force scales linearly with the cluster size  $N_t$  and with the rebinding rate. Above the critical force value, the cluster becomes unstable. Finite lifetimes for the whole force range are obtained only in a stochastic framework. The cluster lifetime depends on cluster size, rebinding rate, and force [111]. The model was extended to distance-dependent binding rates [112].

Using nanopatterned substrates and the theoretical model introduced in Refs. [108, 111] with shared force loading, Selhuber-Unkel et al. suggest two scaling regimes for cluster stability. At slow loading rates, rupture force is independent of the loading rate, but for fast loading, a logarithmic dependence is observed [293]. Qian et al. studied the influence of ECM and cell elasticity under non-uniform stress distributions [263–265]. Their findings suggest that the applied force is equally shared among bonds in the case of rigid substrates. For soft substrates, the stress is concentrated at the adhesion edges, which decreases cluster lifetime [264, 265]. Lifetime is additionally decreased on soft substrates because the elastic recoil after rupture events leads to large membrane separations and thus hinders rebinding [263]. Recently, viscoelastic properties of the cell were incorporated as well [208]. In other models, the cellular response and adhesion stability under cyclic stretching is explained via stochastic bond clusters [86, 180].

The models discussed above assume a constant number of bonds within a single cluster. Experiments however demonstrate that focal complexes and focal adhesions grow and elongate in the direction of force [15, 272]. Additionally, substrate rigidity influences adhesion size with larger clusters on rigid substrates [15, 74, 256]. A number of models explain adhesion growth under force with thermodynamically driven aggregation of new molecules from the surroundings into the adhesion. Nicolas et al. model the adhesion site as a thin, elastic layer subject to a localized force [247]. The resulting deformations lead to compression and dilatation in different areas and thus break the symmetry of the cell. Since it is assumed that anisotropy modulates the molecule association rate, the localized forces allow directed growth. The model was extended by Besser et al., who added a second layer of bonds for the cytoplasmic adhesion proteins, and later by Nicolas

et al. to account for different substrate rigidities [31, 246]. Shemesh et al. introduced a model in which the chemical potential drives new elements into the cluster [300]. The cluster elements are arranged as a one dimensional chain and connected to the underlying substrate at discrete anchoring points. An imbalance of anchoring points and points of force application energetically favours the recruitment of new elements under tension. This universal approach describes the experimentally observed adhesion growth under force without molecular details like the mechanosensors that are assumed in [247]. On the other hand, the effects of substrate rigidity are not considered.

Another group of models focuses on the nucleation stage of adhesions. A common finding is that membrane fluctuations play an important role for the initial seed. Large membrane separations hinder receptor-ligand binding, but when the first bond is established, the bond deforms the membrane and thus facilitates further clustering. In the model of Reister-Gottfried et al., this mechanism is termed “neighbor effect” [269]. They observe that an increased ligand density also promotes nucleation and that both of these local effects can be represented by an effective binding affinity. In a different study, membrane undulations are suggested to induce the activation of integrins from the bent-closed to the extended-open state [162]. The energy landscape for the transition between the two conformations also depends on the substrate rigidity. For the case of cadherin mediated adhesions, Fenz et al. find that low membrane fluctuations promote nucleation of single clusters that grow radially, while high fluctuations lead to dendritic adhesions. They suggest that the whole adhesion process is sensitive to and regulated by membrane fluctuations [121]. A challenge in the study of nascent adhesions lies in the different time scales for membrane fluctuations and single receptor-ligand binding kinetics, which depend on the current membrane position. In the nucleation model of Bihl et al., the dissociation and association rates are averaged over the fast membrane fluctuations [32, 33]. Without the explicit treatment of the membrane height, much longer simulation times can be achieved. This makes it possible to study adhesion clusters from the nucleation stage with less than five bonds to the equilibrium state with thousands of bonds [33].

The whole adhesion machinery as a force transmitter and transducer has been described in a so-called “molecular clutch” model [55, 102, 126, 136]. The original model introduced by Mitchison et al. [238] explains how the retrograde flow produced by the actomyosin cytoskeleton generates tension and movement if the cytoskeleton is coupled to adhesion sites. If integrin-based adhesions are not coupled via adaptor proteins to actin, the clutch is not engaged, leading to a fast retrograde flow. A simple stochastic model introduced by Chan et al. distinguishes two regimes on rigid and soft substrates [58]. The molecular clutches represent linked molecules that connect the substrate and the actin cytoskeleton. They behave as linear springs and bind and unbind stochastically. They are stretched under force and slow down the velocity at which myosin motors contract actin filaments, as observed experimentally [103, 104, 125]. On soft substrates, tension slowly builds up

and leads to a low retrograde flow rate. At a certain point of stretching, a rupture cascade leads to the dissociation of the molecular clutches. The cycle starts again as soon as new clutches bind, so that the overall motion is described as a “load-and-fail” or “stick-and-slip” behaviour. On very rigid substrates, tension builds up fast, so that single clutches rupture before new ones can be formed. This motion with a high retrograde flow rate but low forces is called “frictional slippage”. Force transmission is maximized for intermediate rigidities in this model. The suggested biphasic relationship between rigidity and force is observed in neurons and glioma cells [20]. More models that explain the biphasic relationship between actin flow and traction force are given in Refs. [83, 210, 277]. However a monotonic increase of force with rigidity has also been observed [48, 135].

Similar clutch models have been developed by Bangasser et al. and Elosegui-Artola et al. [18, 19, 103]. Recently, the model introduced by Bangasser et al. was extended to describe cell migration via stochastic molecular clutches [20]. Elosegui-Artola and coworkers incorporated molecular details into the clutch mechanism [104]. They identify the unfolding of talin as the important element in force transmission above a certain rigidity threshold. This threshold is associated with focal adhesion reinforcement mediated by vinculin. Below the threshold, i.e. at low rigidities, tension builds up slowly and the integrin-ligand bond ruptures before talin is stretched sufficiently for unfolding. Above the rigidity threshold, force is transmitted to talin which unfolds and triggers vinculin recruitment. The resulting force-rigidity curve increases monotonically, whereas the biphasic relationship is recovered upon talin depletion [104]. Further extensions of the model cover the effects of a viscous substrate, and ligand density and distribution [28, 251].

## 2.6 Open questions addressed in the thesis

The number and variety of both experimental and theoretical studies discussed above show that cellular adhesions are important objects of research. Their complexity and diverse mechanoresponse pose a challenge for scientific studies. Yet, some shared features are identified in every structure presented above. Commonly, the constituents of cellular adhesions are single or linked molecules that are arranged in a regulated manner [174]. They undergo continuous cycles of rupture and rebinding. These events are measured as stochastic events with certain probabilities per unit time. Additionally, adhesion molecules can enter and leave the cluster, so that the cluster size is variable. Mechanical stress that acts on the system has a variety of different effects [129, 311]. For instance, the rupture rate of many bonds increases exponentially with force [171, 345]. Some adhesion proteins, such as  $\alpha$ -actinin or talin, undergo conformational changes, which causes vinculin recruitment [345–347, 351]. As a consequence, the adhesion is stabilized and further downstream signalling events are triggered [104].

In many theoretical models, simplified systems of bond clusters based on of some

of these characteristics have been investigated. However, the mechanism of unfolding and subsequent recruitment of adaptor proteins has only recently been included in few theoretical studies [104, 113, 320]. Adhesion cluster reinforcement is often not considered, or sometimes assumed *a priori* [103]. Moreover, the chosen transition rates do not always respect the constraint that the process should fulfil microscopic reversibility in equilibrium. Therefore, the objective of this thesis is to set up a minimal, thermodynamically consistent, adhesion cluster model that incorporates the conformational change of proteins, and to study its effects. In particular, the question arises as to what are the minimum ingredients needed to model cluster growth or strengthening under mechanical load.

For this purpose, an idealized adhesion model with only rupture and binding is extended. The major additions are a molecule exchange with the surrounding and an unfolding transition which is motivated by talin in focal adhesions. The step-wise changes in the model variants have the advantage that the effects of different extensions can be considered separately. Thus, factors that promote cluster stabilization can be identified. Furthermore, different geometries are considered: in a first, effectively one-dimensional model version, adhesion clusters under pure pulling or pure shearing are analysed. Subsequently, an extension to two dimensions allows studying the more general case of a combination of both pulling and shearing.

By keeping the model as simple as possible, general mechanisms are observable that might stay hidden in detailed or very specific representations of biological adhesions. With knowledge of such mechanisms, progress can be made in understanding the mechanoresponse of cellular adhesions, but also related systems or in the design of new materials.

# Chapter 3

## Modelling an adhesion cluster under pulling forces

In this chapter, the generic adhesion cluster model is introduced. Motivated by cellular adhesions, the cluster consists of individual bonds that connect two regions with parallel boundaries. For the scope of this chapter, bonds are assumed to be parallel to each other and orthogonal to the boundaries. The cluster is pulled apart by a force that acts in direction of the parallel molecules. Other force directions and arbitrary bond alignments are discussed in Chapters 4 and 5. It is assumed that single molecules undergo stochastic transitions between different states. They are bound or unbound, and they can undergo a reversible conformational change. The set of rates that describe the probability per unit time for each transition to occur determines the time evolution of the cluster. The system is thus described by a stochastic process.

The chapter starts with an introduction of the geometry of the system and the behaviour of single adhesion molecules. Afterwards, the transition rates are defined. For bound molecules, the rates depend on the current bond stretch, which is related to the distance between the two boundaries. Importantly, the chosen rates fulfil detailed balance in equilibrium. Initially, a basic adhesion cluster model is analysed, in which a constant number of bonds ruptures and rebinds. As a first variation, a molecule reservoir is added which allows for a variable adhesion size. In the extended model, the conformational change is introduced as a reversible, partial unfolding of a molecule. Again, constant and variable cluster sizes are considered. Finally, it is assumed that molecules from the surrounding can bind to unfolded adhesion molecules, so that a linked state is formed. All variants are studied with analytical methods and stochastic simulations. The chapter closes with a summary and comparison of the different cluster models under pulling forces.

### 3.1 Introduction

In the model, a single adhesion cluster is described which bridges the gap between two parallel, rigid surfaces. While the lower boundary is fixed in the  $y = 0$  plane, the upper boundary can move in  $y$ -direction. An external force  $F$  is applied on the upper boundary in  $y$ -direction and pulls the surfaces apart. Adhesion is provided by discrete bonds which represent single or linearly linked molecules at a cellular adhesion site, such as cadherins, integrins or an integrin-talin complexes. In the following, cluster elements are generally referred to as molecules, irrespective of their biological equivalent. The bonds are aligned in parallel with the  $y$ -axis, i.e. orthogonal to the boundaries. The native molecule length is given by  $\ell_0$  and for simplicity, a linear force response is assumed. Therefore, bonds behave as elastic springs with stiffness  $\kappa$ . The extension due to a force, i.e. the difference of total length and  $\ell_0$ , is denoted by  $h$ .

In the basic model, bonds can detach from the upper boundary with a rupture rate  $\beta^-(h)$ . In this state, denoted by  $a$ , molecules are still connected to the lower boundary, so that they remain in the cluster. After unbinding from the upper boundary, molecules do not experience the external force, so that they can fluctuate freely around their rest length. The average thermal fluctuation length is given by  $\sigma = \sqrt{k_B T / \kappa}$  with the Boltzmann factor  $k_B$  and the temperature  $T$ . Rebinding to the upper boundary occurs with a rate  $\beta^+(h)$  and changes the state from  $a$  to  $b$ . The external force is shared among all bonds  $b$ .

In an extended model, a conformational change increases the molecule rest length. Inspired by protein unfolding, the length difference is called unfolding length and it is denoted by  $\Delta$ . Bonds with an extension  $h$  experience a reduced stretch  $h_u = h - \Delta$  after unfolding. The reverse process, called refolding, shortens the molecule again. Since both bonds  $b$  and unbound molecules  $a$  can undergo the conformational change, four rates are required to describe it. For unbound molecules,  $\delta_a^+$  is the unfolding rate to go from  $a$  to the state  $a_u$ . Refolding from  $a_u$  to  $a$  occurs with a rate  $\delta_a^-$ . Analogously, the rates  $\delta_b^\pm(h)$  are used to describe the reversible transition between  $b$  and  $b_u$ . Binding and rupture in unfolded states occurs with rates  $\beta_u^+(h)$  and  $\beta_u^-(h)$ , respectively.

In a further extension of the model, molecule unfolding opens a previously buried binding site. This transition is motivated by vinculin recruitment in cell-cell and cell-matrix adhesions. Thereby, molecules from the reservoir can enter the cluster and occupy the binding site at an unfolded molecule with a rate  $\lambda^+$ . These linked states are denoted by  $b_{u,l}$  and  $a_{u,l}$ . The reverse process, in which the new molecule detaches from the unfolded molecule, occurs with a rate  $\lambda^-$ . For simplicity, both  $\lambda^+$  and  $\lambda^-$  are chosen as constants. While the binding site is occupied, the refolding process is hindered. This accounts for the finding that binding of vinculin at unfolded talin domains hinders talin refolding [345]. However, the whole complex can still bind and unbind with the rates  $\beta_u^\pm(h)$ .

Both in basic and extended models, unbound molecules in state  $a$  can detach from the



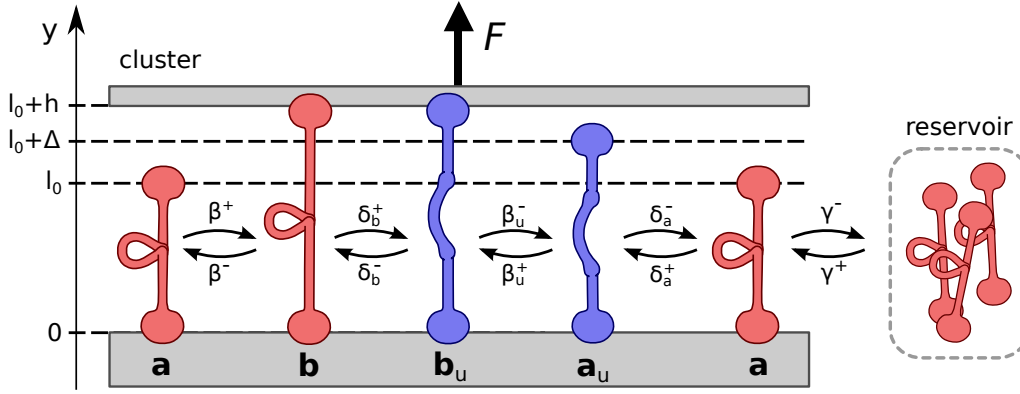


Figure 3.1. Sketch of the model geometry, bond states and transitions. The linked states  $b_{u,l}$  and  $a_{u,l}$  are not shown.

lower boundary and leave the cluster with a rate  $\gamma^-$ . New molecules are added with a rate  $\gamma^+$ . This allows a variable number of elements in the cluster. The molecule reservoir outside the cluster is assumed to be much larger than the cluster itself. The addition of new molecules is hence comparable to a zeroth order synthesis rate  $\emptyset \rightarrow a$  in a system of chemical reactions, see App. A.1. A sketch of the model system is given in Fig. 3.1.

### 3.1.1 Rates

The transition rates that describe binding or unfolding processes of bound states  $b$  and  $b_u$  depend on the extension of the respective bond. The definitions are summarized in Table 3.1.

The binding probability per unit time,  $\beta^+(h)$ , is symmetric around  $h = 0$ , i.e. around the equilibrium length with zero stretch. The maximum value of the probability for binding is given at  $|h| = \ell_b$ , where  $\ell_b$  is the optimal binding length. Biologically, this situation is motivated by a binding pocket, which favors bond association at a small finite distance. Therefore, the quantity  $\ell_b$  is a small length with  $\ell_b < \sigma$ . Besides the dependence on the elastic energy, binding is associated with an energy change  $\epsilon_b$ . This constant comprises the binding affinity, but also entropic contributions. Similar binding rates have been used previously for cellular adhesions models, see section 2.5. For already unfolded molecules, the binding rate is defined analogously with an extension  $h_u = h - \Delta$ .

The rupture rates  $\beta^-(h)$  and  $\beta_u^-(h)$  are closely related to Bell's rupture rate, see section 2.5. In the symmetric version used here, both compression and stretching increases the rupture probability per unit time. The term  $2|h|\ell_b/(2\sigma^2)$  in the exponent of  $\beta^-(h)$  sets the intrinsic force scale to  $F_\beta = k_B T/\ell_B$ . The rupture rate prefactor  $\beta^-(0) = k_\beta \exp(-\ell_b^2/(2\sigma^2))$  is chosen such, that the ratio of binding to unbinding rate corresponds to the Boltzmann distribution, which is connected to the energy difference between the

transition	reaction	rate
binding	$a \rightarrow b$	$\beta^+(h) = k_\beta \exp\left(-\frac{( h  - \ell_b)^2}{2\sigma^2} + \frac{\epsilon_b}{k_B T}\right)$
	$a_u \rightarrow b_u$	$\beta_u^+(h_u) = k_\beta \exp\left(-\frac{( h_u  - \ell_b)^2}{2\sigma^2} + \frac{\epsilon_b}{k_B T}\right)$
rupture	$b \rightarrow a$	$\beta^-(h) = k_\beta \exp\left(\frac{2 h \ell_b - \ell_b^2}{2\sigma^2}\right)$
	$b_u \rightarrow a_u$	$\beta^-(h_u) = k_\beta \exp\left(\frac{2 h_u \ell_b - \ell_b^2}{2\sigma^2}\right)$
unfolding	$b \rightarrow b_u$	$\delta_b^+(h) = k_\delta \exp\left(\frac{2\Delta_1 h - \Delta_1^2}{2\sigma^2} - \frac{\epsilon_f}{k_B T}\right)$
	$a \rightarrow a_u$	$\delta_a^+ = k_\delta \exp\left(-\frac{\epsilon_f}{k_B T}\right)$
folding	$b_u \rightarrow b$	$\delta_b^-(h_u) = k_\delta \exp\left(\frac{-2\Delta_2 h_u - \Delta_2^2}{2\sigma^2}\right)$
	$a_u \rightarrow a$	$\delta_a^- = k_\delta$
linking	$b_u \rightarrow b_{u,l}$	$\lambda^+ = \text{const.}$
	$a_u \rightarrow a_{u,l}$	$\lambda^+ = \text{const.}$
unlinking	$b_{u,l} \rightarrow b_u$	$\lambda^- = \text{const.}$
	$a_{u,l} \rightarrow a_u$	$\lambda^- = \text{const.}$
reservoir exchange	$\emptyset \rightarrow a$	$\gamma^+ = \text{const.}$
	$a \rightarrow \emptyset$	$\gamma^- = \text{const.}$

Table 3.1. Transitions and rate definitions. Bonds in the unfolded state experience a reduced stretch  $h_u = h - \Delta$  compared to folded bonds with extension  $h$ . For the unfolding and refolding rates  $\Delta_1 + \Delta_2 = \Delta$  holds.

neighbouring states in thermal equilibrium,

$$\beta(h) = \frac{\beta^+(h)}{\beta^-(h)} = \exp\left(-\frac{h^2}{2\sigma_b^2} + \frac{\epsilon_b}{k_B T}\right) = \exp\left(-\frac{E_b}{k_B T}\right). \quad (3.1)$$

The binding rates and the rate ratio  $\beta(h)$  are plotted for exemplary parameters in Fig. 3.2a,c. For unfolded molecules, the rate ratio  $\beta_u(h) = \beta_u^+(h)/\beta_u^-(h)$  is related to the binding rate ratio of folded molecules via  $\beta_u(h_u) = \beta(h - \Delta)$ .

The transitions between native and unfolded state are modeled by thermally assisted jumps over a single energy barrier, see section 2.5. The distances to the transition state are denoted by  $\Delta_1$  and  $\Delta_2$ . Their sum corresponds to the length change  $\Delta$ . In the following, equal distances  $\Delta_1 = \Delta_2 = \Delta/2$  are assumed. An energy  $\epsilon_f > 0$  accounts for the stretch-independent amount of energy that is required for unfolding. The explicit forms of unfolding and refolding rates are given in Table 3.1. The rate ratio for bound molecules,

$$\delta_b(h) = \frac{\delta_b^+(h)}{\delta_b^-(h - \Delta)} = \exp\left(\frac{2h\Delta - \Delta^2}{2\sigma^2} - \frac{\epsilon_f}{k_B T}\right) = \exp\left(-\frac{E_f}{k_B T}\right), \quad (3.2)$$

yields the energy difference  $E_f = \kappa(h - \Delta)^2 - \kappa h^2 + \epsilon_f$ . Exemplary plots for the rates and their ratio are shown in Fig. 3.2b,c.

The unfolding and refolding process also allows transitions between the unbound states  $a$  and  $a_u$ . Since unbound molecules fluctuate around their equilibrium length, a Gaussian extension distribution  $p_a(h) \sim \mathcal{N}(0, \sigma_a^2)$  can be assumed. On average, the unfolding probability per unbound molecule in state  $a$  is given by

$$\delta_a^+ = \int_{-\infty}^{\infty} \delta_a^+(h) p_a(h) dh = k_\delta \exp\left(-\frac{\epsilon_f}{k_B T}\right). \quad (3.3)$$

The average refolding rate per unbound, unfolded molecule is obtained similarly as  $\delta_a^- = k_\delta$ . Hence, the rate ratio is given by  $\delta_a = \exp(-\epsilon_f/k_B T)$ . The remaining rates for the linking transition and the exchange with the reservoir are chosen as constants and listed in Table 3.1.

The careful choice of the extension dependent transition rates have an important consequence. When a single molecule goes through a cycle of states, e.g.  $a \rightarrow b \rightarrow b_u \rightarrow a_u \rightarrow a$ , the product of all transition rates along this cycle equals the product of transition rates of the reverse cyclic transitions:

$$1 = \frac{\beta^+(h)\delta_b^+(h)\beta_u^-(h - \Delta)\delta_a^-}{\beta^-(h)\delta_b^-(h - \Delta)\beta_u^+(h - \Delta)\delta_a^+} \quad (3.4)$$

This thermodynamic constraint can be derived from the detailed balance conditions and it follows from the principle of microscopic reversibility [7, 250]. If Eq. (3.4), which is also called Kolmogorov condition [177], holds for any finite sequence of states, the corresponding Markov chain or process is reversible, see A.1. In contrast to the detailed balance conditions, which also imply reversibility of the underlying Markov process, Kolmogorov's criterion only contains the transition probabilities, not the equilibrium distribution.

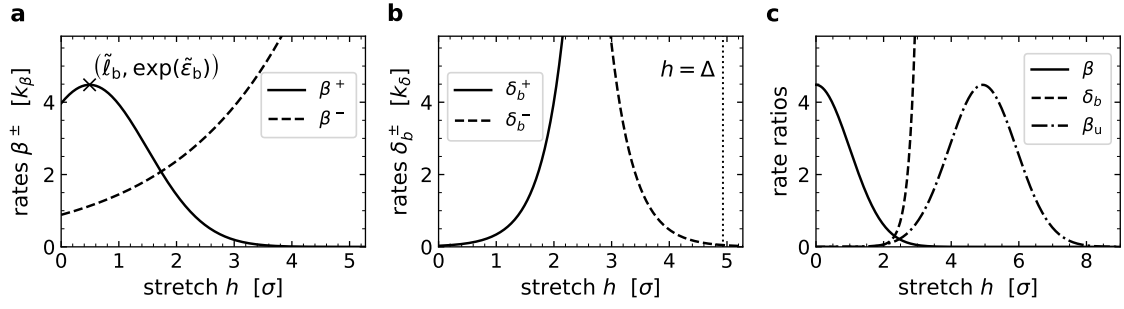


Figure 3.2. Extension dependent rates. a) Binding and rupture rate  $\beta^\pm(h)$  in units of rate prefactor  $k_\beta$ . b) Unfolding and refolding rate  $\delta_b^\pm(h)$  and  $\delta_b^-(h_u)$  in units of rate prefactor  $k_\delta$  with  $h_u = h - \Delta$ . c) Rate ratios  $\beta(h) = \beta^+(h)/\beta^-(h)$ ,  $\delta_b(h) = \delta_b^+(h)/\delta_b^-(h_u)$  and  $\beta_u(h_u) = \beta_u^+(h_u)/\beta_u^-(h_u)$ . Parameter values:  $\kappa = 1 \text{ pN nm}^{-1}$ ,  $\epsilon_b = 1.5 k_B T$ ,  $\ell_b = 1 \text{ nm}$ ,  $\Delta = 10 \text{ nm}$ ,  $\epsilon_f = 0.5 k_B T$ .

### 3.1.2 Units

The rate definitions directly suggest an energy and a length unit:  $E_0 = 1 k_B T$  and  $y_0 = 1 \sigma$ . The thermal energy scale  $k_B T$  is a convenient unit of energy in many molecular systems. At room temperature (298 K),  $1 k_B T$  is equivalent to 4.114 pN nm. The energy unit of  $k_B T$  thus naturally involves the subcellular force and length scales pN and nm. The length scale  $\sigma$  describes the average thermal fluctuations of single bonds in the clusters. It defines the width of the binding rate and hence the range of stretches at which rebinding can be considered to happen in thermal equilibrium. For a bond with a stiffness of  $\kappa = 1 \text{ pN nm}^{-1}$ , thermal length fluctuations have an average of approx. 2 nm. Together,  $k_B T$  and  $\sigma$  set the force unit  $F_0 = k_B T/\sigma$ . With the values from above, we find  $F_0 \approx 2 \text{ pN}$ . This force scale agrees with experimentally observed forces generated by the cell and experienced by adhesion proteins [11, 145, 187, 243].

There are several options for the unit of time. In a system with independent stochastic processes, the inverse sum of all rates defines the average waiting time between two transitions. Because many rates in this adhesion model are stretch-dependent and not constant, the sum of rates changes with the state of the cluster and thus with time. Alternatively, the constants  $k_\beta$ ,  $k_\delta$ ,  $\gamma^+$  and  $\gamma^-$  qualify as rate units. Since the binding transition is of uttermost importance for the integrity of the cluster,  $t_0 = k_\beta^{-1}$  is chosen as the unit of time, if not stated otherwise. For biological processes in cellular adhesions, typical time scales lie on the order of  $\mu\text{s}$ ,  $\text{ms}$  or  $\text{s}$ . In the following, dimensionless quantities will be denoted with a tilde, as in  $\tilde{X} = X/X_0$ .

### 3.1.3 Simulation algorithm

The time evolution of the adhesion cluster is simulated with a kinetic Monte Carlo method, called Gillespie algorithm. The method was originally developed for coupled chemical reactions [137, 138]. Starting from an initial condition, the waiting time until the next reaction and the specific reaction type are drawn iteratively from a reaction probability density function which is an equivalent to the master equation. With this “Direct method”, the simulation algorithm produces statistically correct trajectories of the stochastic system under consideration. Details are given in App. A.1. For the simulation of adhesion clusters, it is assumed that force balance is restored after each transition instantaneously. Thereby, the waiting time between two transitions does not need to be explicitly simulated. Instead, the simulation algorithm updates the state of the cluster and the transition probabilities after each reaction and then directly draws the waiting time until the next reaction. For a simple adhesion cluster with a fixed number of  $N = 10$  molecules, in which the only allowed transition is binding and rupture,  $a \rightleftharpoons b$ , exemplary trajectories of the occupation numbers  $n_b(t)$  and  $n_a(t)$  and the corresponding bond extension  $h(t)$  are shown in Fig. 3.3. Ensemble averages over 50 trajectories are shown in Fig. 3.4 for a ten times longer observation time. The occupation numbers either reach a steady state with a low average bond extension  $h$ , or the cluster dissociates and jumps between  $n_b = 0$  with  $\tilde{h} = 0$  and  $n_b = 1$  with  $\tilde{h} = \tilde{F}$ . For lifetime measurements, the simulations are stopped when the cluster dissociates completely for the first time.

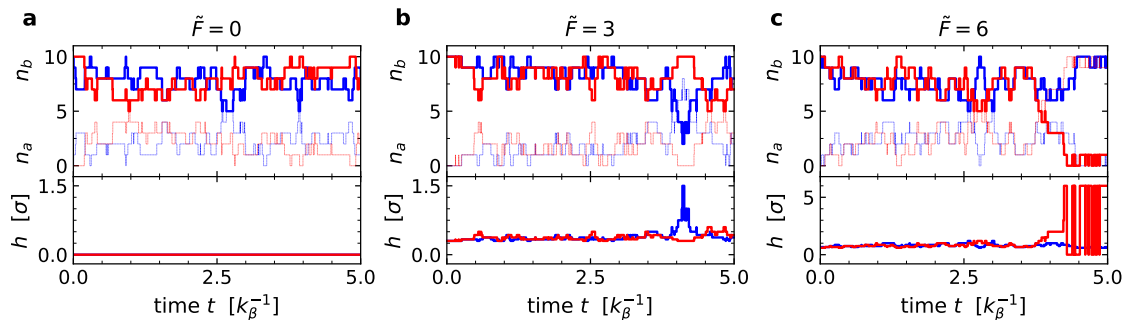


Figure 3.3. Exemplary trajectories  $n_b(t)$  (thick lines),  $n_a(t)$  (thin lines) and resulting extension  $h(t)$  for a cluster with a fixed number of  $N = 10$  molecules and no conformational changes. a) In equilibrium, the boundary separation equals the rest length of bonds, so that  $h = 0$ . b) For small finite forces the bond extension has positive values. c) At high forces, the higher unbinding probability  $\beta^-(h)$  leads to cluster dissociation. Because of molecule rebinding the system jumps between zero bonds with  $h = 0$  and one bond with  $\tilde{h} = \tilde{F}$ .

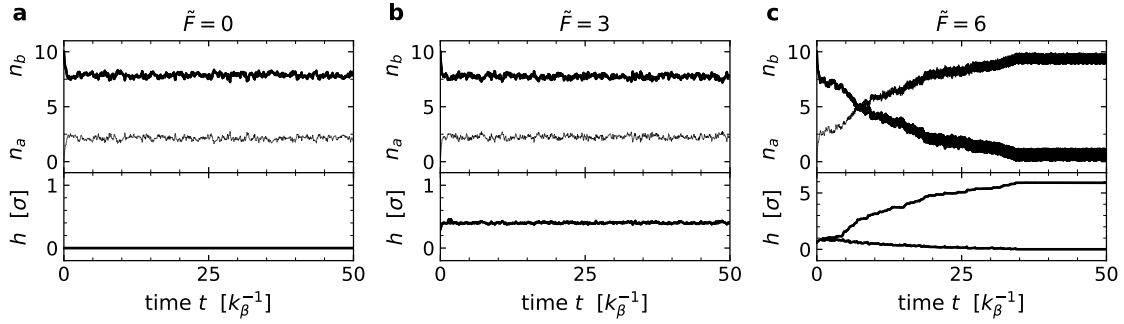


Figure 3.4. Ensemble average of 50 trajectories  $n_b(t)$ ,  $n_a(t)$ , and  $h(t)$  for a cluster with a fixed number of  $N = 10$  molecules and no conformational changes. a,b) In equilibrium and at low forces, a steady state is reached with  $n_b \approx 8$  bonds. c) At high forces, the cluster dissociates and finally jumps between  $n_b = 0$  and  $n_b = 1$ , leading to two different values of  $h$ . Parameter values are given in Table 3.2.

## 3.2 Binding and rupture model

In this section, the basic adhesion cluster model is analysed. In the basic model, molecules can only switch between states  $a$  and  $b$ , conformational changes are not included. A sketch of the cluster and the single molecule transition diagram are shown in Fig 3.5. In this geometry, the upper boundary height imposes the same extension on all bonds  $b$ . Under vertical pulling, the force balance equation simply reads

$$F = n_b \kappa h. \quad (3.5)$$

In equilibrium, i.e. at  $F = 0$ , all bonds stay at their rest length with zero stretch. To estimate the effect of small pulling forces, a Taylor expansion of the binding and unbinding rate for small positive stretches yields

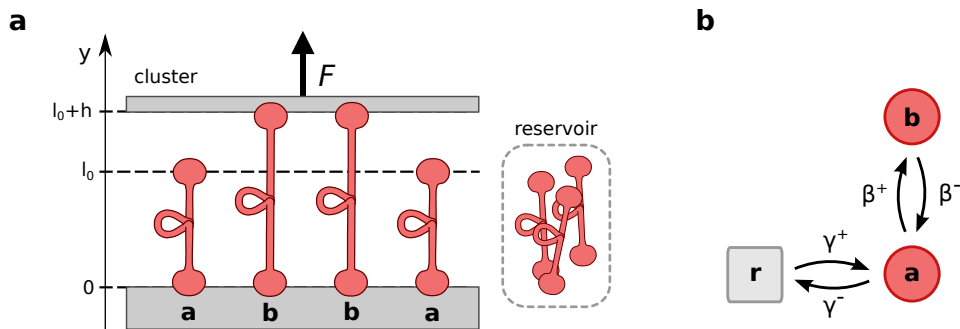


Figure 3.5. Basic adhesion cluster model. Molecules within the cluster can bind and rupture. Unbound molecules are in exchange with the surrounding reservoir. a) Sketch of a small cluster. b) Single molecule transition diagram.

$$\beta^+(h) = \beta^+(0) \left( 1 + \tilde{\ell}_b \tilde{h} - \frac{1}{2} (1 - \tilde{\ell}_b^2) \tilde{h}^2 \right) + \mathcal{O}(\tilde{h}^3), \quad (3.6)$$

$$\beta^-(h) = \beta^-(0) \left( 1 + \tilde{\ell}_b \tilde{h} + \frac{1}{2} \tilde{\ell}_b^2 \tilde{h}^2 \right) + \mathcal{O}(\tilde{h}^3) \quad (3.7)$$

$$\text{with } \beta^+(0) = k_\beta \exp\left(-\tilde{\ell}_b^2/2 + \tilde{\epsilon}_b\right) \text{ and } \beta^-(0) = k_\beta \exp\left(-\tilde{\ell}_b^2/2\right). \quad (3.8)$$

Since  $\tilde{\ell}_b < 1$ , the binding rate  $\beta^+(h)$  decreases in second order, while the rupture rate increases with stretch  $h$ . Thus, there will be more bond dissociation than rebinding with increasing force. A decreasing number of bonds in state  $b$  is expected. When the number  $n_b$  decreases with force, the average bond extension  $h = F/(\kappa n_b)$ , increases further and subsequently bond rupture is promoted. At some point, the last bond ruptures; the cluster is dissociated. For  $n_b = 0$  we define  $h = 0$  to avoid infinitely large separations between the boundaries and to allow rebinding if desired.

### 3.2.1 Constant number of molecules

In the first model variant, the rates to and from the reservoir are set to zero:  $\gamma^+ = \gamma^- = 0$ . Thereby, the total number of molecules in the cluster is fixed to  $N = n_a + n_b$ . The state of the system is thus determined by two of the three quantities  $N$ ,  $n_a$  and  $n_b$ . The only allowed transitions are rupture and rebinding of bonds. Similar adhesion cluster models have been described before by the groups of Erdmann et al., Qian et al., Bihl et al. and others, compare Refs. [32, 108, 208, 264].

Assuming fast relaxation after every transition, the time evolution of the cluster can be described by a stochastic jump process, see App. A.1. For a fixed number of molecules  $N$  and a constant force  $F$ , the probability to find  $n_b \in [0, N]$  bonds in state  $b$  evolves in time according to the master equation

$$\begin{aligned} \frac{d}{dt} p_{n_b}(t) = & -[(N - n_b)\beta^+(n_b) + n_b\beta^-(n_b)]p_{n_b}(t) + (N - n_b + 1)\beta^+(n_b - 1)p_{n_b-1}(t) \\ & + (n_b + 1)\beta^-(n_b + 1)p_{n_b+1}(t). \end{aligned} \quad (3.9)$$

The notation for the binding and rupture rate is an abbreviated form of  $\beta^\pm(h) = \beta^\pm(h(F, n_b))$  to demonstrate the dependence on  $n_b$ . To obtain the correct equations for  $n_b = 0$  and  $n_b = N$ , it is sufficient to set  $p_{-1}(t) = p_{N+1}(t) = 0$  in (3.9). Additionally,  $1 = \sum p_{n_b}(t)$  holds at all times  $t$ .

In the following, exact solutions of the master equation are discussed. For a single molecule, the two linear differential equations for  $p_1(t)$  and  $p_0(t)$  are straight forward to solve. For a cluster with  $N$  molecules, it can be shown that the system of  $N + 1$  differential equations is solved by eigendecomposition of a  $(N + 1) \times (N + 1)$  dimensional matrix. The method is applied to a cluster of two molecules. In the special case of vanishing force, the binding and rupture rates do not depend on the current state of the cluster, i.e.  $\beta^\pm(h(0, n_b)) = \beta^\pm(h = 0)$ . The system of differential equations reduces to a single

differential equation of the generating function of  $p_{n_b}(t)$ , denoted by  $G(s, t)$ . The solution of  $G(s, t)$  and thus  $p_{n_b}(t)$  is given for  $n_b = N$  initially bound molecules. Afterwards, the focus lies on the long-time limit, i.e. steady state solutions of the master equation. The steady state solution of the macroscopic equation for the first moment  $\langle n_b \rangle$  is compared to the simulation results. Finally, the average lifetime of adhesion clusters is studied.

### Exact solution of the master equation

For the special case of a single molecule,  $N = 1$ , the master equations are given by

$$\frac{d}{dt}p_0(t) = -\beta^+(0)p_0(t) + \beta^-(1)p_1(t), \quad (3.10)$$

$$\frac{d}{dt}p_1(t) = -\beta^-(1)p_1(t) + \beta^+(0)p_0(t), \quad (3.11)$$

and additionally,  $1 = p_0(t) + p_1(t)$  has to hold. Again, the abbreviation  $\beta^\pm(h(F, n_b)) = \beta^\pm(n_b)$  is used. The solution reads

$$p_0(t) = \frac{\beta^-(1)}{\beta^+(0) + \beta^-(1)} - K_1 \exp\left(-(\beta^+(0) + \beta^-(1))t\right) \quad (3.12)$$

$$p_1(t) = \frac{\beta^+(0)}{\beta^+(0) + \beta^-(1)} + K_1 \exp\left(-(\beta^+(0) + \beta^-(1))t\right) \quad (3.13)$$

with a constant  $K_1$  that is determined by the initial condition  $p_1(0) = 1 - p_0(0)$  to  $K_1 = p_1(0) - \beta^+(0)/(\beta^+(0) + \beta^-(1))$ . The first terms in (3.12) and (3.13) are obtained in the long time limit. They are called steady state solution. The exponential decay rate towards the steady state solution is determined by the sum of the possible reaction rates.

For more than one bond, it becomes more difficult to obtain an exact solution. In general, the system of differential equations can be written in the form [173]

$$\frac{d}{dt}\mathbf{p}(t) = \mathbf{W}\mathbf{p}(t) \quad (3.14)$$

with a tridiagonal  $(N + 1) \times (N + 1)$  matrix  $\mathbf{W}$  and a vector  $\mathbf{p}(t) = (p_0(t), \dots, p_N(t))$ . Stochastic processes with a master equation that is written with such a tridiagonal matrix are called one-step processes or birth-and-death processes, see App. A.1. In this case, the diagonal elements are given by  $W_{k,k} = -(k\beta^-(k) + (N - k)\beta^+(k))$ . For the off-diagonal elements we find  $W_{k-1,k} = (N - k + 1)\beta^+(k - 1)$  and  $W_{k,k+1} = k\beta^-(k)$ . Because the sum of each column adds up to zero, there exists a left eigenvector  $(1, \dots, 1)$  with eigenvalue  $\lambda = 0$ . The nonnegative right eigenvector to the eigenvalue  $\lambda_0 = 0$  corresponds to time-independent solutions of the system. In the long-time limit, all solutions tend to the stationary solution or to one of the stationary solutions, if there are more than one<sup>1</sup>. For stationary solutions,

---

<sup>1</sup>This is for example the case when the states are decomposable into two subsets with no transitions between them. See [173] for a detailed discussion.



all transitions into a state  $k$  per unit time are balanced by the transitions out of state  $k$ ,

$$\sum_{j=1}^{N+1} W_{k,j} p_j^{(s)} = \sum_{j=1}^{N+1} W_{j,k} p_k^{(s)}. \quad (3.15)$$

This property is called global balance. In many physically motivated systems, the stationary solution corresponds to the equilibrium solution of the system. The system is a so-called equilibrium system, if all individual transitions between neighbouring states are balanced, i.e. if the stronger detailed balance condition

$$W_{k,j} p_j^* = W_{j,k} p_k^* \quad (3.16)$$

holds. The Markov chain that belongs to the transition matrix is called reversible, because the same distribution is obtained when time is reversed.

Symmetry under time-reversal is an essential feature of equilibrium physics on the microscale. Both  $\mathbf{p}^{(s)}$  and  $\mathbf{p}^*$  are stationary distributions that correspond to a so-called steady state of the system. When only global, but not detailed balance holds, net fluxes are still allowed. These non-equilibrium steady states typically occur for instance in models for active particles, molecular motors or other driven systems. Only when the detailed balance condition holds, i.e. for the stationary distribution  $\mathbf{p}^*$ , there are no probability fluxes in steady state. Hence, to consistently model a system without external driving, the detailed balance condition should be fulfilled at vanishing forces.

As a mathematical consequence of the detailed balance property, the matrix  $W$  can be symmetrized by a similarity transformation. For the present case, the diagonal matrix  $D$  with  $D_{1,1} = 1$  and

$$D_{k,k} = \frac{N!}{(k-1)!(N-k+1)!} \prod_{j=1}^{k-1} \sqrt{\frac{\beta^+(j-1)}{\beta^-(j)}} \quad \text{for } k > 1 \quad (3.17)$$

can be used as a transformation matrix to obtain a symmetric matrix  $S = D^{-1}WD$ . The diagonals of  $S$  and  $W$  are identical. The off-diagonals are given by  $S_{k-1,k} = S_{k,k-1} = \sqrt{(N-k+1)\beta^+(k-1)} \cdot \sqrt{k\beta^-(k)}$ . Real symmetric matrices are diagonalizable by an orthogonal matrix  $Q$ . This property can be used to find the eigenvectors of  $S$  and therefore also the eigenvectors  $\mathbf{v}$  of  $W$  by means of the reverse transformation. The decomposition reads  $S = QRQ^\top$ . The columns of  $Q$  are the eigenvectors of  $S$  and  $R$  is the diagonal matrix that contains the real eigenvalues  $\lambda_k$  for  $1 \leq k \leq N$  of  $W$  and  $S$ . Alternatively, the eigenvalues can be determined from the roots of the characteristic polynomial  $\det(S - \lambda I_{N+1})$ , where  $I_{N+1}$  is the  $(N+1) \times (N+1)$  identity matrix. The detailed balance condition further ensures that  $W$  is negative semi-definite and therefore has only negative eigenvalues  $\lambda_i < 0$  for  $i \geq 1$ . The matrix  $W$  is negative semi-definite if for any vector  $\mathbf{x} = (x_1, \dots, x_{N+1})$  the relation  $\mathbf{x}^\top W \mathbf{x} \leq 0$  holds. For the proof, the vector components are written as multiples

of the equilibrium solution,  $x_j = (c_j p_j^*)$ ,

$$\mathbf{x}^\top \mathbf{W} \mathbf{x} = \sum_{j=1}^{N+1} \left( \sum_{k \neq j} x_j W_{j,k} x_k - x_j \sum_{k \neq j} W_{k,j} x_j \right) \quad (3.18)$$

$$= \sum_{j=1}^{N+1} \sum_{k \neq j} c_j p_j^* \left( W_{j,k} c_k p_k^* - W_{k,j} c_j p_j^* \right) \quad (3.19)$$

$$= \sum_{j=1}^{N+1} \sum_{k \neq j} c_j p_j^* W_{j,k} p_k^* (c_k - c_j) \quad (3.20)$$

$$= -\frac{1}{2} \sum_{j=1}^{N+1} \sum_{k \neq j} p_j^* W_{j,k} p_k^* (c_k - c_j)^2. \quad (3.21)$$

Since only the positive entries of  $\mathbf{W}$  appear, the quadratic form is always negative, unless the vector  $\mathbf{x}$  is linear dependent of  $\mathbf{p}^*$ , so that  $c_k = c$ .

Finally, the solution for the system of differential equations in Eq. (3.14) can be written as a linear superposition of the eigenvectors  $\mathbf{v}$  of  $\mathbf{W}$

$$\mathbf{p}(t) = \sum_{j=0}^N K_j \mathbf{v}_j \exp(\lambda_j t) = \mathbf{p}^* + \sum_{j=1}^N K_j \mathbf{v}_j \exp(\lambda_j t). \quad (3.22)$$

Since the detailed balance ensures that the eigenvalues  $\lambda_j$  are negative for  $j \geq 1$ , the long-time solution is the equilibrium distribution  $\mathbf{p}^*$ . The constants  $K_j$  are determined from the initial condition  $\mathbf{p}(0)$  with  $\sum_j p_j(0) = 1$ .

### Example for $N = 2$

For the special case of two molecules,  $N = 2$ , the system of differential equation reads

$$\begin{aligned} \frac{d}{dt} \mathbf{p}(t) &= \mathbf{W} \mathbf{p}(t) \\ &= \begin{pmatrix} -2\beta^+(0) & \beta^-(1) & 0 \\ 2\beta^+(0) & -(\beta^-(1) + \beta^+(1)) & 2\beta^-(2) \\ 0 & \beta^+(1) & -2\beta^-(2) \end{pmatrix} \mathbf{p}(t). \end{aligned} \quad (3.23)$$

The matrix  $\mathbf{W}$  has the eigenvalues

$$\lambda_0 = 0, \quad \lambda_1 = -(S + U), \quad \lambda_2 = -(S - U) \quad (3.24)$$

with

$$2S = 2\beta^+(0) + \beta^-(1) + \beta^+(1) + 2\beta^-(2), \quad (3.25)$$

$$U = \sqrt{S^2 - (2\beta^+(0)(\beta^+(1) + 2\beta^-(0)) + 2\beta^-(1)\beta^-(2))}. \quad (3.26)$$

Note that both  $\lambda_1$  and  $\lambda_2$  are negative, because  $S > U > 0$  holds. The corresponding eigenvectors are given by

$$\mathbf{v}_0 = \frac{1}{\beta^+(1)} \begin{pmatrix} 2\beta^-(1)\beta^-(2) \\ 4\beta^+(0)\beta^-(2) \\ 2\beta^+(0)\beta^+(1) \end{pmatrix}, \quad (3.27)$$

$$\mathbf{v}_1 = \frac{1}{\beta^+(1)} \begin{pmatrix} 2\beta^+(0) + \beta^-(1) - (S - U) \\ 2\beta^-(2) - (S + U) \\ \beta^+(1) \end{pmatrix}, \quad (3.28)$$

$$\mathbf{v}_2 = \frac{1}{\beta^+(1)} \begin{pmatrix} 2\beta^+(0) + \beta^-(1) - (S + U) \\ 2\beta^-(2) - (S - U) \\ \beta^+(1) \end{pmatrix} \quad (3.29)$$

and with an initial condition  $\mathbf{p}(0) = (0, 0, 1)^\top$ , the full solution is given by

$$p_0(t) = \frac{2\beta^-(1)\beta^-(2)}{S^2 - U^2} \left[ 1 - \left( \frac{S}{U} \sinh(Ut) + \cosh(Ut) \right) \exp(-St) \right], \quad (3.30)$$

$$p_1(t) = \frac{4\beta^+(0)\beta^-(2)}{S^2 - U^2} \left[ 1 - \left( \frac{S}{U} \sinh(Ut) + \cosh(Ut) \right) \exp(-St) \right] \\ + \frac{2\beta^-(2)}{U} \sinh(Ut) \exp(-St), \quad (3.31)$$

$$p_2(t) = \frac{2\beta^+(0)\beta^+(1)}{S^2 - U^2} + \frac{2\beta^-(2)(2\beta^+(0) + \beta^-(1))}{S^2 - U^2} \left[ \frac{S}{U} \sinh(Ut) \right. \\ \left. + \cosh(Ut) \right] \exp(-St) - \frac{2\beta^-(2)}{U} \sinh(Ut) \exp(-St). \quad (3.32)$$

In the special case  $\beta^+(0) = 0$ , i.e. without rebinding after the first complete dissociation of the cluster, the exact solution simplifies to

$$p_0(t) = 1 - \left( \frac{S}{U} \sinh(Ut) + \cosh(Ut) \right) \exp(-St), \quad (3.33)$$

$$p_1(t) = \frac{2\beta^-(2)}{U} \sinh(Ut) \exp(-St), \quad (3.34)$$

$$p_2(t) = \left( \frac{S - 2\beta^-(2)}{U} \sinh(Ut) + \cosh(Ut) \right) \exp(-St). \quad (3.35)$$

This case is also discussed in Ref. [111].

### Special case $F = 0$

For vanishing force, the master equation reads

$$\frac{d}{dt} p_{n_b}(t) = -[(N - n_b) \beta^+ + n_b \beta^-] p_{n_b}(t) \\ + (N - n_b + 1) \beta^+ p_{n_b-1}(t) + (n_b + 1) \beta^- p_{n_b+1}(t), \quad (3.36)$$

where  $\beta^+ = \beta^+(h=0)$  and  $\beta^- = \beta^-(h=0)$ . The generating function

$$G(s, t) = \sum_{k=-\infty}^{\infty} s^k p_k(t) \quad (3.37)$$

with  $p_k(t) = 0$  for  $k < 0$  and  $k > N$  is used to find the probability distribution that solves Eq. (3.36). The time derivative of the generating function is given by

$$\begin{aligned} \frac{d}{dt}G(s, t) = \sum_{k=-\infty}^{\infty} s^k \left[ -[(N-k)\beta^+ + k\beta^-] p_k(t) \right. \\ \left. + (N-k+1)\beta^+ p_{k-1}(t) + (k+1)\beta^- p_{k+1}(t) \right]. \end{aligned} \quad (3.38)$$

Shifting the summation indices leads to a linear partial differential equation for  $G(s, t)$ ,

$$\frac{d}{dt}G(s, t) = \beta^- \left( N\beta(s-1)G(s, t) - (s-1)(s\beta+1) \frac{d}{ds}G(s, t) \right), \quad (3.39)$$

where  $\beta = \beta^+/\beta^- = \beta(h=0)$ . The solution for a cluster with  $n_b(t=0) = N$  bonds is given by [233]

$$G(s, t) = \frac{(s\beta+1 + (s-1)\exp(-(\beta^+ + \beta^-)t))^N}{(1+\beta)^N}, \quad (3.40)$$

which fulfils the normalization condition  $G(1, t) = 1$  and the initial condition  $G(s, 0) = s^N$ . The solution for  $p_0(t)$  is simply given by  $G(s, t)|_{s=0}$ . The remaining probabilities are calculated via partial derivatives of  $G(s, t)$  with respect to  $s$ . In summary, the solutions are given by

$$p_k(t) = \binom{N}{k} \left( \frac{\beta + \exp(-(\beta^+ + \beta^-)t)}{1 + \beta} \right)^k \left( \frac{1 - \exp(-(\beta^+ + \beta^-)t)}{1 + \beta} \right)^{N-k}. \quad (3.41)$$

Thus, we find a binomial distribution with time-dependent ‘‘success’’ probability, i.e. the probability to find a bound molecule, of  $(\beta + \exp(-(\beta^+ + \beta^-)t))/(1 + \beta)$ , which decays to  $\beta/(1 + \beta)$  in the long time limit.

### Steady state solution

In the limit of long times, the system reaches a steady state. Since the steady state probability distribution fulfils  $\frac{d}{dt}p^{(s)}(t) = 0$ , a recursive formula can be derived from the master equation (3.9). It reads for  $0 < n_b \leq N$

$$p_{n_b}^{(s)} = \frac{(N - n_b + 1)\beta^+(n_b - 1)}{n_b\beta^-(n_b)} p_{n_b-1}^{(s)}. \quad (3.42)$$

This equation corresponds to the detailed balance condition from Eq. (3.16), so that the stationary solution is an equilibrium distribution  $p_{n_b}^{(s)} = p_{n_b}^*$ . By means of the recursive formula, all steady state probabilities  $p_{n_b}^*$  can be expressed as a multiple of  $p_0^*$ :

$$p_{n_b}^* = \prod_{k=1}^{n_b} \left( \frac{(N - k + 1)\beta^+(k - 1)}{k\beta^-(k)} \right) p_0^* = \binom{N}{n_b} \prod_{k=1}^{n_b} \left( \frac{\beta^+(k - 1)}{\beta^-(k)} \right) p_0^*. \quad (3.43)$$

The sum of all probabilities  $p_{n_b}^*$  add up to one, so that  $p_0^*$  is given by

$$p_0^* = \left( 1 + \sum_{j=1}^N \binom{N}{j} \prod_{k=1}^j \left( \frac{\beta^+(k-1)}{\beta^-(k)} \right) \right)^{-1}. \quad (3.44)$$

For the case of no pulling force, the extension of all bonds is zero and hence, the binding and rupture rates do not depend on the current number of bonds  $n_b$ . The steady state solution for  $n_b = 0$  simplifies to  $p_0^*(F = 0) = (1 + \beta)^{-N}$ . The equilibrium distribution is given by

$$p_{n_b}^*(F = 0) = \binom{N}{n_b} \frac{\beta^{n_b}}{(1 + \beta)^N}, \quad (3.45)$$

with  $\beta = \beta^+/\beta^- = \exp(\tilde{\epsilon}_b)$ . The result agrees with the long time limit of the exact solution for vanishing force, compare Eq. (3.41).

For a cluster of  $N = 10$  molecules, the steady state probabilities  $p_{n_b}^*$  are shown as a function of the external force  $F$  in Fig. 3.6a and the probability distribution for selected force values is shown in Fig. 3.6b. For low forces, i.e.  $\tilde{F} < 4$ , the steady state probabilities are almost constant and close to the equilibrium value at  $\tilde{F} = 0$ . The highest probabilities are found for  $n_b = 8$  and  $n_b = 9$ . At higher forces, all  $p_{n_b}^*$  for  $n_b \geq 2$  drop to zero.  $p_1$  reaches a maximum at  $\tilde{F} \approx 5$  and slowly approaches zero for higher forces, where  $p_0^*$  converges to one. The abrupt change at  $\tilde{F} \approx 4$  can be explained with the rate ratio  $\beta(h)$ , compare Eq. (3.1). As long as the mean stretch per bond is small, rebinding is frequent. But when the force  $F$  and consequently the extension  $h$  increases, the rate ratio goes to zero and thus, the cluster dissociates eventually,  $p_0^* \rightarrow 1$ .

### Average quantities

The first moment of the steady state probability distribution describes the average number of bonds in steady state,  $\langle n_b \rangle = \sum_{n_b} n_b p_{n_b}^*$ , see Fig. 3.6c. The average number of bonds has an almost constant plateau for  $\tilde{F} < 4$  at  $\langle n_b \rangle \approx 8$ , shows a first steep descent to one bond and then slowly decreases to zero. The corresponding dimensionless extension  $\tilde{h} = \tilde{F}/\langle n_b \rangle$  is shown in red in Fig. 3.6c. For  $\tilde{h} > \frac{1}{2}$ , the average stretch per bond diverges, because  $F$  increases and  $\langle n_b \rangle$  goes to zero. The analytical results and the simulation averages are in good agreement. The second moment  $\langle n_b^2 \rangle = \sum_{n_b} n_b^2 p_{n_b}^*$  is used to calculate the variance  $\text{Var}(n_b) = \langle n_b^2 \rangle - \langle n_b \rangle^2$ . The variance exhibits a peak at  $\tilde{F} \approx 4.5$ , i.e. at the force value, at which the cluster changes from many bonds to one bond on average, see Fig. 3.6d. The variance obtained from simulations has a lower peak, possibly because of the restriction to integers.

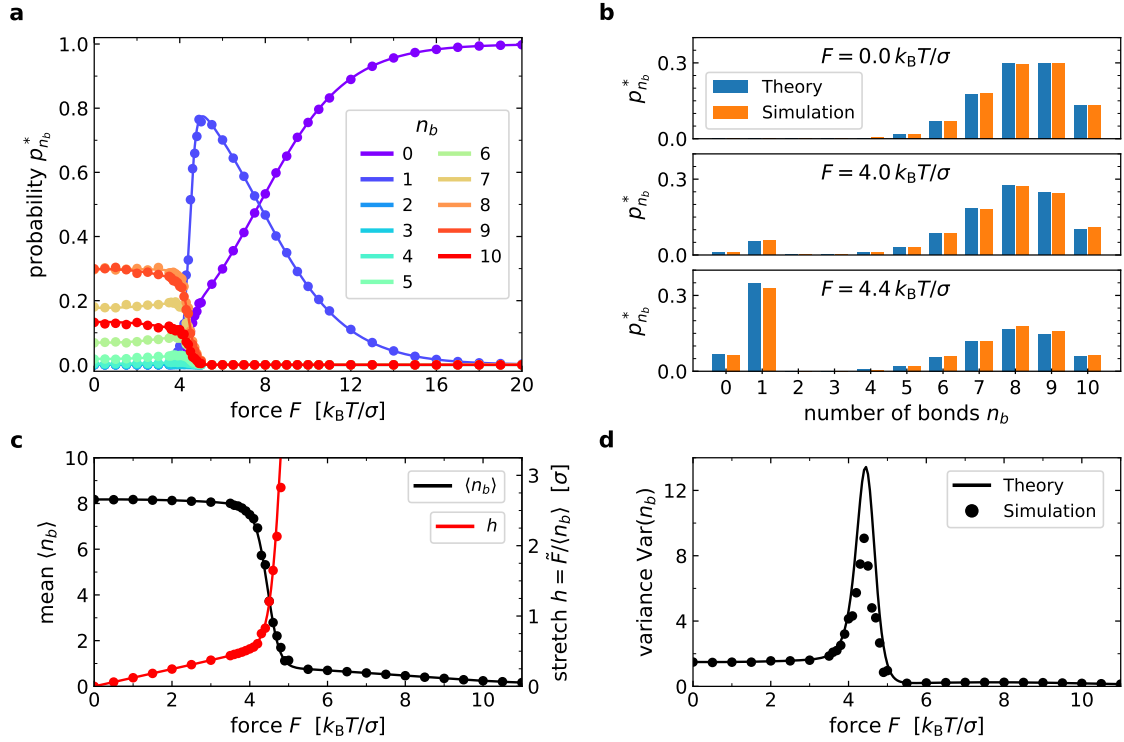


Figure 3.6. Steady state quantities for a basic adhesion cluster with  $N = 10$  molecules. a) Steady state probabilities  $p_{n_b}^*$ . Solid lines correspond to the analytical solution and markers show simulation results. b) Steady state distributions  $p_{n_b}^*$  for selected force values. c) Mean number of bonds and the corresponding bond extension  $h$  in steady state. d) Variance of the number of bonds. Parameter values are given in Table 3.2.

## Macroscopic equations

Macroscopic equations describe the time evolution of the moments  $\langle n^k \rangle(t)$  of the probability distribution  $p_n(t)$ . They are derived from the master equation as sketched in App. A.1. For nonlinear rates, the resulting system of differential equations is typically coupled. Still, the approach is useful if the exact probability distribution is not accessible or if fluctuations are small, so that moments  $k > 1$  are negligible. In this case, the macroscopic equations correspond to a mean field approximation. For the basic adhesion cluster model with binding and rupture, the macroscopic equation for the first moment follows from the master equation (3.9) as

$$\begin{aligned} \frac{d}{dt} \langle n_b \rangle &= \sum_{n_b=0}^N n_b \frac{d}{dt} p_{n_b} = \sum_{n_b=0}^N \left[ (N - n_b) \beta^+(n_b) - n_b \beta^-(n_b) \right] p_{n_b} \\ &= \langle (N - n_b) \beta^+(n_b) \rangle - \langle n_b \beta^-(n_b) \rangle, \end{aligned} \quad (3.46)$$

where the explicit  $t$ -dependence is omitted. In the case  $F = 0$ , i.e. if binding and rupture rate do not depend on  $n_b$ , the rates are constant and can be drawn out of the expected

value. To obtain a linear differential equation in  $\langle n_b \rangle$ , the binding and rupture rates are written again as a function of the extension  $h$  and the extension is considered as a free variable. Thus,  $\langle n_b \rangle$  is determined as a function of  $h$  in steady state. The force balance equation (3.5) restricts the allowed values for  $h$  at a given force  $F$  and hence the solution for  $\langle n_b \rangle(h)$ . The mean field approximation finally reads

$$\frac{d}{dt}\langle n_b \rangle(h) = (N - \langle n_b \rangle(h))\beta^+(h) - \langle n_b \rangle(h)\beta^-(h). \quad (3.47)$$

The possible steady state solutions are found at  $\frac{d}{dt}\langle n_b \rangle(h) = 0$ :

$$\frac{\langle n_b \rangle(h)}{N} = \frac{\beta(h)}{1 + \beta(h)}, \quad (3.48)$$

so that the force balance equation reads

$$\frac{F}{N} = \frac{\kappa h \beta(h)}{1 + \beta(h)}. \quad (3.49)$$

In Fig. 3.7a and b, the relations (3.48) and (3.49) are shown. As it can be seen in Fig. 3.7b, each extension value  $h$  uniquely determines the required external force  $F$ , whereas a given constant force has either two, one or no corresponding steady state solutions. The resulting solutions of  $\langle n_b \rangle$  as a function of  $F$  are shown in Fig. 3.7c.

The force threshold, above which no steady solution exists, is given by the maximum of (3.49). For positive stretches, the necessary condition of a vanishing first derivative is given by

$$\beta(h) = \frac{h^2}{\sigma^2} - 1, \quad (3.50)$$

which can be brought into the form  $ye^y = x$  with  $x = \beta(0)/(2\sqrt{e})$  and  $y = (\tilde{h}^2 - 1)/2$ .

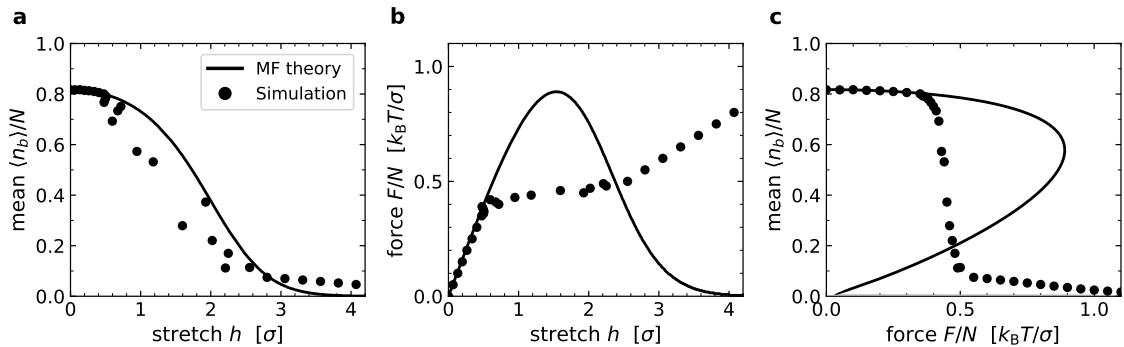


Figure 3.7. Mean field steady state solution. a) Average fraction of bonds as a function of the bond extension  $h$ . b) The force balance equation with the steady state solutions  $\langle n_b \rangle(h)$  connects force and stretch. c) The resulting steady state solutions as a function of external force  $F$  per molecules  $N$ . Parameter values are given in Table 3.2.

Because  $x > 0$  holds, the solution for  $y$  is given by the principal branch of the product logarithm  $y = W_0(x)$ . Therefore the maximum is found at  $(h_{\max}, F_{\max}/N)$  with

$$\tilde{h}_{\max} = \sqrt{2W_0\left(\frac{\beta(0)}{2\sqrt{e}}\right) + 1}, \quad \frac{\tilde{F}_{\max}}{N} = \tilde{h}_{\max} - \tilde{h}_{\max}^{-1}. \quad (3.51)$$

In Fig. 3.7 simulation averages for a cluster with  $N = 10$  are shown with black markers. In simulations, a force  $F$  is given and the resulting average number of bonds  $\langle n_b \rangle$  and their extension  $h$  are measured. Therefore simulations firstly yield  $\langle n_b \rangle(F)$ , as shown in Fig. 3.7c. In simulations, only the upper branch with a high fraction  $\langle n_b \rangle/N$  at a low extension  $h$  is realized. For forces larger than  $\tilde{F} = 4$ , the mean field results do not match with the simulations, although simulations agree well with the exact solution for  $\langle n_b \rangle$ , compare Fig. 3.6c. The deviations coincide with the increase in the variance  $\text{Var}(n_b)$ , see Fig. 3.6d. This demonstrates that the mean field approximation assumes negligible fluctuations. Fluctuations however become important for the adhesion cluster if there are only few bonds under large forces.

## Lifetime

The lifetime of a single bond is determined by the rupture rate  $\beta^-(h)$ . The average waiting time in the bound state is given by the inverse rate  $1/\beta^-(h)$ , which decreases exponentially with  $h$  and hence with force. For multiple bonds, the time until the last bond ruptures and the whole cluster dissociates also depends strongly on the cluster size, the force and on the rebinding rate. The dissociation rate is given by  $D(t) = \frac{d}{dt}p_0(t) = \beta^-(1)p_1(t)$ . The average dissociation time is calculated via [173]

$$\tau = \int_0^{\infty} tD(t) dt = \int_0^{\infty} t\beta^-(1)p_1(t) dt. \quad (3.52)$$

Here, the two limiting cases of vanishing and large forces are discussed.

For vanishing force, the exact solution for the one-step master equation (3.36) is given in Eq. (3.41) for  $N$  initially bound molecules. However, the result does not account for an absorbing boundary and therefore  $p_1(t)$  cannot be inserted directly into the definition of the average dissociation time (3.52). Instead, the mean first arrival time at the state  $n_b = 0$  is required. Using the Laplace transformation of the dissociation rate  $\mathcal{L}(D(t)) = D(s) = \int_0^{\infty} \exp(-st)D(t) dt$ , the relation

$$\tau = \int_0^{\infty} tD(t) dt = -\frac{\partial}{\partial s}D(s)|_{s=0} \quad (3.53)$$

is found. The Laplace transform of the dissociation rate is given by  $D(s) = p_{0,N}(s)/p_{0,0}(s)$ , where  $p_{0,x}(s) = \mathcal{L}(p_{0,x}(t))$  denotes the Laplace transform of  $p_0(t)$  with initial condition  $n_b(t=0) = x$  [173]. The solution with  $N$  initially bound molecules is given in (3.41). The



solution for  $n_b(t=0) = 0$  with unrestricted boundary conditions is known from comparable systems, see [110, 233]. Applied to the basic adhesion cluster, the probability distributions and their Laplace transform are given by

$$p_{0,N}(t) = \frac{(1 - \exp(-(\beta^+ + \beta^-)t))^N}{(1 + \beta)^N}, \quad (3.54)$$

$$p_{0,N}(s) = \frac{1}{(1 + \beta)^N} \sum_{j=0}^N \binom{N}{j} \frac{(-1)^j}{s + j(\beta^+ + \beta^-)}, \quad (3.55)$$

$$p_{0,0}(t) = \frac{(1 + \beta \exp(-(\beta^+ + \beta^-)t))^N}{(1 + \beta)^N}, \quad (3.56)$$

$$p_{0,0}(s) = \frac{1}{(1 + \beta)^N} \sum_{j=0}^N \binom{N}{j} \frac{\beta^j}{s + j(\beta^+ + \beta^-)}. \quad (3.57)$$

The average lifetime results as

$$\tau = \frac{1}{\beta^-(1 + \beta)} \left( H_N + \sum_{j=1}^N \binom{N}{j} \frac{\beta^j}{j} \right) \quad (3.58)$$

with the harmonic number  $H_N$ . In the special case of zero force and vanishing rebinding, i.e.  $\beta = 0$ , the relation simplifies to  $\tau = H_N/\beta^-$ . For small  $\beta$ ,  $\tau$  grows logarithmically with  $N$ , because the harmonic number is bounded by  $\ln(N+1) \leq H_N \leq \ln(N) + 1$ . In general, cluster lifetime increases both with  $\beta$  and the number of molecules  $N$ . The sum in the bracket of (3.58) is a polynomial in  $\beta$  of order  $N$  with the upper bound  $(1 + \beta)^N - 1$ . For  $N = 2$ , the average cluster lifetime is given by

$$\tau = \frac{3/2 + 2\beta + \beta^2/2}{\beta^-(1 + \beta)} = \frac{3 + \beta}{2\beta^-}. \quad (3.59)$$

In the limit of large forces, specifically if the initial extension  $h$  is large, so that  $\beta^+(h) \approx 0$  is a reasonable approximation, all bonds rupture successively. Such a rupture cascade for  $N$  initially bound molecules is described by the master equation

$$\frac{d}{dt} p_{n_b}(t) = -n_b \beta^-(n_b) p_{n_b}(t) + (n_b + 1) \beta^-(n_b + 1) p_{n_b+1}(t). \quad (3.60)$$

The boundary conditions are given by

$$\frac{d}{dt} p_N(t) = -N \beta^-(N) p_N(t), \quad \frac{d}{dt} p_0(t) = \beta^-(1) p_1(t). \quad (3.61)$$

Note that the state with  $n_b = 0$  poses an absorbing boundary condition. For initially two bound molecules, the exact solution of the master equation with an absorbing boundary and no rebinding is given by

$$p_2(t) = \exp(-2\beta^-(2)t) \quad (3.62)$$

$$p_1(t) = \frac{2\beta^-(2)}{2\beta^-(2) - \beta^-(1)} (\exp(-\beta^-(1)t) - \exp(-2\beta^-(2)t)) \quad (3.63)$$

$$p_0(t) = 1 - \frac{2\beta^-(2)}{2\beta^-(2) - \beta^-(1)} \exp(-\beta^-(1)t) + \frac{\beta^-(1)}{2\beta^-(2) - \beta^-(1)} \exp(-2\beta^-(2)t), \quad (3.64)$$

where the notation  $\beta^\pm(h(F, n_b)) = \beta^\pm(n_b)$  is used. This leads to the average dissociation time

$$\tau = \frac{1}{\beta^-(1)} + \frac{1}{2\beta^-(2)}, \quad (3.65)$$

and for  $N$  initially bound bonds, the relation generalizes to

$$\tau = \sum_{k=1}^N \frac{1}{k\beta^-(k)}. \quad (3.66)$$

Without rebinding, the dissociation process can be considered as the sum of independent Poisson processes with parameters  $k\beta^-(k)$ . Therefore the total average dissociation time is given by the sum of the inverse rupture rates. Since  $\beta^-(k) = \beta^-(h(F, n_b = k))$  increases exponentially with the force per bond, the largest contribution to the sum is given by the rupture of the first bond. The average time until the first bond ruptures is proportional to  $\exp(-\tilde{\ell}_b \tilde{F}/N)$ .

In Fig. 3.8, the average first dissociation times  $\tau$  are shown for clusters with different sizes  $N = n_b(t = 0)$  as a function of  $F/N$ . The double logarithmic plot in Fig. 3.8a demonstrates the convergence towards the solution for vanishing force given in (3.58), as indicated with dotted lines. For large forces, the average dissociation time is determined by rupture of the first bond, which occurs with a slope  $-\tilde{\ell}_b$ , see Fig. 3.8b. The curves for different cluster sizes overlap for  $\tilde{F}/N > 1$  (indicated with a dashed vertical line).

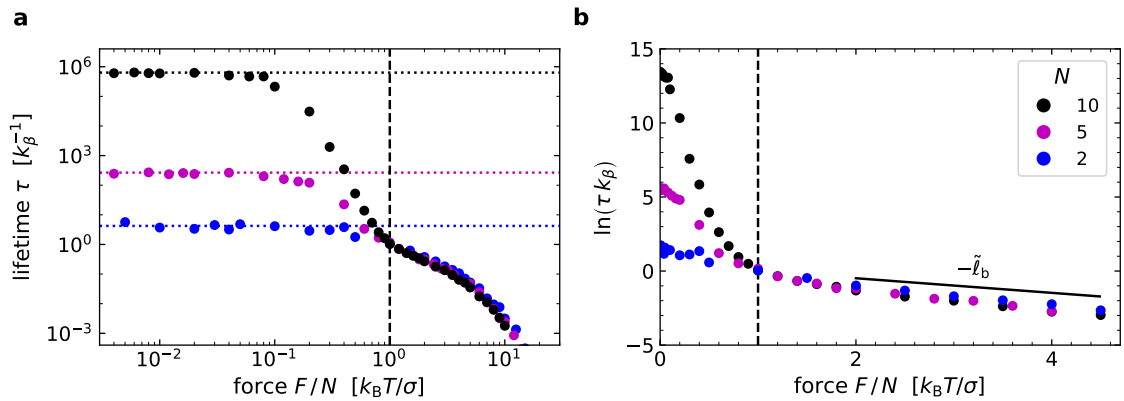


Figure 3.8. Average lifetimes of adhesion clusters with size  $N = 2, 5, 10$ . a) For small forces the lifetimes converge towards a constant value given by (3.58). b) For large forces per molecule, the curves overlap, because rebinding can be neglected and a rupture cascade takes place. The average dissociation time is determined by the rupture of the first bond, which is  $\propto \exp(-\tilde{\ell}_b \tilde{F}/N)$ . Parameter values are given in Table 3.2.

### Approximation of cluster lifetimes with a WKB-ansatz

The WKB-method, named after Wentzel, Kramers and Brillouin, is used to find approximate solutions of linear differential equations. In physics courses, it is often introduced in the field

of quantum mechanics, because it can be used to find a first-order approximation of wave functions that solve Schrödinger's equation, for instance for a particle in a potential energy well [279]. However, WKB-methods are also applied to classical stochastic systems, mostly to describe large deviations, extinctions or switches in populations, as reviewed in Refs. [6, 252]. The approximation makes use of a large parameter  $K$ , which is typically related to the deterministic steady state population size [5, 367]. However, large fluctuations can cause rare events, e.g. the extinction of the population. Such deviations have a small probability, but are often of great importance, for example in the case of infections and diseases or other catastrophic events [101, 172]. There are different WKB-methods that allow a description of the trajectory, or optimal path, from the quasi-stationary solution with large population size to the extinction point, and the mean time to extinction.

In the context of the adhesion cluster model presented here, the extinction point corresponds to the dissociation of the cluster. Therefore the technique yields an approximate expression for the average lifetime  $\tau$ . In the following, a dissipative WKB-approximation is used, as presented in [5], with  $n_b^*$ , the deterministic steady state number of bonds, as the large parameter. For  $n_b \gg 1$  and in leading order, the ansatz  $\exp(-n_b^* S)$  for the quasi-stationary probability distribution transforms the problem from solutions of the stochastic master equation to constant-energy trajectories of a Hamiltonian. However, the approximation breaks down for small bond numbers,  $n_b \sim \mathcal{O}(1)$ , so that a second solution is matched to the WKB-approximation in order to find the expression for the mean lifetime  $\tau$ .

For the WKB-approximation in the regime  $n_b \gg 1$ , it is assumed that the probability distribution function that solves the master equation with an absorbing boundary at  $n_b = 0$  is long lived and has a peak at the (strictly speaking metastable) steady state. Slowly, the distribution decays in time and “leaks” into the absorbing state  $p_0$ . The ansatz for this approximation is given by [5]

$$p_{n_b > 0}(t) = p_{n_b}^* \exp(-t/\tau), \quad p_0(t) = 1 - \exp(-t/\tau), \quad (3.67)$$

where  $p_{n_b}^*$  with  $n_b = 1, 2, \dots$  is the quasi-stationary distribution for  $n_b > 0$  and the decay rate  $\tau^{-1}$  yields an approximation for the inverse average cluster dissociation time. When this ansatz is inserted into the stochastic master equation (3.9), it leads to an eigenvalue problem with  $\lambda = \tau^{-1}$ . Since the eigenvalue  $\lambda$  is exponentially small, stationary solutions can be considered instead of solving the eigenvalue problem. For the WKB-ansatz,  $n_b$  is extended to continuous values. The rescaled variables  $q = n_b/n_b^*$  and  $Q = N/n_b^*$  are introduced, where  $n_b^* \gg 1$  is the number of bonds in the quasi-stationary state. One central assumption is that the rates can be written as [5]

$$(N - n_b)\beta^+(F, n_b) = n_b^* w_{+1}(q) + u_{+1}(q) + \mathcal{O}(1/n_b^*), \quad (3.68)$$

$$n_b \beta^-(F, n_b) = n_b^* w_{-1}(q) + u_{-1}(q) + \mathcal{O}(1/n_b^*), \quad (3.69)$$

and that close to the quasi-stationary state, i.e. for  $q \sim \mathcal{O}(1)$ ,  $w_{\pm 1}(q) \sim \mathcal{O}(1)$  holds. For the chosen rupture and binding rates, this is only guaranteed for  $F = 0$ , so that in the following only the equilibrium case with  $w_{+1}(q) = (Q - q)\beta^+$ ,  $w_{-1}(q) = q\beta^-$ , and  $u_{\pm 1} = 0$  is discussed. The absorbing boundary demands  $w_{\pm 1}(0) = 0$ . Additionally, it is known from (3.48) that  $Q = (1 + \beta)/\beta$  at  $F = 0$ .

For  $n_b \gg 1$ , the ansatz for the quasi-stationary distribution  $p^*(q)$  reads

$$p^*(q) = A \exp(-n_b^* S(q) - S_1(q)), \quad (3.70)$$

where  $S(q) \sim \mathcal{O}(1)$  and  $S_1(q) \sim \mathcal{O}(1)$ . The ansatz is inserted into the stationary master equation. In leading order  $\mathcal{O}(n_b^*)$ , a stationary Hamilton-Jacobi equation  $0 = H(q, S'(q)) = H(q, \rho)$  can be identified with

$$H(q, \rho) = w_{+1}(q) (\exp(\rho) - 1) + w_{-1}(q) (\exp(-\rho) - 1). \quad (3.71)$$

The bond fraction  $q$  acts as the coordinate of an effective mechanical particle and  $\rho = S'(q)$  is the conjugate momentum. Thus, the dynamics are given by zero-energy trajectories of the Hamiltonian  $H$ . The trivial solution  $q = 0$  corresponds to the extinction line. The relaxation trajectory  $\rho = 0$  crosses both the deterministic steady state solution  $(q, p) = (q^*, 0) = (1, 0)$  and the extinction point  $(q, p) = (0, 0)$ . The nontrivial  $H = 0$  solution is given by

$$\rho_0(q) = \ln\left(\frac{w_{-1}(q)}{w_{+1}(q)}\right) = \ln\left(\frac{q}{(Q - q)\beta}\right) = \ln\left(\frac{q}{1 + \beta - q\beta}\right). \quad (3.72)$$

This activation trajectory crosses the  $q$ -axis at  $q = 1$  and reaches  $q = 0$  asymptotically. It describes the most probable path to extinction. Integration yields the action  $S(q)$ :

$$S(q) = \int^q \rho_0(\xi) d\xi = q \ln(q) + \frac{1 + \beta - q\beta}{\beta} \ln(1 + \beta - q\beta). \quad (3.73)$$

In subleading order, the stationary master equation with ansatz (3.70) results in a differential equation for  $S_1(q)$

$$0 = w_{+1}(q) \left( S_1'(q) - \frac{\rho_0'(q)}{2} \right) \exp(S'(q)) + w_{-1}(q) \left( -S_1'(q) - \frac{\rho_0'(q)}{2} \right) \exp(-S'(q)) \\ - w_{+1}'(q) \exp(\rho_0(q)) + w_{-1}'(q) \exp(-\rho_0(q)), \quad (3.74)$$

where the activation trajectory  $\rho_a(q) = S'(q)$  is already inserted. This is solved for  $S_1'(q)$  and simplified to  $S_1'(q) = -\rho_0''(q)/(2\rho_0'(q))$ . Integration yields

$$S_1(q) = -\frac{1}{2} \ln\left(\frac{1 + \beta}{q(1 + \beta - \beta q)}\right). \quad (3.75)$$

The integration constant is covered with the prefactor  $A$  in ansatz (3.70). This prefactor is determined by normalization of the quasi-stationary probability distribution. For this

purpose, it is assumed that  $p^*(q)$  is sharply peaked around  $q^* = 1$ , so that it can be approximated by a Gaussian function of the form

$$p^*(q) \approx A \exp(-n_b^* S(q^*) - S_1(q^*) - S''(q^*) n_b^* (q - q^*)^2 / 2) \quad (3.76)$$

with

$$S(q^*) = 0, \quad S_1(q^*) = -\frac{1}{2} \ln(1 + \beta), \quad S''(q^*) = \rho'_0(q^*) = 1 + \beta. \quad (3.77)$$

The normalization condition reads

$$1 = \int_0^Q p^*(q) dq = A \sqrt{\frac{\pi}{2n_b^*}} \left( \text{Erf} \left( \frac{N}{\sqrt{2}} \right) + \text{Erf} \left( \frac{N\beta}{\sqrt{2}} \right) \right) \stackrel{N \gg 1}{\approx} A \sqrt{\frac{2\pi}{n_b^*}}. \quad (3.78)$$

Therefore the normalization constant is set to the value  $A = \sqrt{n_b^*} / \sqrt{2\pi}$ .

The WKB-ansatz (3.70) is valid for  $n_b \gg 1$ . For  $n_b \sim \mathcal{O}(1)$  it breaks down, so that another solution of the master equation is required to approximate the quasi-stationary distribution for small bond numbers, compare [5, 6]. Here, the detailed balance condition (3.42) is applied recursively until  $p_1^*$  and  $p_1^* = 1/(\beta^{-\tau})$  is inserted. This leads to

$$p_{n_b}^* = \frac{1}{N} \binom{N}{n_b} \beta^{n_b-1} p_1^* = \frac{1}{N\beta^{-\tau}} \binom{N}{n_b} \beta^{n_b-1}. \quad (3.79)$$

The solution resembles a binomial distribution with success probability  $\beta/(1 + \beta)$  which is not normalized.

To match both solutions, the binomial distribution is approximated by a Gaussian distribution with mean  $n_b^*$  and variance  $n_b^*/(1 + \beta)$ ,

$$p^*(q) = \frac{1}{N\beta^{-\tau}} \frac{\sqrt{(1 + \beta)n_b^*}}{\sqrt{2\pi}} \frac{(1 + \beta)^N}{\beta} \exp\left(-\frac{n_b^*(1 + \beta)(q - q^*)^2}{2}\right). \quad (3.80)$$

A comparison with the Gaussian expansion for  $p^*(q)$  from the WKB-ansatz in (3.76) yields the approximation for the average cluster dissociation time

$$\tau = \frac{1}{N\beta^{-\tau}} \frac{(1 + \beta)^N}{\beta}. \quad (3.81)$$

The results for the average cluster dissociation time at  $F = 0$  are shown as functions of  $N$  and  $\beta$  in Fig. 3.9. The exact solution from (3.58) is given with solid lines. The WKB-approximation (3.81) (markers) agrees well with the exact solution.

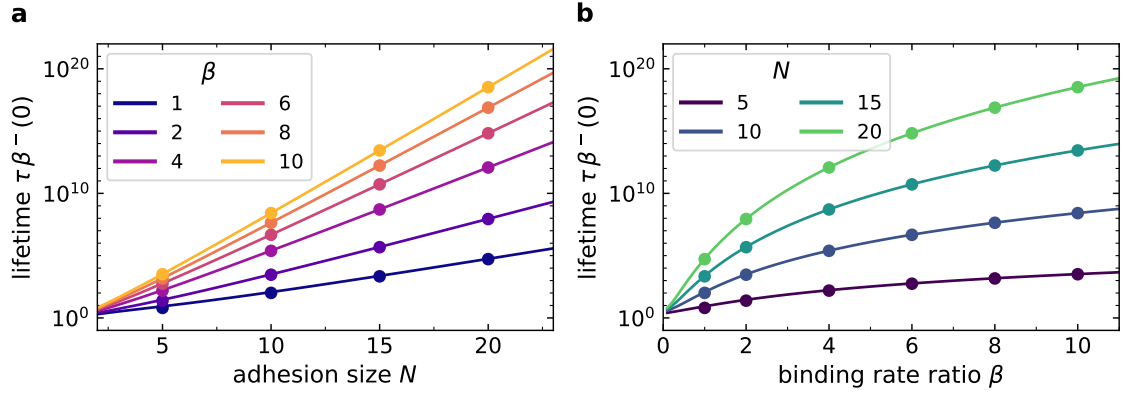


Figure 3.9. Average cluster dissociation time at  $F = 0$  as a function of a) adhesion size  $N$  and b) binding rate ratio  $\beta$ . Lines show exact results, compare Eq. (3.58) and markers indicate the WKB-approximation, compare Eq. (3.81).

### 3.2.2 Variable adhesion size

In the following, the general case for  $\gamma^\pm > 0$  is considered. In this model variant, the basic adhesion cluster with rupture and rebinding events is coupled to a reservoir of molecules. Molecules enter the cluster in state  $a$  with a rate  $\gamma^+$  and leave the cluster from state  $a$  into the reservoir with rate  $\gamma^-$ . As a result, the total number of molecules  $N = n_b + n_a$  is not fixed in time. Thus, the state of the cluster depends on both  $n_b$  and  $n_a$  and the master equation reads

$$\begin{aligned} \frac{d}{dt} p_{n_b, n_a}(t) = & -[n_a \beta^+(n_b) + n_b \beta^-(n_b) + \gamma^+ + n_a \gamma^-] p_{n_b, n_a}(t) \\ & + (n_a + 1) \beta^+(n_b - 1) p_{n_b - 1, n_a + 1}(t) + (n_b + 1) \beta^-(n_b + 1) p_{n_b + 1, n_a - 1}(t) \\ & + \gamma^+ p_{n_b, n_a - 1}(t) + (n_a + 1) \gamma^- p_{n_b, n_a + 1}(t) \end{aligned} \quad (3.82)$$

The state occupation numbers  $n_b$  and  $n_a$  are in general not limited, so that they can cover all non-negative integers  $\mathbb{Z}$ . Therefore the only boundary condition is  $p_{n_b, n_a} = 0$  if  $n_b < 0$  or  $n_a < 0$ . In Fig. 3.10a, a fraction of the full transition diagram is sketched. Apart from the states on the boundaries, i.e. states with  $n_b = 0$  or  $n_a = 0$ , each state has four neighbours, see Fig. 3.10b. Because of the infinite set of states, the derivation of an exact analytical solution is not feasible. But even if the set of states is infinite, the system will tend towards the stationary distribution, so that many  $p_{n_b, n_a}(t)$  are expected to decay quickly. In the following, the focus lies on these steady state solutions.

#### Steady state solution

For a first idea how the reservoir affects the system, the special and simple case of  $\beta^+(h) = \beta^-(h) = 0$  is considered. When there are no transitions between state  $a$  and  $b$ ,

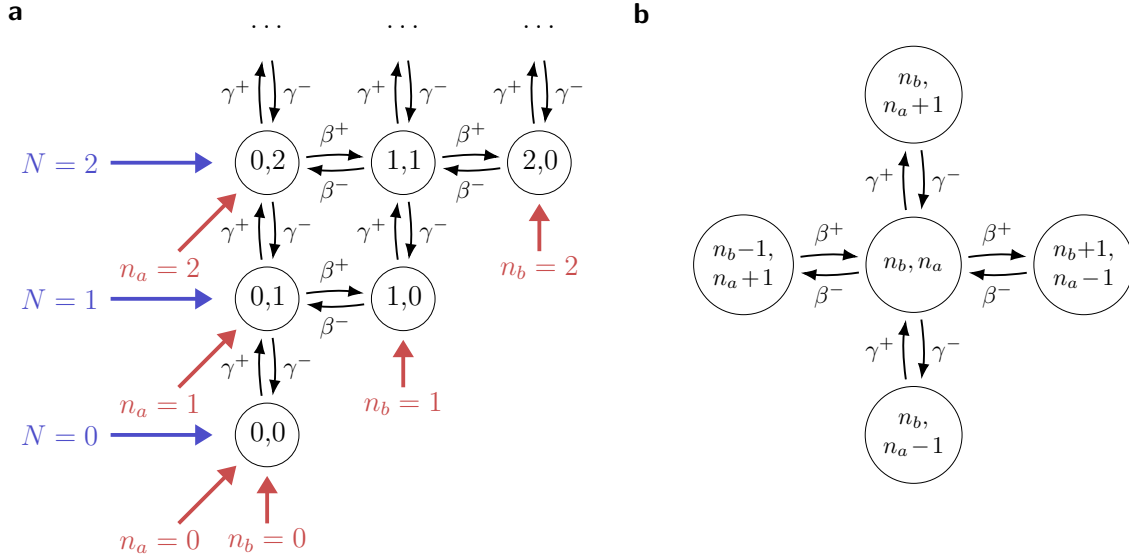


Figure 3.10. Transition diagram for the basic adhesion rupture model with a reservoir connection. a) The full diagram is shown for states  $(n_b, n_a)$  with  $N \leq 2$ . Columns correspond to constant bond numbers  $n_b$ , while constant unbound molecule numbers  $n_a$  are found on the diagonals. The reservoir rates allow jumps between different cluster sizes. b) The state  $(n_b, n_a)$  and its four neighbouring states  $(n_b, n_a \pm 1)$  and  $(n_b \mp 1, n_a \pm 1)$ .

the variables  $n_b$  and  $n_a$  are independent, because the occupation number of state  $b$  is fixed to the constant value  $n_b(t=0)$ . The master equation for the unbound molecules in state  $a$  reads

$$\frac{d}{dt}p_{n_a}(t) = -[\gamma^+ + n_a\gamma^-]p_{n_a}(t) + \gamma^+p_{n_a-1}(t) + (n_a + 1)\gamma^-p_{n_a+1}(t). \quad (3.83)$$

The steady state solution of this process is a Poisson distribution with parameter  $\gamma = \gamma^+/\gamma^-$ :

$$p_{n_a}^* = \frac{\gamma^{n_a}}{n_a!} \exp(-\gamma). \quad (3.84)$$

Expected value and variance are given by  $\langle n_a \rangle = \text{Var}(n_a) = \gamma$ .

With finite binding and rupture rates, the steady state solution cannot be obtained easily from the master equation any more. The detailed balance conditions provide a simpler access to the stationary solution. As it is shown in Fig. 3.10b, states are either connected via binding and rupture or via the reservoir connection. The equilibrium distribution fulfils

$$p_{n_b, n_a}^* = \frac{\gamma}{n_a} p_{n_b, n_a-1}^*, \quad (3.85)$$

$$p_{n_b, n_a}^* = \frac{(n_a + 1)\beta^+(n_b - 1)}{n_b\beta^-(n_b)} p_{n_b-1, n_a+1}^*. \quad (3.86)$$

Iterative application and combination of these two conditions leads to

$$p_{n_b, n_a}^* = \frac{\gamma^{n_b+n_a}}{n_b! n_a!} \left( \prod_{k=1}^{n_b} \frac{\beta^+(k-1)}{\beta^-(k)} \right) p_{0,0}^* \quad (3.87)$$

for  $n_b \geq 1$  and  $n_a \geq 0$ . For  $n_b = 0$ , the equilibrium probability distribution is given by  $p_{0,n_a}^*/p_{0,0}^* = \gamma^{n_a}/n_a!$ . Since all probabilities add up to one, the remaining probability  $p_{0,0}^*$  can be determined to

$$p_{0,0}^* = \exp(-\gamma) \left( 1 + \sum_{n_b=1}^{\infty} \frac{\gamma^{n_b}}{n_b!} \left( \prod_{k=1}^{n_b} \frac{\beta^+(k-1)}{\beta^-(k)} \right) \right)^{-1}. \quad (3.88)$$

The marginal distributions  $p_{n_b}^* = \sum_{n_a} p_{n_b,n_a}^*$  and  $p_{n_a}^* = \sum_{n_b} p_{n_b,n_a}^*$  follow as

$$p_{n_b}^* = \frac{\gamma^{n_b}}{n_b!} \left( \prod_{k=1}^{n_b} \frac{\beta^+(k-1)}{\beta^-(k)} \right) \left( 1 + \sum_{n_b=1}^{\infty} \frac{\gamma^{n_b}}{n_b!} \left( \prod_{k=1}^{n_b} \frac{\beta^+(k-1)}{\beta^-(k)} \right) \right)^{-1}, \quad (3.89)$$

$$p_{n_a}^* = \frac{\gamma^{n_a}}{n_a!} \exp(-\gamma). \quad (3.90)$$

The number of bound and unbound molecules in steady state are independent stochastic variables, because  $p_{n_b,n_a}^* = p_{n_b}^* p_{n_a}^*$ . The stationary number of unbound molecules is only determined by the connection to the reservoir. For vanishing forces, i.e.  $\beta^+(h(F=0, n_b)) = \beta^+$  and  $\beta^-(h(F=0, n_b)) = \beta^-$ , the equilibrium solution simplifies to

$$p_{n_b,n_a}^* = \frac{\gamma^{n_b+n_a} \beta^{n_b}}{n_b! n_a!} \exp(-\gamma(1 + \beta)). \quad (3.91)$$

This is the product of two Poisson distributions with parameters  $\gamma$  and  $\gamma\beta$ . Thus, the expected values are given by  $\langle n_a \rangle = \gamma$  and  $\langle n_b \rangle = \gamma\beta$  and the variances are given by  $\text{Var}(n_a) = \gamma$  and  $\text{Var}(n_b) = \gamma\beta$ . For large forces, the stretch increases and thus the binding rate decreases while the rupture probability grows. This leads to a shift towards the left columns in the transition diagram in Fig. 3.10, so that less bonds  $n_b$  are expected in steady state. The connection to the reservoir is independent of  $n_b$  or the extension  $h$ , so that unbound molecules stay untouched.

In Fig. 3.11, simulation results are compared to the analytical steady state solutions derived above. Fig. 3.11a-c show exemplary histograms of the distribution  $p_{n_b,n_a}^*$  at selected force values. The marginal distributions are shown in Fig. 3.11d-g. The distribution  $p_{n_b,n_a}^*$ , which is centered around  $(n_a^*, n_b^*) = (\gamma, \gamma\beta)$  at  $F = 0$ , shifts towards lower values of  $n_b$  with increasing force. At  $\tilde{F} = 3.2$ , the marginal distribution  $p_{n_b}^*$  exhibits a peak at  $n_b = 1$ , while the distribution of unbound molecules does not depend on the external force, as expected. Simulation results from adhesion clusters with rebinding (markers or orange bars) agree well with the analytical solutions (solid lines or blue bars).

## Macroscopic equations

The macroscopic equations for the average number of molecules  $\langle n_b \rangle$  and  $\langle n_a \rangle$  are obtained from the master equation as

$$\frac{d}{dt} \langle n_b \rangle(t) = -\langle n_b \rangle(t) \beta^-(h) + \langle n_a \rangle(t) \beta^+(h), \quad (3.92)$$

$$\frac{d}{dt} \langle n_a \rangle(t) = -\langle n_a \rangle(t) \beta^+(h) + \langle n_b \rangle(t) \beta^-(h) + \gamma^+ - \langle n_a \rangle(t) \gamma^-. \quad (3.93)$$



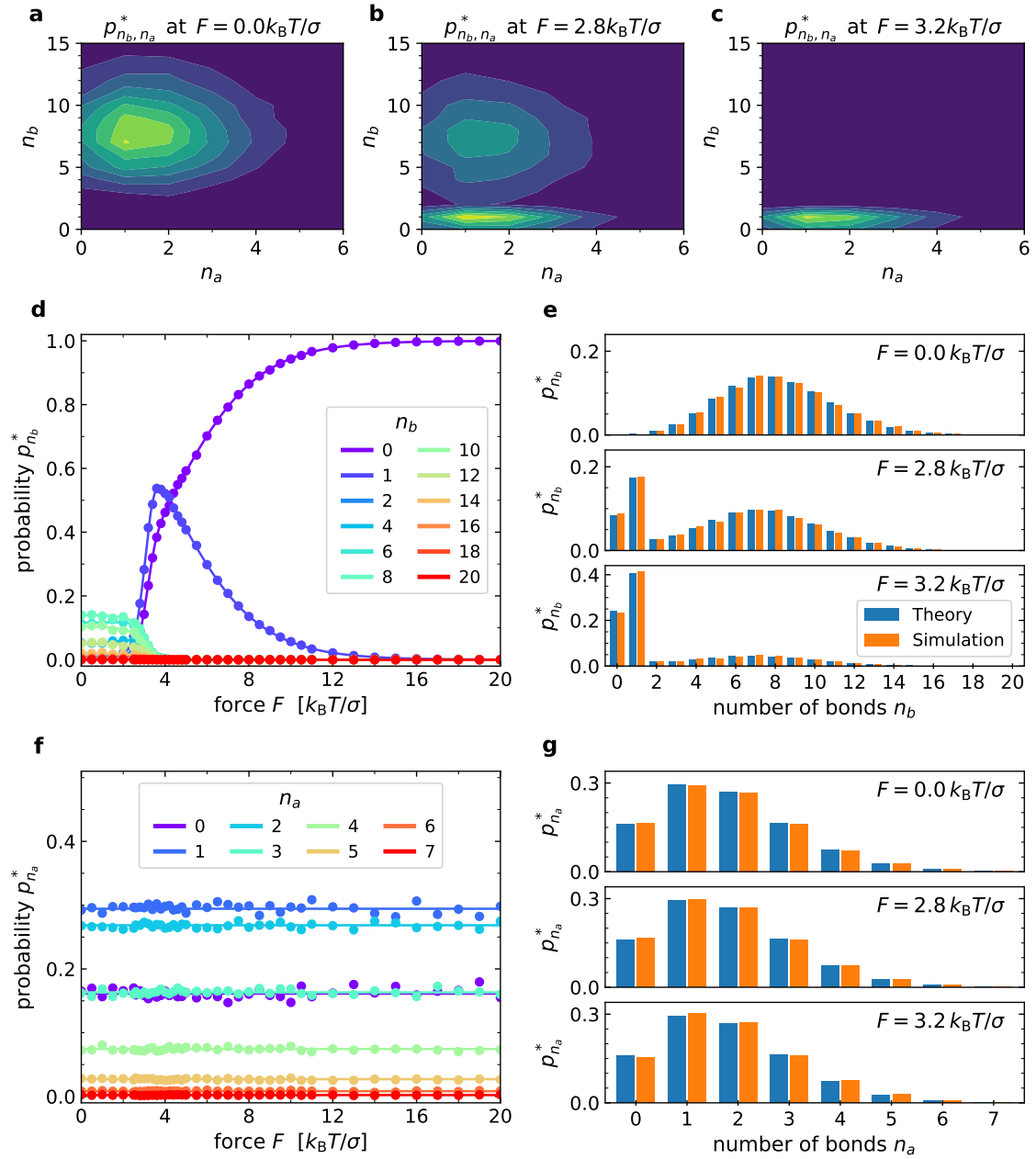


Figure 3.11. Steady state quantities for a cluster with  $N^* \approx 10$  molecules as a function of force  $F$ . a-c) Histograms of the joint steady state distribution  $p_{n_b, n_a}$  at selected force values. Yellow (dark blue) corresponds to maximal (minimal) values. d) Marginal steady state probabilities  $p_{n_b}^*$  up to  $n_b \leq 20$ . e) Marginal steady state distribution  $p_{n_b}$  for selected force values. f) Marginal steady state probabilities  $p_{n_a}^*$  up to  $n_a \leq 7$ . g) Marginal steady state distributions  $p_{n_a}$  for selected force values. Parameter values are given in Table 3.2.

For the derivation, it was again assumed that the rates are functions of the free parameter  $h$ . The force balance equation  $F(h, n_b)$  in Eq. (3.5) thus acts as an additional constraint for steady state solutions. The average total number of molecules  $\langle N \rangle(t) = \langle n_b \rangle(t) + \langle n_a \rangle(t)$  evolves in time as

$$\frac{d}{dt} \langle N \rangle(t) = \gamma^+ - \langle n_a(t) \rangle \gamma^- . \quad (3.94)$$

The steady state solution of the macroscopic equations is given by

$$\langle n_a \rangle = \gamma , \quad \langle n_b \rangle = \gamma \beta(h) = \gamma \exp \left( -\frac{\tilde{h}^2}{2} + \tilde{\epsilon}_b \right) \quad (3.95)$$

with the rate ratios  $\gamma = \gamma^+/\gamma^-$  and  $\beta(h) = \beta^+(h)/\beta^-(h)$ . The fraction of bonds  $\langle n_b \rangle/\langle N \rangle$  agrees with the average fraction of bonds in a cluster without the reservoir connection, compare (3.48). In this case, however, the average number of unbound molecules is regulated by the reservoir and therefore the total number of molecules is proportional to  $\gamma$ . Note that the macroscopic steady state solution fulfils

$$\beta^-(h) \langle n_b \rangle = \beta^+(h) \langle n_a \rangle , \quad (3.96)$$

which corresponds to a macroscopic version of the detailed balance condition. In steady state, the force balance condition reads  $\tilde{F} = \gamma \beta(h) \tilde{h}$  and  $\tilde{F}/\langle N \rangle$  agrees with Eq. (3.49), the force balance equation for the cluster without a reservoir connection. The maximal value of the external force with a steady state solution is found at the positive solution of the extremum condition  $\tilde{F}'(\tilde{h}) = 0$  as  $\tilde{h} = 1$ . At this stretch, the expected number of bound molecules in steady state is given by

$$\langle n_b \rangle (\tilde{h} = 1) = \gamma \exp \left( -\frac{1}{2} + \tilde{\epsilon}_b \right)$$

and the externally applied force reaches  $\tilde{F} = \langle n_b \rangle (\tilde{h} = 1)$  and therefore grows linearly with the reservoir rate ratio  $\gamma$ .

In Fig. 3.12, the results obtained from the macroscopic equations are compared to simulated trajectories with  $\gamma = 1.824$  and  $\tilde{\epsilon}_b = 1.5$ , which leads to  $\langle N \rangle \approx 10$  molecules at  $\tilde{F} = 0$ . Fig. 3.12a shows the average number of bonds in steady state as a function of the stretch  $h$ . The force balance condition of possible steady state solutions is plotted in Fig. 3.12b with a solid line. The simulation results show that the macroscopic solution is only valid for small stretches per bond, so that fluctuations are small. A combination of Fig. 3.12a and b yields the average number of bond  $\langle n_b \rangle$  as a function of force  $F$  in steady state, shown in Fig. 3.12c). As in the case without a reservoir connection, the number of bonds decreases with increasing external force.

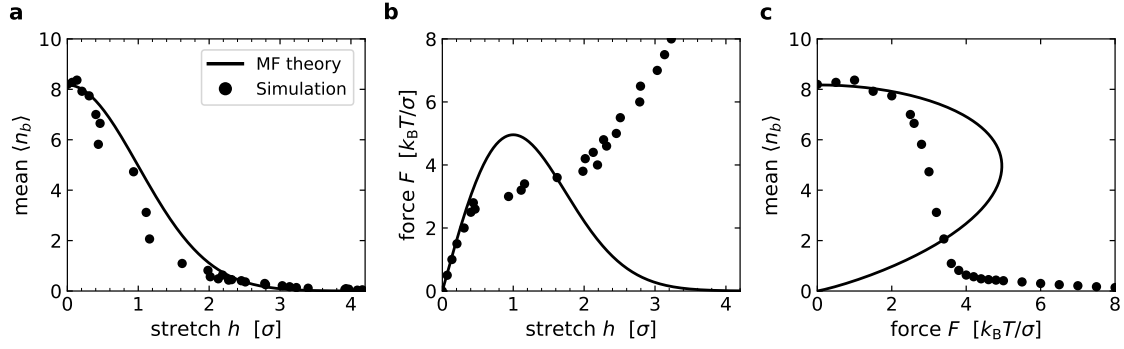


Figure 3.12. Mean field steady state solution for the basic adhesion cluster model with a variable number of molecules. a) Average number of bonds as a function of the bond extension  $h$ . b) The force balance equation with the steady state solutions  $\langle n_b \rangle(h)$  connects force and stretch. c) The resulting steady state solutions as a function of external force  $F$ . Parameter values are given in Table 3.2.

## Lifetimes

As a last aspect, the average cluster dissociation time is studied. For an adhesion cluster with binding, rupture and a reservoir connection, all states with  $n_b = 0$  are end points of possible dissociation pathways. The simulation results in Fig. 3.13 show that qualitatively, the dependence of lifetime on force per initially bound molecule is comparable to adhesion clusters with a constant size.

For low forces, i.e.  $\tilde{F}/N < 1$ , the lifetime curves converge towards a lower value than for constant cluster sizes. One reason for this effect is that the average waiting time between two reactions at  $F = 0$  also depends on  $(\gamma^+)^{-1}$ , so that more transitions happen per unit time for larger clusters. More importantly, the variance of the number of bonds  $n_b$  is higher in the system with a reservoir connection than in a cluster with a constant size. Therefore fluctuations are larger and the system has a higher probability to reach the state of complete dissociation. Since the total number of molecules  $N$  decreases with external force  $F$ , this effect is enhanced for small finite forces. Even without the time-dependent solution for  $p_0(t)$ , the average dissociation time at  $F = 0$  can be approximated with an argumentation that is used for many first-passage time problems, such as for estimations on protein folding and population extinction dynamics [5, 370]. The approach is also given in Ref. [110] for the lifetime of adhesion clusters with rupture and rebinding events, but a constant number of molecules. As in the WKB-approximation, it is assumed that the probability distribution function that solves the master equation with an absorbing boundary at  $n_b = 0$ , is long lived and has a peak at the (strictly speaking metastable) steady state. Slowly, the distribution decays in time and “leaks” into the absorbing state  $p_0$ . The ansatz for this approximation is then given in (3.67). When this ansatz is inserted into the master equation and  $p_{n_b}^*$  for  $n_b \geq 1$  is found, the lifetime of the cluster can be

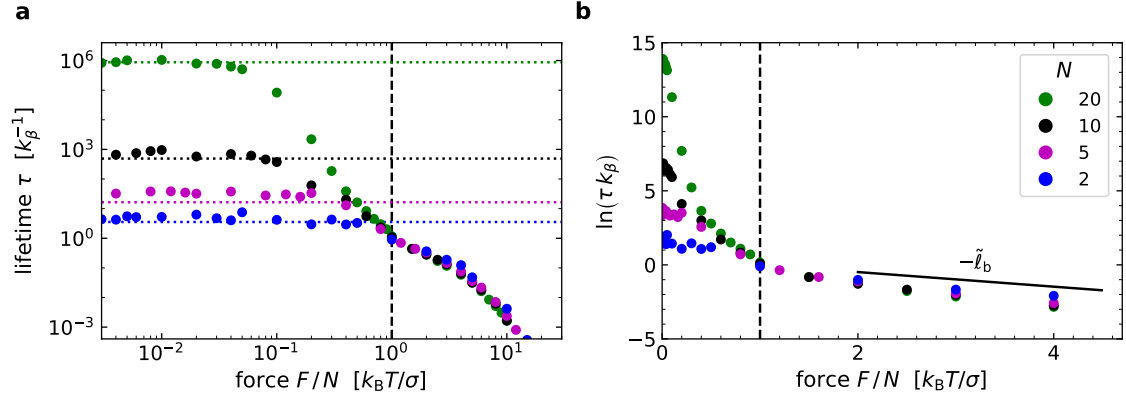


Figure 3.13. Average lifetimes of adhesion clusters with  $N^* \approx 2, 5, 10, 20$  molecules. a) For small forces the lifetimes converges towards a constant value. b) For large forces per molecule, the curves overlap, because rebinding can be neglected and a rupture cascade takes place. The average dissociation time is determined by the rupture of the first bond, which is  $\propto \exp(-\tilde{\ell}_b \tilde{F}/N)$ . Parameter values are given in Table 3.2.

approximated by

$$\tau = \frac{1}{\beta^-(1)p_1^*} = \frac{1}{\beta^-} \frac{\exp(\gamma \exp(\tilde{\epsilon}_b))}{\gamma \exp(\tilde{\epsilon}_b)}, \quad (3.97)$$

where the exact solution for the steady state of the non-absorbing boundary at  $F = 0$  is inserted for  $p_1^*$ . This includes a small normalization error, because the state  $n_b = 0$ , which has a probability of  $\exp(-\gamma\beta)$ , is still included in this distribution. As long as the mean number of bonds at  $F = 0$  is much larger than one, this error is negligible. The lifetime approximation is shown in Fig. 3.13a with dotted lines.

For large forces, the lifetime curves collapse onto one curve with a slope of  $-\tilde{\ell}_b$  in the logarithmic plot, see Fig. 3.13b. In this regime, the rupture cascade dominates the possible dissociation pathways, so that the same behaviour is obtained with and without a reservoir connection.

### 3.3 Extended model with conformational changes

As an extension of the basic model, conformational changes of bound and unbound molecules are added to the set of transitions. A sketch of the different adhesion molecule states and the single bond transition diagram are shown in Fig. 3.14.

The distance between the two boundaries is given by  $\ell_0 + h = \ell_0 + \Delta + h_u$ , where  $\ell_0$  is the rest length of folded adhesion molecules. The stretch of folded and unfolded bonds is given by  $h$  and  $h_u = h - \Delta$ , respectively. Since the difference lies only in the constant unfolding length  $\Delta$ , it is sufficient to specify the value of  $h$ .

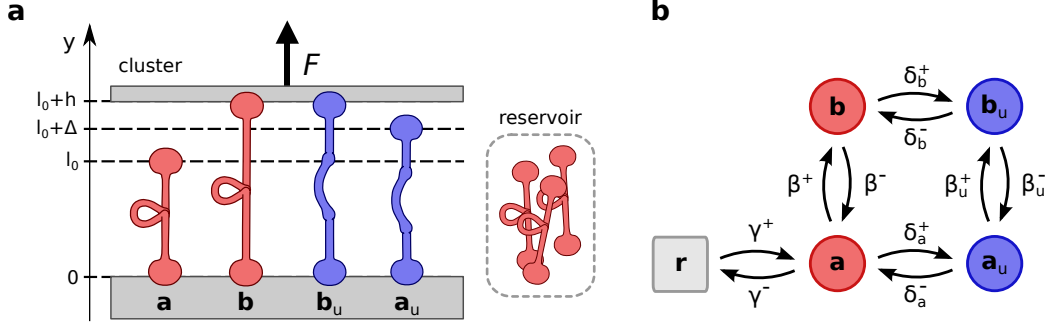


Figure 3.14. Extended adhesion cluster model. Molecules within the cluster can bind and rupture or undergo a conformation change. Unbound molecules are in exchange with the surrounding reservoir. a) Sketch of a small cluster. b) Single molecule transition diagram.

The length difference of folded bonds in state  $b$  and unfolded bonds in state  $b_u$  lead to the force-balance condition

$$F = \kappa n_b h + \kappa n_{b_u} (h - \Delta) \quad \Leftrightarrow \quad \tilde{h} = \frac{\tilde{F} + n_{b_u} \tilde{\Delta}}{n_b + n_{b_u}}, \quad (3.98)$$

where  $n_b$  is the number of bonds  $b$  and  $n_{b_u}$  denotes the number of unfolded bonds, i.e. the occupation of state  $b_u$ . Because of the different lengths, all bonds are either stretched or compressed, as soon as both conformations are present simultaneously. Only if  $n_b = 0$  or  $n_{b_u} = 0$  holds, i.e. if all bonds are either folded or unfolded, a configuration with no elastic energy contributions is possible. To estimate the effect of the unfolding and refolding transitions, the rates  $\delta_b^\pm(h)$  are expanded for small stretches:

$$\delta_b^+(h) = \delta_b^+(0) \left( 1 + \frac{\tilde{\Delta}}{2} \tilde{h} + \frac{\tilde{\Delta}^2}{8} \tilde{h}^2 \right) + \mathcal{O}(\tilde{h}^3), \quad (3.99)$$

$$\delta_b^-(h_u) = \delta_b^-(0) \left( 1 - \frac{\tilde{\Delta}}{2} \tilde{h}_u + \frac{\tilde{\Delta}^2}{8} \tilde{h}_u^2 \right) + \mathcal{O}(\tilde{h}_u^3) \quad (3.100)$$

$$\text{with } \delta_b^+(0) = k_\delta \exp\left(-\tilde{\Delta}^2/8 - \tilde{\epsilon}_f\right) \text{ and } \delta_b^-(0) = k_\delta \exp\left(-\tilde{\Delta}^2/8\right). \quad (3.101)$$

Small positive stretches  $h$  of folded bonds promote unfolding, while the refolding probability increases at negative stretches  $h_u$ , i.e. when unfolded bonds are compressed. In the following the resulting cluster behavior is analysed for a system with a constant and variable number of adhesion molecules. For better readability, all rates are denoted as functions of the folded bond stretch  $h$ .

### 3.3.1 Constant number of molecules

For the case that the reservoir rates  $\gamma^\pm$  are set to zero, the total number of adhesion molecules is constant,  $N = n_a + n_{a_u} + n_b + n_{b_u}$ . The state of the cluster at a constant force  $F$  is therefore determined by the occupation number of three states and  $N$ . The number

of possible configurations grows with  $N^3$ , more specifically, the number of cluster states  $(n_b, n_{b_u}, n_a, n_{a_u})$  for in total  $N$  adhesion molecules is given by  $\binom{N+3}{3}$ . The probability to find a specific configuration with  $n_b$  and  $n_{b_u}$  bound and  $n_a$  and  $n_{a_u}$  unbound molecules is denoted by  $p_{n_b, n_{b_u}, n_a, n_{a_u}}$  with  $n_{a_u} = N - n_b - n_{b_u} - n_a$ . The stochastic master equation describes the time evolution of the probability  $p_{n_b, n_{b_u}, n_a, n_{a_u}}(t)$ . It reads

$$\begin{aligned} \frac{d}{dt} p_{n_b, n_{b_u}, n_a, n_{a_u}} = & - \left[ n_b(\beta^-(h) + \delta_b^+(h)) + n_{b_u}(\beta_u^-(h) + \delta_b^-(h)) \right. \\ & \left. + n_a(\beta^+(h) + \delta_a^+) + n_{a_u}(\beta_u^+(h) + \delta_a^-) \right] p_{n_b, n_{b_u}, n_a, n_{a_u}} \\ & + (n_b + 1)\beta^-(h)p_{n_b+1, n_{b_u}, n_a-1, n_{a_u}} + (n_b + 1)\delta_b^+(h)p_{n_b+1, n_{b_u}-1, n_a, n_{a_u}} \\ & + (n_{b_u} + 1)\beta_u^-(h)p_{n_b, n_{b_u}+1, n_a, n_{a_u}-1} + (n_{b_u} + 1)\delta_b^-(h)p_{n_b-1, n_{b_u}+1, n_a, n_{a_u}} \\ & + (n_a + 1)\beta^+(h)p_{n_b-1, n_{b_u}, n_a+1, n_{a_u}} + (n_a + 1)\delta_a^+ p_{n_b, n_{b_u}, n_a+1, n_{a_u}-1} \\ & + (n_{a_u} + 1)\beta_u^+(h)p_{n_b, n_{b_u}-1, n_a, n_{a_u}+1} + (n_{a_u} + 1)\delta_a^- p_{n_b, n_{b_u}, n_a-1, n_{a_u}+1}, \end{aligned} \quad (3.102)$$

where the  $t$ -dependence was omitted and the stretch depends on the external force and the number of bound molecules,  $h = h(F, n_b, n_{b_u})$ , see Eq. (3.98). For negative occupation numbers or if the sum of molecules does not equal  $N$ , the probability is defined as zero.

### Steady state solution

In the long time limit, the probability distribution approaches a constant value, the steady state distribution. The detailed balance conditions read

$$p_{n_b+1, n_{b_u}, n_a, n_{a_u}-1}^* = \frac{(n_a + 1)\beta^+(n_b, n_{b_u})}{(n_b + 1)\beta^-(n_b + 1, n_{b_u})} p_{n_b, n_{b_u}, n_a+1, n_{a_u}-1}^*, \quad (3.103)$$

$$p_{n_b, n_{b_u}+1, n_a, n_{a_u}-1}^* = \frac{(n_b + 1)\delta_b^+(n_b + 1, n_{b_u})}{(n_{b_u} + 1)\delta_b^-(n_b, n_{b_u} + 1)} p_{n_b+1, n_{b_u}, n_a, n_{a_u}-1}^*, \quad (3.104)$$

$$p_{n_b, n_{b_u}, n_a, n_{a_u}}^* = \frac{(n_{b_u} + 1)\beta_u^-(n_b, n_{b_u} + 1)}{n_{a_u}\beta_u^+(n_b, n_{b_u})} p_{n_b, n_{b_u}+1, n_a, n_{a_u}-1}^*, \quad (3.105)$$

$$p_{n_b, n_{b_u}, n_a+1, n_{a_u}-1}^* = \frac{n_{a_u}\delta_a^-}{(n_a + 1)\delta_a^+} p_{n_b, n_{b_u}, n_a, n_{a_u}}^*, \quad (3.106)$$

where the rates are written as functions of the occupation numbers  $n_b$  and  $n_{b_u}$ . Multiplication of these conditions yields the Kolmogorov condition

$$1 = \frac{\beta^+(n_b, n_{b_u})\delta_b^+(n_b + 1, n_{b_u})\beta_u^-(n_b, n_{b_u} + 1)\delta_a^-}{\beta^-(n_b + 1, n_{b_u})\delta_b^-(n_b, n_{b_u} + 1)\beta_u^+(n_b, n_{b_u})\delta_a^+}. \quad (3.107)$$

For large clusters with  $n_b + n_{b_u} \gg 1$ , we find  $h(F, n_b, n_{b_u}) \approx h(F, n_b + 1, n_{b_u}) \approx h(F, n_b, n_{b_u} + 1)$ , so that Eq. (3.4) is recovered. Even at  $F = 0$ , the rates still depend on the current number of bound molecules  $n_b$  and  $n_{b_u}$ , because  $\tilde{h}(0, n_b, n_{b_u}) = n_{b_u}\tilde{\Delta}/N_b$ , where  $N_b = n_b + n_{b_u}$ . There are two special configurations, where all elastic energy contributions vanish;  $n_{b_u} = 0$  with  $\tilde{h} = 0$  and  $n_b = 0$  with  $\tilde{h} = \tilde{\Delta}$ . In equilibrium, these two cluster configurations are energetically equivalent, as long as  $\tilde{\epsilon}_f = 0$ . For  $\tilde{\epsilon}_f > 0$ , the folded state is favoured.

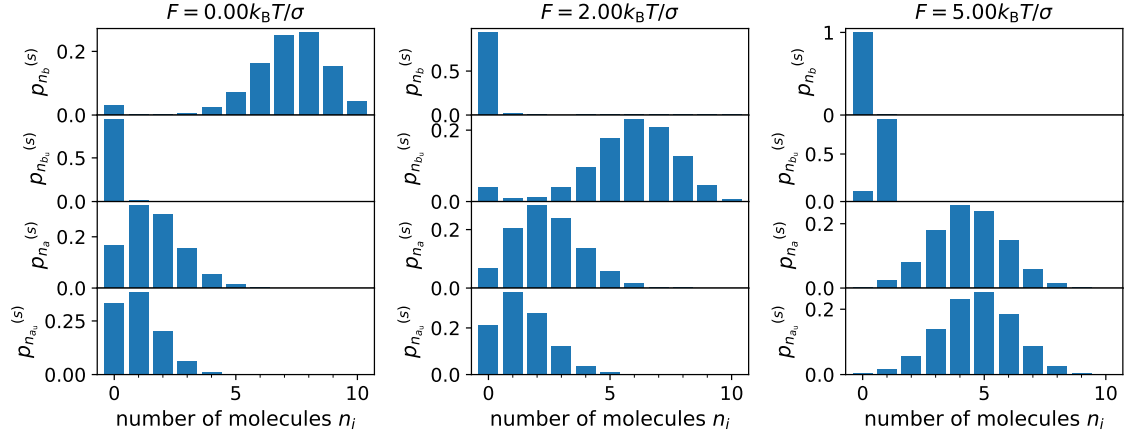


Figure 3.15. Marginal steady state probabilities  $p_{n_i}^{(s)}$  of adhesion clusters with binding, rupture, unfolding and refolding with a constant number of  $N = 10$  molecules at three different force values. Parameter values are given in Table 3.3.

Figure 3.15 shows simulation results of the steady state marginal distributions  $p_{n_i}^{(s)}$  for the four different molecular states at three different force values. As expected, the bound folded state  $b$  is occupied most in equilibrium at  $F = 0$ . For higher forces, the unfolding transition leads to a shift towards the state  $b_u$ . For large forces, the rupture rate dominates and thus, most molecules are in the unbound states  $a$  and  $a_u$ .

### Macroscopic equation

The macroscopic equations for the average number of molecules  $\langle n_b \rangle$ ,  $\langle n_{b_u} \rangle$ ,  $\langle n_a \rangle$  and  $\langle n_{a_u} \rangle$  are obtained from the master equation, as explained in App. A.1. For better readability, the explicit notation of the expected value  $\langle \cdot \rangle$  and the time dependence are omitted. Transition rates are written as functions of the free parameter  $h$ . The mean field approximation reads

$$\frac{d}{dt}n_b = -n_b \left( \beta^-(h) + \delta_b^+(h) \right) + n_a \beta^+(h) + n_{b_u} \delta_b^-(h), \quad (3.108)$$

$$\frac{d}{dt}n_{b_u} = -n_{b_u} \left( \beta_u^-(h) + \delta_b^-(h) \right) + n_{a_u} \beta_u^+(h) + n_b \delta_b^+(h), \quad (3.109)$$

$$\frac{d}{dt}n_a = -n_a \left( \beta^+(h) + \delta_a^+ \right) + n_b \beta^-(h) + n_{a_u} \delta_a^-, \quad (3.110)$$

$$\frac{d}{dt}n_{a_u} = -n_{a_u} \left( \beta_u^+(h) + \delta_a^- \right) + n_{b_u} \beta_u^-(h) + n_a \delta_a^+. \quad (3.111)$$

The stationary solution can be found analytically. Inserting the Kolmogorov condition (3.4) yields the compact form

$$n_b(h) = \beta(h) n_a(h), \quad (3.112)$$

$$n_{b_u}(h) = \beta(h) \delta_b(h) n_a(h), \quad (3.113)$$

$$n_{a_u}(h) = \frac{\beta(h) \delta_b(h)}{\beta_u(h)} n_a(h) = \delta_a n_a(h), \quad (3.114)$$

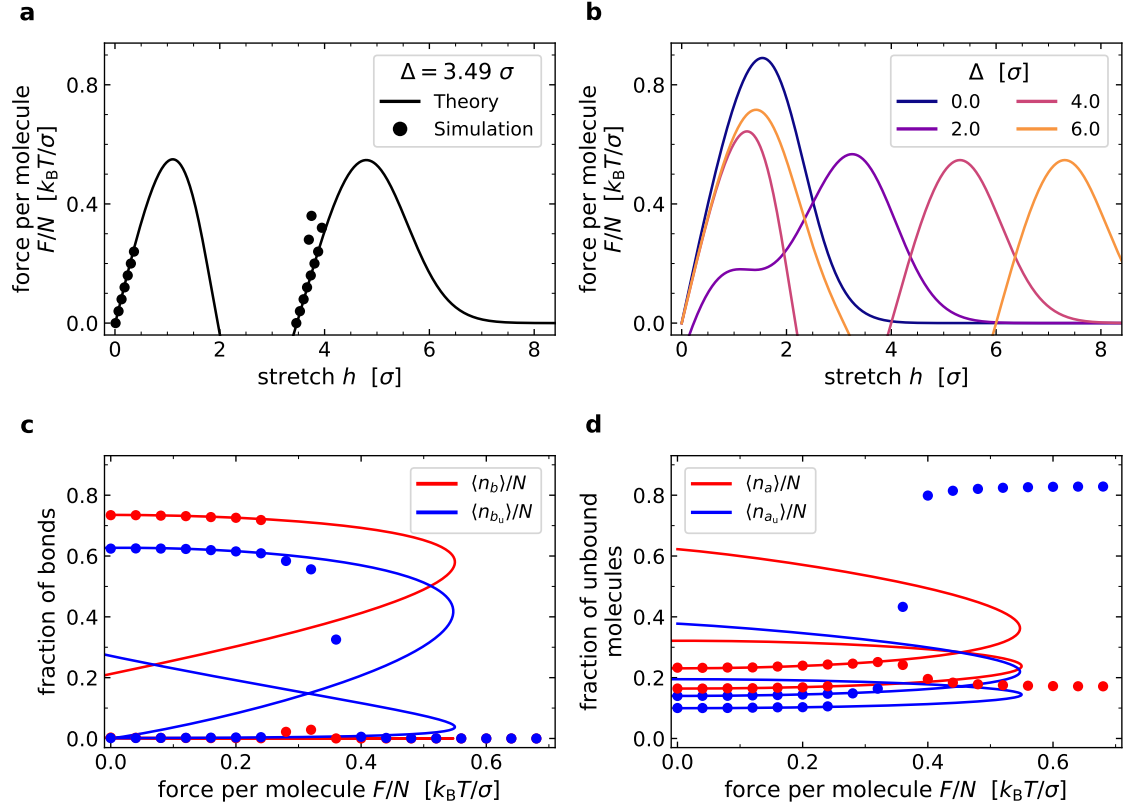


Figure 3.16. Comparison of the possible stationary solutions of the macroscopic equations (lines) and steady state simulation results (markers) for adhesion clusters of the extended model with  $N = 10$  molecules. a) Force per molecule as a function of the stretch for  $\tilde{\Delta} = 3.49$ . b) Force per molecule as a function of the stretch for different values of the unfolding length. c) The fraction of bonds as a function of force per molecule. d) The fraction of unbound molecules as a function of force per molecule. Parameter values are given in Table 3.3.

where the rate ratios  $\beta_{(u)}(h) = \beta_{(u)}^+(h)/\beta_{(u)}^-(h)$ ,  $\delta_b(h) = \delta_b^+(h)/\delta_b^-(h)$  and  $\delta_a = \delta_a^+/\delta_a^-$  are used. Since the total number of molecules is fixed by  $N = n_b(h) + n_{b_u}(h) + n_{a_u}(h) + n_a(h)$ , the remaining solution for  $n_a(h)$  is given by

$$n_a(h) = N \left( 1 + \delta_a + \beta(h) + \beta(h)\delta_b(h) \right)^{-1}. \quad (3.115)$$

Additionally, the force balance condition (3.98) has to hold. The resulting condition  $F = F(h)$  restricts the possible steady state stretch values  $h$  at a constant force. For low force values, multiple solutions exist. In simulations, only two branches of these solutions are observed; a first solution with low stretch  $h$  and a high number of folded bonds in state  $b$  and a second solution with  $h \approx \Delta$  and a high number of unfolded bonds in state  $b_u$ , see Fig. 3.16a. Both branches fulfil  $\partial_h F > 0$ . Above a certain force value, no solution exists. How the relation between force per molecules  $F/N$  and possible steady state stretches



$h$  depends on the unfolding length  $\Delta$  is illustrated in Fig. 3.16b. At  $\tilde{\Delta} = 0$ , folded and unfolded bonds are indistinguishable, which results in a single branch with  $\partial_h F > 0$ . For  $\tilde{\Delta} = 0$  and  $\tilde{\epsilon}_f = 0$  the steady state solution of the basic adhesion cluster model is obtained. For  $\tilde{\Delta} > 2$ , two local maxima are found. Their separation grows with increasing unfolding length. In Fig. 3.16c and 3.16d the fraction of bound and unbound molecules in steady state are shown as functions of the external force per molecule. Besides the restriction to two branches of the solution, it can be seen that the macroscopic equations provide a valid approximation for the average state occupation numbers for small forces. At large forces, the steady state simulation results deviate from the possible analytical solutions, because fluctuations become important.

## Lifetimes

Complete cluster dissociation occurs, when the last bond ruptures. In the extended model, the dissociation pathways has to reach either a state  $(1, 0, n_a, n_{a_u})$  or  $(0, 1, n_a, n_{a_u})$  with  $N = 1 + n_a + n_{a_u}$ . Therefore the mean lifetime can be approximated by

$$\tau = \frac{1}{\beta^-(1, 0) \sum_{n_a} p_{1,0,n_a,N-1-n_a}^* + \beta_u^-(0, 1) \sum_{n_a} p_{0,1,n_a,N-1-n_a}^*}, \quad (3.116)$$

where the rupture rates are written as functions of the state occupation numbers  $n_b$  and  $n_{b_u}$ , i.e.  $\beta^-(n_b, n_{b_u})$ .

Figure 3.17 shows the simulation results for average cluster lifetime as a function of force per molecule for clusters with size  $N = 10$ ,  $N = 5$  and  $N = 2$ . Initially, all molecules are

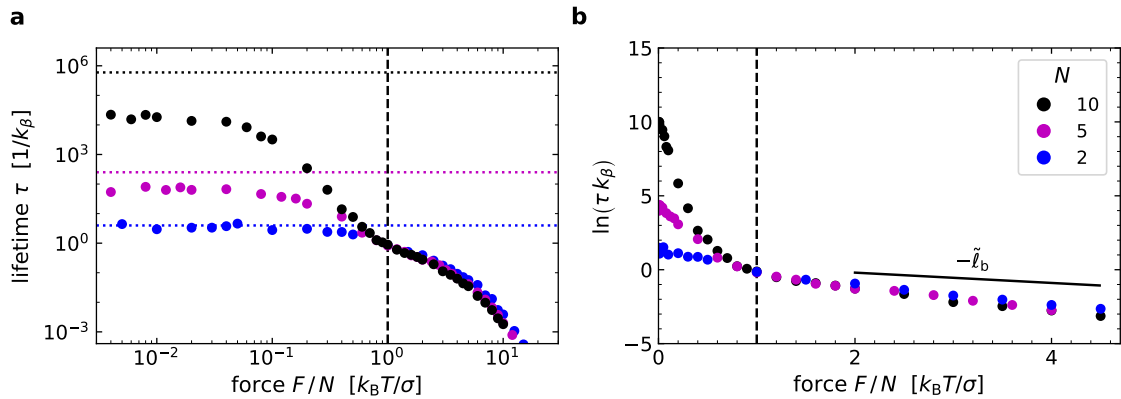


Figure 3.17. Average lifetimes of adhesion clusters in the extended model and with  $N = 2, 5, 10$  molecules. a) For small forces, lifetimes converges towards a constant value, which is for  $N > 2$  lower than in the basic adhesion model (dotted lines). b) For large forces per molecule, the curves overlap, as in the basic cluster model. The initially folded bonds either rupture directly or first unfold and then rupture. Parameter values are given in Table 3.3.

in the bound, folded state  $b$ . In comparison to the basic adhesion model, the competition between folded and unfolded length decreases the average lifetime for  $N = 10$  and  $N = 5$ . For large forces  $F/N > 1$ , the curves overlap, because rebinding can be neglected and a rupture cascade dominates.

### 3.3.2 Variable adhesion size

In the following, a molecule reservoir is added to the extended cluster model. The reservoir leads to an exchange of unbound, folded molecules, i.e. molecules in state  $a$ , with the surrounding. Unbound, but unfolded molecules first need to refold before they can leave the cluster.

The master equation that describes the time evolution of the probability to find a configuration  $(n_b, n_{b_u}, n_a, n_{a_u})$  is given by

$$\begin{aligned}
 \frac{d}{dt} p_{n_b, n_{b_u}, n_a, n_{a_u}} = & - \left[ n_b(\beta^-(h) + \delta_b^+(h)) + n_{b_u}(\beta_u^-(h) + \delta_b^-(h)) \right. \\
 & \left. + n_a(\beta^+(h) + \delta_a^+ + \gamma^-) + n_{a_u}(\beta_u^+(h) + \delta_a^-) + \gamma^+ \right] p_{n_b, n_{b_u}, n_a, n_{a_u}} \\
 & + (n_b + 1)\beta^-(h)p_{n_b+1, n_{b_u}, n_a-1, n_{a_u}} + (n_b + 1)\delta_b^+(h)p_{n_b+1, n_{b_u}-1, n_a, n_{a_u}} \\
 & + (n_{b_u} + 1)\beta_u^-(h)p_{n_b, n_{b_u}+1, n_a, n_{a_u}-1} + (n_{b_u} + 1)\delta_b^-(h)p_{n_b-1, n_{b_u}+1, n_a, n_{a_u}} \\
 & + (n_a + 1)\beta^+(h)p_{n_b-1, n_{b_u}, n_a+1, n_{a_u}} + (n_a + 1)\delta_a^+ p_{n_b, n_{b_u}, n_a+1, n_{a_u}-1} \\
 & + (n_{a_u} + 1)\beta_u^+(h)p_{n_b, n_{b_u}-1, n_a, n_{a_u}+1} + (n_{a_u} + 1)\delta_a^- p_{n_b, n_{b_u}, n_a-1, n_{a_u}+1} \\
 & + (n_a + 1)\gamma^- p_{n_b, n_{b_u}, n_a+1, n_{a_u}} + \gamma^+ p_{n_b, n_{b_u}, n_a-1, n_{a_u}} , \tag{3.117}
 \end{aligned}$$

where the explicit  $t$ -dependence is omitted and rates are written as functions of the stretch  $h = h(F, n_b, n_{b_u})$ . As before, the focus lies in the following on the steady state quantities.

#### Steady state

The detailed balance conditions (3.103)-(3.106) are supplemented by

$$p_{n_b, n_{b_u}, n_a, n_{a_u}}^* = \frac{\gamma}{n_a} p_{n_b, n_{b_u}, n_a-1, n_{a_u}}^* \tag{3.118}$$

for the connection with the reservoir. Summation over the occupation numbers  $n_b$ ,  $n_{b_u}$  and  $n_{a_u}$  or  $n_a$  together with the detailed balance conditions lead to the marginal distributions of unbound molecules

$$p_{n_a}^* = \frac{\gamma^{n_a}}{n_a!} \exp(-\gamma) , \quad p_{n_{a_u}}^* = \frac{(\gamma\delta_a)^{n_{a_u}}}{n_{a_u}!} \exp(-\gamma\delta_a) , \tag{3.119}$$

which describe Poisson distributions with parameters  $\gamma$  and  $\gamma\delta_a$ . The reservoir thus controls the occupation of unbound states. The marginal distributions for  $n_b$  and  $n_{b_u}$  cannot be obtained similarly, because the rates  $\beta_{(u)}^\pm(h)$  and  $\delta_b^\pm(h)$  depend on both occupation numbers. Figure 3.18 shows simulation results for the steady state marginal distributions for clusters

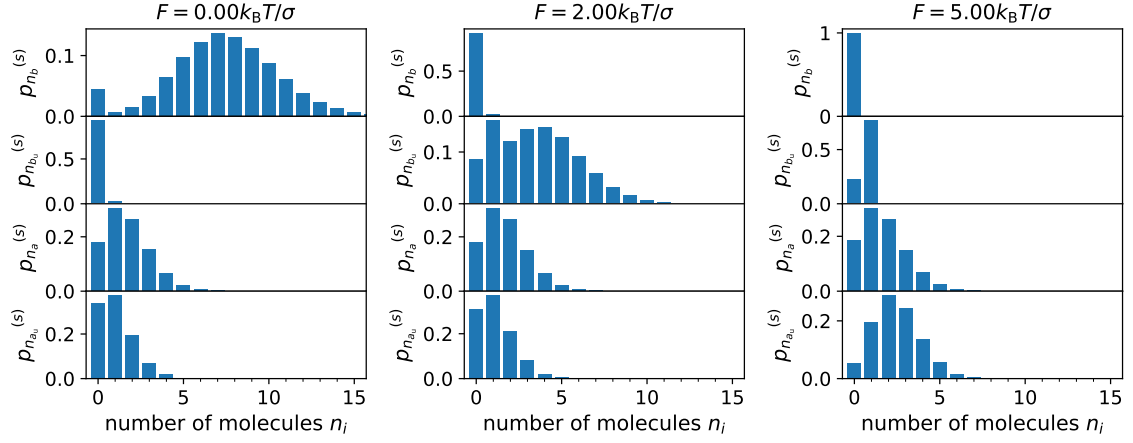


Figure 3.18. Marginal steady state probabilities  $p_{n_i}^{(s)}$  of adhesion clusters with conformational changes and molecule exchange at three different force values. The reservoir rate ratio  $\gamma = 1.72$  leads to  $N \approx 10$  molecules at  $F = 0$  in steady state. Parameter values are given in Table 3.3.

with reservoir rate ratio  $\gamma = 1.72$ , which leads to an approximate cluster size of  $N = 10$  for  $F = 0$ . The marginal distributions are exemplarily given for three different force values. As in the case without the reservoir, the folded state is occupied most at  $F = 0$ . For larger forces, the unfolding transition leads to an accumulation of unfolded bonds until the rupture process starts. As a result, the number of bound molecules decreases at large forces. Only one molecule can rebind and rupture repeatedly, because for  $n_b + n_{b_u} = 0$ , the distance between the boundaries is set to  $h = 0$ .

## Macroscopic equations

The macroscopic equations for the extended adhesion cluster model with a reservoir connection read

$$\frac{d}{dt}n_b = -n_b \left( \beta^-(h) + \delta_b^+(h) \right) + n_a \beta^+(h) + n_{b_u} \delta_b^-(h), \quad (3.120)$$

$$\frac{d}{dt}n_{b_u} = -n_{b_u} \left( \beta_u^-(h) + \delta_b^-(h) \right) + n_{a_u} \beta_u^+(h) + n_b \delta_b^+(h), \quad (3.121)$$

$$\frac{d}{dt}n_a = -n_a \left( \beta^+(h) + \delta_a^+ + \gamma^- \right) + n_b \beta^-(h) + n_{a_u} \delta_a^- + \gamma^+, \quad (3.122)$$

$$\frac{d}{dt}n_{a_u} = -n_{a_u} \left( \beta_u^+(h) + \delta_a^- \right) + n_{b_u} \beta_u^-(h) + n_a \delta_a^+, \quad (3.123)$$

where again the explicit notation for the expected value  $\langle \cdot \rangle$  and the time dependence are omitted. For the stationary solution, the sum of all equations directly leads to the steady state solution  $n_a = \gamma = \gamma^+ / \gamma^-$ . With this, the remaining solutions

$$n_b(h) = \gamma \beta(h), \quad n_{b_u}(h) = \gamma \beta(h) \delta_b(h), \quad n_{a_u} = \gamma \delta_a \quad (3.124)$$

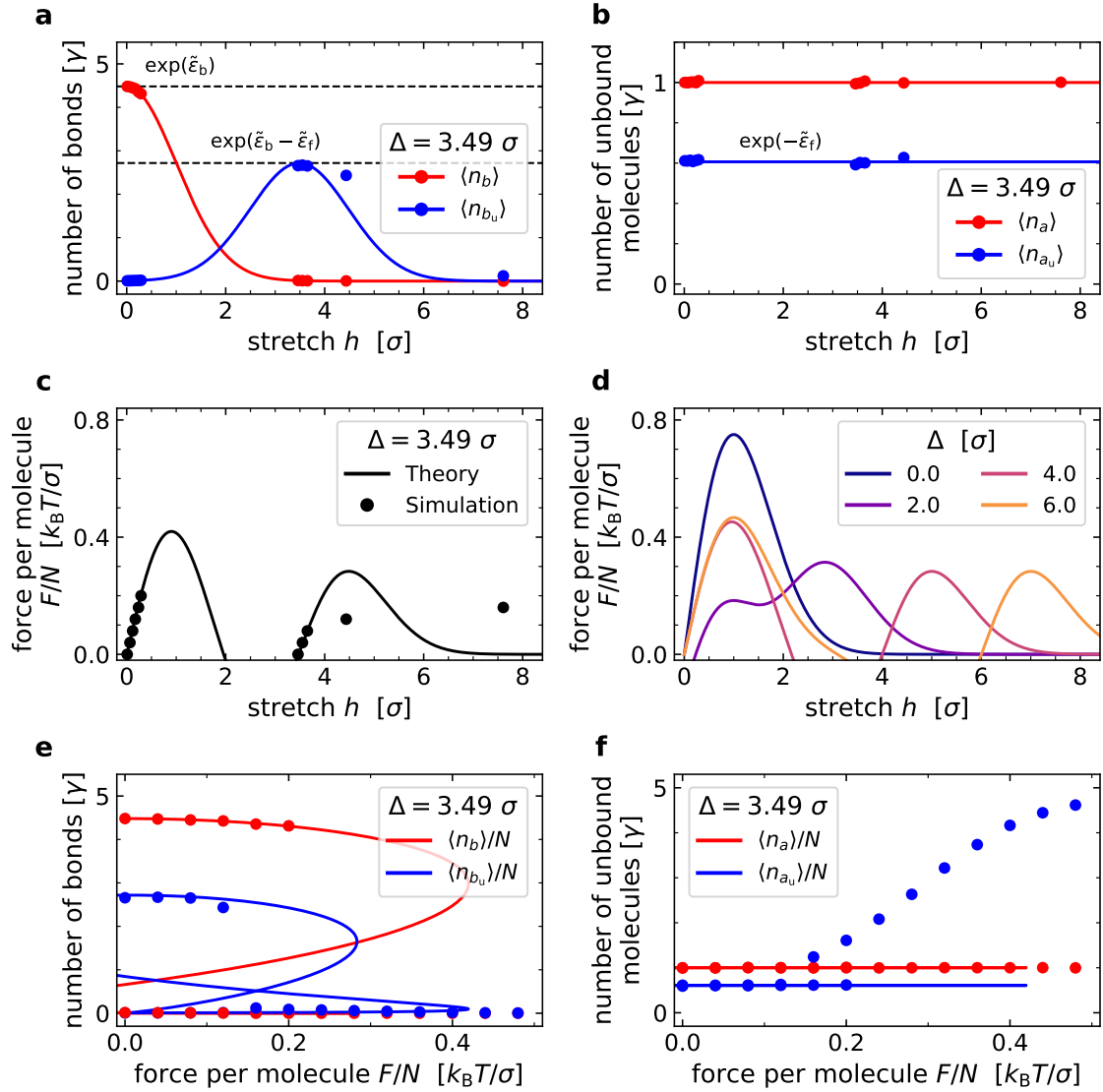


Figure 3.19. Comparison of the possible stationary solutions of the macroscopic equations and steady state simulation results for the extended adhesion cluster model with  $N \approx 50$  molecules at  $F = 0$  by means of a reservoir rate ratio  $\gamma = 8.59$ . Parameter values are given in Table 3.3.

are found. All expected values are proportional to the number of unfolded molecules  $n_a$ . The solution further corresponds to a macroscopic version of the detailed balance conditions. The Kolmogorov condition additionally ensures  $n_{b_u} = \gamma \delta_a \beta_u(h)$ .

A comparison of the stationary solution of the macroscopic equations and averaged simulation results is shown in Fig. 3.19 for a cluster with  $N \approx 50$  at  $F = 0$ . In simulations, only a limited stretch regime is realized. Clusters either consist of many folded bonds  $b$  with a low extension  $h$ , or of many unfolded bonds  $b_u$  with a low extension  $h_u$ , see Fig. 3.19a. This behaviour was already observed for the extended model with a constant adhesion size. The expected value of unbound molecules in states  $a$  and  $a_u$  is constant, see Fig. 3.19b. The relation  $F = F(h)$  is shown in Fig. 3.19c with the corresponding simulation results. Above a force of  $\tilde{F}/N \approx 0.2$ , the average stretch in simulations results from a single bond that rebinds and ruptures repeatedly. The force balance condition is shown for different values of the unfolding length  $\Delta$  in Fig. 3.19d. As in the case without the reservoir, the observed steady state branches exhibit a positive slope, i.e.  $\partial_h F(h) > 0$ . The branch with the higher extension is determined by the unfolding length  $\Delta$ . In Fig. 3.19e and f, the number of bound and unbound molecules is shown as a function of force per molecules  $F/N$ . The number of bonds decreases with increasing force per bond, until rupture dominates and the unfolded, unbound state is accumulated.

## Lifetime

The average lifetime  $\tau$  of adhesion clusters with conformational changes and a reservoir connection are shown in Fig. 3.20 for four different reservoir rate ratios  $\gamma$ . For low forces,  $\tau$

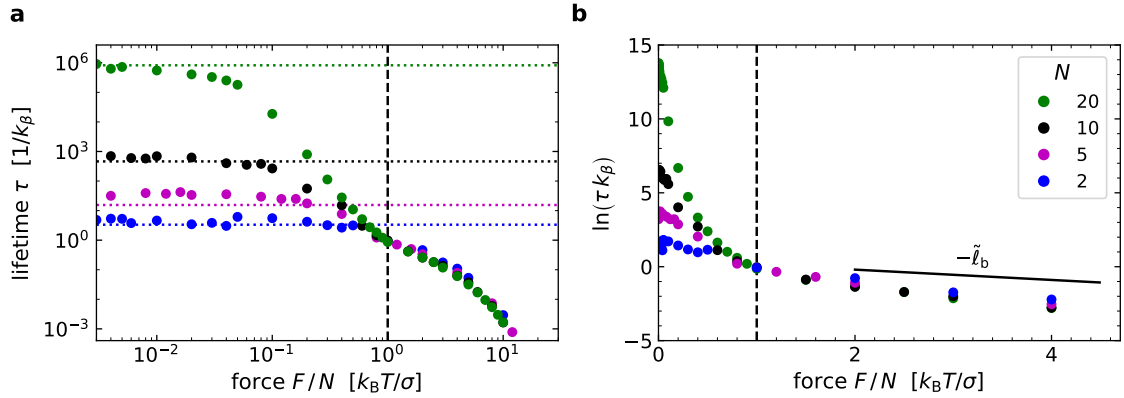


Figure 3.20. Average lifetimes of adhesion clusters with  $\gamma = 0.365, 0.912, 1.824, 3.649$ , which leads to clusters with  $N \approx 2, 5, 10, 20$  molecules at  $F = 0$ . a) For small forces the lifetimes converge towards a constant value, which is similar to the value without unfolding (dotted lines). b) For large forces per molecule, the curves overlap, as in the basic cluster model. The initially folded bonds either rupture directly or first unfold and then rupture. Parameter values are given in Table 3.3.

converges towards a value that is similar to the lifetime of adhesion clusters with a variable molecule number, but without the unfolding transition (dotted lines), compare Fig. 3.13a. For a large force per molecule, the lifetime curves overlap because of a cascade-like rupture process, in which bonds unbind directly or after unfolding.

### 3.4 Extended model with conformational changes and adhesion molecule recruitment

As a second extension, an adhesion cluster model with conformational changes and subsequent recruitment of new adhesion molecules into the cluster is considered. The motivation for this extension is based on biological adhesions in which protein binding sites are opened after unfolding. Consequently, it is assumed in this model variant that unfolded molecules offer new binding sites for molecules from the surrounding. In the following, the compound of an unfolded and a recruited molecule is called linked state. In this linked state, detachment and rebinding from the upper boundary is still possible, but the occupied binding site prevents refolding. Therefore the two new states  $a_{u,1}$  and  $b_{u,1}$  are introduced to account for the unbound, linked and bound, linked state, respectively. In the sketch in Fig. 3.21a, the different adhesion molecule states are depicted. The extended transition diagram is shown in Fig. 3.21b. The rates for the linking and unlinking process are denoted by  $\lambda^+$  and  $\lambda^-$ . For simplicity, they are chosen as constants. To study the effect of recruitment alone, it is assumed that the new molecule does not change the force response. Therefore the binding and rupture rates for linked molecules are given by  $\beta_u^\pm(h)$ , i.e. by the same rates that also describe binding and rupture of unfolded molecules.

The state of the cluster in this model is determined by the occupation numbers of the bound states  $n_b$ ,  $n_{b_u}$  and  $n_{b_{u,1}}$ , and the unbound states  $n_a$ ,  $n_{a_u}$  and  $n_{a_{u,1}}$ . As before, only the bound molecules experience the force, which acts on the upper boundary and pulls the surfaces apart. Since linked bonds have the same force response as unfolded bonds, the

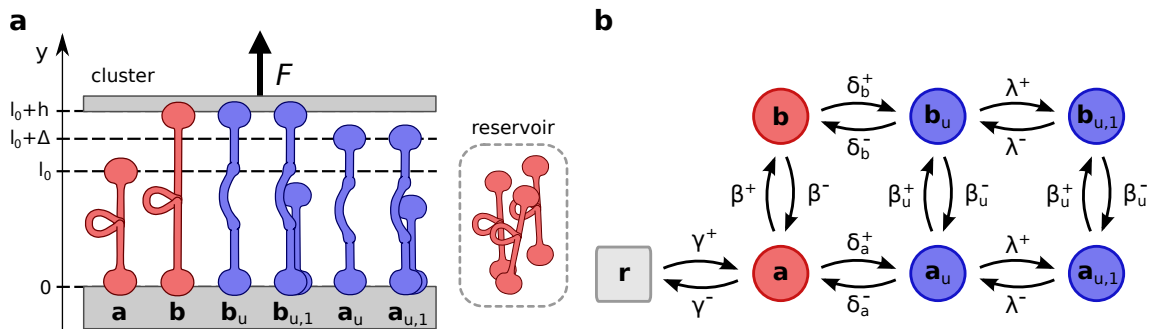


Figure 3.21. Extended adhesion cluster model with molecule unfolding and subsequent molecule recruitment. a) Sketch of a small cluster. b) Single molecule transition diagram.

force balance equation reads

$$F = \kappa n_b h + \kappa (n_{b_u} + n_{b_{u,1}})(h - \Delta). \quad (3.125)$$

The stationary solutions of the macroscopic equations are a convenient starting point to estimate the impact of the two new states on the average steady state cluster behaviour. The time evolution of bonds  $b$  and unbound molecules  $a$  are described by Eq. (3.120) and (3.122), because the linking transition does not effect the folded states. The macroscopic equations for the unfolded states are supplemented by two linking terms each. Together with the two new equations for the linked states, the modified macroscopic equations read

$$\frac{d}{dt} n_{b_u} = -n_{b_u} (\beta_u^-(h) + \delta_b^-(h) + \lambda^+) + n_{a_u} \beta_u^+(h) + n_b \delta_b^+(h) + n_{b_{u,1}} \lambda^-, \quad (3.126)$$

$$\frac{d}{dt} n_{b_{u,1}} = -n_{b_{u,1}} (\beta_u^-(h) + \lambda^-) + n_{a_{u,1}} \beta_u^+(h) + n_{b_u} \lambda^+, \quad (3.127)$$

$$\frac{d}{dt} n_{a_u} = -n_{a_u} (\beta_u^+(h) + \delta_a^-(h) + \lambda^+) + n_{b_u} \beta_u^-(h) + n_a \delta_a^+ + n_{a_{u,1}} \lambda^-, \quad (3.128)$$

$$\frac{d}{dt} n_{a_{u,1}} = -n_{a_{u,1}} (\beta_u^+(h) + \lambda^-) + n_{b_{u,1}} \beta_u^-(h) + n_{a_u} \lambda^+, \quad (3.129)$$

where, as before, the explicit notation for the expected value and the time dependence are omitted. The stationary solution for the linked states is given by

$$n_{b_{u,1}}(h) = \lambda n_{b_u}(h), \quad n_{a_{u,1}}(h) = \lambda n_{a_u}(h), \quad (3.130)$$

with the linking rate ratio  $\lambda = \lambda^+/\lambda^-$ . For the remaining states, the stationary solution agrees with the solution of the model with conformational changes and a reservoir connection, see Eq. (3.124). Thus, the number of linked bonds is proportional to the number of unfolded molecules.

Figure 3.22 shows the comparison of the stationary solution of the macroscopic equations and steady state simulation results. The stationary solution for the average total number of bonds  $N_B(h) = n_b(h) + n_{b_u}(h) + n_{b_{u,1}}(h)$  in Fig. 3.22a has two maxima at  $h \approx 0$  and  $h \approx \Delta = 3.49\sigma$ . The linking transition increases the number of bonds close to the second maximum linearly. The relation between the external force and the resulting steady state stretch,  $F(h)$ , is shown in Fig. 3.22b. Again, only the second branch of solutions with  $h \approx \Delta$  is affected by the linking transition, because molecule recruitment only takes place when bonds are unfolded. The combination of Fig. 3.22a and b makes it possible to show the average number of bonds in steady state as a function of the given external force in Fig. 3.22c. Besides increasing the average number of bonds in steady state for small forces, the linking transition also increases the force threshold, above which bond rupture dominates. Thus, the linking transition increases the total number of adhesion molecules, which leads to a lower force per bond and thus allows a steady state under higher forces. The qualitative behaviour however is similar to adhesion clusters without the linking transition, i.e. the model with conformational changes and a reservoir connection.

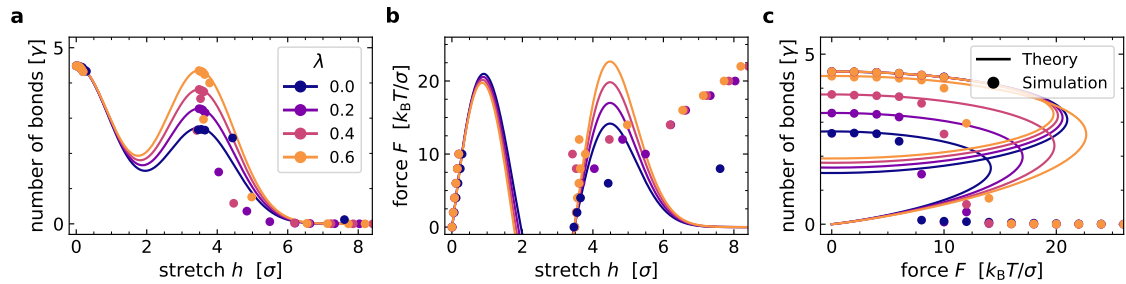


Figure 3.22. Stationary solutions of the macroscopic equations (solid lines) and steady state simulation results (round markers) for different linking rate ratios  $\lambda = \lambda^+ / \lambda^-$ . For the steady state solution at  $h \approx \Delta$ ,  $\lambda$  increases the number of bonds linearly. Parameter values are given in Table 3.3.

### 3.5 Summary

In this chapter, models for adhesion clusters under pulling forces are introduced and discussed. An adhesion cluster consists of discrete, elastic bonds which bridge the gap between two rigid surfaces. While the lower surface is fixed in the plane  $y = 0$ , the upper surface is subject to an external force. The force acts orthogonally to the surface, i.e. in  $y$ -direction, and it is shared by all bound molecules, which thereby keep the adhesion intact. The parallel alignment of all bonds in the direction of force reduces the degrees of freedom to one: the distance between the two surfaces. However, the results for this geometry can be transferred to other force directions, as long as the bonds are aligned in parallel and the force has a positive component in  $y$ -direction. Since the upper boundary can move freely, it will be pulled such, that the bonds realign in force direction. In this case, the vertical component of the bond extension determines the distance between the surfaces.

Motivated by the probabilistic nature of reactions in biological systems, the time evolution of the adhesion cluster is described by a stochastic process. A master equation is used to describe the cluster dynamics. Analytical methods and kinetic Monte Carlo simulations are employed to study the response of an adhesion cluster to a constant force with a special emphasis on steady state quantities and the average cluster lifetime. The different cluster models of this chapter differ in the choice of allowed transitions whose rates determine the stochastic process.

In the basic adhesion model, the only transitions allowed are bond rupture and rebinding. For low or vanishing forces, the cluster approaches a steady state configuration with many bonds under low stretch. A complete cluster dissociation, i.e. a subsequent rupture of all bonds, is a rare event that can be caused by large fluctuations. Under higher forces, the rupture probability increases while the rebinding probability decreases, so that the fraction of bound molecules decreases with force. This leads to larger fluctuations and inevitably, to a faster dissociation of the whole cluster.



In a first extension, a reversible unfolding transition is introduced, through which adhesion molecules become longer. Since the parallel bonds are confined between rigid surfaces, this transition gives rise to a competition between the native, i.e. folded, bond state  $b$  and the longer, unfolded state  $b_u$ . Folded bonds are favoured energetically at low forces, but also configurations with many unfolded and few folded bonds are observed. At large forces, bond rupture dominates again, so that the average fraction of bound molecules decreases with force, as it is observed in the basic model. However, clusters with unfolded bonds can bridge larger separations.

Both the basic model with rupture and rebinding and the extended model with conformational changes are initially introduced with a constant number of adhesion molecules. To analyse clusters with variable size, both models are also studied with an additional transition, the connection to a molecule bath. Folded, unbound molecules are thus exchangeable with the surrounding. The process is controlled by two constant rates. The addition of such a reservoir leads to a constant number of molecules in state  $a$ , to which the reservoir is coupled. As a consequence, the average occupation numbers of all other states are proportional to the reservoir rate ratio  $\gamma$  and thus to the average number of molecules  $n_a$ . For a constant value of  $\gamma$ , clusters in the extended model are larger than clusters with only rupture and binding, because more states are accessible. The qualitative response to force however is similar to the case of constant cluster sizes; the increased rupture probability reduces the average number of bonds. Moreover, also the adhesion size  $N$  decreases with force. Therefore, fluctuations are larger in the variants with a reservoir connection, so that the probability for complete cluster dissociation is higher.

As a second extension, an adhesion cluster model is presented, in which new bonds are recruited to binding sites at unfolded molecules. The unfolding process opens the previously buried binding pocket and thus gives rise to a linked state of an unfolded bond coupled to another adhesion molecule. The molecule recruitment increases the average bond number compared to the system with unfolding, but without linking at otherwise identical parameter values. Therefore, the force value above which fast cluster dissociation is observed is increased by molecule binding to unfolded domains. This effect is a consequence of cluster growth, because bonds in the linked and unfolded state have the same force response. Despite this higher resistance, the qualitative behaviour of the cluster is unaltered and both the fraction and total number of bonds decreases with increasing force.

In summary, vertical pulling destabilizes a cluster of adhesion molecules with equal force sharing. In the basic model, bond extension increases with force, which leads to a higher rupture probability. The unfolding transition allows bridging a larger distance, but at the same time it causes a competition between folded and unfolded bonds within the cluster, which can increase fluctuations and shorten lifetime. The linking mechanism induces cluster growth, so that the average extension per bond is reduced. However, it

does not change the steady state characteristics qualitatively. Therefore, neither the basic nor the extended cluster models presented here are able to grow under increasing forces. Cluster strengthening under force could however be observed, if the linked state in the extended model with molecule recruitment at unfolded domains is able to hold more force than single bonds.

### 3.6 Parameter values

The parameter values for simulations of adhesion clusters with binding and rupture are given in Table 3.2. Values that are used for the extended cluster models, which include conformational changes and linked state are given in Table 3.3. In all cases, the energy unit is given by  $1k_B T = 4.114 \text{ pN nm}$ , the time unit is given by the inverse binding rate prefactor  $t_0 = 1/k_\beta$ , and the restlength of a folded molecule is  $\ell_0 = 100 \text{ nm}$ .

The averages are taken from  $N_{\text{sim}}$  trajectories. After reaching the steady state,  $N_{\text{meas}}$  measurements are taken in intervals of  $N_{\text{wait}}$  single molecule reactions.

Unit		Value for data in Fig.					
		3.3	3.4	3.6/3.7	3.8	3.11/3.12	3.13
$\kappa$	[pN nm <sup>-1</sup> ]	1	1	1	1	1	1
$\sigma$	[nm]	2.03	2.03	2.03	2.03	2.03	2.03
$\ell_b$	[nm]	1	1	1	1	1	1
$\epsilon_b$	[ $k_B T$ ]	1.5	1.5	1.5	1.5	1.5	1.5
$\gamma^+$	[ $k_\beta$ ]	0	0	0	0	1.824	0.365, 0.912, 1.824, 3.649
$\gamma^-$	[ $k_\beta$ ]	0	0	0	0	1	1
$N_{\text{sim}}$		5	50	50	50	50	50
$N_{\text{meas}}$		$10^3$	$10^4$	$10^3$	$10^3$	$10^3$	$10^3$
$N_{\text{wait}}$		0	0	10	$10^6$	10	$10^6$

Table 3.2. Parameter values for simulations of the basic adhesion cluster model with binding and rupture.

Unit		Value for data in Fig.						
		3.15	3.16	3.17	3.18	3.19	3.20	3.22
$\kappa$	[pN nm <sup>-1</sup> ]	0.5	0.5	1	0.5	0.5	1	1
$\sigma$	[nm]	2.87	2.87	2.03	2.87	2.87	2.03	2.03
$\ell_b$	[nm]	1	1	1	1	1	1	1
$\epsilon_b$	[ $k_B T$ ]	1.5	1.5	1.5	1.5	1.5	1.5	1.5
$k_\delta$	[ $k_\beta$ ]	1	1	1	1	1	1	1
$\Delta$	[nm]	10	10	10	10	10	10	10
$\epsilon_f$	[ $k_B T$ ]	0.5	0.5	0.5	0.5	0.5	0.5	0.5
$\gamma^+$	[ $k_\beta$ ]	0	0	0	1.72	8.59	0.365, 0.912 1.824, 3.649	8.59
$\gamma^-$	[ $k_\beta$ ]	0	0	0	1	1	1	1
$\lambda^+$	[ $k_\beta$ ]	0	0	0	0	0	0	0.0, 0.2 0.4, 0.6
$\lambda^-$	[ $k_\beta$ ]	0	0	0	0	0	0	1
$N_{\text{sim}}$		50	50	50	50	50	50	50
$N_{\text{meas}}$		$5 \cdot 10^3$	$5 \cdot 10^3$	$10^3$	$5 \cdot 10^3$	$5 \cdot 10^3$	$10^3$	$5 \cdot 10^3$
$N_{\text{wait}}$		$10^2$	$10^2$	$10^6$	$10^2$	$10^2$	$10^6$	$10^2$

Table 3.3. Parameter values for simulations of the extended adhesion cluster model with binding, rupture and conformational changes.



# Preface to chapter 4

In the following chapter, the response of adhesion clusters to shearing forces is studied. For this purpose a constant force is applied in  $x$ -direction on the upper boundary. Bonds are aligned in  $x$ -direction as well, so that the gap between the two surfaces disappears. The proximity of the surfaces allows molecules to bind at different stretches  $h$ . For a large number of bonds, the set of molecules in state  $b$  and  $b_u$  can be described by a continuous distribution  $n_b(h)$  and  $n_{b_u}(h)$ . This modification has striking consequences for the cluster behaviour under load.

The chapter is a manuscript under peer-review and published as a pre-print, see Ref. [36]<sup>2</sup>. It starts with an abstract, followed by introduction, results and discussion. Afterwards, the methods and supplementary information are given. The following declaration specifies the authors' contributions.

## Declaration of individual contribution

The study of adhesion clusters under shearing forces is a central element of the doctoral thesis project presented here. As such, B.S. and A.B. designed the work. A.B. developed the analytical model, wrote the simulation code and analysed simulation data. All authors contributed to discussions and to writing of the manuscript.

---

<sup>2</sup>After approval of this thesis, the article was published, see Braeutigam, A., Simsek, A.N., Gompper, G. et al. Generic self-stabilization mechanism for biomolecular adhesions under load. Nat Commun 13, 2197 (2022). <https://doi.org/10.1038/s41467-022-29823-2>.



# Chapter 4

## A generic self-stabilization mechanism for biomolecular adhesions under load

### 4.1 Abstract

Mechanical loading generally weakens adhesive structures and eventually leads to their rupture. However, biological systems can adapt to loads by strengthening adhesions, which is essential for maintaining integrity of tissue and whole organisms. Inspired by cellular focal adhesions, we suggest here a generic, molecular mechanism that allows adhesion systems to harness applied loads for self-stabilization under non-equilibrium conditions. The mechanism is based on conformation changes of adhesion molecules that are dynamically exchanged with a reservoir. Tangential loading drives the occupation of some stretched conformation states out of equilibrium, which, for thermodynamic reasons, leads to association of further molecules with the adhesion. Self-stabilization robustly increases adhesion lifetimes in broad parameter ranges. Unlike for catch-bonds, bond dissociation rates do not decrease with force. The self-stabilization principle can be realized in many ways in complex adhesion-state networks; we show how it naturally occurs in cellular adhesions involving the adaptor proteins talin and vinculin.

### 4.2 Introduction

From cells to tissues, muscles and whole organisms, the adaptation of living systems to changing mechanical loads is crucial for maintaining structural integrity [290]. Mechanical adaptation often proceeds through global, slow feedback, e.g., in muscle growth. However, adaptability can also be encoded in molecular properties of load-bearing structures. The

principles underlying molecular load adaptation are often unknown, albeit of fundamental importance.

A paradigmatic example of biological structures that adapt and stabilize under load are focal adhesions, which are crucial for cell physiology [131, 283], cell motility [166], cancer metastasis [44, 286], and development [106, 155]. Focal adhesions consist of transmembrane integrins and adaptor proteins that connect the force-generating actomyosin cytoskeleton with the extracellular matrix. Focal adhesions have been likened to a “molecular clutch” [58, 102, 125, 238, 240, 312] and their biology has been extensively studied. Local application of centripetal forces to adherent cells induces focal adhesion growth [272] with adhesion sizes increasing proportionally to the load [15]. Biological mechanisms for adhesion stabilization are complex and include a mechanosensitive activation of integrins [312], catch-bond behavior of integrins and vinculin-actin binding [161], non-linear mechanical response of unfolded proteins, and downstream signaling, e.g., mediated by the adaptor protein p130Cas [281, 337]. During the past years, however, the pivotal role of the adaptor protein talin for adhesion maturation has been established [54, 143]. Talin directly transmits forces by binding with its globular head domain to integrin, while its rod domain links to F-actin [213]. Under stretch, conformation changes in talin occur, leading to an unfolding of protein domains and to the exposure of cryptic binding sites for vinculin [266, 271, 347]. Vinculin, in turn, further recruits F-actin and thereby strengthens the linkage [8, 11, 223].

In spite of the considerable amount of theoretical work [31, 85, 195, 201, 210, 247, 277, 295, 300] and pioneering work combining modeling and experiment [34, 58, 104], the interplay of stochastic reactions underlying focal-adhesion load adaptation remains vaguely defined. Moreover, other adhesion types such as adherens junctions are also capable of a load adaptation that is based on molecule unfolding and subsequent recruitment of further constituent molecules [69]. To understand nature’s intricate design principles behind load adaptation of bioadhesions, we construct thermodynamically consistent, minimal models combining two aspects, namely an unfolding of adhesion molecules under force [104, 320] and the dynamical exchange of molecules with a reservoir [247, 300]. Our main result is a generic mechanism through which molecular adhesions harness mechanical load for achieving self-stabilization in non-equilibrium states.

### 4.3 Results

**Molecular adhesion model.** We consider a generic adhesion system consisting of  $N$  molecules that form harmonic bonds between two planar surfaces, see Fig. 4.1. The molecule extension, i.e., the difference between actual length and rest length, is denoted by  $h$  and the spring constant by  $\kappa$ . The bottom surface is fixed in space and a constant tangential loading force  $F$  is exerted on the top, leading to a time-dependent tangential shift  $s$ . The model is two-dimensional and forces normal to the plane are not considered. The



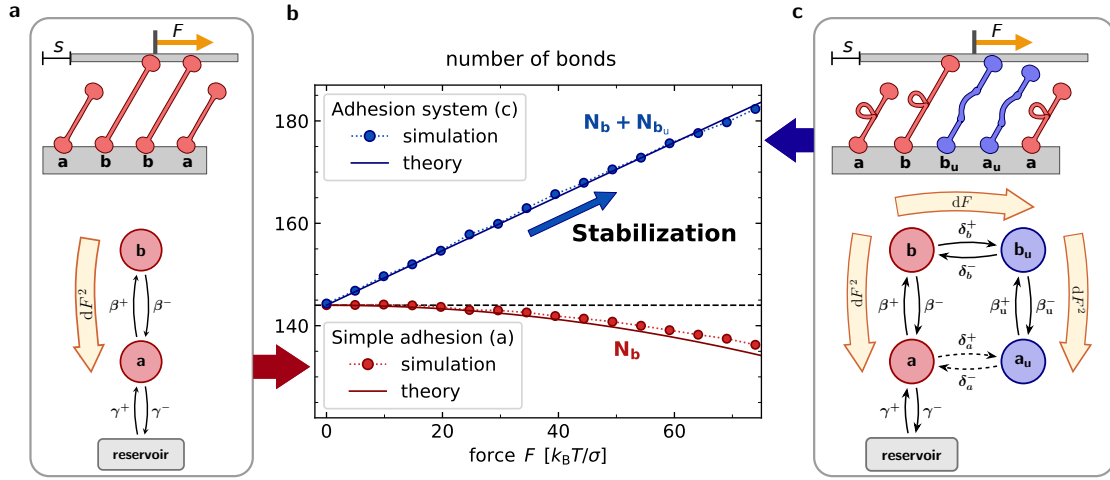


Figure 4.1. Adhesion self-stabilization. a) Illustration of the basic adhesion model which consists of unbound molecules  $a$  and bonds  $b$  that connect two parallel rigid planes. A tangential load stretches all molecules in state  $b$  as it shifts the upper boundary by  $s$ . Molecules can transition between states  $b$  and  $a$  with extension-dependent rupture and binding rates given by  $\beta^-(h)$  and  $\beta^+(h)$ . Molecules can enter or leave the adhesion cluster with rate constants given by  $\gamma^\pm$ . b) Mean number of bonds in steady state as a function of loading force. Symbols show simulation results and lines correspond to approximate analytical results. In the basic model, an increased load on the adhesion reduces the number of bonds (red). In contrast, an increased load produces a growth of the number of bonds in the generalized model (blue). c) Illustration of the generalized adhesion model incorporating molecule unfolding and refolding with rates  $\delta_{a,b}^\pm(h)$  as well as a molecule-exchange with the reservoir. Mechanical load drives the system out of equilibrium, shifting the state occupations. See also SI movies 1,2.

adhesion-molecule number  $N$  can vary and the rate constants  $\gamma^\pm$  determine the molecule exchange with a reservoir. Individual molecules undergo stochastic state transitions and the transition rates are chosen as to fulfill detailed balance when  $F = 0$ , see Sec. 4.5. Thereby, we avoid unphysical energy injection that can produce an apparent motor-like behavior.

In a first, basic model, see Fig. 4.1a, molecules from the reservoir associate reversibly with the adhesion via the state  $a$ , in which they have not yet formed a bond between the upper and lower plane. The state featuring a bond between the two planes is denoted by  $b$ . The bond formation rate is  $\beta^+(h)$ , which is maximal when the extension of the adhesion molecule equals an optimal binding distance  $|h| = \ell_b$ . For bond formation, it is assumed that the extension  $h$  fluctuates thermally with magnitude  $\sigma = \sqrt{k_B T / \kappa}$ , where  $k_B T$  is the thermal energy scale. For bond dissociation, we focus on slip-bond dynamics with rupture rates  $\beta^-(h)$  that increase exponentially with bond extension, see Secs. 4.5 A-B.

In a second, generalized model, see Fig. 4.1c, the molecules can undergo sudden

conformation changes. Unfolded states are denoted with a subscript  $u$ , such that  $a_u$  are the unfolded, unbound states and  $b_u$  the unfolded, bound states. The overall number of bound molecules, irrespective of their conformational state, is written as  $N_B = \sum N_{b\dots}$  and the corresponding overall number of unbound molecules is  $N_A = \sum N_{a\dots}$ . Details of the reaction rates are given in Secs. 4.5 A-C. We assume that mechanical relaxations occur instantaneously and viscous damping is neglected so that the sum of the forces borne by the bonds equals the applied load  $F$  at all times. Stochastic bond dynamics are simulated with an exact algorithm, see Supplementary II.

**Self-stabilization of macromolecular adhesions.** We first consider the basic adhesion model, in which molecules do not change conformation, see Fig. 4.1a and SI movie 1. Simulations reveal that a load  $F$  can lead to a quasi-stationary adhesive state where perpetual rupture and binding events result in a tangential sliding of the surfaces. For these adhesions, the mean number of bonds always decreases monotonically with  $F$ , Fig. 4.1b. Therefore, increasing load on adhesions consisting of simple molecules promotes adhesion failure characterized by rupture of all bonds. Next, we consider the generalized adhesion model consisting of molecules that undergo an unfolding transition under force, see Fig. 4.1c and SI movie 2. For simplicity, we assume here that unfolding only entails an increase in the rest length while the elastic properties remain unchanged. Remarkably, the mean number of bonds now initially grows with increasing load  $F$ , Fig. 4.1b, which depends on state-network features that will be discussed below. The growth of the mean number of bound molecules prevents early adhesion failure. This striking effect, which we call “self-stabilization”, is the central finding of this work.

The simulation results can be corroborated with an analytical mean-field approximation [277]. The stationary distributions of molecules with extension  $h$  in the bound and unbound states are denoted by  $n_b(h)$  and  $n_a(h)$ , respectively. For the basic adhesion model without molecule unfolding, a drift-reaction equation is assumed where the average sliding velocity of the adhesion  $v = \langle \dot{s} \rangle$  stretches the molecule distributions as

$$\partial_t n_b(h) + v \partial_h n_b(h) = \beta^+(h) n_a(h) - \beta^-(h) n_b(h). \quad (4.1)$$

Only solutions with  $\partial_t n_b(h) = 0$  are considered. The total number of molecules in the adhesion is obtained as  $N = N_B + N_A = \int_{-\infty}^{\infty} [n_b(h) + n_a(h)] dh$ , where the extension of the unbound molecules obeys a Gaussian distribution,  $n_a(h) \propto \mathcal{N}(0, \sigma_a^2)$ . Using the binding constant  $k_\beta$  as time unit and the extension variance of bound molecules  $\sigma_b^2$  as length unit, the non-linear equations are solved by expanding the distributions for small absolute values of  $\tilde{v} = v/(k_\beta \sigma_b)$ . For example,  $n_b(h) = n_b^*(h) + \tilde{v} n_{b1}(h) + \frac{1}{2} \tilde{v}^2 n_{b2}(h) + \mathcal{O}(\tilde{v}^3)$ . The asterisk (\*) here and in the following denotes equilibrium quantities calculated with  $F = 0$ . Using the additional assumption that the optimal molecule extension for binding,  $\ell_b$ , is much smaller than the typical length fluctuations,  $\tilde{\ell}_b = \ell_b/\sigma_b \ll 1$ , we find

$$N_B - N_B^* \approx -(2/\pi)^{1/2} \tilde{\ell}_b N_B^* \tilde{v}^2 \propto -F^2. \quad (4.2)$$

Due to symmetry under reversal of the force direction, we have to leading order  $\tilde{v} \propto F$ . For the general case, where  $\ell_b \ll \sigma_b$  does not hold, the first non-vanishing correction to the equilibrium solution for the bonds  $N_B$  can be shown to be of second order  $\propto \tilde{v}^2$  and strictly negative, see Supplementary III. Thus, tension reduces the number of bonds and thereby destabilizes simple adhesions consisting of molecules that do not undergo conformation changes, as expected from intuition.

To support the effect of self-stabilization in the generalized model shown in Fig. 4.1c with analytical theory, we supplement Eq. (4.1) by two additional equations for binding and unfolding transitions (see Supplementary IV). For  $|\tilde{v}| \ll 1$ , the overall number of bound molecules,  $N_B = N_b + N_{b_u}$ , results as

$$N_B - N_B^* \approx N_{B,1}\tilde{v} + N_{B,2}\tilde{v}^2/2 \propto F. \quad (4.3)$$

Note that the leading contribution is linear in  $\tilde{v}$  for self-stabilization. A numerical analysis shows that the coefficient  $N_{B,1}$  is positive for  $\tilde{\ell}_b < 1$ . The second-order correction  $\propto \tilde{v}^2$  can be positive or negative, see Supplementary Fig. S3. Hence, analytical models confirm the existence of a self-stabilization regime where the number of adhesion bonds initially increases with load.

**Mechanism of self-stabilization.** To identify the necessary ingredients for self-stabilization, we compare in Fig. 4.2 a simple adhesion model with fixed molecule number (model I), a model comprising a molecule reservoir and therefore adhesions of variable size (model II), a model with a fixed number of molecules that can unfold under force (model III), and a model combining unfolding molecules with a molecule reservoir (model IV). Some results from models II and IV are also shown in Fig. 4.1. For models I-III, the mean number of bonds  $N_B$  decreases with force, see Fig. 4.2b. For model II with variable system size, even the number of molecules in the adhesion decreases with force, leading to an earlier adhesion failure on average. Thus, neither a variable adhesion size nor molecule unfolding alone result in self-stabilization. In model IV, which combines a variable adhesion size with molecule unfolding, both the total number of molecules  $N$  and the number of bonds  $N_B$  initially grow with increasing load on the adhesion, Figs. 4.2a,b. The increased number of bonds improves load sharing among the molecules. One consequence is a significant reduction of the sliding motion of the adhesion, Fig. 4.2c. The inset in Fig. 4.2b shows that the bound fractions of molecules,  $N_B/N$ , as a function of  $F$  collapse onto a single master curve for all models (I-IV). Hence, self-stabilization results from force-induced growth of the adhesion and not from changes of the rupture properties of individual molecules. This is the key difference to established catch-bond models, where individual molecules exhibit an increase of bond lifetime within limited force regimes.

Figure 4.2d illustrates the underlying mechanism of self-stabilization. The tangential load  $F$  causes a continuous molecular-state turnover with recurring stretch, unfolding, and rupture of molecules along the transitions  $a \rightarrow b \rightarrow b_u \rightarrow a_u$ . Overall, the load

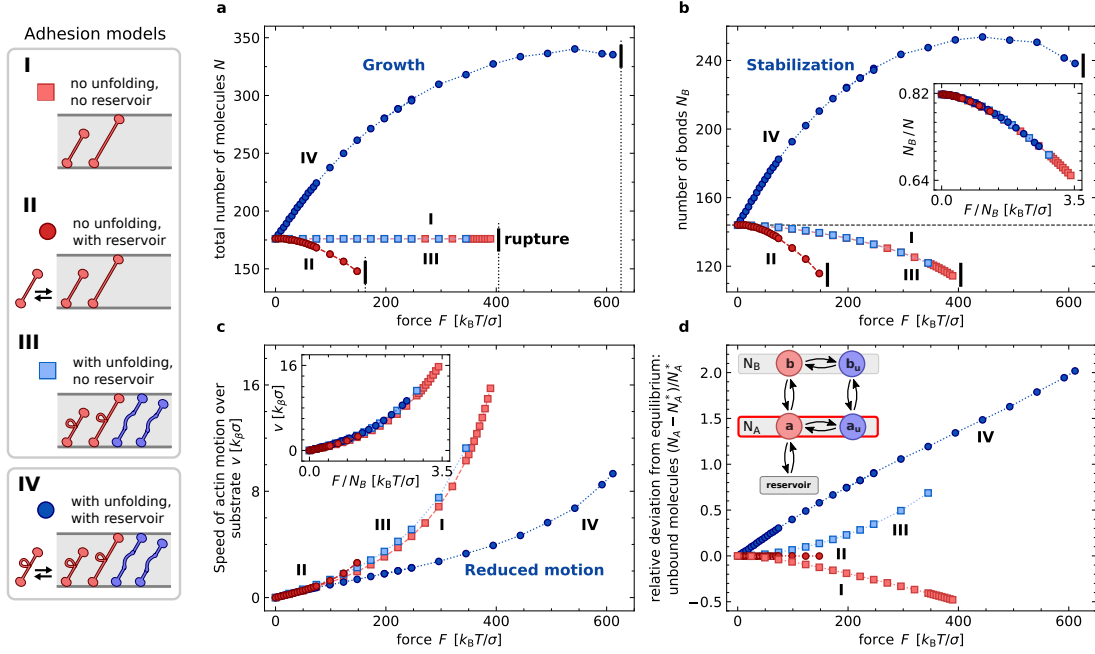


Figure 4.2. Comparison of models I-IV for adhesions with and without molecule unfolding and reservoir exchange. Steady-state quantities are plotted until forces at which first complete adhesion ruptures occur. a) Averaged total number of molecules  $N$ . b) Averaged number of bonds  $N_B$  in steady state. Only model IV shows self-stabilization where the mean number of bonds increases initially with force. c) Continuous rupture-rebinding transitions lead to a relative motion of the two planes bounding the adhesion. Self-stabilization reduces the motion. d) Relative deviation of the average number of unbound molecules  $N_A$  from equilibrium. Note the increased molecule accumulation in the  $a$  states for self-stabilization. See Supplementary I for parameters.

increases the occupation of state  $a_u$ . Meanwhile, the state  $a$ , representing unbound, folded molecules, is in contact with the reservoir and molecules are replenished here, which allows a concurrent increase of overall molecule number. The recruitment of molecules from the reservoir crucially depends on the intermediate state  $a_u$  not being equilibrated, see Suppl. Figs. S6,S8. It is important to note that without the reservoir, self-stabilization cannot occur because it requires growth of the adhesion cluster. Generically, the principle behind self-stabilization is that molecular-state occupation statistics are driven out of equilibrium in a way that results in further influx of molecules from a reservoir.

**Self-stabilization is a robust mechanism.** To be an effective mechanism, self-stabilization must compensate load changes in non-stationary conditions and should not depend on a fine-tuning of parameters. To investigate these aspects, we simulate step-like load changes for different parameters. Following a load jump from  $F_1 = 0$  to  $F_2 = F$ , adhesion clusters either dissociate quickly or reach a non-equilibrium steady state. Self-

stabilization after a load jump depends on the strength of the molecule exchange with the reservoir, which is controlled by the values of  $\gamma^+$  and  $\gamma^-$ , Fig. 4.3a. Exemplary trajectories for the number of bonds in the folded and unfolded states,  $b$  and  $b_u$ , are shown in Fig. 4.3b. The forces at which rupture occurs most likely in self-stabilizing adhesions are higher than those for non-self-stabilizing adhesions and grow with increasing reservoir-exchange rates, see Supplementary Fig. S4. The self-stabilization mechanism can thus also work under dynamic load conditions and a strong reservoir coupling ( $\gamma^\pm > k_\beta$ ) ensures sufficient molecule influx.

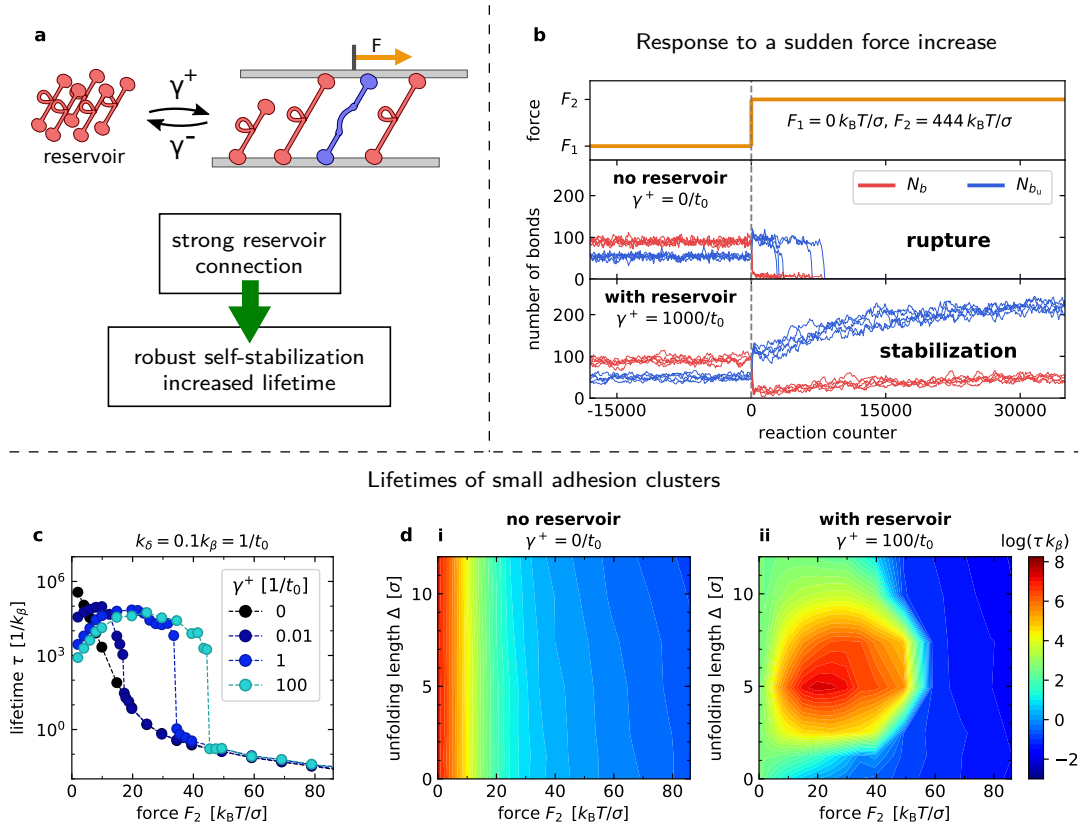


Figure 4.3. Rupture behavior and lifetimes of adhesion clusters. a) The reservoir-exchange rates  $\gamma^\pm$  control the association of and dissociation of molecules with the adhesion. b) Exemplary force-response of adhesion clusters without reservoir connection and with strong reservoir connection. A force jump amplifies molecule unfolding. Without self-stabilization, the cluster does not reach a non-equilibrium steady state but dissociates shortly after the force application. c) Average lifetimes of the adhesion clusters with  $N^* \approx 10$  for different values of  $\gamma^\pm$  with  $\gamma = \gamma^+/\gamma^-$  held constant. A strong reservoir connection results in an adhesion lifetime maximum at finite, non-vanishing external forces. d) Average cluster lifetimes as a function of force and the unfolding length  $\Delta$  for  $k_\delta = 0.1$ ,  $k_\beta = 1/t_0$  and  $\gamma^\pm = 0$  (i) and  $\gamma^\pm = 100/t_0$  (ii). See Supplementary I for other parameter values.

To measure adhesion lifetimes, we simulate systems consisting of few molecules. Load-jump simulations are carried out for a reservoir-exchange rate ratio  $\gamma = 1$ , which leads to adhesions with  $N^* \approx 10$  molecules in equilibrium. Lifetime is measured as the time from the force jump,  $F_1 \rightarrow F_2$ , to the rupture of the last adhesion bond. While lifetimes of adhesions with no reservoir coupling decrease monotonically with force, i.e., show a pure slip-bond behavior, lifetimes of self-stabilizing adhesions exhibit a maximum at non-vanishing forces, Fig. 4.3c. This lifetime maximum becomes more pronounced for increasing  $\gamma^+$  and also depends on the rate-constant ratio  $k_\delta/k_\beta$ , see Supplementary Fig. S5. To further assess the robustness of the adhesion-lifetime increase to parameter choices, we vary the unfolding length  $\Delta$ , which determines the width of the energy barrier between the native and the unfolded molecule state. For adhesions without reservoir coupling,  $\gamma^\pm = 0$ , the unfolding length  $\Delta$  does not have a large impact on the adhesion lifetime, see Fig. 4.3d(i). However, a significant increase in adhesion lifetimes is observed for a broad range of unfolding lengths  $\Delta > 0$  if the reservoir coupling is strong, see Fig. 4.3d(ii). Self-stabilization is less effective for very small or very large values of  $\Delta$ , where native and unfolded state become indistinguishable or the unfolded state becomes inaccessible, respectively.

**Cell-matrix adhesions.** The principle of self-stabilization can be realized in a large variety of molecular-state networks as long as they allow for unbound molecules that are not directly exchanged with the reservoir. As a specific biological realization of the self-stabilization mechanism, we study a model for talin unfolding and interaction with an adaptor protein, such as vinculin, that reduces the dissociation of talin from focal adhesions, see Fig. 4.4a. The talin rod domain contains 11 cryptic vinculin binding sites. Under load, subdomains of the rod successively unfold. Vinculin that is recruited to the adhesion blocks talin refolding and promotes focal adhesion growth [9, 345]. Talin unfolding typically starts at forces around 5 pN [11, 271, 345] with the R3 domain, by which two vinculin binding sites are exposed. In our model, we focus on this first unfolding transition. Six additional vinculin-bound states  $b_u$ , and  $a_u$ , are introduced as both sites in the R3 domain can be occupied independently, see Fig. 4.4b. Rate constants for binding and unbinding of vinculin to unfolded talin are denoted by  $\lambda^\pm$  and are assumed to be the same for all transitions. Other model parameter values are estimated according to experimental results [213, 320, 347], see Supplementary I.

In the vinculin-bound states, talin refolding is blocked. Thus, vinculin binding generates talin states that are not in direct contact with the reservoir and can therefore be driven out of equilibrium. Simulation results for different values of the parameter  $\lambda = \lambda^+/\lambda^-$  are shown in Fig. 4.4c. For  $\lambda = 0$ , all unbound states are equilibrated with the reservoir and no self-stabilization occurs. For  $\lambda > 1$ , the number of bonds increases with force, which not only stabilizes the adhesion but also translates to a reduction of adhesion sliding, see Fig. 4.4d. Given the high affinity with a dissociation constant in the range  $10^{-7} - 10^{-8}$  M of unfolded talin for vinculin, we expect the vinculin binding constant to be larger than

unity [23, 65, 320, 339]. Moreover, we conjecture that the remaining cryptic binding sites in talin that open at higher forces extend the demonstrated self-stabilization effect to larger loads. In summary, the minimal adhesion model can be applied to biological systems like the integrin adhesome, where vinculin binding at unfolded talin domains results in a reaction network containing bond reservoirs that are populated by force application. This leads to self-stabilization. Analytical treatment of a simplified, corresponding mean-field model is given in Supplementary VI.

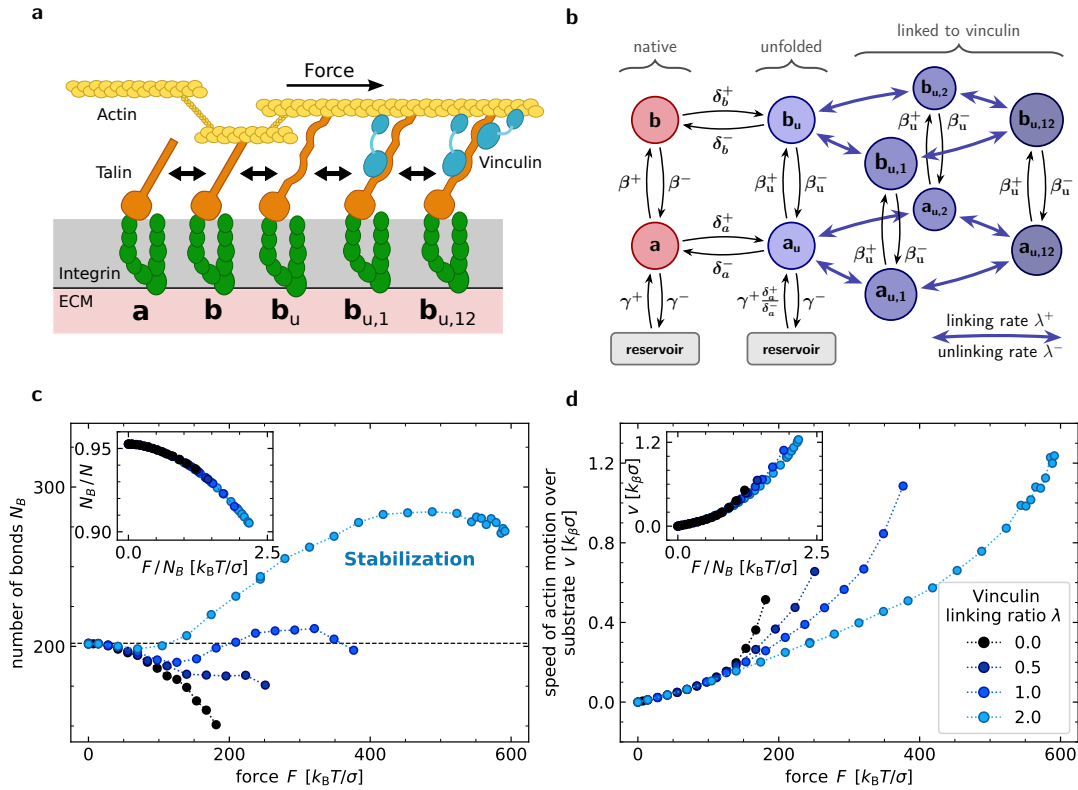


Figure 4.4. Exemplary realization of self-stabilization in focal adhesions. a) Talin binds with its globular head to integrin and with its rod to actin filaments. The first domain to unfold under force is the R3 domain with two vinculin-binding sites. b) State diagram for talin molecules. c-d) Averaged steady-state simulation results for different linking ratios  $\lambda = \lambda^+/\lambda^-$ . See Supplementary I for parametrization. c) Vinculin recruitment produces self-stabilization. d) The relative motion of the top plane modeling actin fibers is reduced through vinculin-based self-stabilization.

## 4.4 Discussion

Our theory reveals a strikingly simple mechanism to produce a counter-intuitive load-response of adhesions, in which tangential mechanical load can result in adhesion en-

hancement instead of adhesion weakening and rupture. This self-stabilization relies on molecular-conformation state-networks that are driven out of equilibrium by a mechanical load. By shifting the state occupations, the load causes a net influx of adhesion molecules from a surrounding reservoir. Notably, this self-stabilization does not require extra chemical energy, but the non-equilibrium conditions produced by the load suffice.

The primary motivation for our theoretical work are experimental results on integrin-based focal adhesions that adapt their size to the applied load in planar cell cultures. Different focal adhesion stabilization mechanisms presumably act in parallel, including actin polymerization, transcription regulation, integrin activation, and conformation changes of the adaptor protein talin. Contrasting this complexity, we find that adhesion self-stabilization emerges naturally in models that merely incorporate the unfolding transition of talin and a mechanism preventing rapid bulk-exchange of unfolded states, e.g., vinculin binding. Since the models respect basic physical constraints such as the detailed-balance conditions, no energy is artificially injected in the system. Additional chemical driving, e.g., through the Rap1-GTP-interacting adaptor molecule [142] or phosphorylation of vinculin or paxillin [305, 359], can provide an additional layer of biological control over the suggested adhesion-stabilization mechanism.

Mechanosensitive conformation changes of adhesion-linked proteins and subsequent recruitment of additional molecules are recurring motifs in many fundamental adhesion structures besides focal adhesions, for instance adherens junctions [189, 345, 351] and hemidesmosomes [361]. Motor proteins also undergo mechanosensitive conformation changes and can form dynamical ensembles. Therefore, we expect that the suggested non-equilibrium mechanism for self-stabilization can help to decipher many physiological and pathophysiological processes controlled by mechano-chemical factors, and may even allow novel designs of bio-inspired, artificial adhesion systems.

## 4.5 Model and Methods

### A Binding

Different states are allowed to have their own spring constants and corresponding quantities are denoted by subscripts, e.g.,  $\kappa_a$  and  $\sigma_a = \sqrt{k_{\text{BT}}/\kappa_a}$ . The probability per unit time for an unbound molecule to bind at an extension  $h$  is given by the function

$$\beta^+(h) \frac{n_a(h)}{N_a} = \frac{k_\beta}{\sqrt{2\pi}\sigma_b} e^{-\frac{(|h|-\ell_b)^2}{2\sigma_b^2} + \frac{\epsilon_b}{k_{\text{BT}}}}, \quad (4.4)$$

where  $k_\beta$  is the intrinsic binding rate constant and  $\epsilon_b$  is a constant. Similar binding rate expressions have been used previously [32]. The total binding rate is obtained by



integration over  $h$  so that

$$\beta^+ = k_\beta \left( 1 + \text{Erf} \left( \tilde{\ell}_b / \sqrt{2} \right) \right) e^{\tilde{\epsilon}_b}, \quad (4.5)$$

where  $\text{Erf}(x)$  denotes the error function and the dimensionless quantities  $\tilde{\ell}_b = \ell_b / \sigma_b$  and  $\tilde{\epsilon}_b = \epsilon_b / (k_B T)$  are used. Binding of unfolded molecules via  $\beta_u^+(h)$  is defined analogously with the extension  $h_u$  of unfolded molecules.

## B Unbinding

The rupture rate  $\beta^-(h)$  is defined by the detailed-balance condition in thermal equilibrium [90],

$$\beta^+(h) / \beta^-(h) = e^{-h^2 / (2\sigma_b^2) + h^2 / (2\sigma_a^2) + \bar{\epsilon}_b}, \quad (4.6)$$

where  $\bar{\epsilon}_b = \tilde{\epsilon}_b + \ln(\sigma_a / \sigma_b)$  is the effective binding affinity. The rupture rate results as

$$\beta^-(h) = k_\beta e^{(2|h|\ell_b - \ell_b^2) / (2\sigma_b^2)}. \quad (4.7)$$

The rupture rate of unfolded bonds,  $\beta_u^-(h)$ , is defined analogously with the extension  $h_u$  of unfolded molecules.

## C Unfolding and refolding

The unfolding and refolding reaction is modeled as the transition between two local energy minima separated by a single barrier. The distance to the barrier is denoted by  $\Delta_1$  for unfolding and by  $\Delta_2$  for refolding. Their sum is equal to the total unfolding length  $\Delta$ . The unfolding rates are thus defined as

$$\delta_{a,b}^+(h) = k_\delta e^{(2\Delta_1 h - \Delta_1^2) / (2\sigma_{a,b}^2) - \tilde{\epsilon}_f}, \quad (4.8)$$

where  $\tilde{\epsilon}_f = \epsilon_f / (k_B T)$  is a constant energy contribution for the conformation change. The reverse rates are given by

$$\delta_{a,b}^-(h) = k_\delta e^{(-2\Delta_2 h - \Delta_2^2) / (2\sigma_{a,b}^2)}. \quad (4.9)$$

The ratio of unfolding to refolding rate of bonds is given by the energy change of a bond going from extension  $h$  to  $h - \Delta$  as

$$\delta_b^+(h) / \delta_b^-(h - \Delta) = e^{(2h\Delta - \Delta^2) / (2\sigma_b^2) - \tilde{\epsilon}_f}. \quad (4.10)$$

For unbound molecules, the total unfolding probability per time and bond is given by  $\delta_a^+ = k_\delta \exp(-\tilde{\epsilon}_f)$ . The total refolding rate is  $\delta_a^- = k_\delta$ .

## Supplementary Information

### I Parameters

The minimal model for self-stabilization presented in the main text is motivated by focal cell-matrix adhesions. Model parameters were chosen accordingly. Table S1 contains all model parameters and their numerical values employed for the simulations if not stated otherwise in the text.

Variable	Description	sim. model	sim. talin	unit
$k_B T$	thermal energy	4.114	4.114	pN nm
$\kappa_a$	spring constant	0.25	0.5	pN nm <sup>-1</sup>
$\kappa_b$	spring constant	0.25	0.5	pN nm <sup>-1</sup>
$\sigma$	thermal fluctuation length	4.057	2.868	nm
$k_\beta$	rate, binding	1	1	1/ $t_0$
$\ell_b$	binding distance	1	1	nm
$\epsilon_b$	energy, binding	1.50	3.00	$k_B T$
$k_\delta$	rate, folding	1	100	1/ $t_0$
$\epsilon_f$	energy, folding	0.50	5.83	$k_B T$
$\Delta$	unfolding length	10	12	nm
$\Delta_1$	transition state distance, unfolding	5	7	nm
$\Delta_2$	transition state distance, refolding	5	5	nm
$\lambda^+$	rate, linking	{0, 1, 2}	{0.0, 0.5, 1.0, 2.0}	1/ $t_0$
$\lambda^-$	rate, unlinking	1	1	1/ $t_0$
$\gamma^+$	rate, addition from reservoir	{20.0, 14.5, 11.4}	{1., 0.996, 0.991, 0.977}	1/ $t_0$
$\gamma^-$	rate, removal to reservoir	1	0.1	1/ $t_0$

Table S1. Model parameters and values employed for simulations.

In focal adhesions, mechanical force is transmitted along single or multiple proteins linked in series. In the latter case, the overall spring constant  $\kappa_b$  will be dominated by the element with the smallest spring constant. The stiffness of cellular adhesion proteins lies in the order of pN nm<sup>-1</sup> [180, 274]. The employed value of 0.25 pN nm<sup>-1</sup> is similar to values

used for previous adhesion models [112, 121, 263, 288]. The values of  $\kappa_{a,b}$  used for the talin simulations were chosen to match the experimentally measured unfolding and refolding behavior, as explained below. The thermal energy scale  $k_B T$  and the spring constant  $\kappa$  determine the mean thermal fluctuation length  $\sigma$ , which is used as a length unit.

Experimentally, turnover of talin is significantly faster than turnover of integrin [147]. The binding and unbinding rates of talin are determined by the intrinsic rate  $k_\beta$ , the optimal binding distance  $\ell_b$ , and the constant energy contribution  $\epsilon_b$ . The intrinsic binding rate constant  $k_\beta$  sets the time unit  $t_0$ . The value of the binding distance  $\ell_b$  agrees with the value employed in Ref. [263] and is smaller than the fluctuation length. The strength of individual bonds is determined by  $F_0 = k_B T / \ell_b \approx 4$  pN, as the rupture rate depends on force  $F$  as  $\propto \exp(F/F_0)$ . The constant  $\epsilon_b$  can be understood as an effective affinity parameter. Its value is chosen to be rather low to fix the adhesion cluster size at equilibrium, which is proportional to  $\exp(\epsilon_b/k_B T)$ , compare Refs. [32, 33].

The unfolding and refolding rates depend on  $k_\delta$ ,  $\epsilon_f$ ,  $\Delta$  and  $\Delta_{1,2}$  with  $\Delta = \Delta_1 + \Delta_2$ . The energy contribution  $\epsilon_f$  determines the ratio between folded and unfolded molecules in equilibrium. It shifts the energy barrier between both states that are separated by the distances  $\Delta_1$  and  $\Delta_2$ . For the simulations of talin molecules, the unfolding and refolding rate constants are chosen in accordance with the experimental results in Ref. [347]. For a time unit  $t_0 = 1$  s, unfolding occurs at a rate of  $0.015 \text{ s}^{-1}$  at zero force. The folding and unfolding rates intersect at a force of 5 pN, the value at which talin R3 domain unfolding and refolding is observed [320, 345, 347].

The cross-linking by additional adaptor proteins is described by making use of two rate constants  $\lambda^\pm$ . In the general simulation model, the value of these constants lies within the same order of magnitude as the intrinsic rate constants  $k_\delta$  and  $k_\beta$ . For integrin-based adhesions, this reaction is realized by the association of vinculin to unfolded talin domains. The molecular interactions of talin and vinculin are highly complex. At low forces, vinculin binding at unfolded talin domains strengthens the adhesion [76, 156, 345]. The recruitment of vinculin is proposed to act as a negative feedback loop that stabilizes the force acting on the complex [320]. Additionally, the vinculin-talin interaction also depends on the direction of forces [179]. In our model, we assume linking-rate constants with a value comparable to the intrinsic binding rate  $k_\beta$ . In recent experiments addressing the association of vinculin with the talin R3 domain, vinculin binding has been observed with a rate on the order of  $10^{-1} \text{ s}^{-1}$  when sufficient tension was applied to talin to induce unfolding [320].

The exchange of molecules with a reservoir is governed by the two rate constants  $\gamma^+$  and  $\gamma^-$ . Their ratio  $\gamma$  is proportional to the number of molecules in the adhesion-cluster at equilibrium, i.e., when  $F = 0$ . For comparability of the results of different models, the rate for adding molecules was increased from  $\gamma^+$  to  $\tilde{\gamma}^+ = \gamma^+(1 + \exp(-\epsilon_f/k_B T))$  for the model without unfolding, and similarly when linking is included. This choice ensures the same number of molecules and bonds at  $F = 0$ . As described in the main text, the molecule-

exchange with the reservoir plays a fundamental role for the self-stabilization mechanism. A strong connection to the reservoir allows the adhesion to grow with increasing force.

The construction of molecular state models for talin in integrin-based adhesions poses a challenge due to the large number of states and due to the fact that addition and removal of an adhesion molecule requires several steps *in vivo* [176, 241]. Furthermore, several pathways have been suggested for the recruitment of talin to integrin-based adhesions [178]. Values for the halftime of fluorescence recovery after photobleaching (FRAP) experiments for talin in focal adhesions are on the order of seconds or tens of seconds, depending on the cell type and substrate stiffness [199, 305]. The exchange of single molecules can therefore be expected to occur on timescales of seconds or even faster. Hence, the values for  $\gamma^\pm$  are chosen such, that they ensure a frequent exchange of molecules with the reservoir, but still allow to observe the processes within the cluster.

## II Stochastic simulations

Molecule-state trajectories are simulated with the Gillespie algorithm [137, 138]. Its basis is provided by the stochastic formulation of chemical kinetics where the probability that a reaction  $i$  will happen in the infinitesimal time interval  $\delta\tau$  is determined by the product of the available reactants or reactant pairs  $N_i$  and a parameter  $\mu_i$ . Assuming  $j \in [1, \dots, m]$  available reactions, the function  $P(i, \tau)$  describes the probability that the reaction  $i$  is the first one to occur after a waiting time  $\tau$  in the next infinitesimal time interval. For  $0 \leq \tau < \infty$  we have

$$P(i, \tau) = N_i \mu_i \exp \left( - \sum_{j=1}^m N_j \mu_j \tau \right). \quad (4.11)$$

Starting from an initial configuration, the time for the next reaction and the type of reaction are drawn according to  $P(i, \tau)$  repeatedly. Force balance is restored instantaneously after each event.

In response to the tangential external force, adhesion clusters either reach a quasi-steady-state or dissociate. The time- and ensemble averages are calculated for trajectories that do not lead to complete dissociation during the simulation time. If not stated otherwise, 50 trajectories are tracked for  $> 10^6$  single-bond transitions for the measurements of steady-state quantities, during which the tangential force is held constant. To measure adhesion lifetime, more than 200 cluster trajectories are simulated until their dissociation.

### III Adhesion model without unfolding

The following mean-field equations are used to approximate the dynamics of the stretch-dependent state-occupation numbers in the basic adhesion model without molecule unfolding

$$\frac{\partial}{\partial t} N_a = -\beta^+ N_a + \int_{-\infty}^{\infty} \beta^-(h) n_b(h) dh - \gamma^- N_a + \gamma^+, \quad (4.12)$$

$$\frac{\partial}{\partial t} n_b(h) = -v \frac{\partial}{\partial h} n_b(h) - \beta^-(h) n_b(h) + \beta^+(h) n_a(h), \quad (4.13)$$

where we omitted explicit  $t$ -dependence in our notation. Since the unbound molecules in state  $a$  are assumed to relax quickly mechanically, their extensions obey a Gaussian distribution. Equation (4.12) describes the mean total number of unbound molecules. The mean number of bonds  $n_b(h)$  evolves according to Eq. (4.13). The drift term in (4.13) accounts for the average relative velocity  $v = \langle \dot{s} \rangle$  between the adhesion planes that is due to the tangential force  $F$ . An expansion of  $n_b(h)$  as

$$n_b(h) = \sum_{j=0}^{\infty} \frac{1}{j!} n_{b_j}(h) \tilde{v}^j, \quad (4.14)$$

with  $\tilde{v} = v/(k_\beta \sigma_b)$  solves the steady state conditions  $\frac{\partial}{\partial t} N_a = 0$  and  $\frac{\partial}{\partial t} n_b(h) = 0$  if

$$n_{b_0}(h) = n_b^*(h) = \frac{\gamma^+ \beta^+(h)}{\gamma^- \beta^-(h)} p_a(h), \quad n_{b_j}(h) = -j \frac{n'_{b_{j-1}}(h)}{\beta^-(h)} \quad \text{for } j > 0, \quad (4.15)$$

where  $p_a(h)$  is a Gaussian function with zero mean and variance  $\sigma_a^2$  and the prime denotes the derivative with respect to the extension  $h$ . The first correction  $n_{b_1}(h)$  is an odd function, so that its integral vanishes. The first non-vanishing correction is given by the term for  $j = 2$ . Up to second order, the integrated steady state solution for the mean number of bonds  $N_B = N_b$  is given by

$$N_B = \int_{-\infty}^{\infty} n_b(h) dh = N_B^* \left( 1 - \sqrt{\frac{2}{\pi}} \tilde{\ell}_b e^{\tilde{\ell}_b^2} \left( 1 - \sqrt{2\pi} \tilde{\ell}_b e^{2\tilde{\ell}_b^2} \text{Erfc}(\sqrt{2}\tilde{\ell}_b) \right) \tilde{v}^2 \right) \quad (4.16)$$

$$\text{with } N_B^* = \frac{\gamma^+}{\gamma^-} e^{\tilde{\epsilon}_b},$$

where  $\tilde{v} = v/(\sigma_b k_\beta)$  and  $\tilde{\ell}_b = \ell_b/\sigma_b$  have been used and  $\text{Erfc}(x)$  denotes the complementary error function. This first correction  $\propto v^2$  is negative since the complementary error function for an argument  $x > 0$  is bounded by

$$\text{Erfc}(\sqrt{2}\tilde{\ell}_b) \leq \frac{2}{\sqrt{\pi}} \frac{e^{-2\tilde{\ell}_b^2}}{\sqrt{2}\tilde{\ell}_b + \sqrt{2\tilde{\ell}_b^2 + 4/\pi}} < \frac{e^{-2\tilde{\ell}_b^2}}{\sqrt{2\pi}\tilde{\ell}_b}. \quad (4.17)$$

The force-balance equation  $F = \int_{-\infty}^{\infty} n_b(h) \kappa_b h dh$  connects the external force with the resulting mean velocity  $v$ . The lowest-order contribution ( $j = 0$ ) to the force balance

vanishes because  $n_{b_0}(h)$  is symmetric. For the first non-vanishing correction, we find

$$\tilde{F} = \frac{F\sigma_b}{k_B T} = N_B^* e^{\tilde{\ell}_b^2/2} \left( -\frac{2\tilde{\ell}_b}{\sqrt{2\pi}} + \left(1 + \tilde{\ell}_b^2\right) e^{\tilde{\ell}_b^2/2} \text{Erfc}\left(\frac{\tilde{\ell}_b}{\sqrt{2}}\right) \right) \tilde{v}. \quad (4.18)$$

The bracketed term on the right hand side of Eq. (4.18) is strictly positive. The approximations for  $\tilde{\ell}_b \ll 1$  are given in the main text.

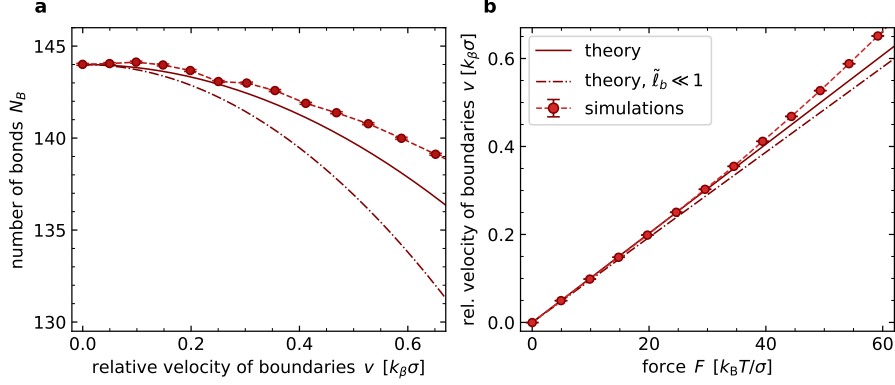


Figure S2. The average steady-state behavior of basic adhesions without unfolding. Symbols: Simulation results. Solid lines: analytical approximations using an expansion in  $\tilde{v}$  up to second order. Dash-dotted lines without symbols: Approximation of the expansion for  $\tilde{\ell}_b \ll 1$ . a) The analytical approximation slightly underestimates the mean number of bonds in steady state. b) The force-balance condition connects the external force  $F$  with the drift  $v$ .

## IV Adhesion model with unfolding

The numbers of unbound molecules obey the following approximate rate equations

$$\frac{\partial}{\partial t} N_a = -\beta^+ N_a + \int_{-\infty}^{\infty} \beta^-(h) n_b(h) dh - \delta_a^+ N_a + \delta_a^- N_{a_u} - \gamma^- N_a + \gamma^+, \quad (4.19)$$

$$\frac{\partial}{\partial t} N_{a_u} = -\beta_u^+ N_{a_u} + \int_{-\infty}^{\infty} \beta_u^-(h) n_{b_u}(h) dh - \delta_a^- N_{a_u} + \delta_a^+ N_a. \quad (4.20)$$

The distributions of molecule numbers with extension  $h$  experience a drift due to the velocity  $v$  of the upper boundary and obey

$$\begin{aligned} \frac{\partial}{\partial t} n_b(h) = & -v \frac{\partial}{\partial h} n_b(h) - \beta^-(h) n_b(h) + \beta^+(h) n_a(h) - \delta_b^+(h) n_b(h) \\ & + \delta_b^-(h - \Delta) n_{b_u}(h - \Delta), \end{aligned} \quad (4.21)$$

$$\begin{aligned} \frac{\partial}{\partial t} n_{b_u}(h) = & -v \frac{\partial}{\partial h} n_{b_u}(h) - \beta_u^-(h) n_{b_u}(h) + \beta_u^+(h) n_{a_u}(h) - \delta_b^-(h) n_{b_u}(h) \\ & + \delta_b^+(h + \Delta) n_b(h + \Delta). \end{aligned} \quad (4.22)$$

The steady-state solution for  $v = 0$ , i.e., the equilibrium solution, is given by

$$\begin{aligned} N_a^* &= \frac{\gamma^+}{\gamma^-}, & N_{a_u}^* &= \frac{\gamma^+ \delta_a^+}{\gamma^- \delta_a^-}, \\ n_b^*(h) &= \frac{\gamma^+ \beta^+(h)}{\gamma^- \beta^-(h)} p_a(h), & n_{b_u}^*(h) &= \frac{\gamma^+ \beta_u^+(h)}{\gamma^- \beta_u^-(h)} p_{a_u}(h). \end{aligned} \quad (4.23)$$

Integration yields the total number of bonds in equilibrium as

$$N_B^* = \int_{-\infty}^{\infty} [n_b^*(h) + n_{b_u}^*(h)] dh = \frac{\gamma^+}{\gamma^-} e^{\tilde{\epsilon}_b} (1 + e^{-\tilde{\epsilon}_f}). \quad (4.24)$$

To investigate the case  $F > 0$ , the state distributions are expanded in powers of the average velocity  $\tilde{v}$  as above, see Supplementary III. The connection of the state  $a$  with the reservoir enforces  $N_{a_j} = 0$  for  $j > 0$ . The solutions of the above equations cannot be found with an exact iterative formula. Instead, a numerical approach is used to find the corrections  $N_{a_{u,j}}$ , which can then be inserted back into the rate equations to solve for  $n_{b_j}(h)$  and  $n_{b_{u,j}}(h)$ . Up to first order in  $\tilde{v}$ , the mean number of bonds remains unaffected or increases with the velocity, as demonstrated for different unfolding steps  $\Delta$  and optimal binding lengths  $\tilde{l}_b$  in Fig. S3a. The first-order correction vanishes for  $\Delta \rightarrow 0$  and  $\Delta \rightarrow \infty$ . The second-order correction can be both positive or negative, Fig. S3b. Strong self-stabilization is found for  $\tilde{l}_b \ll 1$ .

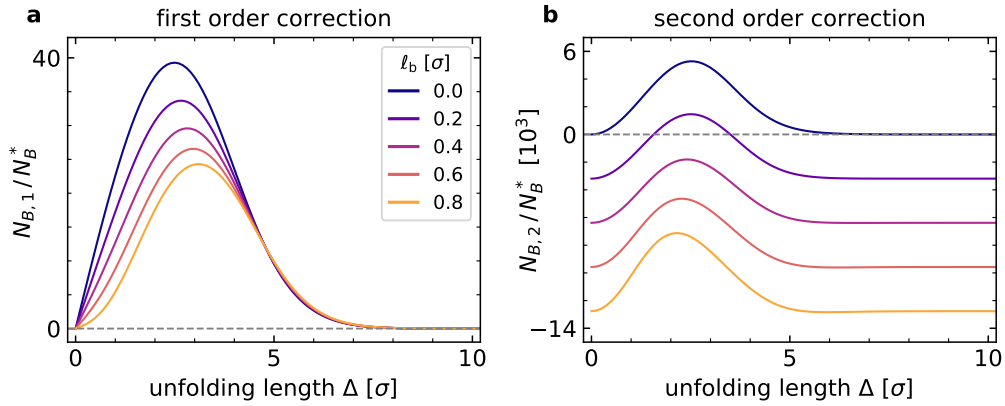


Figure S3. Numerical results for the coefficients of the first- and second-order corrections to the equilibrium solution for the number of bonds. The adhesion cluster connected to a molecule reservoir and results for different values for the molecule unfolding length  $\Delta$  and the binding parameter  $l_b$  are shown. The first-order correction  $\propto v$  is positive for  $l_b < \sigma_b$  and vanishes in the limits  $\Delta \rightarrow 0$  and  $\Delta \gg \sigma_b$ . The second-order correction  $\propto v^2$  can be both positive and negative.

## Rupture behavior and adhesion cluster lifetimes

Application of a sudden force jump from  $F_1 = 0$  to  $F_2 > 0$  either leads to a quick dissociation of the adhesion or the adhesion system relaxes to a non-equilibrium steady state. For large adhesion clusters ( $N > 20$ ), the lifetimes of those adhesions that reach the non-equilibrium steady-state usually exceeds the finite simulation time. The fraction of those adhesion clusters that rupture almost immediately,  $\Phi_{\text{rupt}}$ , is shown in Fig. S4a as a function of  $F_2$  for different reservoir rates  $\gamma^+$ . Without reservoir connection, when no self-stabilization occurs, the fraction of ruptured adhesion clusters sharply increases at a threshold force. Self-stabilization broadens the curves and increases the typical forces at which rupture occurs. The numerical results are well-fitted by a shifted and scaled error function.

The fraction of ruptured adhesion clusters after sufficiently long simulation times represents the cumulative probability distribution for cluster dissociation after a sudden force application. Therefore, the force value  $F_2$  at which  $\Phi_{\text{rupt}}(F_2) = 0.5$  corresponds to the highest rupture probability, see Fig. S4b. The most probable rupture force increases

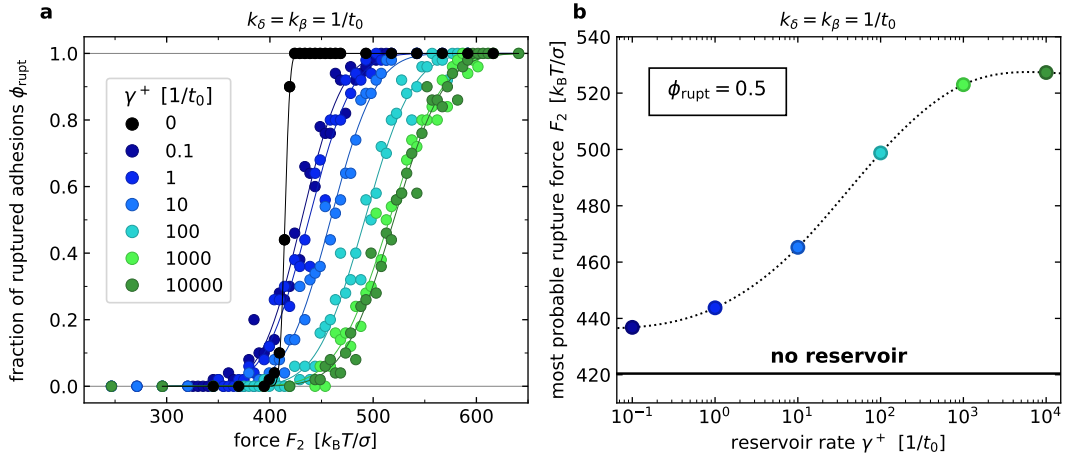


Figure S4. Fraction of ruptured adhesions after a sudden load-jump from  $F_1 = 0$  to  $F_2$  for different reservoir-exchange rates  $\gamma^\pm$ . The ratio  $\gamma = \gamma^+/\gamma^- = 20$  is fixed. Systems were simulated for  $5 \cdot 10^5$  reaction steps after the force jump. a) The fraction of ruptured adhesion clusters as a function of the magnitude of the force step. The strength of the reservoir connection, determined by  $\gamma^\pm$ , is varied while the ratio  $\gamma = \gamma^+/\gamma^-$  is held constant. For comparison, the fraction of ruptured adhesion clusters in simulations without reservoir connection is shown with black bullets. A reservoir connection implies here self-stabilization. Due to the large system size ( $N^* \approx 176$ ), most systems that did not rupture initially after the load jump remained stable for the rest of the simulation time. Lines show fits to error functions. b) Force  $F_2$  at which rupture is most likely for different reservoir rate values  $\gamma^+$ . Values are extracted from the fit curves in a). The black horizontal line shows the most probable rupture force for  $\gamma^+ = 0$ .



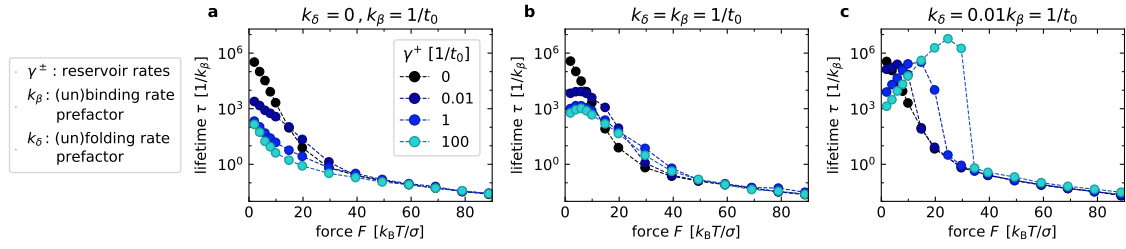


Figure S5. Lifetimes of small adhesions ( $N^* \approx 10$ ) for different values of the rate prefactors  $k_\beta$  and  $k_\delta$  and the reservoir-exchange rates  $\gamma^\pm$ . The ratio  $\gamma = \gamma^+/\gamma^- = 1$  is fixed. a)  $k_\delta = 0$ , no unfolding b)  $k_\delta = k_\beta$  c)  $k_\delta = 0.01k_\beta$ . Only the lifetime results for the adhesion model IV, which exhibits self-stabilization, display a maximum at finite, non-vanishing forces. The lifetime of the adhesions is substantially increased for intermediate forces if  $\gamma^+$  and  $k_\beta$  are larger than  $k_\delta$ , such that molecules coming from the reservoir establish new bonds frequently.

with increasing reservoir rate  $\gamma^+$ .

Fig. S5 shows adhesion lifetimes, defined as the time until first complete dissociation of all bonds in an adhesion after application of a force jump. Small adhesion clusters ( $N^* \approx 10$ ) with different values for the reservoir rates  $\gamma^\pm$  are studied. The small molecule-numbers allow a direct measurement of the lifetimes by simulating the clusters until the last bond dissociates. For an adhesion system without molecule unfolding, realized by setting  $k_\delta = 0$ , the lifetime decreases monotonically with increasing force for any value of  $\gamma^\pm$ , see Fig. S5a. The equilibrium lifetime is largest for adhesion clusters without reservoir connection, realized by  $\gamma^\pm = 0$ . Figs S5b,c display lifetimes of adhesion models with unfolding molecules. The lifetime of adhesions without molecule exchange with a reservoir decrease monotonically with increasing force (black bullets). However, when the system is coupled to a molecule reservoir, so that the self-stabilization mechanism takes effect, the adhesion lifetime curves have a maximum at non-zero, finite forces. A substantial lifetime increase through self-stabilization is realized when both the reservoir rates and the intrinsic binding rate  $k_\beta$  are large compared to the unfolding rate  $k_\delta$ .

### Special case: no unfolding in the unbound state *a*

To investigate how cyclic fluxes along the state network  $a - b - b_u - a_u - a$  affect self-stabilization, we set  $\delta_a^\pm = 0$ . Thereby, the cycle in the single-molecule transition-diagram is broken. Physically, this modification means that unfolding is only allowed when the molecule is bound between both planes. It should be emphasized that this model variant still allows the emergence of cyclic fluxes in the high-dimensional continuous state space spanned by the extensions of the molecules.

In Fig. S6, results from the new model variant are compared with results from model IV

defined in the main text. For  $\delta_a^\pm = 0$ , the increase of the adhesion molecule number with force is significantly stronger than for the model IV with cyclic flux. Thus, self-stabilization is enhanced in the absence of cyclic flux, see Fig. S6a,b. The relative velocity of the two planes bounding the adhesion is reduced accordingly, see Fig. S6c. The enhanced self-stabilization can be attributed to a stronger accumulation of molecules in the state  $a_u$ , from which molecules can only escape via state  $b_u$  in this model variant. Note that the force value at which first rupture events are observed does not increase greatly, see black, vertical lines in Fig. S6a. A comparison with the inset in Fig. S6b shows, that the force per bond,  $F/N_B$ , is strongly reduced because of the increased number of bonds  $N_B$ .

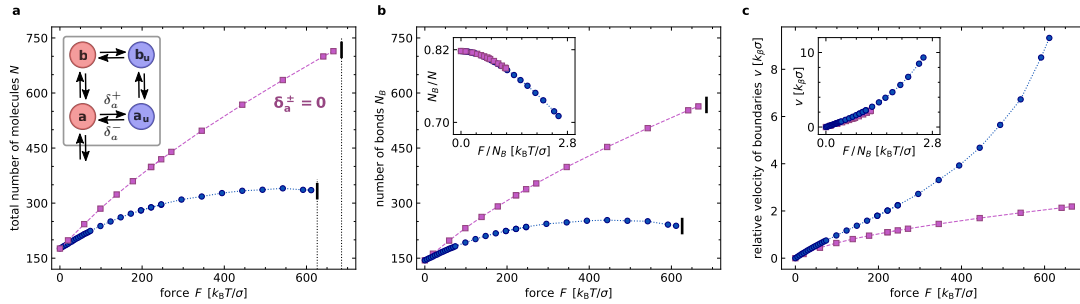


Figure S6. Steady state results of adhesion model IV (compare Fig. 4.2) and adhesion clusters with  $\delta_a^\pm = 0$ . When unbound unfolding and refolding is inhibited, the self-stabilization effect is more pronounced.

## V Adhesion model with unfolding and catch bonds

In the models considered so far, a slip-bond behavior is assumed, i.e., the increase of the single-bond rupture rate with the applied extension  $h$  is monotonic, see sec. IV B. Thus, so far, single-bond lifetimes decreased when tension increased. Bonds that become longer-lived when tension increases are called catch bonds [339]. A number of molecular bonds in cellular adhesions have been described as catch-slip bonds [68, 181, 218, 221]. These interactions behave like a catch bond up to some force threshold while the slip-bond behavior takes effect at higher forces. To further test the generality of the self-stabilization mechanism, simulations of different adhesion models are performed where the bonds behave like pure catch bonds. The binding and unbinding rate of folded bonds are changed to

$$\beta^+(h) \frac{n_a(h)}{N_a} = \frac{k_\beta}{\sqrt{2\pi}\sigma_b} \exp\left(-\frac{(|h| + \ell_b)^2}{2\sigma_b^2} + \frac{\epsilon_b}{k_B T}\right), \quad (4.25)$$

$$\beta^-(h) = k_\beta \exp\left(\frac{-2|h|\ell_b - \ell_b^2}{2\sigma_b^2}\right).$$

The rates for unfolded bonds are defined analogously with the extension  $h_u$ . Note that the difference to the slip bond rates given in sec. IV A-B lies only in one sign in each

exponential function. Thus, detailed balance still holds in equilibrium at  $F = 0$ . The steady-state simulation results are shown in Fig. S7. Again, only for model IV with a combination of unfolding and association of new molecules from the reservoir, a pronounced increase in the number of bonds is observed for small forces, see Fig. S7b. Figure S7d shows that the self-stabilization is caused by an accumulation of unbound molecules. Beyond this regime, at high forces, the pure catch-bond dynamics leads to a separation of the bond distribution into two subpopulations. Firstly, one has few, rather static molecules that carry most of the tension. Therefore, these molecules have a large extension and long lifetime. Secondly, a large number molecules form transient bonds with low, symmetrically distributed extensions. As a result, the cluster stops moving, as can be seen in the velocity-force curve in Fig. S7c for high forces.

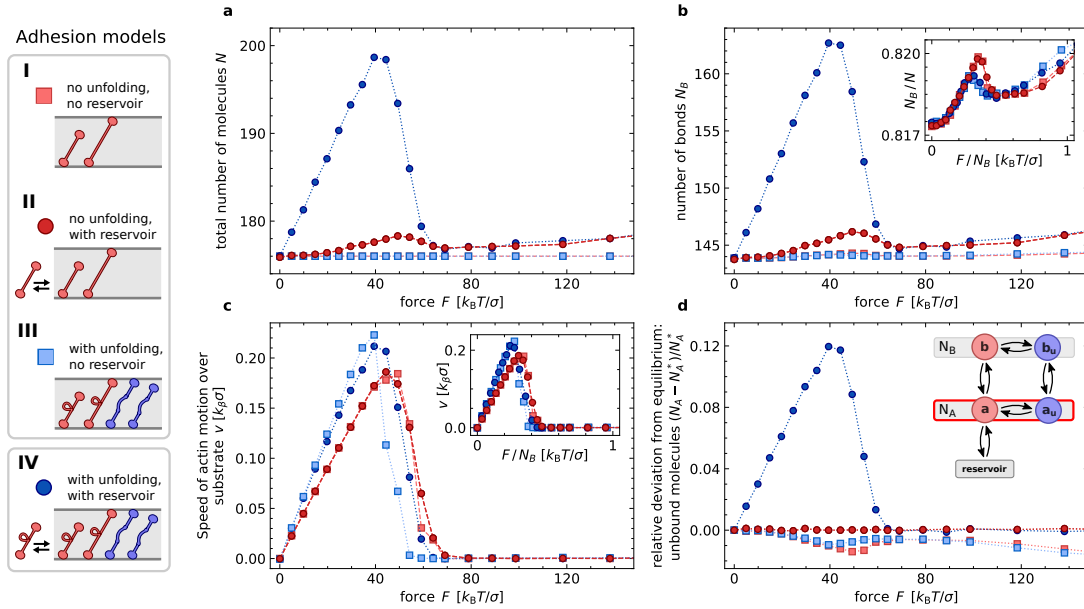


Figure S7. Simulation results for adhesion models in which single molecules behave like catch bonds. a) Averaged total number of molecules  $N$  in steady state. b) Averaged number of bonds  $N_B$  in steady state. Adhesion clusters with a reservoir connection (dark red and dark blue) show a regime, where the mean number of bonds increases with force. The self-stabilizing mechanism is particularly pronounced for the model IV (dark blue) in which molecules can unfold and are in exchange with a reservoir. c) The continuous binding and rupture leads to an on average constant relative shift of the boundaries per time. Adhesion models with bond unfolding show an increased velocity. d) The relative deviation of the average number of unbound molecules  $N_A$  from equilibrium shows that the self-stabilization mechanism is connected to an increased accumulation of adhesion molecules in unbound states (dark blue). The parameter values are given in I.

## VI Adhesion model with unfolding and cross-linking

We consider an extended adhesion model that also contains the effect of adaptor protein binding. Figure S8a shows the corresponding single-molecule state-transition diagram with linking rates  $\lambda^\pm$ . Linking the load-bearing molecules with adaptor proteins to the adhesion prevents a dissociation of the molecules from the adhesion. Thereby, the linking generates states that are not directly connected to the molecule reservoir.

For an approximate analytical description of the system, the set of equations from IV is extended to account for the linked states. The unbound states obey

$$\frac{\partial}{\partial t} N_a = -\beta^+ N_a + \int_{-\infty}^{\infty} \beta^-(h) n_b(h) dh - \delta_a^+ N_a + \delta_a^- N_{a_u} - \gamma^- N_a + \gamma^+, \quad (4.26)$$

$$\begin{aligned} \frac{\partial}{\partial t} N_{a_u} = & -\beta_u^+ N_{a_u} + \int_{-\infty}^{\infty} \beta_u^-(h) n_{b_u}(h) dh - \delta_a^- N_{a_u} + \delta_a^+ N_a - \gamma^- N_{a_u} + \gamma^+ \frac{\delta_a^+}{\delta_a^-} \\ & - \lambda^+ N_{a_u} + \lambda^- N_{a_{u,1}}, \end{aligned} \quad (4.27)$$

$$\frac{\partial}{\partial t} N_{a_{u,1}} = -\beta_u^+ N_{a_{u,1}} + \int_{-\infty}^{\infty} \beta_u^-(h) n_{b_{u,1}}(h) dh - \lambda^- N_{a_{u,1}} + \lambda^+ N_{a_u}. \quad (4.28)$$

The equations determining the evolution of the extension-dependent state distributions read

$$\begin{aligned} \frac{\partial}{\partial t} n_b(h) = & -v \frac{\partial}{\partial h} n_b(h) - \beta^-(h) n_b(h) + \beta^+(h) n_a(h) - \delta_b^+(h) n_b(h) \\ & + \delta_b^-(h - \Delta) n_{b_u}(h - \Delta), \end{aligned} \quad (4.29)$$

$$\begin{aligned} \frac{\partial}{\partial t} n_{b_u}(h) = & -v \frac{\partial}{\partial h} n_{b_u}(h) - \beta_u^-(h) n_{b_u}(h) + \beta_u^+(h) n_{a_u}(h) - \delta_b^-(h) n_{b_u}(h) \\ & + \delta_b^+(h + \Delta) n_b(h + \Delta) - \lambda^+ n_{b_u}(h) + \lambda^- n_{b_{u,1}}(h), \end{aligned} \quad (4.30)$$

$$\begin{aligned} \frac{\partial}{\partial t} n_{b_{u,1}}(h) = & -v \frac{\partial}{\partial h} n_{b_{u,1}}(h) - \beta_u^-(h) n_{b_{u,1}}(h) + \beta_u^+(h) n_{a_{u,1}}(h) - \lambda^- n_{b_{u,1}}(h) \\ & + \lambda^+ n_{b_u}(h). \end{aligned} \quad (4.31)$$

The steady-state results for the number of molecules in state  $a$ ,  $b$ ,  $b_u$ ,  $a_u$  are given by Eq. (4.23). The additional linked states fulfill

$$n_{b_{u,1}}^*(h) = \frac{\lambda^+}{\lambda^-} n_{b_u}^*(h), \quad N_{a_{u,1}}^* = \frac{\lambda^+}{\lambda^-} N_{a_u}^*. \quad (4.32)$$

As before, an expansion of the distributions for small speeds  $|\tilde{v}|$  yields the first corrections to the equilibrium distribution. Figure S8 shows a comparison between steady-state results obtained in simulations and in the analytical approximation. Figure S9 shows simulation results for a range of parameters.

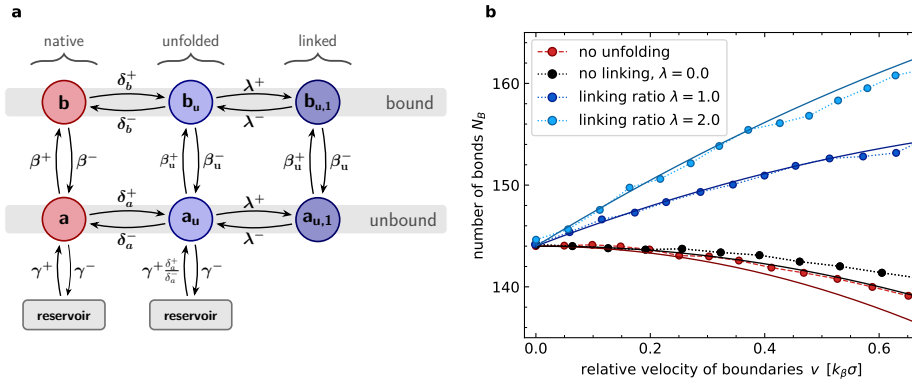


Figure S8. Model for adhesion clusters with self-stabilization realized by linking of auxiliary molecules. a) Single-molecule state transition diagram. Unfolded molecules can establish an additional link to the adhesion that prevents one-step dissociation of the molecule from the adhesion. b) Comparison between simulation results (symbols connected by dashed lines) and the expansion of bond states up to second order in the speed  $|\bar{v}|$  (solid lines) for different linking ratios  $\lambda$ . Results for an adhesion model without the unfolding transition are shown for comparison. Parameter values are given in I.

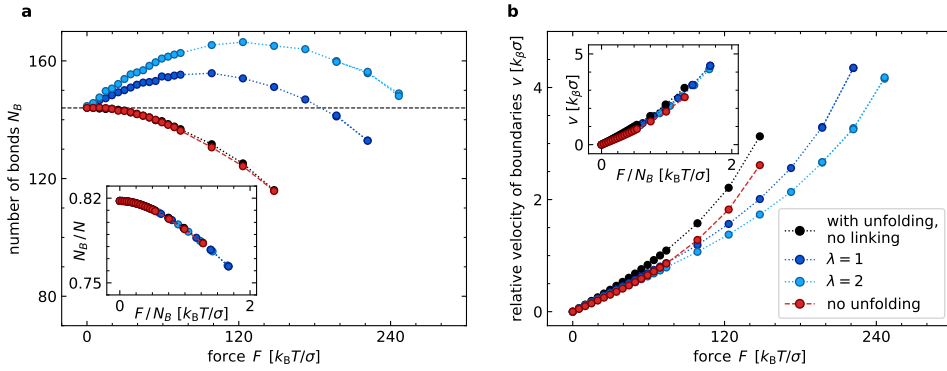


Figure S9. Averaged steady-state simulation results for adhesion models with the unfolding-linking mechanism and two reservoir connections. Black and blue symbols show results for different linking ratios  $\lambda = \lambda^+/\lambda^-$ . Red: Adhesions without unfolding for comparison. a) Only adhesions with a positive linking ratio show a self-stabilization regime where the number of bonds increases with force. b) Relative motion of the upper plane and the adhesion. Inset: The fraction of bonds and the velocity as a function of force per bond show the same behavior for all systems. The parameter values are given in I.



# Chapter 5

## Extension to two dimensions

In the two preceding Chapters 3 and 4, adhesion clusters under pure pulling and pure shearing forces are introduced and investigated. Since force and bonds are parallel at all times in these special cases, both systems are effectively one-dimensional. In this chapter, the restriction of parallel bond alignment is lifted and clusters under arbitrary force directions are considered. Thus, bonds experience a mixture of pulling and shearing forces in a two-dimensional geometry. This is a big step towards a more realistic picture of adhesion clusters.

The chapter starts with the required modifications to the model. Especially the binding rate has to be adjusted carefully. Furthermore, the simulation algorithm is extended by a numerical procedure to find the cluster configuration that fulfils the force balance condition. In the following sections, the results are shown for clusters with conformational changes and a variable number of molecules. For the limiting case of a force that acts orthogonally to the connected surfaces, the system is compared to the one-dimensional model of Chapter 3. The models are not equivalent, since the bond angle with the surfaces is not restricted to a single value any more. The strong competition of different bond conformations is hence relaxed. In the limiting case of pure shearing forces, the model of Chapter 4 is recovered, because the geometry again results in a parallel alignment of all bonds and the force vector. Therefore, pure shearing forces again show a self-stabilization regime for low forces. Naturally, the question arises, whether the self-stabilization mechanism also occurs in the case of intermediate force angles, in which bonds are not only sheared, but also pulled. Therefore, intermediate force angles are applied, so that adhesion molecules experience a superposition of pulling and shearing. As in previous chapters, steady state configurations and average cluster lifetimes are discussed.

## 5.1 Modifications to the model

The extension to two dimension requires a number of modifications to the model. Again, the adhesion cluster connects two parallel boundaries that are subject to a constant force. Only now, the force is represented by the vector  $\mathbf{F} = (F_x, F_y)$ . The angle between force vector and the adhesion boundary is denoted by  $\theta \in [0, \pi/2]$ . Adhesion molecules are elastic with a linear force-stretch relationship, but cannot bend. The angle between adhesion molecule  $i$  and the boundaries is denoted by  $\alpha_i$ , so that the force balance conditions read

$$F_x = \kappa \sum_{n_b, n_{b_u}} h_{x,i} = \kappa \sum_{n_b, n_{b_u}} h_i \cos(\alpha_i), \quad F_y = \kappa \sum_{n_b, n_{b_u}} h_{y,i} = \kappa \sum_{n_b, n_{b_u}} h_i \sin(\alpha_i) \quad (5.1)$$

To restore force balance after every reaction, the upper boundary can be shifted in  $x$ - and  $y$ -direction. Since the lower boundary and all bonds are fixed, the coordinates of the upper boundary, described by the total shift  $\mathbf{s} = (s_x, s_y)$ , are the only degrees of freedom. Individual molecules can rupture and rebind, and unfold and refold. Additionally, unbound, folded molecules in state  $a$  are in exchange with a molecule reservoir. Figure 5.1 shows a sketch of an exemplary model cluster and the allowed transitions.

The transition rates for unfolding and refolding,  $\delta_b^\pm(h)$ , and the constant rates,  $\delta_a^\pm$  and  $\gamma^\pm$ , can be adopted from the one-dimensional models, with the bond stretch  $h = \sqrt{h_x^2 + h_y^2}$ , compare Tab. 3.1. This also holds for the rupture rates  $\beta^-(h)$  and  $\beta_u^-(h)$ . The binding process, which is crucial for cluster development, however needs to be redefined.

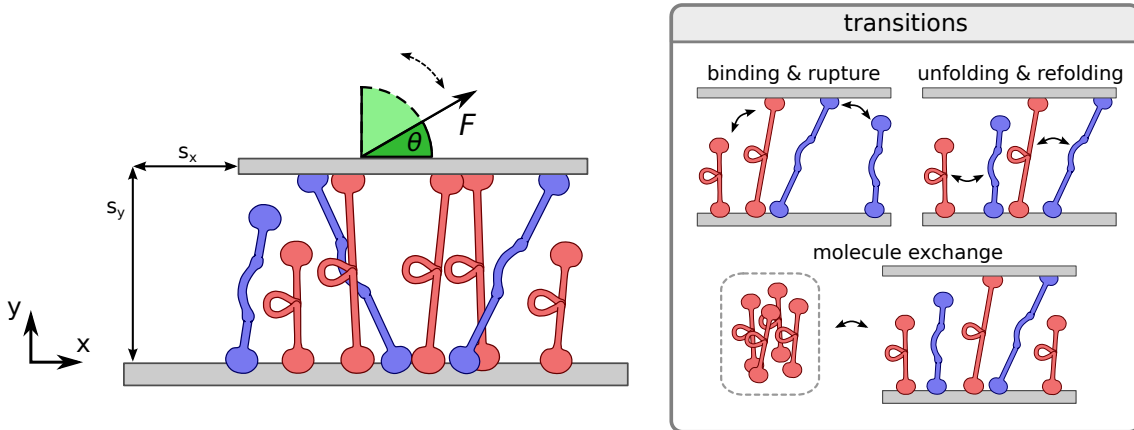


Figure 5.1. Sketch of the twodimensional adhesion cluster model. The box shows the different single molecule transitions.

### 5.1.1 Binding rate

In the models studied so far, adhesion molecules bind only parallel to the force vector, which is either parallel or orthogonal to the boundaries. For clusters with parallel binding



only, i.e.  $\alpha_i = \theta$ , the stretch for binding is determined by the current distance between the boundaries given by  $s_y$ . For folded bonds, the only possible binding stretch is then given by

$$h_x = h_y / \tan(\theta), \quad h_y = s_y - \ell_0 \sin \theta \quad (5.2)$$

For unfolded bonds, the vertical stretch component is given by  $h_{u,y} = h_y - \Delta \sin \theta$ . Once a molecule binds, its binding point stays fixed. Therefore all shifts of the upper boundary due to bond transitions like unbinding, unfolding or folding, will take place in direction of the force vector. The system is therefore effectively only one-dimensional and comparable to the model in Chapter 3 with rescaled forces and lengths.

For an actual two-dimensional system, the bond angle has to be variable. In general, possible bond angles lie in the range  $\alpha \in [0, \pi]$ . The angle, with which the molecule binds, is determined by the chosen binding stretch  $h$  and the current distance  $s_y$ . To demonstrate, how the binding position is obtained from  $h$  and  $s_y$ , the binding point of adhesion molecules at the lower surface is considered to be at the origin. For an upper boundary shift ( $s_x, s_y > 0$ ), the binding point  $\mathbf{r} = (r_x, r_y)$  along the upper surface of a folded bond can be obtained via

$$r_x = r_y / \tan(\alpha) = \pm \sqrt{(\ell_0 + h)^2 - s_y^2}, \quad r_y = s_y. \quad (5.3)$$

For unfolded bonds,  $\ell_0$  has to be replaced with  $\ell_0 + \Delta$ .

In the case  $s_y < |\ell_0 + h|$ , two values are possible for the  $x$ -coordinate of  $\mathbf{r}$ , which lead to two options for the bond angle,  $\alpha_1 < \pi/2$  and  $\alpha_2 = \pi - \alpha_1$ . For  $s_y < \ell_0$ , the range of possible binding stretches is limited by the value  $h \geq h_{\min} = s_y - \ell_0 < 0$ . The minimal value  $h_{\min}$  is the point where the bond is compressed most, which is the case for  $\alpha = \pi/2$ . The binding interval is therefore narrowed to  $h \in [h_{\min}, |h_{\min}|]$ . This choice ensures that molecule binding occurs symmetrically around  $h = 0$  and no energy is artificially injected. The total binding rate in this case is therefore obtained as the integral of  $\beta^+(h)$  as defined in Tab. 3.1 over the possible stretch values

$$\beta^+ \Big|_{h_{\min}} = \frac{1}{A(h_{\min})} \int_{h_{\min}}^{|h_{\min}|} \frac{\beta^+(h)}{\sqrt{2\pi\sigma^2}} dh = \frac{k_\beta \exp(\tilde{\epsilon}_b)}{A(h_{\min})} \left( \text{Erf} \left( \frac{\ell_b}{\sqrt{2}\sigma} \right) + \text{Erf} \left( \frac{|h_{\min}| - \ell_b}{\sqrt{2}\sigma} \right) \right), \quad (5.4)$$

where the factor  $\sqrt{2\pi\sigma^2}$  already appeared in Chapter 4. The new normalization  $A(h_{\min})$  accounts for a limited stretch range for the equilibrium distribution  $p_b^*(h)$ . It is given by

$$A(h_{\min}) = \int_{h_{\min}}^{|h_{\min}|} p_b^*(h) dh = \int_{h_{\min}}^{|h_{\min}|} \frac{1}{\sqrt{2\pi\sigma^2}} \exp \left( -\frac{h^2}{2\sigma^2} \right) dh = \text{Erf} \left( \frac{|h_{\min}|}{\sqrt{2}\sigma} \right). \quad (5.5)$$

In the limiting case  $s_y = 0$ , the threshold of binding stretches can be extended to the limit  $|h_{\min}| \rightarrow \infty$ , which leads to  $A(h_{\min}) = 1$ . Thus, the normalization correctly reproduces the one-dimensional model with pure shearing forces of Chapter 4.

When  $h_{\min}$  approaches zero, the integration interval becomes small. The normalization constant for a small finite binding interval  $\epsilon$  is given by

$$A(0) = \int_{-\epsilon/2}^{\epsilon/2} \frac{1}{\sqrt{2\pi\sigma^2}} \exp\left(-\frac{h^2}{2\sigma^2}\right) dh = \text{Erf}\left(\frac{\epsilon/2}{\sqrt{2}\sigma}\right) \approx \frac{\epsilon}{\sqrt{2\pi\sigma^2}}. \quad (5.6)$$

In the last step, the error function is expanded until first order in  $\epsilon$ . This normalization constant is used for the case  $s_y \geq \ell_0$ , in which folded bonds can only bind vertically at  $(0, s_y)$  with  $\alpha = \pi/2$ . The total binding rate for a single binding stretch  $h \geq 0$  is then given by

$$\beta^+ \Big|_{h \geq 0} = \frac{k_\beta \exp(\tilde{\epsilon}_b)}{2A(0)} \left( \text{Erf}\left(\frac{h - \ell_b + \epsilon/2}{\sqrt{2}\sigma}\right) + \text{Erf}\left(\frac{h - \ell_b - \epsilon/2}{\sqrt{2}\sigma}\right) \right) \quad (5.7)$$

$$\approx k_\beta \exp(\tilde{\epsilon}_b) \exp\left(-\frac{(h - \ell_b)^2}{2\sigma^2}\right) \quad (5.8)$$

so that the initially introduced binding rate of Tab. 3.1 is recovered. The binding rate therefore also reproduces the correct values for the limiting case of parallel bonds under pulling forces of Chapter 3.

So far, only the geometry of the system determines the binding process. It allows in general all binding angles in the full range of  $[0, \pi]$ . This leads occasionally, e.g. in the case  $\theta = 0$ , to the counterintuitive result of two groups of bonds that are oriented in opposite directions. In biological adhesions, however, clusters elongate in direction of force [15, 272]. Therefore a final modification is introduced to prevent the formation of oppositely oriented subclusters: In the case  $s_y < \ell_0$ , i.e. if two binding angles are possible, the second angle is only allowed, if it encloses not more than  $90^\circ$  with the force vector. Hence, at  $\theta = 0$ , binding is restricted to the angles  $[0, \pi/2]$ , while at  $\theta = \pi/2$ , the full range  $[0, \pi]$  is allowed.

### 5.1.2 Restoring force balance

As in the one-dimensional models, it is assumed that the system relaxes fast to the configuration which fulfils force balance. For two dimensions, the resulting new shift  $\mathbf{s}' = \mathbf{s} + \mathbf{x}$  with the displacement  $\mathbf{x}$  cannot be determined analytically. Therefore a numerical Newton-Raphson method is implemented. The algorithm starts from an initial guess for  $\mathbf{x}_0$  and approaches the correct solution  $\mathbf{x}$  by means of the iteration

$$\mathbf{x}_{j+1} = \mathbf{x}_j - \mathbf{J}^{-1}(\mathbf{x}_j) \mathbf{g}(\mathbf{x}_j), \quad (5.9)$$

where  $\mathbf{J}$  denotes the Jacobi-matrix of the equation system

$$\mathbf{g}(\mathbf{x}_j) = \begin{pmatrix} \tilde{F}_x - \sum_{n_b, n_{b_u}} \tilde{h}_{x,i}(\mathbf{x}_j) \\ \tilde{F}_y - \sum_{n_b, n_{b_u}} \tilde{h}_{y,i}(\mathbf{x}_j) \end{pmatrix}. \quad (5.10)$$

The iteration stops, when the root of  $\mathbf{g}$  is found within the precision goal. As a precautionary measure, so that the iteration indeed follows the direction of the gradient towards the root, the condition  $g(x_{j+1}) \cdot g(x_{j+1}) < g(x_j) \cdot g(x_j)$  has to be met. If the proposed next value, which is obtained with Eq. 5.9, leads to an increase of the square value of  $\mathbf{g}$ , only a fraction  $0 < \mu < 1$  of the step is proposed,

$$\mathbf{x}_{j+1} = \mathbf{x}_j - \mu \left( \mathbf{J}^{-1}(\mathbf{x}_j) \mathbf{g}(\mathbf{x}_j) \right). \quad (5.11)$$

Close to the root of  $\mathbf{g}$ , the method converges quadratically. Rarely, but especially for clusters with only few bonds, the Newton-Raphson method does not lead to the correct solution, which restores force balance. In such a case, the trajectory is rejected and the simulation starts from the beginning.

## 5.2 Limiting cases of pure pulling and shearing

To test the modifications, the force directions that are discussed in Chapters 3 and 4 are analysed first. A pure pulling force is achieved by setting the angle between force vector and the surfaces to  $\theta = \pi/2$ . However, results are expected to differ from those presented in Chapter 3, because adhesion bonds can bind at variable angles in the two-dimensional model. A shearing force is realized by choosing  $\theta = 0$ , which leads to a vanishing distance  $s_y$  between the two surfaces. In this case, the bonds can only align in parallel with the surface and the force vector, so that the results of Chapter 4 are expected to be recovered.

### 5.2.1 Pulling force

For the case  $\theta = \pi/2$ , Fig. 5.2 shows the marginal steady state probabilities  $p_{n_i}^{(s)}$  for the four adhesion molecule states for a reservoir rate ratio  $\gamma = 1.72$  and at three different force values (orange bars). The results from the one-dimensional model under pulling forces are given for comparison as well (blue bars), compare Fig. 3.18. While the chosen reservoir rate ratio led to  $N^* \approx 10$  molecules in steady state for the one-dimensional model, the average number of molecules in steady state in the two-dimensional system is increased to  $N^* \approx 15$ . This difference occurs, because the competition between folded and unfolded bonds is lifted. Instead of switching between configurations with either a high number of folded or a high number of unfolded bonds, both conformations are observed in equilibrium at the same time. The distribution is centered around lower occupation numbers for unfolded

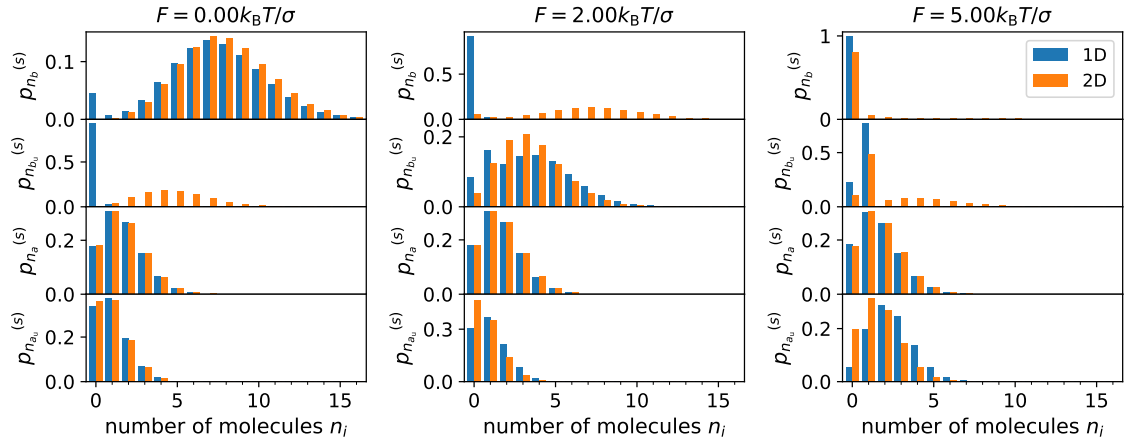


Figure 5.2. Histograms of the marginal steady state probabilities  $p_{n_i}^{(s)}$  for the two-dimensional adhesion cluster model at  $\theta = \pi/2$  and a reservoir rate ratio  $\gamma = 1.72$ . Results from the one-dimensional model are shown for comparison as well, compare Fig. 3.18. Parameter values are given in Table 5.1.

bonds than for folded bonds. The distributions of unbound molecules are comparable to the one-dimensional model. They are determined by the reservoir rate ratio. For small, finite forces, the majority of bonds unfolds, as in the one-dimensional case, but the effect is shifted to higher force values because of the larger cluster size. At high forces, the high rupture probability leads to a decreased number of bound molecules.

The steady state quantities for larger clusters at  $\theta = 0$  are shown in Fig. 5.3 and Fig. 5.4. In Fig. 5.3, averaged simulation results for the two-dimensional model are shown as square markers. For comparison, the steady state quantities of the one-dimensional system are indicated with round markers and thin lines. The reservoir rate ratio  $\gamma = 8.59$  leads to  $N^* \approx 70$  molecules in the cluster, compared to only  $N^* \approx 50$  in the one-dimensional model. The bound states do not switch between two different configurations, but exhibit both folded and unfolded bonds simultaneously, see Fig. 5.3a. The average number of unbound molecules in states  $a$  and  $a_u$  is comparable to the one-dimensional state and almost constant, until progressive rupture of bonds leads to an accumulation in the unbound, unfolded state, see Fig. 5.3b. The presence of both conformations under different angles leads to a lower average distance between the two surfaces than in the one-dimensional case, see Fig. 5.3c. Additionally, the larger number of molecules reduces the average stretch per bond, so that the onset of cluster dissociation is shifted to higher force values. Figure 5.4 demonstrates the difference between the angular distributions of folded and unfolded bonds. The boxplots show the averaged values of median, first and third quartile, and maximum and minimum of the steady state angle distributions. While the averaged median value of both distributions equals the force angle  $\theta = \pi/2$ , folded bonds cover a smaller range of angles, which furthermore decreases with increasing force. Unfolded bonds are found at

angles between  $60^\circ$  and  $120^\circ$ , and the range of binding angles decreases only slightly with force.

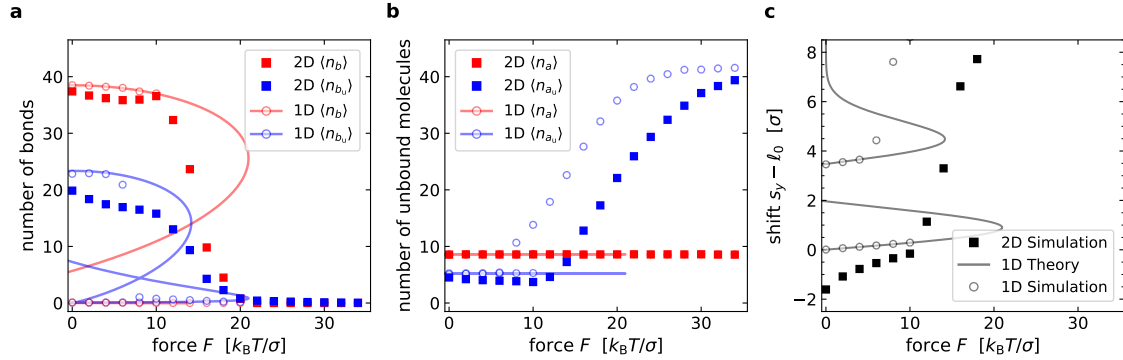


Figure 5.3. Steady state quantities as a function of force  $F$  for the two-dimensional adhesion cluster model at  $\theta = \pi/2$  and a reservoir rate ratio  $\gamma = 8.59$  (square markers). Results from the one-dimensional model are indicated for comparison with round markers and thin lines, see Fig. 3.19. a) Average occupation number of states  $b$  and  $b_u$ . b) Average occupation number of states  $a$  and  $a_u$ . c) Average distance between the surfaces  $s_y$ , reduced by the folded rest length  $l_0$ . Parameter values are given in Table 5.1.

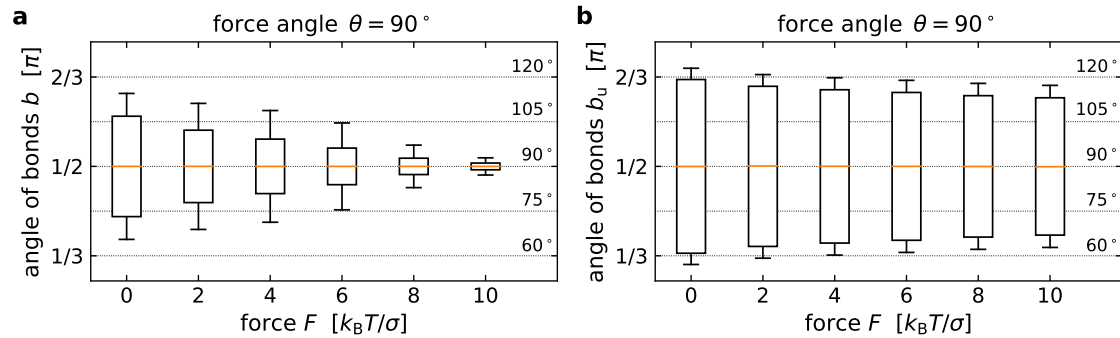


Figure 5.4. Averaged angular distributions in steady state for  $\theta = \pi/2$  and a reservoir rate ratio  $\gamma = 8.59$ . Whiskers show the averaged maximum and minimum angle, orange lines indicate the average median value. a) Boxplots for folded bonds  $b$ . b) Boxplots for unfolded bonds  $b_u$ . Parameter values are given in Table 5.1.

## 5.2.2 Shearing force

To compare the two-dimensional model for  $\theta = 0$  with the one-dimensional model under shearing forces, Fig. 4.2 is reproduced. The results are shown in Fig. 5.5, where the steady state quantities of four different cluster models are compared. The basic adhesion cluster with rupture and rebinding as the only allowed transitions is denoted with number I (light

red squares). Model II is additionally coupled to a molecule reservoir and thus has a variable total number of molecules, compare Fig. 5.5a (red circles). The models in which the conformational change is included are indicated with blue colors. In model III, an exchange with the surrounding is not allowed (light blue squares), unlike in model IV (blue circles). Only model IV with both conformational changes and the reservoir connection exhibits the self-stabilization mechanism that is also observed for the one-dimensional horizontal system. The increased number of bonds leads to a reduced relative velocity of the two separated boundaries. The accumulation of unbound molecules is an indicator for the shift out of equilibrium. In fact, the steady state values of the one- and two-dimensional system at  $\theta = 0$  coincide as expected, because in both systems, all bonds bind parallel to the force vector.

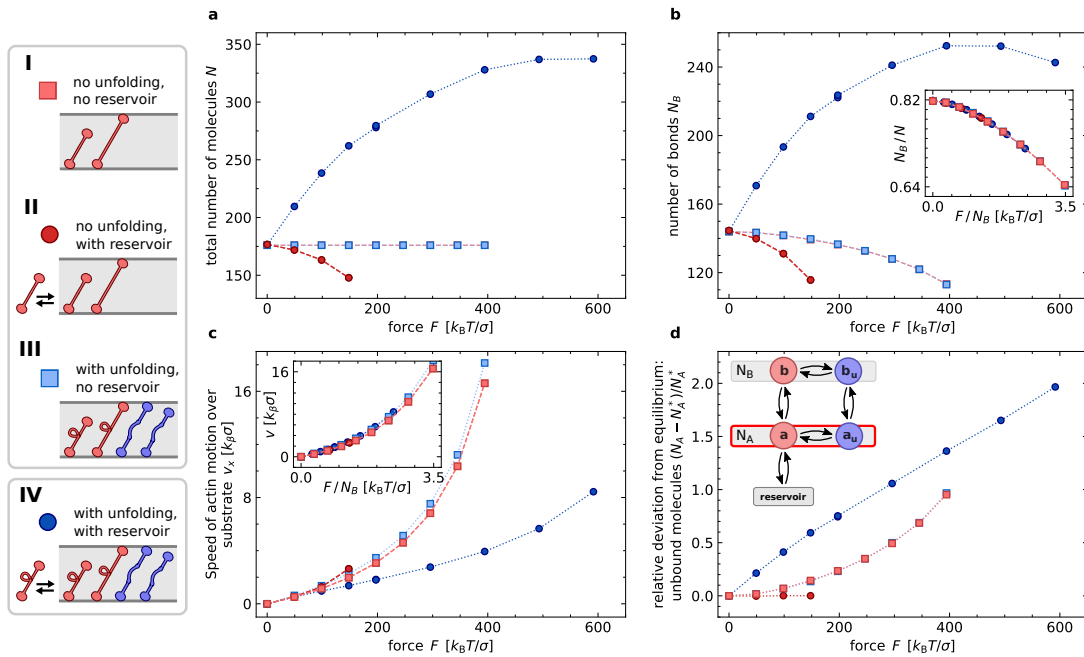


Figure 5.5. Steady state averages obtained from simulations for the two-dimensional adhesion cluster model at pure shearing force, i.e. at  $\theta = 0$ . The results agree with the one-dimensional model for shearing forces, compare Fig. 4.2. Data points are connected with dashed lines for better visibility. Parameter values are given in Table 5.1.

### 5.3 Intermediate force directions

In the previous sections, the limiting cases of  $\theta = 0^\circ$  and  $\theta = 90^\circ$  are discussed and compared to the one-dimensional systems. Here, the picture is completed by application of forces at intermediate angles. For force angles  $0^\circ < \theta < 90^\circ$ , bonds within the adhesion cluster are subject to both pulling and shearing forces. The steady state results for force

angles in steps of  $10^\circ$  are shown in Fig. 5.6. Data points are plotted until first cluster dissociation events are observed within the simulation time. The force value at which the first dissociation events are observed increases with decreasing force angle. Many steady state quantities show a strong dependence on the force angle  $\theta$ . The simulation results indicate a threshold between  $30^\circ$  and  $40^\circ$  with a qualitatively different cluster behaviour below and above this threshold.

For low force angles, i.e.  $\theta \leq 30^\circ$ , the number of bonds  $N_B = n_b + n_{b_u}$  in Fig. 5.6a increases with force in a similar manner as in the one-dimensional horizontal system. At force angles above the threshold, here  $\theta \geq 40^\circ$ , the average number of bound molecules stays below the respective equilibrium value at  $F = 0$ . For all angles  $\theta < 90^\circ$ , the number of unbound molecules,  $N_A = n_a + n_{a_u}$  increases with force, see Fig. 5.6b. However, the increase is stronger for low force angles. Within both groups, a quantitatively similar

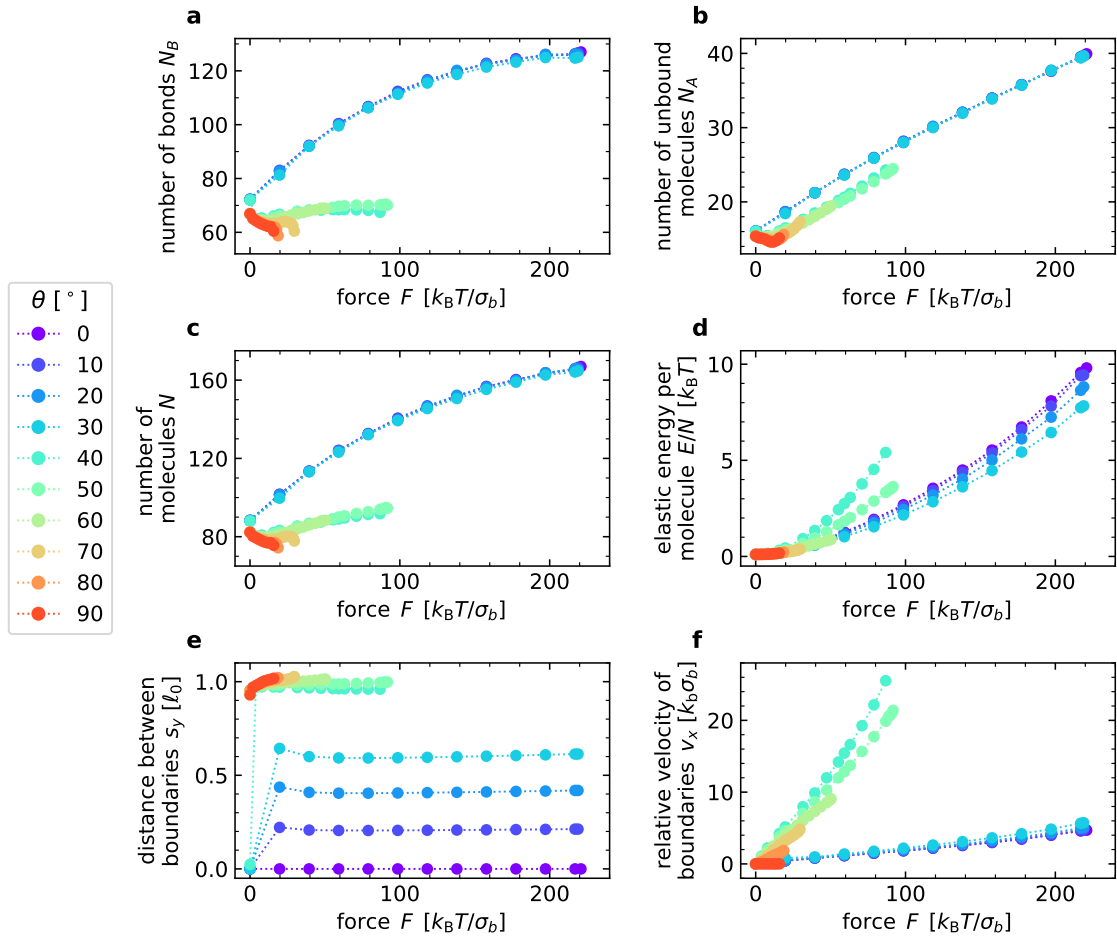


Figure 5.6. Steady state averages for adhesion clusters with conformational changes and a reservoir rate ratio  $\gamma = 10$  at selected force angles in the range  $\theta \in [0, \pi/2]$ . Data points are shown until first complete cluster dissociation is observed within the simulation time. Parameter values are given in Table 5.1.

behaviour is observed. The results from Fig. 5.6a and b are brought together in Fig. 5.6c, which shows the total number of molecules  $N$  in the cluster.

The average elastic energy per adhesion molecule,  $E/N = \sum_{j=1}^{N_B} \kappa h^2 / (2N)$ , is shown in Figure 5.6d. It is lowest for  $\theta = 30^\circ$ , whereas the highest increase of the elastic energy per molecule with external force is found just above the threshold, i.e. at  $\theta = 40^\circ$ . The strong difference coincides with a strong difference in the average separation  $s_y$  between the two boundaries, compare Fig. 5.6e. At low force angles, the cluster finds a steady state with a small finite distance close to the value  $F \sin \theta$ . Binding is in many cases only allowed with an angle  $\alpha_1 < \pi/2$ , so that bound molecules are aligned and stretched in the same direction. For the group of higher force angles, the cluster separation  $s_y$  is similar to the case of pure pulling forces, i.e. close to the folded bond's rest length  $\ell_0$ . In this configuration, binding is allowed at both binding angles  $\alpha_1 < \pi/2$  and  $\alpha_2 = \pi - \alpha_1$ . Hence, bonds are stretched in different directions, which explains the higher elastic energy per molecule for  $\theta = 40^\circ$ , compared to the case  $\theta = 30^\circ$ .

For all angles  $\theta < 90^\circ$ , a constant velocity in  $x$ -direction is observed, see Fig. 5.6f. The approximately linear increase of  $v_x$  with the external force is strongly reduced for the group of small force angles, i.e.  $\theta \leq 30^\circ$ . The average velocity with which the surfaces slide against each is highest at  $\theta = 40^\circ$ . The observation agrees with the finding of the highest elastic energy increase per molecule.

To further illustrate and understand the difference between low and large force angles, averaged boxplots of the angular distributions of bound molecules at  $\theta = 30^\circ$  and  $\theta = 60^\circ$  as a function of force  $F$  are shown in Fig. 5.7. Whiskers represent the average maximal and minimal angles of the distribution and the average median is indicated with an orange line. At  $\theta = 30^\circ$  and low positive forces, the distribution of folded bonds in state  $b$  is centered around the vertically aligned position at  $\alpha = 90^\circ$ , while unfolded bonds are tilted towards lower angles. Unfolded bonds cover a broader range of binding angles than folded molecules. For forces  $\tilde{F} \geq 20$ , both distributions become narrower with an average median between  $30^\circ$  and  $45^\circ$ . The molecules in state  $b_u$  cover a broader range of angles than in state  $b$  at all presented force values. The force angle of  $\theta = 60^\circ$  thus leads on average to a cluster configuration, in which bonds are oriented in different directions. Thus, all bonds are oriented in a similar direction. For a force angle  $\theta = 60^\circ$ , the average median of the angular distributions for folded bonds stays close to  $90^\circ$  at all force values. The range of observed angles narrows only moderately. The average median of the unfolded bonds' angle drops from  $90^\circ$  at  $\tilde{F} = 0$  to a value between  $60^\circ$  and  $75^\circ$ .

The steady state results reveal a grouping into two qualitatively different cluster configurations: At high force angles, the separation between the boundaries is close to the native molecule length, which enables molecule association at the second binding angle  $\alpha_2$ . Therefore the cluster exhibits a broad distribution of bond angles. The large range of binding angles leads to oppositely oriented bonds, so that the elastic energy per molecule



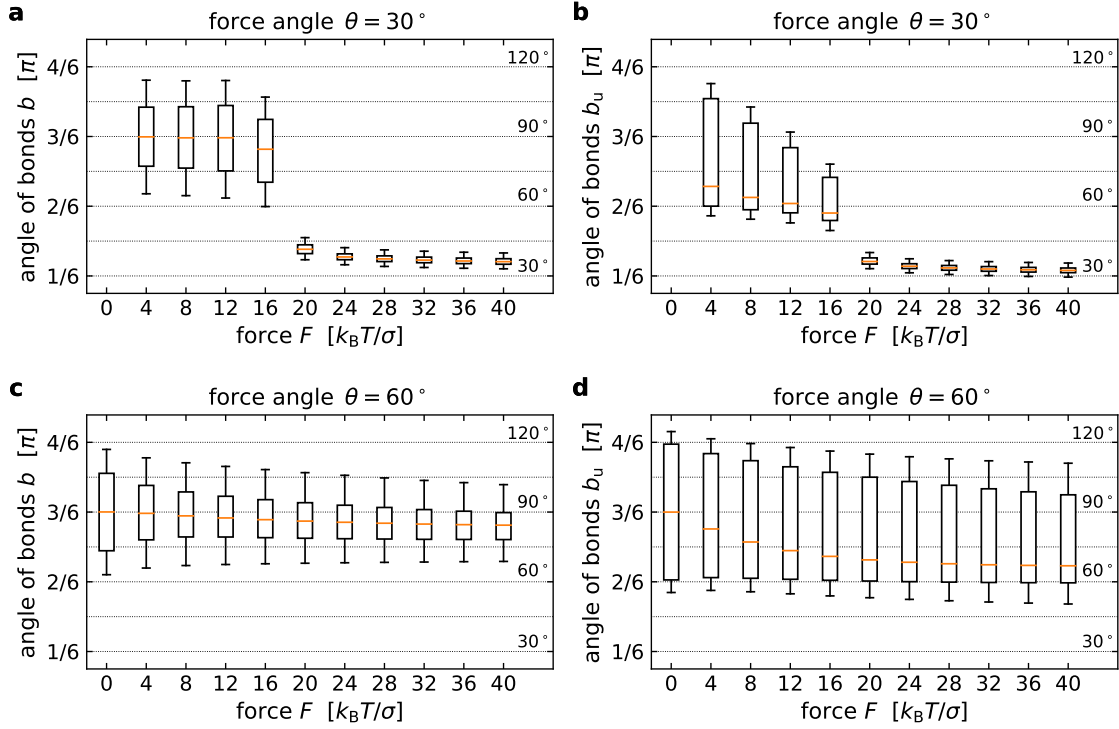


Figure 5.7. Averaged angular distributions in steady state at a reservoir rate ratio  $\gamma = 10$ . Whiskers show the averaged maximum and minimum angle, the orange line indicates the average median value. Dashed horizontal lines indicate steps of  $15^\circ$ . a,b) Boxplots for bonds  $b$  and  $b_u$  at  $\theta = 30^\circ$ . At  $\tilde{F} = 0$ , all bonds are aligned in parallel with an angle  $\alpha = 0^\circ$ . c,d) Boxplots for bonds  $b$  and  $b_u$  at  $\theta = 60^\circ$ . Parameter values are given in Table 5.1.

is large. The number of bonds does not exceed its equilibrium value at vanishing force, although molecules are accumulated in the unbound states. At low force angles, i.e. under predominantly shearing forces, the self-stabilization mechanism is observed with an increase of bonds despite increasing force. As in the one-dimensional horizontal case this coincides with an increase of the number of unbound unfolded molecules. They are not coupled to a reservoir and can thus be driven out of equilibrium. With increasing force, bonds align in the same direction. Thereby, the force is shared efficiently, so that the elastic energy per molecule is lower than under pulling forces.

Besides the increase of bound molecules with increasing force, the self-stabilization mechanism leads to an increased lifetime of the whole cluster in the one-dimensional model, compare Chapter 4. To test if the average lifetime also increases in the two-dimensional model, the time until complete cluster dissociation is measured and averaged for small adhesions. The results are shown in Fig. 5.8. In Fig. 5.8a, the average time until complete cluster dissociation is shown as a function of force and for different values of the unfolding length  $\Delta$ . The reservoir rate ratio  $\gamma = 1.14$  leads to  $N^* \approx 10$  molecules in steady state. Cluster lifetime increases with force for the cases  $\tilde{\Delta} \in \{2, 4, 6\}$  at  $\theta = 0^\circ$  and  $\theta = 30^\circ$ . In

Fig. 5.8b, the average lifetime is shown for a large range of force angles  $\theta$  for adhesion clusters with  $\tilde{\Delta} \approx 2.5$ . The thick dashed line indicates  $\theta = 40^\circ$ . For angles  $\theta < 40^\circ$ , cluster lifetime increases under small, but increasing forces. At large forces, lifetime decreases exponentially with force. A quantitatively similar behaviour is observed, because all bonds rupture successively, independent of unfolding length or angle.

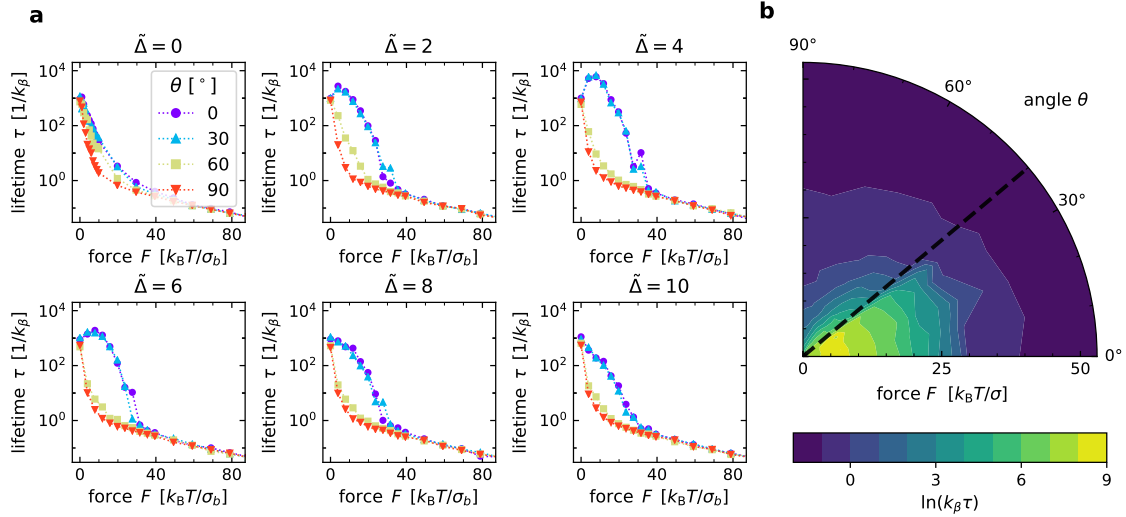


Figure 5.8. Average time until complete dissociation for the two-dimensional cluster model with unfolding and a reservoir rate ratio  $\gamma = 1.14$ . Clusters are initialized with  $N = 10 \approx N^*$  folded bonds. a) Lifetimes for a wide range of unfolding lengths  $\tilde{\Delta}$  and selected force angles. b) Lifetimes at  $\tilde{\Delta} \approx 2.5$ . The thick line indicates the force angle  $\theta = 40^\circ$ , below which a significant increase in lifetime despite increasing force is observed. Parameter values are given in Table 5.1.

## 5.4 Summary

In this chapter, the extension of the adhesion cluster model from one to two dimensions is presented. Even if the general idea, the possible molecule transitions and assumptions remain unchanged, some modifications are required. One important difference concerns the binding mechanism. In contrast to the one-dimensional systems, the bonds in the two-dimensional cluster are in general not in parallel to each other and to the force vector. The distance between the two boundaries determines the possible range of stretches, with which a molecule can rebind to the upper surface. The chosen binding stretch determines the angle  $\alpha_1 \leq \pi/2$ , under which the molecule binds. The alternative angle  $\alpha_2 = \pi - \alpha_1$  is chosen with a 50% chance, if it encloses less than  $90^\circ$  with the force angle. The binding rate is defined such, that in the limiting cases  $\theta = 0^\circ$  and  $\theta = 90^\circ$ , the binding rates of the one-dimensional systems are recovered. As a second modification, the simulation

algorithm is adjusted to account for the two-dimensional geometry. Large parts of the algorithm can be straightforwardly transferred from the one-dimensional system. Only the relaxation step, which is required after each stretch-dependent reaction and which restores the force balance, is revised. Because of the individual bond stretches and angles, a numerical method is employed to calculate the typically small shift of the upper surface that corrects the imbalance of forces.

The analysis of simulated cluster trajectories shows that the cluster evolution depends strongly on the angle  $\theta$  between force vector and the bounding surface. For a cluster under pure shearing force at  $\theta = 0$ , all bonds can align in parallel, so that the dimensionality is effectively reduced to one. Thus, the steady state configuration agrees with the results from the one-dimensional horizontal system presented in Chapter 4. Bonds have a broad range of possible binding stretches. Continuous cycles of binding, stretching, unfolding and rupture lead to an on average constant relative velocity of the two bounding surfaces. For force angles until  $\theta = 30^\circ$ , the average occupation numbers of molecule states stay largely unaltered. The separation between the two bounding surfaces stabilizes at a value that lies closely above  $F \sin \theta$  for low forces. All bonds are aligned in the direction of force with a narrow distribution of bond angles, which reduces the average stretch per bond and thus the elastic energy per molecule. As a result, the relative motion of the two surfaces is slow.

For force angles  $\theta \geq 40^\circ$ , a very different picture emerges. The distance that is bridged by the cluster stabilizes at a value close to the folded bonds' rest length  $\ell_0$ , so that the distribution of folded bonds is centered around the vertical binding position at  $90^\circ$ . Due to their longer rest length, the average distribution of unfolded bonds' angles is shifted towards lower values with an average median of  $\arcsin(\ell_0/(\ell_0 + \Delta)) \approx 65^\circ$  at positive forces. The large width of the distribution leads to a larger elastic energy per molecule than at low force angles, because not all bonds are aligned in direction of force. The average number of bonds stays below its equilibrium value, although unbound molecules are accumulated in the cluster with increasing force. The resulting relative velocity of the two surfaces increases stronger with force than at low force angles. In the limiting case  $\theta = 90^\circ$ , there is no net motion. The number of bonds decreases monotonously with force. Yet, the situation is different from the one-dimensional model, where all bonds are aligned in parallel with the force vector. In the two-dimensional system, the bond angles are distributed from approximately  $60^\circ$  to  $120^\circ$ . The width of the distribution decreases strongly with increasing force for folded bonds, but only moderately for bonds in the unfolded state.

The different effects of predominantly pulling or shearing forces are also reflected in the results on average cluster lifetime. For large force angles, i.e.  $\theta \geq 40^\circ$ , the average time until the last bond ruptures decreases with force. For low force angles, i.e.  $\theta < 40^\circ$ , the average time until the cluster dissociates increases in a limited regime of increasing forces. This prolonged lifetime, which is already observed in the one-dimensional horizontal system, is a consequence of the self-stabilization mechanism. The high number of bound molecules

reduces the rupture probability of individual bonds and thus stabilizes the whole cluster. The increase in the average cluster lifetimes is found for large ranges of the unfolding parameter  $\Delta$ . It does not occur for  $\tilde{\Delta} = 0$ , because the unfolding and refolding rates reduce to constants and the molecules have the same response to force. At very large unfolding lengths, the high energy barrier between folded and unfolded state suppresses the conformational change, so that the connection between folded, bound and unfolded, bound states is effectively broken.

In summary, the generalization of the extended adhesion cluster model to two dimensions demonstrates that the binding mechanism and the geometry of the cluster have a strong influence on the response of adhesion clusters to force. The effect is observed both in the steady state configuration and in the average time until complete cluster dissociation. While under shearing forces, the so-called self-stabilization mechanism occurs under low surface separations, pulling forces lead to a broad distribution of bond angles at comparably large surface separations, but not to self-stabilization.

## 5.5 Parameter values

The parameter values for the simulations of two-dimensional adhesion clusters are given in Table 5.1. In all cases, the energy unit is given by  $1k_{\text{B}}T = 4.114 \text{ pN nm}$ , the time unit is given by the inverse binding rate prefactor  $t_0 = 1/k_{\beta}$ , and the restlength of a folded molecule is  $\ell_0 = 100 \text{ nm}$ .

The averages are taken from  $N_{\text{sim}}$  trajectories. After reaching the steady state,  $N_{\text{meas}}$  measurements are taken in intervals of  $N_{\text{wait}}$  single molecule reactions.

Parameter		Value for data in Fig.						
		5.2	5.3	5.4	5.5	5.6	5.7	5.8
$\kappa$	[pN nm <sup>-1</sup> ]	0.5	0.5	0.5	0.25	0.25	0.25	0.25
$\sigma$	[nm]	2.87	2.87	2.87	4.06	4.06	4.06	4.06
$\ell_{\text{b}}$	[nm]	1	1	1	1	1	1	1
$\epsilon_{\text{b}}$	[ $k_{\text{B}}T$ ]	1.5	1.5	1.5	1.5	1.5	1.5	1.5
$k_{\delta}$	[ $k_{\beta}$ ]	1	1	1	0, 1	1	1	1
$\Delta$	[nm]	10	10	10	10	10	10	10
$\epsilon_{\text{f}}$	[ $k_{\text{B}}T$ ]	0.5	0.5	0.5	0.5	0.5	0.5	0.5
$\gamma^{+}$	[ $k_{\beta}$ ]	1.72	8.59	8.59	0, 20, 32.13	10	10	1.14
$\gamma^{-}$	[ $k_{\beta}$ ]	1	1	1	1	1	1	1
$N_{\text{sim}}$		50	50	50	10	40	40	50
$N_{\text{meas}}$		$5 \cdot 10^3$	$5 \cdot 10^3$	$5 \cdot 10^3$	$1.5 \cdot 10^4$	$5 \cdot 10^3$	$5 \cdot 10^3$	$10^4$
$N_{\text{wait}}$		$10^2$	$10^2$	$1 \cdot 10^2$	10	$10^2$	$10^2$	$10^5$

Table 5.1. Parameter values for simulations of the two-dimensional adhesion cluster model with binding, rupture and conformational changes.



# Chapter 6

## Conclusions and outlook

In this dissertation, a stochastic model is presented to describe the response of cellular adhesions to pulling and shearing forces. One of the main objectives was to study the effects of conformational changes of adhesion proteins and to find possible mechanism of cluster growth or strengthening under mechanical load. For this purpose, an idealized model for a single cluster of adhesion molecules is introduced. As a first extension, reversible protein unfolding is added to the set of possible transitions that change a molecule's state. Carefully chosen transition rates guarantee that the stochastic process, which describes the evolution of the cluster, satisfies microscopic reversibility in equilibrium. Steady state configurations and the average cluster lifetime are studied analytically and by means of kinetic Monte Carlo simulations. The results show that the unfolding step has interesting effects in both geometries, but cluster stabilization is only observed when shearing forces are dominant. In this case, application of force leads to an accumulation of molecules in unfolded states and as a consequence, cluster size increases.

### 6.1 Modelling an adhesion cluster

The model is motivated by cellular adhesions, which are based on local aggregations of numerous different proteins. The nanometer- to micrometer-sized assemblies connect the cytoskeleton to neighbouring cells or the extracellular matrix. On the molecular level, the interactions that constitute the connection to the cell's environment are diverse and the resulting biochemical pathways are not yet fully understood. Nevertheless, common elements and recurrent mechanisms emerge from the underlying laws of physics and the stochastic nature of biological processes. The interplay of individual molecular bonds results in a regulated and cooperative collective behaviour, a fundamental basis for the integrity of tissues and migration on surfaces. In a process called mechanotransduction, cell-cell and cell-matrix adhesions transmit and respond to mechanical signals that are generated by the cell or perceived as cues from the environment. As one remarkable way of

adaptation, cell-matrix adhesions grow under increasing tension [272]. The adaptor proteins talin and vinculin have been ascribed an important role in the process of adhesion growth and strengthening: domains along talin unfold under force and thereby open vinculin binding sites [347]. Vinculin molecules bind with high affinity to both talin and actin filaments and thus strengthen the connection [8]. In cell-cell adhesions,  $\alpha$ -actenin and vinculin are suggested to interact similarly [345].

In the model presented here, adhesion molecules are represented by elastic ligand-receptor bonds that connect two surfaces. They share the force that acts on the upper surface, while the lower surface is fixed. This basic concept has been used in many idealized theoretical models of adhesion clusters before, compare Refs. [111, 264, 292]. The molecules in the cluster undergo stochastic transitions between different states. The transition rate definitions are of great importance, because they determine the cluster evolution. After each transition, force balance is restored.

In the basic version of the model, molecules are either bound (state  $b$ ) or unbound (state  $a$ ). The Bell-like rupture rate  $\beta^-(h)$  increases exponentially with the absolute stretch value  $|h|$  of the bound molecule. The probability for binding per unit time,  $\beta^+(h)$ , depends on the required extension of the new bond and is maximal at the distance  $\ell_b$  to the binding point. Its definition ensures that the ratio of binding to unbinding rate equals the Boltzmann factor for the energy difference between bound and unbound state.

In an extended version of the model, molecules can also change between their native, folded state and a partially unfolded conformation via the unfolding and refolding rates  $\delta_{a,b}^+(h)$  and  $\delta_{a,b}^-(h)$ . It is assumed, that the two conformations are separated by a single energy barrier. Force shifts the thermodynamic potential linearly, so that the rates depend exponentially on the stretch. The sum of the distances to the transition state  $\Delta_1 + \Delta_2 = \Delta$  yields the length change due to unfolding. The chosen values of  $\Delta_{1,2} = 5$  nm are close to the fitting parameters obtained from measurements on talin R3 domain unfolding [321]. Again, the rate ratios yield a Boltzmann relation with the energy difference of unfolded and folded state.

The remaining rates are for simplicity chosen as constants. Importantly, the probability for a single molecule to go through the cycle of states  $a \rightarrow b \rightarrow b_u \rightarrow a_u$ , where  $b_u$  and  $a_u$  denote unfolded states, equals the probability for passing the reverse cycle, when no force acts on the cluster. Thus, symmetry of time is conserved.

The idealized model inherently includes many simplifications and cannot depict the molecular details, nor reach the complexity of cellular adhesion clusters *in vivo*. As one example, the receptor-ligand bonds behave like Hookean springs and do not bend. Also, their lateral distribution does not influence the cluster dynamics, which is furthermore strongly restricted due to the selection of few possible reactions. The force acts on two rigid planes, so that force is shared equally. Although these and other simplifications may impede the comparability to specific experimental results, they do allow us to observe generic



mechanisms that are hard to detect in detailed molecular or atomistic representations of a crowded system like cellular adhesions. Therefore the level of abstraction is helpful to observe and understand possible mechanically induced changes in cluster configurations.

## 6.2 Response to pulling forces

For an adhesion cluster with parallel bonds under pulling forces, five model variants are studied. In the simplest case with no conformational changes and a constant number of adhesion molecules, the master equation that describes the evolution of the probability distribution to find  $n_b$  bound molecules can be solved exactly. For vanishing force, the probability distribution is given by a time-dependent binomial distribution. In the long time limit, the probability to find a bound molecule is given by  $\beta(0)/(1 + \beta(0))$ . This result agrees with previous similar models [111, 292]. With increasing force, the rupture rate increases, while the rebinding rate decreases. Therefore, the probability to find more than one bound molecule approaches zero and the cluster switches between a configuration with one highly stretched bond and complete dissociation. In a mean field approximation, the average fraction of bonds equals  $\beta(h)/(1 + \beta(h))$ , but this relation holds only for small fluctuations and hence small forces.

If unbound adhesion molecules can enter and leave the cluster, the number of unbound molecules is regulated by the reservoir of molecules in the surrounding and fluctuates around the value of the transition rate ratio  $\gamma = \gamma^+/\gamma^-$ . The average number of bound molecules is proportional to  $\gamma$ . For vanishing force, the equilibrium probability distribution  $p_{n_b, n_a}^*$  is given by the product of two Poisson distributions with parameters  $\gamma$  and  $\gamma\beta(0)$ . Yet, the average fraction of bound molecules, which is obtained from the macroscopic equations, agrees with the cluster model without a reservoir connection. Thus, without conformation changes, fraction and total number of bonds decrease monotonously with increasing force, as it is expected from the Taylor expansion of binding and unbinding rate. If unbound molecules are exchanged with the surrounding, their number stays constant, so that the total number of molecules decreases under load. For clusters of fixed size, the number of unbound molecules increases.

The average time until complete cluster dissociation  $\tau$  is derived analytically for vanishing force and a constant adhesion size. It can also be approximated under the assumption that cluster dissociation occurs as a rare event due to fluctuations around a metastable steady state. The average lifetime is reduced for clusters with  $\gamma > 0$  under low forces per molecule compared to clusters with a constant size. In all model variants, average cluster lifetime decreases monotonously with force. For large forces per molecule, the reservoir exchange does not affect average cluster lifetime, because all bonds rupture successively.

In the extended model, partial unfolding increases the length of adhesion molecules

by  $\Delta$ . Again, clusters with constant and variable number of molecules are considered. Approximate solutions for the average occupation numbers in steady state are obtained from the system of macroscopic equations. The force balance equation imposes an additional constraint. Simulations reveal that only some of the possible steady state solutions are realized. For low forces, the cluster is found either close to  $h = 0$  with a large number of folded bonds or close to  $h = \Delta$  with a large number of unfolded bonds. A configuration with both conformations is energetically unfavourable. Unfolding is promoted under increasing bond extensions, so that at small positive forces, the majority of bonds is in state  $b_u$  in steady state. As a result, the distance, which is bridged by the cluster, is increased. The general response to force is qualitatively similar to the basic adhesion model without conformational changes: the number of bonds decreases with force. For clusters with a constant number of molecules, this leads to an increasing number of unbound molecules. In the model variant with a reservoir rate ratio  $\gamma > 0$ , the occupation number of both folded and unfolded unbound molecules is constant in equilibrium. The number of bonds is proportional to  $\gamma$ , but the same qualitative behaviour is observed as for constant cluster sizes.

Interestingly, the conformational change increases the probability for complete cluster dissociation at low forces for clusters with a constant number of molecules. Coupled to a reservoir, the average lifetimes for clusters with and without the conformational change are similar.

Lastly, the complexity of the model is increased by assuming that unfolding events open a binding site for new adhesion molecules. In the resulting linked state, bond refolding is blocked. As a result, the average occupation numbers of linked states grow linearly with the occupation numbers of unfolded states. The number of bonds in the configuration around  $h = \Delta$  increases with the linking rate ratio  $\lambda = \lambda^+/\lambda^-$ , so that the average extension per bond is reduced. Thus, the force threshold, beyond which the rupture process dominates, is shifted to higher values. However, the qualitative cluster behaviour does not change; the fraction of bonds still decreases with increasing force.

### 6.3 Response to shearing forces

In this geometry, bonds are aligned in parallel with the direction of force, but the force vector acts in  $x$ -direction. As a result, the separation between the two surfaces vanishes. Therefore bonds are not restricted to one binding stretch value. Instead, all stretches within the range of the binding rate  $\beta^+(h)$  are realized. The master equation that was used so far for the occupation number of bonds in state  $b$  is replaced by a master equation for the distribution  $b(h)$ , the number of bonds in state  $b$  at stretch  $h$ . The contributions for transitions to and from other states remain unchanged, but a drift term is added to account for stretch changes while the bond stays in state  $b$ . The total occupation number

in steady state is obtained after integration of the stationary solution over all possible stretch values. Unbound molecules can fluctuate freely around their rest length. Thus, their stretches can be approximated by Gaussian distributions with zero mean and variance  $\sigma_a^2$ . The integration can be carried out straightforwardly in the master equation, only the influx due to bond rupture is an unknown quantity.

For the different variants of the adhesion cluster model, steady state configuration and average lifetimes are studied in equilibrium and under shearing forces. At vanishing force, the steady state occupation numbers of all states are equal for clusters with and without unfolding, and with and without a reservoir connection. Because of the distribution of bond extensions, there are more bonds in the shearing geometry than for finite surface separations, which were discussed before, at otherwise identical parameters. In all systems, a constant sliding velocity  $v$  between the upper and lower surface is observed for positive forces,  $F > 0$ . The motion results from continuous cycles of binding at mostly low stretches, unfolding (if included), and rupture at high stretches. In equilibrium, i.e. at  $F = 0$ , there is no net motion, because each transition has the same probability as its reverse. The dependence of  $v$  and the fraction of bonds on the average force per bond is similar in all model variants. However, the state occupation numbers as functions of force differ strongly. For basic and extended model with a constant number of molecules, the numbers of bonds  $n_b$  and  $n_b + n_{b_u}$  decrease with force identically. In the basic model with a connection to the reservoir, the number of bonds and also the total number of adhesion molecules are reduced under load. Complete cluster dissociation is therefore observed already at low forces.

While the first three model variants show a qualitatively similar response to pulling and shearing forces, adhesion cluster models with unfolding and a reservoir connection behave fundamentally different under shear: the total number of molecules and the number of bonds increases with increasing forces. This reduces the sliding velocity, stabilizes the adhesion and enhances the average cluster lifetime. Notably, the average lifetime peaks at non-vanishing forces. Even though all individual molecules act as slip bonds, the cluster response resembles the rupture characteristics of a catch-slip mechanism. The counter-intuitive response to force results from an accumulation of unfolded molecules. Since the unbound, unfolded state is not in contact with the reservoir, the system finds a non-equilibrium steady state, in which the cycle  $a \rightarrow b \rightarrow b_u \rightarrow a_u \rightarrow a$  occurs more frequently than its reverse. The effect is amplified, when the unfolding and refolding rates of unbound molecules are set to zero. Even though the cycle in the single molecule transition diagram is opened, the unfolded states are strongly accumulated, because rupture dominates at high stretches, while the binding process is unaffected by force.

The discovered self-stabilization mechanism also occurs when unfolded, unbound molecules are equilibrated by a reservoir, as long as other states that are connected to the unfolded conformation can be shifted out of equilibrium. This is demonstrated for a

model variant that is motivated by talin R3 domain unfolding with subsequent vinculin binding. In this case, the linked states are accumulated and lead to an increasing number of bonds despite increasing forces.

## 6.4 Extension to arbitrary directions of force

The extension of the model to two dimensions is an important step towards a more realistic picture of adhesions. In the one-dimensional systems discussed before, all bonds are aligned in parallel with the force direction. Even though both focal adhesions and cadherin-based cell-cell adhesions show a well-organized structure [30, 174], the parallel alignment poses a strong restriction. In the case of pulling forces, it leads to a competition between folded and unfolded bonds. For a cluster under shear, the separation between the surfaces vanishes, although typically at least a small finite distance is bridged by an adhesion [2]. Additionally, the mechanical cues that are generated and perceived by cells are of different origins, so that a superposition of pulling and shearing can be expected.

For the two-dimensional adhesion cluster model, only the variant with unfolding and with a reservoir connection is considered. In this combination, the self-stabilization mechanism is discovered under pure shearing forces. In the one-dimensional model under pulling forces, two steady state configurations are found with either many folded or many unfolded bonds. In simulations with force angles  $\theta \in [0^\circ, 90^\circ]$  relative to the  $x$ -axis, a grouping into two regimes is observed.

For high force angles, i.e.  $\theta \geq 40^\circ$ , the separation between the surfaces allows molecule binding in a broad range of angles. As a consequence, the steady state separation is found close to the folded bond's rest length. While folded bonds are found within a small range of binding angles around  $\theta = 90^\circ$ , unfolded bonds exhibit a broad angular distribution. Hence, the competition between both conformations is lifted, and folded and unfolded bonds are present in steady state at the same time. However, under increasing load, the different bond directions are not energetically favourable, because force cannot be shared efficiently. The average number of bonds decreases or stays at a value close to the equilibrium case, even though the number of unbound molecules increases. The decrease is strongest for  $\theta = 90^\circ$ . For force angles  $\theta < 90^\circ$ , a constant sliding velocity in  $x$ -direction is observed. Until  $\theta = 40^\circ$ , the change of velocity with force increases with decreasing force angles. For all angles  $40^\circ \leq \theta \leq 90^\circ$ , average cluster lifetime decreases monotonously with force.

For low force angles, i.e.  $\theta \leq 30^\circ$ , the cluster behaviour resembles the one-dimensional system under shearing forces. For small finite forces, a constant surface separation close to the value  $\ell_0 \sin \theta$  is found in steady state. The bonds are aligned approximately in the same direction, so that they are under similar extensions. The average elastic energy per molecule as a function of force is lowest for  $\theta = 30^\circ$ . The sliding velocity is strongly reduced compared to the case  $\theta = 40^\circ$ . In this regime, the number of bonds increases with

increasing force. Also, the number of unbound molecules grows. The self-stabilization also affects the time until complete cluster dissociation. Under small forces, the average lifetime is higher for  $0 \leq \theta \leq 30^\circ$  than for larger force angles and it has its maximum at positive forces.

In summary, the self-stabilization mechanism is not only observed under pure shearing forces, but also up to a force angle of  $30^\circ$  with respect to the surface boundaries. Cycles of binding, unfolding and rupture drive the system out of equilibrium and lead to an on average constant sliding motion in direction of force. The constantly low surface separation and accumulation of unbound adhesion molecules allow frequent rebinding, so that in total the number of bonds grows, although more force acts on the cluster.

## 6.5 Outlook

Despite its simplicity, the presented adhesion cluster model shows strikingly different reactions to external pulling and shearing forces. In particular, the model demonstrates that a conformational change which is enhanced under load, and a variable number of molecules suffice as ingredients for a self-stabilization mechanism, if shearing forces are dominant. Nevertheless, the results also raise new questions and open several opportunities for further research.

To observe new generic features or to apply the model to a concrete system, many aspects of the model can be varied. One example that was already mentioned above concerns the mechanical response of individual single ligand-receptor bonds. Instead of a linear force response, a more complex polymer model could be applied. The force-extension curve of proteins under force is often fitted to or estimated by means of a worm-like chain interpolation formula, which includes persistence length and contour length of the molecule [11, 43, 64]. Alternatively, it would be interesting to study adhesion clusters with unfolding and linking with a different force response of bonds in the linked state. Since tensions of few pN have been measured for vinculin in focal adhesions [145], it is reasonable to assume that a linked bond, which represents the compound of talin with one or more bound vinculin molecules, carries more force than the single bond alone.

As another modification towards a more realistic adhesion model, the rigid surfaces could be replaced by elastic or viscoelastic media. In models similar to the basic cluster model with a constant number of molecules under pulling forces presented here, the effects of elastic substrates and viscoelastic cells have been studied already, compare e.g. Refs. [208, 263]. It was found that soft substrates tend to suppress rebinding while the viscoelastic properties of the cell have an enhancing effect on rebinding. In other models, a transducer is situated between the point of force application and the upper boundary of the cluster, which controls how force is shared among the bonds and thus represents an effective stiffness parameter [58, 112].

A final example concerns the force application. In the model presented here, a constant external force acts on the adhesion cluster. However, in many experiments, force ramps are applied to single molecules, cells, or tissues. Moreover, the force which acts on a cluster in cellular adhesions is naturally not a simple constant, but changes constantly due to the dynamics of the system. The loading rate has even been called the “master regulator” of cell dynamics and mechanotransduction [102]. Therefore it would be useful to know, how the results presented here change, when a force ramp is applied.

# References

- [1] M. Abercrombie, J. E. Heaysman, and S. M. Pegrum. “The locomotion of fibroblasts in culture. IV. Electron microscopy of the leading lamella”. In: *Exp. Cell Res.* 67.2 (1971), pp. 359–367.
- [2] B. Alberts et al. *Molecular Biology of the Cell*. Sixth Edition. New York: Garland Science, Taylor & Francis Group, 2015.
- [3] H. L. Anderson. “Metropolis, Monte Carlo, and the MANIAC”. in: *Los Alamos Science* Fall 1986 (1986), pp. 96–108.
- [4] Y. Aratyn-Schaus and M. L. Gardel. “Transient frictional slip between integrin and the ECM in focal adhesions under myosin II tension”. In: *Curr. Biol.* 20.13 (2010), pp. 1145–1153.
- [5] M. Assaf and B. Meerson. “Extinction of metastable stochastic populations”. In: *Phys. Rev. E* 81.2 (2010), p. 021116.
- [6] M. Assaf and B. Meerson. “WKB theory of large deviations in stochastic populations”. In: *J. Phys. A: Math. Theor.* 50.26 (2017).
- [7] R. D. Astumian. “Kinetic asymmetry allows macromolecular catalysts to drive an information ratchet”. In: *Nat. Commun.* 10.3837 (2019).
- [8] P. Atherton et al. “Vinculin controls talin engagement with the actomyosin machinery”. In: *Nat. Commun.* 6.10038 (2015).
- [9] P. Atherton et al. “Mechanosensitive components of integrin adhesions: Role of vinculin”. In: *Exp. Cell Res.* 343.1 (2016), pp. 21–27.
- [10] P. Atherton et al. *Force-independent interactions of talin and vinculin govern integrin-mediated mechanotransduction*. 2019. bioRxiv: <https://www.biorxiv.org/content/early/2019/05/07/629683.full.pdf>.
- [11] K. Austen et al. “Extracellular rigidity sensing by talin isoform-specific mechanical linkages”. In: *Nat. Cell Biol.* 17.12 (2015), pp. 1597–1606.
- [12] K. Autumn et al. “Frictional adhesion: A new angle on gecko attachment”. In: *J. Exp. Biol.* 209.18 (2006), pp. 3569–3579.

## REFERENCES

---

- [13] L. Bachelier. “Théorie de la spéculation”. In: *Annales scientifiques de l’École Normale Supérieure* Série 3, 17 (1900), pp. 21–86.
- [14] A. I. Bachir et al. “Integrin-associated complexes form hierarchically with variable stoichiometry in nascent adhesions”. In: *Curr. Biol.* 24.16 (2014), pp. 1845–1853.
- [15] N. Q. Balaban et al. “Force and focal adhesion assembly: A close relationship studied using elastic micropatterned substrates”. In: *Nat. Cell Biol.* 3.5 (2001), pp. 466–472.
- [16] C. Ballestrem et al. “Marching at the front and dragging behind: Differential  $\alpha V\beta 3$ -integrin turnover regulates focal adhesion behavior”. In: *J. Cell Biol.* 155.7 (2001), pp. 1319–1332.
- [17] S. Banerjee, M. L. Gardel, and U. S. Schwarz. “The Actin Cytoskeleton as an Active Adaptive Material”. In: *Annu. Rev. Condens. Matter Phys.* 11 (2020), pp. 421–439.
- [18] B. L. Bangasser and D. J. Odde. “Master equation-based analysis of a motor-clutch model for cell traction force”. In: *Cell. Mol. Bioeng.* 6.4 (2013), pp. 449–459.
- [19] B. L. Bangasser, S. S. Rosenfeld, and D. J. Odde. “Determinants of maximal force transmission in a motor-clutch model of cell traction in a compliant microenvironment”. In: *Biophys. J.* 105.3 (2013), pp. 581–592.
- [20] B. L. Bangasser et al. “Shifting the optimal stiffness for cell migration”. In: *Nat. Commun.* 8.15313 (2017).
- [21] W. J. P. Barnes, C. Oines, and J. M. Smith. “Whole animal measurements of shear and adhesive forces in adult tree frogs: Insights into underlying mechanisms of adhesion obtained from studying the effects of size and scale”. In: *J. Comp. Physiol. A Neuroethol. Sens. Neural. Behav. Physiol.* 192.11 (2006), pp. 1179–1191.
- [22] F. Basoli et al. “Biomechanical characterization at the cell scale: Present and prospects”. In: *Front. Physiol.* 9.1449 (2018).
- [23] M. D. Bass et al. “Further characterization of the interaction between the cytoskeletal proteins talin and vinculin”. In: *Biochem. J.* 362.3 (2002), pp. 761–768.
- [24] J. L. Bays and K. A. DeMali. “Vinculin in cell–cell and cell–matrix adhesions”. In: *Cell. Mol. Life Sci.* 74.16 (2017), pp. 2999–3009.
- [25] E. Bazellères et al. “Control of cell-cell forces and collective cell dynamics by the intercellular adhesome”. In: *Nat. Cell Biol.* 17.4 (2015), pp. 409–420.
- [26] Beentree. *Hedera helix root system, Bialowieza*. 2005. URL: [https://commons.wikimedia.org/wiki/File:Hedera\\_helix\\_1\\_beentree\\_bialowieza\\_2005.jpg](https://commons.wikimedia.org/wiki/File:Hedera_helix_1_beentree_bialowieza_2005.jpg) (visited on 09/13/2021).



- 
- [27] G. I. Bell. “Models for the Specific Adhesion of Cells to Cells”. In: *Science* 200.4342 (1978), pp. 618–627.
- [28] M. Bennett et al. “Molecular clutch drives cell response to surface viscosity”. In: *Proc. Natl. Acad. Sci. U.S.A.* 115.6 (2018), pp. 1192–1197.
- [29] C. Berne et al. “Bacterial adhesion at the single-cell level”. In: *Nat. Rev. Microbiol.* 16.10 (2018), pp. 616–627.
- [30] C. Bertocchi et al. “Nanoscale architecture of cadherin-based cell adhesions”. In: *Nat. Cell Biol.* 19.1 (2017), pp. 28–37.
- [31] A. Besser and S. A. Safran. “Force-induced adsorption and anisotropic growth of focal adhesions”. In: *Biophys. J.* 90.10 (2006), pp. 3469–3484.
- [32] T. Bihl, U. Seifert, and A. S. Smith. “Nucleation of ligand-receptor domains in membrane adhesion”. In: *Phys. Rev. Lett.* 109.25 (2012), p. 258101.
- [33] T. Bihl, U. Seifert, and A. S. Smith. “Multiscale approaches to protein-mediated interactions between membranes - Relating microscopic and macroscopic dynamics in radially growing adhesions”. In: *New J. Phys.* 17.8 (2015), p. 083016.
- [34] T. Bornschlöggl et al. “Filopodial retraction force is generated by cortical actin dynamics and controlled by reversible tethering at the tip”. In: *Proc. Natl. Acad. Sci. U.S.A.* 110.47 (2013), pp. 18928–18933.
- [35] A. B. Bortz, M. H. Kalos, and J. L. Lebowitz. “A new algorithm for Monte Carlo simulation of Ising spin systems”. In: *J. Comput. Phys.* 17.1 (1975), pp. 10–18.
- [36] A. Braeutigam et al. *A generic self-stabilization mechanism for biomolecular adhesions under load*. 2021. arXiv: 2107.03714 [physics.bio-ph].
- [37] J. Brasch et al. “Thinking outside the cell: How cadherins drive adhesion”. In: *Trends Cell Biol.* 22.6 (2012), pp. 299–310.
- [38] R. Brown. “A Brief Account of Microscopical Observations made in the Months of June, July and August 1827, on the Particles contained in the Pollen of Plants; and on the general Existence of Active Molecules in Organic and Onorganic Bodies”. In: *Edinburgh New Philos. J.* 5 (1828), pp. 358–371.
- [39] A. Brugués et al. “Forces driving epithelial wound healing”. In: *Nat. Phys.* 10.9 (2014), pp. 683–690.
- [40] K. Burridge and L. Connell. “A new protein of adhesion plaques and ruffling membranes.” In: *J. Cell Biol.* 97.2 (1983), pp. 359–367.
- [41] K. Burridge and J. R. Feramisco. “Microinjection and localization of a 130K protein in living fibroblasts: a relationship to actin and fibronectin”. In: *Cell* 19.3 (1980), pp. 587–595.

- [42] K. Burridge and P. Mangeat. “An interaction between vinculin and talin”. In: *Nature* 308.5961 (1984), pp. 744–746.
- [43] C. Bustamante et al. “Entropic Elasticity of X-Phage DNA Explicit and Implicit Learning and Maps of Cortical Motor Output”. In: *Science* 265.5178 (1994), pp. 1599–1600.
- [44] D. T. Butcher, T. Alliston, and V. M. Weaver. “A tense situation: forcing tumour progression”. In: *Nat. Rev. Cancer* 9.2 (2009), pp. 108–122.
- [45] R. S. Buxton and A. I. Magee. “Structure and interactions of desmosomal and other cadherins.” In: *Semin. Cell Biol.* 3.3 (1992), pp. 157–167.
- [46] D. Cai et al. “Mechanical feedback through E-cadherin promotes direction sensing during collective cell migration”. In: *Cell* 157.5 (2014), pp. 1146–1159.
- [47] D. A. Calderwood, I. D. Campbell, and D. R. Critchley. “Talins and kindlins: Partners in integrin-mediated adhesion”. In: *Nat. Rev. Mol. Cell Biol.* 14.8 (2013), pp. 503–517.
- [48] J. P. Califano and C. A. Reinhart-King. “Substrate stiffness and cell area predict cellular traction stresses in single cells and cells in contact”. In: *Cell. Mol. Bioeng.* 3.1 (2010), pp. 68–75.
- [49] O. Campàs et al. “Quantifying cell-generated mechanical forces within living embryonic tissues”. In: *Nat. Methods* 11.2 (2014), pp. 183–189.
- [50] I. D. Campbell and M. J. Humphries. “Integrin structure, activation, and interactions”. In: *Cold Spring Harb. Perspect. Biol.* 3.a004994 (2011).
- [51] H. Capella-Monsonís et al. “Battling adhesions: from understanding to prevention”. In: *BMC Biomedical Engineering* 1.5 (2019), pp. 1–12.
- [52] M. Capitanio and F. S. Pavone. “Interrogating biology with force: Single molecule high-resolution measurements with optical tweezers”. In: *Biophys. J.* 105.6 (2013), pp. 1293–1303.
- [53] A. Carisey et al. “Vinculin regulates the recruitment and release of core focal adhesion proteins in a force-dependent manner”. In: *Curr. Biol.* 23.4 (2013), pp. 271–281.
- [54] L. B. Case and C. M. Waterman. “Integration of actin dynamics and cell adhesion by a three-dimensional, mechanosensitive molecular clutch”. In: *Nat. Cell Biol.* 17.8 (2015), pp. 955–963.
- [55] L. B. Case et al. “Molecular mechanism of vinculin activation and nanoscale spatial organization in focal adhesions”. In: *Nat. Cell Biol.* 17.7 (2015), pp. 880–892.

- 
- [56] E. A. Cavalcanti-Adam et al. “Cell Spreading and Focal Adhesion Dynamics Are Regulated by Spacing of Integrin Ligands”. In: *Biophys. J.* 92.8 (2007), pp. 2964–2974.
- [57] C. Cerutti and A. J. Ridley. “Endothelial cell-cell adhesion and signaling”. In: *Exp. Cell Res.* 358.1 (2017), pp. 31–38.
- [58] C. E. Chan and D. J. Odde. “Traction dynamics of filopodia on compliant substrates”. In: *Science* 322.5908 (2008), pp. 1687–1691.
- [59] Y. C. Chang et al. “Structural and mechanistic insights into the recruitment of talin by RIAM in integrin signaling”. In: *Structure* 22.12 (2014), pp. 1810–1820.
- [60] R. Changede and M. Sheetz. “Integrin and cadherin clusters: A robust way to organize adhesions for cell mechanics”. In: *BioEssays* 39.1 (2017), p. 1600123.
- [61] R. Changede et al. “Nascent Integrin Adhesions Form on All Matrix Rigidities after Integrin Activation”. In: *Dev. Cell* 35.5 (2015), pp. 614–621.
- [62] A. Chatterjee and D. G. Vlachos. “An overview of spatial microscopic and accelerated kinetic Monte Carlo methods”. In: *J. Computer-Aided Mater. Des.* 14.2 (2007), pp. 253–308.
- [63] C. P. Chen et al. “Specificity of cell-cell adhesion by classical cadherins: Critical role for low-affinity dimerization through  $\beta$ -strand swapping”. In: *Proc. Natl. Acad. Sci. U.S.A.* 102.24 (2005), pp. 8531–8536.
- [64] H. Chen et al. “Dynamics of Equilibrium Folding and Unfolding Transitions of Titin Immunoglobulin Domain under Constant Forces”. In: *J. Am. Chem. Soc.* 137.10 (2015), pp. 3540–3546.
- [65] H. Chen, D. M. Choudhury, and S. W. Craig. “Coincidence of actin filaments and talin is required to activate vinculin”. In: *J. Biol. Chem.* 281.52 (2006), pp. 40389–40398.
- [66] W. Chen, J. Lou, and C. Zhu. “Forcing switch from short- to intermediate- and long-lived states of the  $\alpha A$  domain generates LFA-1/ICAM-1 catch bonds”. In: *J. Biol. Chem.* 285.46 (2010), pp. 35967–35978.
- [67] Y. Chen et al. “Orientation-specific responses to sustained uniaxial stretching in focal adhesion growth and turnover”. In: *Proc. Natl. Acad. Sci. U.S.A.* 110.26 (2013), E2352–E2361.
- [68] Y. Chen et al. “Force regulated conformational change of integrin  $\alpha V\beta 3$ ”. In: *Matrix Biol.* 60-61 (2017), pp. 70–85.
- [69] Y. Chen et al. “Receptor-mediated cell mechanosensing”. In: *Mol. Biol. Cell* 28.23 (2017), pp. 3134–3155.

## REFERENCES

---

- [70] S. E. Chesla, P. Selvaraj, and C. Zhu. “Measuring two-dimensional receptor-ligand binding kinetics by micropipette”. In: *Biophys. J.* 75.3 (1998), pp. 1553–1572.
- [71] L. S. L. Cheung et al. “Biophysics of Selectin-Ligand interactions in inflammation and cancer”. In: *Phys. Biol.* 8.1 (2011), p. 015013.
- [72] K. Chinthalapudi et al. “Lipid binding promotes oligomerization and focal adhesion activity of vinculin”. In: *J. Cell Biol.* 207.5 (2014), pp. 643–656.
- [73] C. K. Choi et al. “Actin and  $\alpha$ -actinin orchestrate the assembly and maturation of nascent adhesions in a myosin II motor-independent manner”. In: *Nat. Cell Biol.* 10.9 (2008), pp. 1039–1050.
- [74] D. Choquet, D. P. Felsenfeld, and M. P. Sheetz. “Extracellular matrix rigidity causes strengthening of integrin- cytoskeleton linkages”. In: *Cell* 88.1 (1997), pp. 39–48.
- [75] P. Chugh and E. K. Paluch. “The actin cortex at a glance”. In: *J. Cell Sci.* 131.14 (2018).
- [76] C. Ciobanasu, B. Faivre, and C. Le Clainche. “Actomyosin-dependent formation of the mechanosensitive talin-vinculin complex reinforces actin anchoring”. In: *Nat. Commun.* 5 (2014), p. 3095.
- [77] S. Citi. “The mechanobiology of tight junctions”. In: *Biophysical Reviews* 11.5 (2019), pp. 783–793.
- [78] D. Clements. *Foot of a Tokay Gecko, showing adhesive pads*. 2006. URL: [https://commons.wikimedia.org/wiki/File:Tokay\\_foot.jpg](https://commons.wikimedia.org/wiki/File:Tokay_foot.jpg) (visited on 09/13/2021).
- [79] D. M. Cohen et al. “Two distinct head-tail interfaces cooperate to suppress activation of vinculin by talin”. In: *J. Biol. Chem.* 280.17 (2005), pp. 17109–17117.
- [80] C. Collins and W. J. Nelson. “Running with neighbors: Coordinating cell migration and cell-cell adhesion”. In: *Curr. Opin. Cell Biol.* 36 (2015), pp. 62–70.
- [81] J. R. Conway and G. Jacquemet. “Cell matrix adhesion in cell migration”. In: *Essays Biochem.* 63.5 (2019), pp. 535–551.
- [82] C. Cozens-Roberts, D. A. Lauffenburger, and J. A. Quinn. “Receptor-mediated cell attachment and detachment kinetics. I. Probabilistic model and analysis”. In: *Biophys. J.* 58.4 (1990), pp. 841–856.
- [83] E. M. Craig et al. “Model for adhesion clutch explains biphasic relationship between actin flow and traction at the cell leading edge”. In: *Phys. Biol.* 12.3 (2015), p. 035002.
- [84] A. S. Curtis. “The Mechanism of Adhesion of Cells to Glass. A Study by Interference Reflection Microscopy.” In: *J. Cell Biol.* 20 (1964), pp. 199–215.

- 
- [85] G. Danuser, J. Allard, and A. Mogilner. “Mathematical modeling of eukaryotic cell migration: insights beyond experiments”. In: *Annu. Rev. Cell Dev. Biol.* 29 (2013), pp. 501–528.
- [86] R. De. “A general model of focal adhesion orientation dynamics in response to static and cyclic stretch”. In: *Commun. Biol.* 1.81 (2018).
- [87] M. De Odroważ Piramowicz et al. “Dynamic force measurements of avidin-biotin and streptavidin-biotin interactions using AFM”. in: *Acta Biochim. Pol.* 53.1 (2006), pp. 93–100.
- [88] C. De Pascalis and S. Etienne-Manneville. “Single and collective cell migration: The mechanics of adhesions”. In: *Mol. Biol. Cell* 28.14 (2017), pp. 1833–1846.
- [89] E. Delva, D. K. Tucker, and A. P. Kowalczyk. “The desmosome.” In: *Cold Spring Harb. Perspect. Biol.* 1.a002543 (2009).
- [90] M. Dembo et al. “The reaction-limited kinetics of membrane-to-surface adhesion and detachment”. In: *Proc. Royal Soc. B* 234.1274 (1988), pp. 55–83.
- [91] J.-H. Dirks and W. Federle. “Fluid-based adhesion in insects – principles and challenges”. In: *Soft Matter* 7 (2011), pp. 11047–11053.
- [92] D. E. Discher, P. Janmey, and Y. L. Wang. “Tissue cells feel and respond to the stiffness of their substrate”. In: *Science* 310.5751 (2005), pp. 1139–1143.
- [93] P. Drechsler and W. Federle. “Biomechanics of smooth adhesive pads in insects: influence of tarsal secretion on attachment performance”. In: *J. Comp. Physiol. A Neuroethol. Sens. Neural. Behav. Physiol.* 192 (2006), pp. 1213–1222.
- [94] F. Drees et al. “ $\alpha$ -catenin is a molecular switch that binds E-cadherin- $\beta$ -catenin and regulates actin-filament assembly”. In: *Cell* 123.5 (2005), pp. 903–915.
- [95] C. C. Dufort, M. J. Paszek, and V. M. Weaver. “Balancing forces: Architectural control of mechanotransduction”. In: *Nat. Rev. Mol. Cell Biol.* 12.5 (2011), pp. 308–319.
- [96] Y. F. Duf r ne and A. E. Pelling. “Force nanoscopy of cell mechanics and cell adhesion”. In: *Nanoscale* 5.10 (2013), pp. 4094–4104.
- [97] D. W. Dumbauld et al. “How vinculin regulates force transmission”. In: *Proc. Natl. Acad. Sci. U.S.A.* 110.24 (2013), pp. 9788–9793.
- [98] S. Dupont et al. “Role of YAP/TAZ in mechanotransduction”. In: *Nature* 474.7350 (2011), pp. 179–184.
- [99] A. J. Ehrlicher et al. “Mechanical strain in actin networks regulates FilGAP and integrin binding to filamin A”. in: *Nature* 478.7368 (2011), pp. 260–263.

## REFERENCES

---

- [100] A. Einstein. “Über die von der molekularkinetischen Theorie der Wärme geforderte Bewegung von in ruhenden Flüssigkeiten suspendierten Teilchen”. In: *Ann. Phys. (Berl.)* 322.8 (1905), pp. 549–560.
- [101] V. Elgart and A. Kamenev. “Rare event statistics in reaction-diffusion systems”. In: *Phys. Rev. E* 70.4 (2004), p. 041106.
- [102] A. Elosegui-Artola, X. Trepata, and P. Roca-Cusachs. “Control of Mechanotransduction by Molecular Clutch Dynamics”. In: *Trends Cell Biol.* 28.5 (2018), pp. 356–367.
- [103] A. Elosegui-Artola et al. “Rigidity sensing and adaptation through regulation of integrin types”. In: *Nat. Mater.* 13.6 (2014), pp. 631–637.
- [104] A. Elosegui-Artola et al. “Mechanical regulation of a molecular clutch defines force transmission and transduction in response to matrix rigidity”. In: *Nat. Cell Biol.* 18.5 (2016), pp. 540–548.
- [105] J. T. Emerman and D. R. Pitelka. “Maintenance and induction of morphological differentiation in dissociated mammary epithelium on floating collagen membranes”. In: *In Vitro* 13.5 (1977), pp. 316–328.
- [106] A. J. Engler et al. “Matrix Elasticity Directs Stem Cell Lineage Specification”. In: *Cell* 126.4 (2006), pp. 677–689.
- [107] P. Érdi and G. Lente. *Stochastic Chemical Kinetics - Theory and (Mostly) Systems Biological Applications*. Berlin, Heidelberg: Springer, 2014.
- [108] T. Erdmann and U. S. Schwarz. “Stability of Adhesion Clusters under Constant Force”. In: *Phys. Rev. Lett.* 92.10 (2004), p. 108102.
- [109] T. Erdmann and U. S. Schwarz. “Impact of receptor-ligand distance on adhesion cluster stability”. In: *Eur. Phys. J. E* 22.2 (2007), pp. 123–137.
- [110] T. Erdmann. “Stochastic dynamics of adhesion clusters under force”. PhD thesis. Potsdam: Universität Potsdam, 2005.
- [111] T. Erdmann and U. S. Schwarz. “Stochastic dynamics of adhesion clusters under shared constant force and with rebinding”. In: *J. Chem. Phys.* 121.18 (2004), pp. 8997–9017.
- [112] T. Erdmann and U. S. Schwarz. “Bistability of cell-matrix adhesions resulting from nonlinear receptor-ligand dynamics”. In: *Biophys. J.* 91.6 (2006), pp. 60–62.
- [113] J. Escribano, M. T. Sánchez, and J. M. García-Aznar. “A discrete approach for modeling cell-matrix adhesions”. In: *Computational Particle Mechanics* 1.2 (2014), pp. 117–130.

- [114] E. Evans. “Energy landscapes of biomolecular adhesion and receptor anchoring at interfaces explored with dynamic force spectroscopy.” In: *Faraday Discuss.* 111 (1998), pp. 1–16.
- [115] E. Evans and F. Ludwig. “Dynamic strengths of molecular anchoring and material cohesion in fluid biomembranes”. In: *J. Phys. Condens. Matter* 12 (2000), A315.
- [116] E. Evans and K. Ritchie. “Dynamic strength of molecular adhesion bonds”. In: *Biophys. J.* 72 (1997), pp. 1541–1555.
- [117] J. Eyckmans et al. “A Hitchhiker’s Guide to Mechanobiology”. In: *Dev. Cell* 21.1 (2011), pp. 35–47.
- [118] H. Eyring. “The activated complex in chemical reactions”. In: *J. Chem. Phys.* 3.2 (1935), pp. 63–71.
- [119] P. M. Favi et al. “Inspiration from the natural world: From bio-adhesives to bio-inspired adhesives”. In: *J. Adhes. Sci. Technol.* 28.3-4 (2014), pp. 290–319.
- [120] W. Federle et al. “An Integrative Study of Insect Adhesion: Mechanics and Wet Adhesion of Pretarsal Pads in Ants”. In: *Integr. Comp. Biol.* 42 (2002), pp. 1100–1106.
- [121] S. F. Fenz et al. “Membrane fluctuations mediate lateral interaction between cadherin bonds”. In: *Nat. Phys.* 13.9 (2017), pp. 906–913.
- [122] A. D. Fokker. *Over Brown’sche Bewegingen in het Stralingsveld, en Waarschijnlijkheids-Beschouwingen in de Stralingstheorie*. Haarlem: J. Enschedé en zonen, 1913.
- [123] C. G. Gahmberg et al. “Regulation of cell adhesion: a collaborative effort of integrins, their ligands, cytoplasmic actors, and phosphorylation”. In: *Q. Rev. Biophys.* 52.e10 (2019), pp. 1–24.
- [124] C. G. Galbraith, K. M. Yamada, and M. P. Sheetz. “The relationship between force and focal complex development”. In: *J. Cell Biol.* 159.4 (2002), pp. 695–705.
- [125] M. L. Gardel et al. “Traction stress in focal adhesions correlates biphasically with actin retrograde flow speed”. In: *J. Cell Biol.* 183.6 (2008), pp. 999–1005.
- [126] M. L. Gardel et al. “Mechanical integration of actin and adhesion dynamics in cell migration”. In: *Annu. Rev. Cell Dev. Biol.* 26 (2010), pp. 315–333.
- [127] C. Gardiner. *Stochastic Methods - A Handbook for the Natural and Social Sciences*. Fourth Edition. Wiesbaden: Springer Berlin Heidelberg, 2010.
- [128] T. R. Garrett, M. Bhakoo, and Z. Zhang. “Bacterial adhesion and biofilms on surfaces”. In: *Prog. Nat. Sci.* 18.9 (2008), pp. 1049–1056.

## REFERENCES

---

- [129] N. C. Gauthier and P. Roca-Cusachs. “Mechanosensing at integrin-mediated cell–matrix adhesions: from molecular to integrated mechanisms”. In: *Curr. Opin. Cell Biol.* 50 (2018), pp. 20–26.
- [130] B. Geiger. “A 130K Protein from Chicken Gizzard: Its Localization at the Termini of Microfilament Bundles in Cultured Chicken Cells”. In: *Cell* 18.1 (1979), pp. 193–205.
- [131] B. Geiger, J. P. Spatz, and A. D. Bershadsky. “Environmental sensing through focal adhesions”. In: *Nat. Rev. Mol. Cell Bio.* 10.1 (2009), pp. 21–33.
- [132] B. Geiger et al. “Transmembrane crosstalk between the extracellular matrix and the cytoskeleton”. In: *Nat. Rev. Mol. Cell Biol.* 2.11 (2002), pp. 793–805.
- [133] A. K. Geim et al. “Microfabricated adhesive mimicking gecko foot-hair”. In: *Nat. Mater.* 2.7 (2003), pp. 461–463.
- [134] P. G. de Gennes and S. Edwards. *Soft Interfaces: The 1994 Dirac Memorial Lecture*. Cambridge University Press, 1997.
- [135] S. Ghassemi et al. “Cells test substrate rigidity by local contractions on submicrometer pillars”. In: *Proc. Natl. Acad. Sci. U.S.A.* 109.14 (2012), pp. 5328–5333.
- [136] G. Giannone and M. P. Sheetz. “Substrate rigidity and force define form through tyrosine phosphatase and kinase pathways”. In: *Trends Cell Biol.* 16.4 (2006), pp. 213–223.
- [137] D. T. Gillespie. “A general method for numerically simulating the stochastic time evolution of coupled chemical reactions”. In: *J. Comput. Phys.* 22.4 (1976), pp. 403–434.
- [138] D. T. Gillespie. “Exact stochastic simulation of coupled chemical reactions”. In: *J. Phys. Chem.* 81.25 (1977), pp. 2340–2361.
- [139] D. T. Gillespie. “Stochastic simulation of chemical kinetics”. In: *Annu. Rev. Phys. Chem.* 58 (2007), pp. 35–55.
- [140] A. R. Gingras et al. “Structural determinants of integrin binding to the talin rod”. In: *J. Biol. Chem.* 284.13 (2009), pp. 8866–8876.
- [141] V. Gkretsi and T. Stylianopoulos. “Cell adhesion and matrix stiffness: Coordinating cancer cell invasion and metastasis”. In: *Front. Oncol.* 8.145 (2018).
- [142] B. T. Goult et al. “RIAM and vinculin binding to talin are mutually exclusive and regulate adhesion assembly and turnover”. In: *J. Biol. Chem.* 288.12 (2013), pp. 8238–8249.
- [143] B. T. Goult, J. Yan, and M. A. Schwartz. “Talin as a mechanosensitive signaling hub”. In: *J. Cell Biol.* 217.11 (2018), pp. 3776–3784.



- 
- [144] B. T. Goult et al. “Structural studies on full-length talin1 reveal a compact auto-inhibited dimer: Implications for talin activation”. In: *J. Struct. Biol.* 184.1 (2013), pp. 21–32.
- [145] C. Grashoff et al. “Measuring mechanical tension across vinculin reveals regulation of focal adhesion dynamics”. In: *Nature* 466.7303 (2010), pp. 263–266.
- [146] M. Gupta et al. “Single cell rigidity sensing: A complex relationship between focal adhesion dynamics and large-scale actin cytoskeleton remodeling”. In: *Cell Adhesion and Migration* 10.5 (2016), pp. 554–567.
- [147] S. L. Gupton and C. M. Waterman-Storer. “Spatiotemporal feedback between actomyosin and focal-adhesion systems optimizes rapid cell migration”. In: *Cell* 125.7 (2006), pp. 1361–1374.
- [148] A. W. M. Haining et al. “All Subdomains of the Talin Rod Are Mechanically Vulnerable and May Contribute to Cellular Mechanosensing”. In: *ACS Nano* 10.7 (2016), pp. 6648–6658.
- [149] A. Hamadi et al. “Regulation of focal adhesion dynamics and disassembly by phosphorylation of FAK at tyrosine 397”. In: *J. Cell Sci.* 118.19 (2005), pp. 4415–4425.
- [150] D. A. Hammer and D. A. Lauffenburger. “A dynamical model for receptor-mediated cell adhesion to surfaces in viscous shear flow”. In: *Biophys. J.* 52 (1987), pp. 475–487.
- [151] S. J. Han et al. “Traction microscopy to identify force modulation in subresolution adhesions”. In: *Nat. Methods* 12.7 (2015), pp. 653–656.
- [152] S. J. Han et al. “Pre-complexation of talin and vinculin without tension is required for efficient nascent adhesion maturation”. In: *eLife* 10.e66151 (2021).
- [153] A. K. Harris, P. Wild, and D. Stopak. “Silicone rubber substrata: A new wrinkle in the study of cell locomotion”. In: *Science* 208.4440 (1980), pp. 177–179.
- [154] W. K. Hastings. “Monte carlo sampling methods using Markov chains and their applications”. In: *Biometrika* 57.1 (1970), pp. 97–109.
- [155] C.-P. Heisenberg and Y. Bellaïche. “Forces in tissue morphogenesis and patterning”. In: *Cell* 153.5 (2013), pp. 948–962.
- [156] H. Hirata et al. “Force-dependent vinculin binding to talin in live cells: a crucial step in anchoring the actin cytoskeleton to focal adhesions”. In: *Am. J. Physiol. Cell Physiol.* 306.6 (2014), pp. C607–C620.
- [157] R. M. Hochmuth. “Micropipette aspiration of living cells”. In: *J. Biomech.* 33.1 (2000), pp. 15–22.

## REFERENCES

---

- [158] C. N. Holenstein, U. Silvan, and J. G. Snedeker. “High-resolution traction force microscopy on small focal adhesions – Improved accuracy through optimal marker distribution and optical flow tracking”. In: *Sci. Rep.* 7.41633 (2017).
- [159] E. R. Horton et al. “Definition of a consensus integrin adhesome and its dynamics during adhesion complex assembly and disassembly”. In: *Nat. Cell Biol.* 17.12 (2015), pp. 1577–1587.
- [160] E. R. Horton et al. “The integrin adhesome network at a glance”. In: *J. Cell Sci.* 129.22 (2016), pp. 4159–4163.
- [161] D. L. Huang et al. “Vinculin forms a directionally asymmetric catch bond with F-actin”. In: *Science* 357.6352 (2017), pp. 703–706.
- [162] J. Huang et al. “Influence of substrate rigidity on primary nucleation of cell adhesion: A thermal fluctuation model”. In: *J. Colloid Interface Sci.* 366.1 (2012), pp. 200–208.
- [163] Y. Huang et al. “Traction force microscopy with optimized regularization and automated Bayesian parameter selection for comparing cells”. In: *Sci. Rep.* 9.539 (2019).
- [164] J. D. Humphries, A. Byron, and M. J. Humphries. “Integrin ligands at a glance”. In: *J. Cell Sci.* 119.19 (2006), pp. 3901–3903.
- [165] J. D. Humphries et al. “Vinculin controls focal adhesion formation by direct interactions with talin and actin”. In: *J. Cell Biol.* 179.5 (2007), pp. 1043–1057.
- [166] A. Huttenlocher and A. R. Horwitz. “Integrins in cell migration”. In: *Cold Spring Harb. Perspect. Biol.* 3.a005074 (2011).
- [167] R. O. Hynes. “The emergence of integrins: A personal and historical perspective”. In: *Matrix Biol.* 23.6 (2004), pp. 333–340.
- [168] O. C. Ibe. *Elements of Random Walk and Diffusion Processes*. New York: John Wiley & Sons, 2013.
- [169] B. Jagannathan and S. Marqusee. “Protein folding and unfolding under force”. In: *Biopolymers* 99.11 (2013), pp. 860–869.
- [170] K. A. Jansen et al. “A guide to mechanobiology: Where biology and physics meet”. In: *Biochim. Biophys. Acta Mol. Cell Res.* 1853.11 (2015), pp. 3043–3052.
- [171] G. Jiang et al. “Two-piconewton slip bond between fibronectin and the cytoskeleton depends on talin”. In: *Nature* 424.6946 (2003), pp. 334–337.
- [172] A. Kamenev and B. Meerson. “Extinction of an infectious disease: A large fluctuation in a nonequilibrium system”. In: *Phys. Rev. E* 77.6 (2008), pp. 5–8.

- 
- [173] N. G. V. Kampen. *Stochastic processes in physics and chemistry*. Third Edition. North-Holland Personal Library. Elsevier, 2007.
- [174] P. Kanchanawong et al. “Nanoscale architecture of integrin-based cell adhesions”. In: *Nature* 468.7323 (2010), pp. 580–584.
- [175] S. Kasas, P. Stupar, and G. Dietler. “AFM contribution to unveil pro- and eukaryotic cell mechanical properties”. In: *Seminars in Cell and Developmental Biology* 73 (2018), pp. 177–187.
- [176] J. Z. Kechagia, J. Ivaska, and P. Roca-Cusachs. “Integrins as biomechanical sensors of the microenvironment”. In: *Nat. Rev. Mol. Cell Biol.* 20.8 (2019), pp. 457–473.
- [177] F. P. Kelly. *Reversibility and Stochastic Networks*. John Wiley & Sons, 1979.
- [178] B. Klapholz and N. H. Brown. “Talin - The master of integrin adhesions”. In: *J. Cell Sci.* 130.15 (2017), pp. 2435–2446.
- [179] C. Kluger et al. “Different Vinculin Binding Sites Use the Same Mechanism to Regulate Directional Force Transduction”. In: *Biophys. J.* 118.6 (2020), pp. 1344–1356.
- [180] D. Kong, B. Ji, and L. Dai. “Stability of adhesion clusters and cell reorientation under lateral cyclic tension”. In: *Biophys. J.* 95.8 (2008), pp. 4034–4044.
- [181] F. Kong et al. “Demonstration of catch bonds between an integrin and its ligand”. In: *J. Cell Biol.* 185.7 (2009), pp. 1275–1284.
- [182] F. Kong et al. “Cyclic mechanical reinforcement of integrin-ligand interactions”. In: *Mol. Cell* 49.6 (2013), pp. 1060–1068.
- [183] H. A. Kramers. “Brownian motion in a field of force and the diffusion model of chemical reactions”. In: *Physica* 7.4 (1940), pp. 284–304.
- [184] A. Kumar et al. “Talin tension sensor reveals novel features of focal adhesion force transmission and mechanosensitivity”. In: *J. Cell Biol.* 213.3 (2016), pp. 371–383.
- [185] A. Kumar et al. “Local Tension on Talin in Focal Adhesions Correlates with F-Actin Alignment at the Nanometer Scale”. In: *Biophys. J.* 115.8 (2018), pp. 1569–1579.
- [186] B. Ladoux and R. M. Mège. “Mechanobiology of collective cell behaviours”. In: *Nat. Rev. Mol. Cell Biol.* 18.12 (2017), pp. 743–757.
- [187] B. Ladoux and A. Nicolas. “Physically based principles of cell adhesion mechanosensitivity in tissues”. In: *Rep. Prog. Phys.* 75.11 (2012).
- [188] P. Langevin. “Sur la théorie du mouvement brownien”. In: *C. R. Acad. Sci. (Paris)* 146 (1908), pp. 530–533.

## REFERENCES

---

- [189] Q. Le Duc et al. “Vinculin potentiates E-cadherin mechanosensing and is recruited to actin-anchored sites within adherens junctions in a myosin II-dependent manner”. In: *J. Cell Biol.* 189.7 (2010), pp. 1107–1115.
- [190] P. Lecca. “Stochastic chemical kinetics: A review of the modelling and simulation approaches”. In: *Biophys. Rev.* 5.4 (2013), pp. 323–345.
- [191] D. Leckband and J. de Rooij. “Cadherin Adhesion and Mechanotransduction”. In: *Annu. Rev. Cell Dev. Biol.* 30.1 (2014), pp. 291–315.
- [192] D. Leckband and S. Sivasankar. “Cadherin recognition and adhesion”. In: *Curr. Opin. Cell Biol.* 24.5 (2012), pp. 620–627.
- [193] T. Lecuit and P. F. Lenne. “Cell surface mechanics and the control of cell shape, tissue patterns and morphogenesis”. In: *Nat. Rev. Mol. Cell Biol.* 8.8 (2007), pp. 633–644.
- [194] T. Lecuit, P. F. Lenne, and E. Munro. “Force generation, transmission, and integration during cell and tissue morphogenesis”. In: *Annu. Rev. Cell Dev. Biol.* 27 (2011), pp. 157–184.
- [195] S. E. Lee, R. D. Kamm, and M. R. Mofrad. “Force-induced activation of talin and its possible role in focal adhesion mechanotransduction”. In: *J. Biomech.* 40.9 (2007), pp. 2096–2106.
- [196] J. M. Leerberg et al. “Tension-sensitive actin assembly supports contractility at the epithelial zonula adherens”. In: *Curr. Biol.* 24.15 (2014), pp. 1689–1699.
- [197] W. R. Legant et al. “Measurement of mechanical tractions exerted by cells in three-dimensional matrices”. In: *Nat. Methods* 7.12 (2010), pp. 969–971.
- [198] M. Leiss et al. “The role of integrin binding sites in fibronectin matrix assembly in vivo”. In: *Curr. Opin. Cell Biol.* 20.5 (2008), pp. 502–507.
- [199] T. P. Lele et al. “Investigating complexity of protein-protein interactions in focal adhesions”. In: *Biochem. Biophys. Res. Commun.* 369.3 (2008), pp. 929–934.
- [200] G. Lente. *Deterministic Kinetics in Chemistry and Systems Biology - The Dynamics of Complex Reaction Networks*. Berlin, Heidelberg: Springer, 2015.
- [201] M. Leoni and P. Sens. “Model of cell crawling controlled by mechanosensitive adhesion”. In: *Phys. Rev. Lett.* 118.22 (2017), p. 228101.
- [202] K. Ley. “The role of selectins in inflammation and disease”. In: *Trends Mol. Med.* 9.6 (2003), pp. 263–268.
- [203] D. Li and B. Ji. “Predicted Rupture Force of a Single Molecular Bond Becomes Rate Independent at Ultralow Loading Rates”. In: *Phys. Rev. Lett.* 112.7 (2014), p. 078302.

- 
- [204] J. Li and T. A. Springer. “Integrin extension enables ultrasensitive regulation by cytoskeletal force”. In: *Proc. Natl. Acad. Sci. U.S.A.* 114.18 (2017), pp. 4685–4690.
- [205] J. Li and T. A. Springer. “Energy landscape differences among integrins establish the framework for understanding activation”. In: *J. Cell Biol.* 217.1 (2018), pp. 397–412.
- [206] J. Li et al. “Conformational equilibria and intrinsic affinities define integrin activation”. In: *EMBO J.* 36.5 (2017), pp. 629–645.
- [207] J. Li et al. “Insights into adhesion of abalone: A mechanical approach”. In: *J. Mech. Behav. Biomed. Mater.* 77.September 2017 (2018), pp. 331–336.
- [208] L. Li, W. Zhang, and J. Wang. “A viscoelastic–stochastic model of the effects of cytoskeleton remodelling on cell adhesion”. In: *Royal Soc. Open Sci.* 3.10 (2016), p. 160539.
- [209] P. T. X. Li et al. “Probing the Mechanical Folding Kinetics of TAR RNA by Hopping, Force-Jump, and Force-Ramp Methods”. In: *Biophys. J.* 90.January (2006), pp. 250–260.
- [210] Y. Li, P. Bhimalapuram, and A. R. Dinner. “Model for how retrograde actin flow regulates adhesion traction stresses”. In: *J. Phys. Condens. Matter* 22.19 (2010).
- [211] Z. Li, H. Lee, and C. Zhu. “Molecular mechanisms of mechanotransduction in integrin-mediated cell-matrix adhesion”. In: *Exp. Cell Res.* 349.1 (2016), pp. 85–94.
- [212] S. Linder and P. Kopp. “Podosomes at a glance”. In: *J. Cell Sci.* 118.10 (2005), pp. 2079–2082.
- [213] J. Liu et al. “Talin determines the nanoscale architecture of focal adhesions”. In: *Proc. Natl. Acad. Sci. U.S.A.* 112.35 (2015), E4864–E4873.
- [214] C. M. Lo et al. “Cell movement is guided by the rigidity of the substrate”. In: *Biophys. J.* 79.1 (2000), pp. 144–152.
- [215] Y. S. Lo and T. Beebe. “Loading-rate dependence of individual ligand-receptor bond-rupture forces studied by atomic force microscopy”. In: *Langmuir* 17.12 (2001), pp. 3741–3748.
- [216] J. Lou and C. Zhu. “A Structure-Based Sliding-Rebinding Mechanism for Catch Bonds”. In: *Biophys. J.* 92.5 (2007), pp. 1471–1485.
- [217] J. L. Maître et al. “Adhesion functions in cell sorting by mechanically coupling the cortices of adhering cells”. In: *Science* 338.6104 (2012), pp. 253–256.
- [218] K. Manibog et al. “Resolving the molecular mechanism of cadherin catch bond formation”. In: *Nat. Commun.* 5.3941 (2014).

## REFERENCES

---

- [219] K. Manibog et al. “Molecular determinants of cadherin ideal bond formation: Conformation-dependent unbinding on a multidimensional landscape”. In: *Proc. Natl. Acad. Sci. U.S.A.* 113.39 (2016), E5711–E5720.
- [220] F. Margadant et al. “Mechanotransduction in vivo by repeated talin stretch-relaxation events depends upon vinculin”. In: *PLoS Biol.* 9.12 (2011).
- [221] B. T. Marshall et al. “Direct observation of catch bonds involving cell-adhesion molecules”. In: *Nature* 423.6936 (2003), pp. 190–193.
- [222] S. J. Marshall et al. “A review of adhesion science”. In: *Dent. Mater.* 26 (2010), pp. 11–16.
- [223] S. Massou et al. “Cell stretching is amplified by active actin remodelling to deform and recruit proteins in mechanosensitive structures”. In: *Nat. Cell Biol.* 22.8 (2020), pp. 1011–1023.
- [224] MBInfo. *How are actin filaments distributed in cells and tissues?* n.d. URL: <https://www.mechanobio.info/cytoskeleton-dynamics/what-is-the-cytoskeleton/what-are-actin-filaments/how-are-actin-filaments-distributed-in-cells-and-tissues/> (visited on 09/16/2021).
- [225] MBInfo. *How is cadherin recruited to the adherens junction?* n.d. URL: <https://www.mechanobio.info/what-is-mechanotransduction/what-are-cell-cell-adhesions/what-are-adherens-junctions/how-is-cadherin-recruited-to-the-adherens-junction/> (visited on 09/16/2021).
- [226] MBInfo. *How is integrin activated?* n.d. URL: <https://www.mechanobio.info/what-is-mechanotransduction/what-is-the-extracellular-matrix-and-the-basal-lamina/what-is-integrin/how-is-integrin-activated/> (visited on 09/13/2021).
- [227] MBInfo. *What are mature focal adhesions composed of?* n.d. URL: <https://www.mechanobio.info/what-is-mechanotransduction/what-is-the-extracellular-matrix-and-the-basal-lamina/what-are-focal-adhesions/what-are-mature-focal-adhesions-composed-of/> (visited on 09/16/2021).
- [228] MBInfo. *What is cadherin?* n.d. URL: <https://www.mechanobio.info/what-is-mechanotransduction/what-are-cell-cell-adhesions/what-are-adherens-junctions/what-is-cadherin/> (visited on 09/16/2021).
- [229] MBInfo. *What is the Cytoskeleton?* n.d. URL: <https://www.mechanobio.info/cytoskeleton-dynamics/what-is-the-cytoskeleton/> (visited on 09/13/2021).
- [230] MBInfo. *What mechanisms drive invadopodia extension?* n.d. URL: <https://www.mechanobio.info/cytoskeleton-dynamics/what-are-invadopodia/what-mechanisms-drive-invadopodia-extension/> (visited on 09/16/2021).

- 
- [231] R. P. McEver and C. Zhu. “Rolling Cell Adhesion”. In: *Annu. Rev. Cell Dev. Biol.* 26.1 (2010), pp. 363–396.
- [232] P. McMillen and S. A. Holley. “Integration of cell-cell and cell-ECM adhesion in vertebrate morphogenesis”. In: *Curr. Opin. Cell Biol.* 36 (2015), pp. 48–53.
- [233] D. A. McQuarrie. “Kinetics of small systems. I”. in: *J. Chem. Phys.* 38.2 (1963), pp. 433–436.
- [234] R. Merkel et al. “Energy landscapes of receptor-ligand bonds explored with dynamic force spectroscopy”. In: *Nature* 397.6714 (1999), pp. 50–53.
- [235] R. Merkel. “Force spectroscopy on single passive biomolecules and single biomolecular bonds”. In: *Phys. Rep.* 346.5 (2001), pp. 343–385.
- [236] N. Metropolis and S. Ulam. “The Monte Carlo Method”. In: *J. Am. Stat. Assoc.* 44.247 (1949), pp. 335–341.
- [237] N. Metropolis et al. “Equation of state calculations by fast computing machines”. In: *J. Chem. Phys.* 21.6 (1953), pp. 1087–1092.
- [238] T. Mitchison and M. Kirschner. “Cytoskeletal dynamics and nerve growth”. In: *Neuron* 1.9 (1988), pp. 761–772.
- [239] L. Molony et al. “Properties of talin from chicken gizzard smooth muscle.” In: *J. Biol. Chem.* 262.16 (1987), pp. 7790–7795.
- [240] S. W. Moore, P. Roca-Cusachs, and M. P. Sheetz. “Stretchy proteins on stretchy substrates: The important elements of integrin-mediated rigidity sensing”. In: *Dev. Cell* 19.2 (2010), pp. 194–206.
- [241] P. Moreno-Layseca et al. “Integrin trafficking in cells and tissues”. In: *Nat. Cell Biol.* 21.2 (2019), pp. 122–132.
- [242] V. A. Morikis and S. I. Simon. “Neutrophil mechanosignaling promotes integrin engagement with endothelial cells and motility within inflamed vessels”. In: *Front. Immunol.* 9.2774 (2018).
- [243] M. Morimatsu et al. “Molecular tension sensors measure forces generated by single integrin molecules in living cells”. In: *Nano Lett.* 13.9 (2013), pp. 3985–3989.
- [244] D. A. Murphy and S. A. Courtneidge. “The ‘ins’ and ‘outs’ of podosomes and invadopodia: Characteristics, formation and function”. In: *Nat. Rev. Mol. Cell Biol.* 12.7 (2011), pp. 413–426.
- [245] K. C. Neuman and A. Nagy. “Single-molecule force spectroscopy: Optical tweezers, magnetic tweezers and atomic force microscopy”. In: *Nat. Methods* 5.6 (2008), pp. 491–505.

## REFERENCES

---

- [246] A. Nicolas, A. Besser, and S. A. Safran. “Dynamics of cellular focal adhesions on deformable substrates: Consequences for cell force microscopy”. In: *Biophys. J.* 95.2 (2008), pp. 527–539.
- [247] A. Nicolas, B. Geiger, and S. A. Safran. “Cell mechanosensitivity controls the anisotropy of focal adhesions”. In: *Proc. Natl. Acad. Sci. U.S.A.* 101.34 (2004), pp. 12520–12525.
- [248] P. H. Niewiarowski, A. Y. Stark, and A. Dhinojwala. “Sticking to the story: Outstanding challenges in gecko-inspired adhesives”. In: *J. Exp. Biol.* 219.7 (2016), pp. 912–919.
- [249] P. W. Oakes et al. “Tension is required but not sufficient for focal adhesion maturation without a stress fiber template”. In: *J. Cell Biol.* 196.3 (2012), pp. 363–374.
- [250] L. Onsager. “Reciprocal Relations in Irreversible Processes I”. in: *Phys. Rev.* 37.405 (1931), pp. 183–196.
- [251] R. Oria et al. “Force loading explains spatial sensing of ligands by cells”. In: *Nature* 552.7684 (2017), pp. 219–224.
- [252] O. Ovaskainen and B. Meerson. “Stochastic models of population extinction”. In: *Trends Ecol. Evol.* 25.11 (2010), pp. 643–652.
- [253] E. K. Paluch et al. “Mechanotransduction: Use the force(s)”. In: *BMC Biol.* 13.47 (2015).
- [254] J. T. Parsons, A. R. Horwitz, and M. A. Schwartz. “Cell adhesion: Integrating cytoskeletal dynamics and cellular tension”. In: *Nat. Rev. Mol. Cell Biol.* 11.9 (2010), pp. 633–643.
- [255] A. M. Pasapera et al. “Myosin II activity regulates vinculin recruitment to focal adhesions through FAK-mediated paxillin phosphorylation”. In: *J. Cell Biol.* 188.6 (2010), pp. 877–890.
- [256] R. J. J. Pelham and Y.-L. Wang. “Cell locomotion and focal adhesions are regulated by substrate flexibility”. In: *Proc. Natl. Acad. Sci. U.S.A.* 94 (1997), pp. 13661–13665.
- [257] X. Peng et al. “Vinculin regulates cell-surface E-cadherin expression by binding to  $\beta$ -catenin”. In: *J. Cell Sci.* 123.4 (2010), pp. 567–577.
- [258] Y. V. Pereverzev et al. “The Two-Pathway Model for the Catch-Slip Transition in Biological Adhesion”. In: *Biophys. J.* 89.3 (2005), pp. 1446–1454.
- [259] D. Pinheiro and Y. Bellaïche. “Mechanical Force-Driven Adherens Junction Remodeling and Epithelial Dynamics”. In: *Dev. Cell* 47.1 (2018), pp. 3–19.



- [260] M. Planck. “Über einen Satz der statistischen Dynamik und seine Erweiterung in der Quantentheorie”. In: *Sitzungsberichte der Königlich Preussischen Akademie der Wissenschaften zu Berlin* Jan-Dec 1917 (1917), pp. 324–341.
- [261] S. V. Plotnikov et al. “Force fluctuations within focal adhesions mediate ECM-rigidity sensing to guide directed cell migration”. In: *Cell* 151.7 (2012), pp. 1513–1527.
- [262] W. J. Polacheck and C. S. Chen. “Measuring cell-generated forces: A guide to the available tools”. In: *Nat. Methods* 13.5 (2016), pp. 415–423.
- [263] J. Qian and H. Gao. “Soft matrices suppress cooperative behaviors among receptor-ligand bonds in cell adhesion”. In: *PLoS ONE* 5.8 (2010).
- [264] J. Qian, J. Wang, and H. Gao. “Lifetime and strength of adhesive molecular bond clusters between elastic media”. In: *Langmuir* 24.4 (2008), pp. 1262–1270.
- [265] J. Qian et al. “Lifetime and strength of periodic bond clusters between elastic media under inclined loading”. In: *Biophys. J.* 97.9 (2009), pp. 2438–2445.
- [266] R. Rahikainen et al. “Mechanical stability of talin rod controls cell migration and substrate sensing”. In: *Sci. Rep.* 7.3571 (2017).
- [267] S. Rakshit et al. “Ideal, catch, and slip bonds in cadherin adhesion”. In: *Proc. Natl. Acad. Sci. U.S.A.* 109.46 (2012), pp. 18815–18820.
- [268] S. Ray, H. P. Foote, and T. Lechler. “ $\beta$ -Catenin protects the epidermis from mechanical stresses”. In: *J. Cell Biol.* 202.1 (2013), pp. 45–52.
- [269] E. Reister-Gottfried et al. “Dynamics of specific vesicle-substrate adhesion: From local events to global dynamics”. In: *Phys. Rev. Lett.* 101.20 (2008), p. 208103.
- [270] P. Ringer et al. “Multiplexing molecular tension sensors reveals piconewton force gradient across talin-1”. In: *Nat. Methods* 14.11 (2017), pp. 1090–1096.
- [271] A. del Rio et al. “Stretching Single Talin Rod”. In: *Science* 323.5914 (2009), pp. 638–641.
- [272] D. Riveline et al. “Focal contacts as mechanosensors: Externally applied local mechanical force induces growth of focal contacts by an mDia1-dependent and ROCK-independent mechanism”. In: *J. Cell Biol.* 153.6 (2001), pp. 1175–1185.
- [273] P. Roca-Cusachs, V. Conte, and X. Trepap. “Quantifying forces in cell biology”. In: *Nat. Cell Biol.* 19.7 (2017), pp. 742–751.
- [274] P. Roca-Cusachs, T. Iskratsch, and M. P. Sheetz. “Finding the weakest link – exploring integrin-mediated mechanical molecular pathways”. In: *J. Cell Sci.* 125.13 (2012), pp. 3025–3038.

- [275] P. Roca-Cusachs et al. “Integrin-dependent force transmission to the extracellular matrix by  $\alpha$ -actinin triggers adhesion maturation”. In: *Proc. Natl. Acad. Sci. U.S.A.* 110.15 (2013).
- [276] O. Rossier et al. “Integrins  $\beta_1$  and  $\beta_3$  exhibit distinct dynamic nanoscale organizations inside focal adhesions”. In: *Nat. Cell Biol.* 14.10 (2012), pp. 1057–1067.
- [277] B. Sabass and U. S. Schwarz. “Modeling cytoskeletal flow over adhesion sites: Competition between stochastic bond dynamics and intracellular relaxation”. In: *J. Phys. Condens. Matter* 22.19 (2010), p. 194112.
- [278] B. Sabass and H. A. Stone. “Role of the Membrane for Mechanosensing by Tethered Channels”. In: *Phys. Rev. Lett.* 116.25 (2016), p. 258101.
- [279] J. J. Sakurai and J. Napolitano. *Modern Quantum Mechanics*. 3rd ed. Cambridge University Press, 2020.
- [280] B. R. Sarangi et al. “Coordination between intra- and extracellular forces regulates focal adhesion dynamics”. In: *Nano Lett.* 17.1 (2017), pp. 399–406.
- [281] Y. Sawada et al. “Force Sensing by Mechanical Extension of the Src Family Kinase Substrate p130Cas”. In: *Cell* 127.5 (2006), pp. 1015–1026.
- [282] H. B. Schiller and R. Fässler. “Mechanosensitivity and compositional dynamics of cell-matrix adhesions”. In: *EMBO Rep.* 14.6 (2013), pp. 509–519.
- [283] I. Schoen, B. L. Pruitt, and V. Vogel. “The Yin-Yang of Rigidity Sensing: How Forces and Mechanical Properties Regulate the Cellular Response to Materials”. In: *Annu. Rev. Mater. Res.* 43.1 (2013), pp. 589–618.
- [284] P. Schuster. *Stochasticity in Processes - Fundamentals and Applications to Chemistry and Biology*. Berlin, Heidelberg: Springer, 2016.
- [285] M. Schwartzman et al. “Nanolithographic control of the spatial organization of cellular adhesion receptors at the single-molecule level”. In: *Nano Lett.* 11.3 (2011), pp. 1306–1312.
- [286] S. C. Schwager, P. V. Taufalele, and C. A. Reinhart-King. “Cell–cell mechanical communication in cancer”. In: *Cell. Mol. Bioeng.* 12.1 (2019), pp. 1–14.
- [287] M. A. Schwartz. “Integrins and extracellular matrix in mechanotransduction”. In: 2.a005066 (2012), pp. 1–9.
- [288] U. S. Schwarz, T. Erdmann, and I. B. Bischofs. “Focal adhesions as mechanosensors: The two-spring model”. In: *BioSystems* 83 (2006), pp. 225–232.
- [289] U. S. Schwarz and M. L. Gardel. “United we stand - Integrating the actin cytoskeleton and cell-matrix adhesions in cellular mechanotransduction”. In: *J. Cell Sci.* 125.13 (2012), pp. 3051–3060.

- 
- [290] U. S. Schwarz and S. A. Safran. “Physics of adherent cells”. In: *Rev. Mod. Phys.* 85.3 (2013), pp. 1327–1381.
- [291] U. S. Schwarz and J. R. Soiné. “Traction force microscopy on soft elastic substrates: A guide to recent computational advances”. In: *Biochim. Biophys. Acta* 1853.11 (2015), pp. 3095–3104.
- [292] U. Seifert. “Rupture of Multiple Parallel Molecular Bonds under Dynamic Loading”. In: *Phys. Rev. Lett.* 84.12 (2000), pp. 2750–2753.
- [293] C. Selhuber-Unkel et al. “Cell adhesion strength is controlled by intermolecular spacing of adhesion receptors”. In: *Biophys. J.* 98.4 (2010), pp. 543–551.
- [294] C. Selhuber-Unkel et al. “Cooperativity in adhesion cluster formation during initial cell adhesion”. In: *Biophys. J.* 95.11 (2008), pp. 5424–5431.
- [295] P. Sens. “Stick–slip model for actin-driven cell protrusions, cell polarization, and crawling”. In: *Proc. Natl. Acad. Sci. U.S.A.* 117.40 (2020), pp. 24670–24678.
- [296] F. Serwane et al. “In vivo quantification of spatially varying mechanical properties in developing tissues”. In: *Nat. Methods* 14.2 (2017), pp. 181–186.
- [297] L. Shapiro and W. I. Weis. “Structure and biochemistry of cadherins and catenins.” In: *Cold Spring Harb. Perspect. Biol.* 1.a003053 (2009).
- [298] S. J. Shattil, C. Kim, and M. H. Ginsberg. “The final steps of integrin activation: The end game”. In: *Nat. Rev. Mol. Cell Biol.* 11.4 (2010), pp. 288–300.
- [299] F. Sheikh et al. “ $\alpha$ -E-catenin inactivation disrupts the cardiomyocyte adherens junction, resulting in cardiomyopathy and susceptibility to wall rupture”. In: *Circulation* 114.10 (2006), pp. 1046–1055.
- [300] T. Shemesh et al. “Focal adhesions as mechanosensors: A physical mechanism”. In: *Proc. Natl. Acad. Sci. U.S.A.* 102.35 (2005), pp. 12383–12388.
- [301] H. G. Silverman and F. F. Roberto. “Understanding marine mussel adhesion”. In: *Mar. Biotechnol.* 9.6 (2007), pp. 661–681.
- [302] M. von Smoluchowski. “Zur kinetischen Theorie der Brownschen Molekularbewegung und der Suspensionen”. In: *Annalen der Physik* 326.14 (1906), pp. 756–780.
- [303] J. Stricker et al. “Myosin II-Mediated Focal Adhesion Maturation Is Tension Insensitive”. In: *PLoS ONE* 8.7 (2013).
- [304] N. Strohmeyer et al. “Fibronectin-bound  $\alpha 5 \beta 1$  integrins sense load and signal to reinforce adhesion in less than a second”. In: *Nat. Mater.* 16.12 (2017), pp. 1262–1270.

## REFERENCES

---

- [305] B. Stutchbury et al. “Distinct focal adhesion protein modules control different aspects of mechanotransduction”. In: *J. Cell Sci.* 130.9 (2017), pp. 1612–1624.
- [306] R. W. Style et al. “Traction force microscopy in physics and biology”. In: *Soft Matter* 10.23 (2014), pp. 4047–4055.
- [307] Y. Su et al. “Relating conformation to function in integrin  $\alpha_5\beta_1$ ”. In: *Proc. Natl. Acad. Sci. U.S.A.* 113.27 (2016), E3872–E3881.
- [308] K. Sugimura, P. F. Lenne, and F. Graner. “Measuring forces and stresses in situ in living tissues”. In: *Development* 143.2 (2016), pp. 186–196.
- [309] T. Sulchek, R. W. Friddle, and A. Noy. “Strength of multiple parallel biological bonds”. In: *Biophys. J.* 90.12 (2006), pp. 4686–4691.
- [310] L. Sun et al. “Molecular Simulations Suggest a Force-Dependent Mechanism of Vinculin Activation”. In: *Biophys. J.* 113.8 (2017), pp. 1697–1710.
- [311] Z. Sun, M. Costell, and R. Fässler. “Integrin activation by talin, kindlin and mechanical forces”. In: *Nat. Cell Biol.* 21.1 (2019), pp. 25–31.
- [312] Z. Sun et al. “Kank2 activates talin, reduces force transduction across integrins and induces central adhesion formation”. In: *Nat. Cell Biol.* 18.9 (2016), pp. 941–953.
- [313] R. Sunyer et al. “Collective cell durotaxis emerges from long-range intercellular force transmission”. In: *Science* 353.6304 (2016), pp. 1157–1161.
- [314] Takeichi Masatoshi. “The cadherins: Cell-cell adhesion molecules controlling animal morphogenesis”. In: *Development* 102.4 (1988), pp. 639–655.
- [315] M. Tamada, M. P. Sheetz, and Y. Sawada. “Activation of a signaling cascade by cytoskeleton stretch”. In: *Dev. Cell* 7.5 (2004), pp. 709–718.
- [316] J. W. Tamkun et al. “Structure of integrin, a glycoprotein involved in the transmembrane linkage between fibronectin and actin”. In: *Cell* 46.2 (1986), pp. 271–282.
- [317] J. L. Tan et al. “Cells lying on a bed of microneedles: An approach to isolate mechanical force”. In: *Proc. Natl. Acad. Sci. U.S.A.* 100.4 (2003), pp. 1484–1489.
- [318] N. Taneja et al. “Focal adhesions control cleavage furrow shape and spindle tilt during mitosis”. In: *Sci. Rep.* 6.29846 (2016).
- [319] N. Taneja et al. “The balance between adhesion and contraction during cell division”. In: *Curr. Opin. Cell Biol.* 56.Figure 1 (2019), pp. 45–52.
- [320] R. Tapia-Rojo, A. Alonso-Caballero, and J. M. Fernandez. “Direct observation of a coil-to-helix contraction triggered by vinculin binding to talin”. In: *Sci. Adv.* 6.21 (2020), eaaz4707.

- 
- [321] R. Tapia-Rojo, Á. Alonso-Caballero, and J. M. Fernández. “Talin folding as the tuning fork of cellular mechanotransduction”. In: *Proc. Natl. Acad. Sci. U.S.A.* 117.35 (2020), pp. 21346–21353.
- [322] D. F. Tees, J. T. Woodward, and D. A. Hammer. “Reliability theory for receptor-ligand bond dissociation”. In: *J. Chem. Phys.* 114.17 (2001), pp. 7483–7496.
- [323] T. N. Thiele. *Sur la compensation de quelques erreurs quasi-systématiques par la méthode des moindres carrés*. Copenhagen: C. A. Reitzel, 1880.
- [324] J. P. Thiery et al. “Epithelial-Mesenchymal Transitions in Development and Disease”. In: *Cell* 139.5 (2009), pp. 871–890.
- [325] I. Thievensen et al. “Vinculin-actin interaction couples actin retrograde flow to focal adhesions, but is dispensable for focal adhesion growth”. In: *J. Cell Biol.* 202.1 (2013), pp. 163–177.
- [326] W. Thomas et al. “Catch-bond model derived from allostery explains force-activated bacterial adhesion”. In: *Biophys. J.* 90.3 (2006), pp. 753–764.
- [327] W. E. Thomas. “Mechanochemistry of receptor-ligand bonds”. In: *Curr. Opin. Struct. Biol.* 19 (2009), pp. 50–55.
- [328] W. A. Thomas et al. “ $\alpha$ -Catenin and vinculin cooperate to promote high E-cadherin-based adhesion strength”. In: *J. Biol. Chem.* 288.7 (2013), pp. 4957–4969.
- [329] H. A. Thomason et al. “Desmosomes: Adhesive strength and signalling in health and disease”. In: *Biochem. J.* 429.3 (2010), pp. 419–433.
- [330] S. Tiwari et al. “Divalent cations regulate the folding and activation status of integrins during their intracellular trafficking”. In: *J. Cell Sci.* 124.10 (2011), pp. 1672–1680.
- [331] L. Trichet et al. “Evidence of a large-scale mechanosensing mechanism for cellular adaptation to substrate stiffness”. In: *Proc. Natl. Acad. Sci. U.S.A.* 109.18 (2012), pp. 6933–6938.
- [332] C. G. Vasquez and A. C. Martin. “Force transmission in epithelial tissues”. In: *Dev. Dyn.* 245.3 (2016), pp. 361–371.
- [333] M. Vicente-Manzanares and A. R. Horwitz. “Adhesion dynamics at a glance”. In: *J. Cell Sci.* 124.23 (2011), pp. 3923–3927.
- [334] M. Vicente-Manzanares et al. “Segregation and activation of myosin IIB creates a rear in migrating cells”. In: *J. Cell Biol.* 183.3 (2008), pp. 543–554.
- [335] V. Vogel and M. Sheetz. “Local force and geometry sensing regulate cell functions”. In: *Nat. Rev. Mol. Cell Biol.* 7.4 (2006), pp. 265–275.

## REFERENCES

---

- [336] G. Walko, M. J. Castañón, and G. Wiche. “Molecular architecture and function of the hemidesmosome”. In: *Cell Tissue Res.* 360.2 (2015), pp. 363–378.
- [337] N. Wang. “Review of cellular mechanotransduction”. In: *J. Phys. D: Appl. Phys.* 50.23 (2017), p. 233002.
- [338] X. Wang and T. Ha. “Defining Single Molecular Forces Required to Activate Integrin and Notch Signaling”. In: *Science* 340.6135 (2013), pp. 991–994.
- [339] Y. Wang, J. Yan, and B. T. Goult. “Force-Dependent Binding Constants”. In: *Biochemistry* 58 (2019), pp. 4696–4709.
- [340] G. N. Wheeler et al. “Desmosomal glycoproteins I, II and III: Novel members of the cadherin superfamily”. In: *Biochem. Soc. Trans.* 19.4 (1991), pp. 1060–1064.
- [341] E. B. Wilson. *The Cell in Development and Heredity*. 3rd Edition with corrections. New York: MacMillan, 1925.
- [342] S. E. Winograd-Katz et al. “The integrin adhesome: From genes and proteins to human disease”. In: *Nat. Rev. Mol. Cell Biol.* 15.4 (2014), pp. 273–288.
- [343] C. Wolgemuth. “Does cell biology need physicists?” In: *Physics* 4.4 (2011).
- [344] S. Yamada et al. “Deconstructing the cadherin-catenin-actin complex”. In: *Cell* 123.5 (2005), pp. 889–901.
- [345] M. Yao et al. “Force-dependent conformational switch of  $\alpha$ -catenin controls vinculin binding”. In: *Nat. Commun.* 5 (2014).
- [346] M. Yao et al. “Mechanical activation of vinculin binding to talin locks talin in an unfolded conformation”. In: *Sci. Rep.* 4.4610 (2014).
- [347] M. Yao et al. “The mechanical response of talin”. In: *Nat. Commun.* 7.11966 (2016).
- [348] A. S. Yap, G. A. Gomez, and R. G. Parton. “Adherens Junctions Revisualized: Organizing Cadherins as Nanoassemblies”. In: *Dev. Cell* 35.1 (2015), pp. 12–20.
- [349] F. Ye et al. “Recreation of the terminal events in physiological integrin activation”. In: *J. Cell Biol.* 188.1 (2010), pp. 157–173.
- [350] T. Yeung et al. “Effects of substrate stiffness on cell morphology, cytoskeletal structure, and adhesion”. In: *Cell Motil. Cytoskel.* 60.1 (2005), pp. 24–34.
- [351] S. Yonemura et al. “ $\alpha$ -Catenin as a tension transducer that induces adherens junction development”. In: *Nat. Cell Biol.* 12.6 (2010), pp. 533–542.
- [352] C. Yoshida and M. Takeichi. “Teratocarcinoma cell adhesion: Identification of a cell-surface protein involved in calcium-dependent cell aggregation”. In: *Cell* 28.2 (1982), pp. 217–224.

- 
- [353] C. Yoshida-Noro, N. Suzuki, and M. Takeichi. “Molecular nature of the calcium-dependent cell-cell adhesion system in mouse teratocarcinoma and embryonic cells studied with a monoclonal antibody”. In: *Dev. Biol.* 101.1 (1984), pp. 19–27.
- [354] T. Young. “An Essay on the Cohesion of Fluids”. In: *Philos. Trans. R. Soc.* 95 (1805), pp. 65–87.
- [355] W. M. Young and E. W. Elcock. “Monte Carlo studies of vacancy migration in binary ordered alloys: I”. in: *Proc. Phys. Soc.* 89.3 (1966), pp. 735–746.
- [356] B. Yurdumakan et al. “Synthetic gecko foot-hairs from multiwalled carbon nanotubes”. In: *Chem. Commun.* 30 (2005), pp. 3799–3801.
- [357] R. Zaidel-Bar. “Cadherin adhesome at a glance”. In: *J. Cell Sci.* 126.2 (2013), pp. 373–378.
- [358] R. Zaidel-Bar and B. Geiger. “The switchable integrin adhesome”. In: *J. Cell Sci.* 123.9 (2010), pp. 1385–1388.
- [359] R. Zaidel-Bar et al. “Functional Atlas of the integrin adhesome”. In: *Nat. Cell Biol.* 9.8 (2007), pp. 858–867.
- [360] E. Zamir et al. “Dynamics and segregation of cell-matrix adhesions in cultured fibroblasts”. In: *Nat. Cell Biol.* 2.4 (2000), pp. 191–196.
- [361] H. Zhang et al. “A tension-induced mechanotransduction pathway promotes epithelial morphogenesis”. In: *Nature* 471.7336 (2011), pp. 99–103.
- [362] M. Zhang et al. “Lotus effect in wetting and self-cleaning”. In: *Biotribology* 5 (2016), pp. 31–43.
- [363] X. Zhang et al. “Talin depletion reveals independence of initial cell spreading from integrin activation and traction”. In: *Nat. Cell Biol.* 10.9 (2008), pp. 1062–1068.
- [364] Y. Zhao et al. “Bio-inspired reversible underwater adhesive”. In: *Nat. Commun.* 8.2218 (2017).
- [365] C. Zhu. “Kinetics and mechanics of cell adhesion”. In: *J. Biomech.* 33.1 (2000), pp. 23–33.
- [366] W. H. Ziegler, R. C. Liddington, and D. R. Critchley. “The structure and regulation of vinculin”. In: *Trends Cell Biol.* 16.9 (2006), pp. 453–460.
- [367] P. Zilber, N. R. Smith, and B. Meerson. “Giant disparity and a dynamical phase transition in large deviations of the time-averaged size of stochastic populations”. In: *Phys. Rev. E* 99.5 (2019), p. 52105.
- [368] B. Zimmerman, T. Volberg, and B. Geiger. “Early molecular events in the assembly of the focal adhesion-stress fiber complex during fibroblast spreading”. In: *Cell Motil. Cytoskel.* 58.3 (2004), pp. 143–159.

## REFERENCES

---

- [369] T. Zulueta-Coarasa and R. Fernandez-Gonzalez. “Laser ablation to investigate cell and tissue mechanics in vivo”. In: *Integrative Mechanobiology – Micro- and Nano-Techniques in Cell Mechanobiology*. Ed. by Y. Sun, D.-H. Kim, and C. A. Simmons. Cambridge: Cambridge University Press, 2015. Chap. 8, pp. 128–147.
- [370] R. Zwanzig. “Simple model of protein folding kinetics”. In: *Proc. Natl. Acad. Sci. U.S.A.* 92.21 (1995), pp. 9801–9804.



# Appendix A

## Mathematical background: Stochastic processes and applications

This chapter starts with basic concepts from the mathematical field of stochastic processes. Special focus lies on the class of Markov processes, which are of great importance for various fields in natural sciences. A Markov process with a discrete state space is often characterized by a Master equation, a differential form of the Chapman-Kolmogorov equation. It intuitively describes the time evolution of the system using a balance of in- and outgoing fluxes. For a continuous state space, which is a common feature of processes including drift and diffusion, the Fokker-Planck Equation serves as a useful approximation of the dynamics.

The second part of the chapter introduces an important application for stochastic processes: modeling the kinetic behavior of chemical reaction systems. A stochastic approach provides an appropriate method to represent the chemical kinetics of small or fluctuation dominated systems, because the deterministic rate equation cannot account for the discrete nature of the reactants. For this purpose, the system parameters, i.e. the deterministic rate constants, need to be converted to their stochastic counterpart. The central equation for a discrete state space is called chemical master equation. As it often cannot be solved analytically, computational methods are frequently employed. The Gillespie algorithm offers two rejection-free methods to generate statistically correct samples of the system. It is used to simulate trajectories of the presented adhesion cluster models.

## A.1 Stochastic processes

Stochasticity are elementary features of nature. A groundbreaking discovery towards this insight was made in 1828 by Brown who observed an erratic motion of pollen particles in liquid under a microscope [38]. The first mathematical models that could describe Brown's observations were developed by Thiele in 1880 and by Bachelier in 1900, but they actually discuss a least squares method and the stock market in Paris, respectively [13, 323]. Finally, Einstein published an explanation in 1905 which is often considered as the starting point of stochastic modeling [100, 284]. One year later, Smoluchowski independently published similar results [302]. Motion of the pollen is caused by frequent collisions with liquid molecules that move in a complicated and irregular manner. Einstein treated the collisions as probabilistic events and derived the diffusion equation for the effective behavior of the grains. A few years after Einstein, Langevin presented an alternative model, in which random forces are added to an otherwise deterministic equation of motion [188]. The transport equation for diffusive motion was later developed by Fokker and generalized by Planck [122, 260]. Since then, the mathematical field of stochastic processes has expanded strongly and its importance for understanding experimental observations and designing theoretical models was increasingly appreciated. In this section, a brief introduction to some features and examples of stochastic processes is given. The topics covered here provide a basis for the theoretical model introduced in chapter 3. The standard works of van Kampen [173] and Gardiner [127] give a comprehensive description.

### A.1.1 Definition

A stochastic process  $S_X(t)$  describes the time evolution of a random variable  $X$ . A realization of the process is a trajectory  $x(t)$ . Both the state space  $X$  and the time span  $t$  can be discrete or continuous. For discrete state space and discrete time span, the trajectory or sample path is given by the measurement pairs  $(x_1, t_1; x_2, t_2; \dots; x_n, t_n)$  that are determined by a set of joint probability distribution functions (pdf)  $p_n(x_1, t_1; x_2, t_2; \dots; x_n, t_n)$  with  $n \in \mathbb{N}$ . Alternatively, the system is determined by a hierarchy of conditional pdf  $p_{1|n-1}(x_n, t_n | x_{n-1}, t_{n-1}; \dots; x_1, t_1)$ . They describe the probability, that measurement  $n$  yields  $(x_n, t_n)$ , given that  $n - 1$  previous measurements resulted in  $(x_1, t_1; \dots; x_{n-1}, t_{n-1})$ . Both sets are connected via

$$p_n(x_1, t_1; \dots; x_n, t_n) = p_{1|n-1}(x_n, t_n | x_{n-1}, t_{n-1}; \dots; x_1, t_1) p_{n-1}(x_1, t_1; \dots; x_{n-1}, t_{n-1}). \quad (\text{A.1})$$

A stochastic process is called stationary if the corresponding set of pdf do not change under a time shift  $\tau$ . Consequently, the moments are not effected by a time shift either.

### A.1.2 Markov processes

An important subclass for the fields of physics are so-called Markov processes. The conditional pdf  $p_{1|n-1}$  of a Markov process fulfills the Markov property

$$p_{1|n-1}(x_n, t_n | x_{n-1}, t_{n-1}; \dots; x_1, t_1) = p_{1|1}(x_n, t_n | x_{n-1}, t_{n-1}) \quad (\text{A.2})$$

for arbitrary  $n$  and  $t_1 < t_2 < \dots < t_n$ . Therefore the current state  $(x_n, t_n)$  of a Markov process only depends on its preceding state  $(x_{n-1}, t_{n-1})$ . The process has no memory of earlier values. The whole set of pdf can be constructed from  $p_1(x_1, t_1)$  and the transition probability  $p_{1|1}(x_2, t_2 | x_1, t_1)$  with successive application of (A.1). For example, the function  $p_3(x_1, t_1; x_2, t_2; x_3, t_3)$  is obtained via

$$\begin{aligned} p_3(x_1, t_1; x_2, t_2; x_3, t_3) &= p_{1|2}(x_3, t_3 | x_2, t_2; x_1, t_1) p_2(x_1, t_1; x_2, t_2) \\ &= p_{1|1}(x_3, t_3 | x_2, t_2) p_{1|1}(x_2, t_2 | x_1, t_1) p_1(x_1, t_1). \end{aligned} \quad (\text{A.3})$$

From this, the Chapman-Kolmogorov equation can be derived. For a continuous state space and  $t_1 < t_2 < t_3$  it is given by

$$p_{1|1}(x_3, t_3 | x_1, t_1) = \int p_{1|1}(x_3, t_3 | x_2, t_2) p_{1|1}(x_2, t_2 | x_1, t_1) dx_2. \quad (\text{A.4})$$

The Chapman-Kolmogorov equation and the relation

$$p_1(x_2, t_2) = \int p_{1|1}(x_2, t_2 | x_1, t_1) p_1(x_1, t_1) dx_1 \quad (\text{A.5})$$

need to be fulfilled by  $p_1$  and  $p_{1|1}$  to define a Markov process.

One famous example for a Markov process is the Wiener process. The Wiener process is continuous in time with independent increments, i.e. the differences  $S_X(t_2) - S_X(t_1), \dots, S_X(t_n) - S_X(t_{n-1})$  are independent for all  $t_n > t_{n-1} > \dots > t_2 > t_1$ . The transition probability from  $(x_1, t_1)$  to  $(x_2, t_2)$  is given by a Gaussian distribution with mean  $x_2 - x_1$  and variance  $(t_2 - t_1)^2$ . The initial condition is  $p_1(x_1, t_1 = 0) = \delta(x_1)$ . Thus, the Wiener process is non-stationary, but as the transition probability depends only on the time-difference  $t_2 - t_1$ , it is called (time-)homogeneous. The trajectories originally describe the position of a one dimensional Brownian particle. This is the basis for a broad range of applications from diffusion models over stochastic calculus to financial markets [168]. It is also closely related to the random walk in discrete state space.

A Markov chain is a time-homogeneous Markov process with a discrete state space and discrete time span. When the state space is finite with  $n$  states, the initial pdf can be written as a vector  $\mathbf{p}(t = 0)$  with  $n$  nonnegative entries and the transition probability as a stochastic  $n \times n$  matrix  $\mathbf{T}$ . Since the matrix  $\mathbf{T}$  does not depend on time, the pdf after  $k$  timesteps can be obtained via

$$\mathbf{p}(t = k) = \mathbf{T}^k \mathbf{p}(t = 0). \quad (\text{A.6})$$

Markov chains can be extended to a continuous time span. One important example for a continuous time Markov chain is the Poisson process. The Poisson process counts the occurrences  $n_2$  of a certain event until time  $t_2$  given that  $n_1 < n_2$  events were counted at time  $t_1 < t_2$ . The defining functions are

$$p_{1|1}(n_1 + n, t_1 + \tau | n_1, t_1) = \frac{(r\tau)^n}{n!} \exp(-r\tau) , \quad (\text{A.7})$$

$$p_1(n_1, t_1) = \frac{(rt_1)^{n_1}}{n_1!} \exp(-rt_1) , \quad (\text{A.8})$$

with  $n = n_2 - n_1$  and the waiting time  $\tau = t_2 - t_1$ . The pdf  $p_1(n_1, t_1)$  describes a Poisson distribution with parameter  $rt_1$ . Thus, the mean and variance grow linearly with time and rate  $r$ . The rate  $r$  gives the average number of events per time. The waiting time between two consecutive events is exponentially distributed with parameter  $r$ . A superposition of independent Poisson processes with rates  $r_1$  and  $r_2$  results in a Poisson process with rate  $r_1 + r_2$ . The Poisson process finds numerous applications where successive independent events are modeled, e.g. particle emission, radioactive decay, arrival of customers, emails or phone calls, occurrence of device failures or catastrophes.

### A.1.3 Master equation

For many systems the master equation offers a more convenient version of the probabilistic time evolution for time-homogeneous Markov processes. It is derived from the Chapman-Kolmogorov equation in the limit of small time differences  $\tau$  [173]. For a continuous state space, the master equation for the pdf  $p(x, t)$  is given by

$$\frac{\partial}{\partial t} p(x, t) = \int \left[ w(x|x', t) p(x', t) - w(x'|x, t) p(x, t) \right] dx' \quad (\text{A.9})$$

with the transition probability per unit time to go from  $x_1$  to  $x_2 \neq x_1$

$$w(x_2|x_1, t_1) = \frac{\partial}{\partial \tau} p(x_2, t_1 + \tau | x_1, t_1) \Big|_{\tau=0} . \quad (\text{A.10})$$

In case of a discrete state space with  $n$  possible states the integral is replaced by a sum,

$$\frac{\partial}{\partial t} p_n(t) = \sum_{n'} \left[ w_{nn'} p_{n'}(t) - w_{n'n} p_n(t) \right] , \quad (\text{A.11})$$

and the transition probabilities are elements of a  $n \times n$  matrix  $W$ . In both cases, the master equation describes the time evolution of the probability density as the balance of gains and losses. All fluxes into  $p(x, t)$  or  $p_n$  from any other state are accounted for with a positive sign, while all possible fluxes out of the current state are subtracted.

The class of continuous time and discrete space Markov processes in which jumps are only allowed to neighboring states are often called birth-and-death processes. These one-step processes are described by the master equation

$$\frac{\partial}{\partial t} p_n(t) = -(b_n + d_n) p_n + b_{n-1} p_{n-1} + d_{n+1} p_{n+1} \quad (\text{A.12})$$

with the birth rate  $b_n$  for the transition  $n \rightarrow n + 1$  and the death rate  $d_n$  for  $n \rightarrow n - 1$ . The transitions are illustrated in Fig. 1.1a. For constant rates  $b_n = b$  and  $d_n = d$ , the processes are referred to as random walks. In the special case  $d = 0$  with the initial condition  $p_n(0) = \delta_{n,0}$  and state space  $n \in \mathbb{N}$  the Poisson process with rate  $b$  is recovered.

A special situation occurs, when the right hand side of the master equation (A.11) vanishes, so that  $\dot{p}_n(t) = 0$ . This state, which does not change in time, is called steady or stationary state. The solution for  $p_n$  fulfills the global balance condition

$$\sum_{n'} w_{nn'} p_{n'} = \sum_{n'} w_{n'n} p_n. \quad (\text{A.13})$$

The sum of all fluxes out of  $p_n$  are balanced by the incoming fluxes. If additionally, the detailed balance condition

$$w_{nn'} p_{n'} = w_{n'n} p_n \quad (\text{A.14})$$

for each pair  $n, n'$  holds, fluxes vanish between all neighbouring states. In this case, the  $p_n$  describe the equilibrium distribution of the process. A stationary Markov process with an equilibrium distribution is called reversible. Since the detailed balance condition connects the equilibrium distribution with the transition rates of a process, it is also possible to test for reversibility on the basis of the transition rates alone. The prerequisite is a Markov process, continuous or discrete in time, with states  $n_1, n_2, \dots, n_N$  and a transition matrix with elements  $w_{ij}$  for the transition from  $n_i$  to  $n_j$ . The theorem called Kolmogorov's criterion states that a necessary and sufficient condition for this process to be reversible is, that the product of transition probabilities in any closed loop must be equal to the product of transition probabilities for the reversed loop [177]. In the exemplary process in Fig. 1.1b with the loop  $n_1 \rightarrow n_2 \rightarrow n_3 \rightarrow n_1$ , the Kolmogorov criterion reads

$$w_{1,2} w_{2,3} w_{3,1} = w_{1,3} w_{3,2} w_{2,1}. \quad (\text{A.15})$$

Because of its connection to the equilibrium distribution and time reversibility, detailed balance is an important concept for physical and chemical applications.

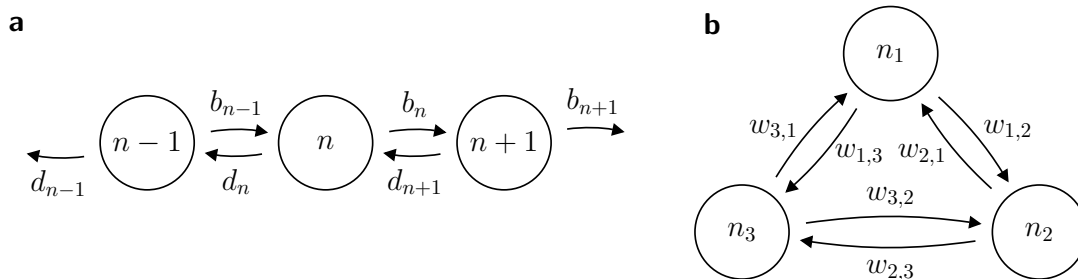


Figure 1.1. Examples for Markov chains. a) A Birth-and-death process with rates  $b_n$  and  $d_n$ . b) A system with three states forming a closed loop.

### A.1.4 Macroscopic equations

In many cases a quantity of interest is the mean value of a variable in a stochastic process, especially when fluctuations are assumed to be small. The time evolution of such a macroscopic observable can be derived from the master equation of the underlying Markov process. For simplicity, the derivation is sketched for a continuous time span and discrete state space with pdf  $p_n(t)$ , starting from the definition of the first moment

$$\langle n(t) \rangle = \sum_n n p_n(t). \quad (\text{A.16})$$

When the time derivative is taken on both sides, the master equation (A.11) can be inserted:

$$\frac{d}{dt} \langle n(t) \rangle = \sum_n \sum_{n'} n [w_{nn'} p_{n'}(t) - w_{n'n} p_n(t)]. \quad (\text{A.17})$$

Index substitutions lead to the expression

$$\frac{d}{dt} \langle n(t) \rangle = \sum_n \sum_{n'} (n' - n) w_{n'n} p_n(t). \quad (\text{A.18})$$

In the case of a birth-death process with rates  $b(n)$  and  $d(n)$ , the macroscopic equation is given by

$$\frac{d}{dt} \langle n(t) \rangle = \sum_n (b(n) - d(n)) p_n(t) = \langle b(n) \rangle - \langle d(n) \rangle. \quad (\text{A.19})$$

For linear rates the average can be drawn inside the functions, e.g.  $\langle b(n) \rangle = b(\langle n \rangle)$ . The mean coincides with the deterministic solution. The macroscopic equations for higher moments, such as  $\langle n^2(t) \rangle$  can be derived analogously. However, for nonlinear rates, the resulting differential equations are in general coupled. A truncation after the first or second order leads to an approximation that is valid when fluctuations are small or negligible. In this case the macroscopic equations are sometimes termed mean-field equations.

### A.1.5 Fokker-Planck equation

The pendant of the master equation, which typically describes jump processes, is the Fokker-Planck equation for continuous trajectories subject to drift and diffusion. It is derived from the Chapman-Kolmogorov equation in the limit of small jumps [127, 173]. Up to the second order, the approximation is given by

$$\frac{\partial}{\partial t} p(x, t) = -\frac{\partial}{\partial x} A(x) p(x, t) + \frac{1}{2} \frac{\partial^2}{\partial x^2} B(x) p(x, t) \quad (\text{A.20})$$

with  $B(x) \geq 0$ . The first term, also called drift term, relates to the deterministic features of the process. The second term, the diffusion term, contains information about the diffusive motion, fluctuations or noise. The diffusion constant  $D$  is related to the coefficient  $B(x)$  via  $2D = B(x)$ . An example for pure diffusion ( $A = 0$ ) is the Wiener process.

For a process which is neither solely a drift-diffusion nor a pure jump process, the terms from the Fokker-Planck equation in (A.20) and the master equation (A.9) can be combined to a more general differential equation [284].

## A.2 Stochastic chemical reaction kinetics

The traditional mathematical approach to describe the kinetics of chemical reactions is a deterministic formulation in terms of differential equations. The concentration  $c$  of each species is modeled as a continuous function in time that evolves according to an equation of motion. The parameters of the equation are typically called rate coefficients or rate constants and the equation itself rate equation. Knowledge about a single point, e.g. the initial configuration  $c_0(t_0)$ , uniquely determines the whole trajectory  $c(t)$ . A detailed introduction to deterministic chemical reaction kinetics is given for example in [200]. For numerous chemical reaction systems, this approach has proven most useful. It has been adopted to other fields, such as population dynamics and systems biology.

However, the deterministic description implies that the discrete number of chemical species, such as molecules, ions or other particles, can be neglected and replaced by a continuous variable, the concentration. Certainly this approximation is justified and acceptable for large particle numbers, as it is the case for many chemical applications. Additionally, a continuous mathematical formulation typically simplifies the analysis. Yet, the mismatch exists and the difference between actual system and its mathematical model becomes more pronounced, the smaller the number of molecules gets. In a limiting case, only a description with integer-valued quantities can represent the kinetic behavior appropriately. Advances in experimental methods, such as single molecule techniques, bring new significance to the molecular representation of chemical and biological processes. Moreover, fluctuations are typically neglected in deterministic models. Therefore, a stochastic description of chemical reaction kinetics is a promising approach.

Even if stochastic chemical kinetics can model a system on a molecular level, a total knowledge of the system down to every atomistic detail is (for now) unattainable. Thus, the basic assumption is that a probabilistic approach gives an appropriate representation of reactants within a homogeneous environment. In some cases the deterministic behavior emerges in observables such as the expected value. On the molecular level, thermal noise causes random collisions that allow molecules or particles to interact.

Stochastic processes serve as a basis for the concrete modeling of this scenario: Chemical reactions happen independently after an exponentially distributed waiting time. Consequently, the number of reactions follows a Poisson process. A chemical master equation can be derived to describe the changing number of molecules in integers. Since analytical solutions are only accessible in few cases, numerical methods have been developed. A simple and powerful tool was introduced by Gillespie in the 1970s. His algorithm yields trajectories

of a well-mixed system in thermal equilibrium. Detailed information on stochastic chemical kinetics and numerical methods is given for example in [107, 139, 190, 284]. Here, we can only give an overview on selected topics. The focus lies on the chemical master equation, because it is used to model bonds in adhesion clusters.

### A.2.1 Reactions and rates

Traditional chemical kinetics is based on the idea that molecules undergo a change or collide and react with a certain probability. Since random collisions of three or more reactants are considered to have a low likelihood, the important elementary reaction types are categorized into zero-molecular, monomolecular or bimolecular reactions. All complicated systems or complex networks are decomposed into these elementary classes. The zero-molecular reaction, the synthesis  $\emptyset \rightarrow A$ , is important for open systems with a variable number of particles. The reverse reaction, the degradation  $A \rightarrow \emptyset$ , belongs to the monomolecular reactions. Also, the transformation into a different species  $A \rightarrow B$  or a splitting up  $A \rightarrow B + C$  can be modeled. Bimolecular reactions comprise all events, in which pairs of the same or different species undergo a transition, e.g.  $A + B \rightarrow \dots$  or  $2A \rightarrow \dots$ .

The probability for the occurrence of such reactions depends on different factors, such as the amount of available reactants, the volume in which they need to come together and the temperature of the system. While a larger volume reduces the probability per unit time, higher temperature typically speeds up a reaction. The temperature dependence of the collision frequency is often modeled by an Arrhenius equation which states that the rate constant is proportional to the exponential  $\exp(-E_a/(k_B T))$  with the activation energy  $E_a$ , the Boltzmann constant  $k_B$  and the temperature  $T$ . For each reaction, all these dependencies are gathered in the reaction rate constant.

The difference in the stochastic rate constant compared to the deterministic rate constant results from registering molecule numbers in integers, rather than molar concentrations of a molecule species. The total number of molecules in a solution with molar concentration  $c$  is given by the product of  $c$ , the volume  $V$ , and the number of molecules per mole, the Avogadro constant  $N_A \approx 6 \cdot 10^{23} \text{ mol}^{-1}$ . Therefore, the deterministic rate constant  $k_0$  for the synthesis of a molecule in units of  $\text{mol m}^{-3} \text{ s}^{-1}$  is related to its stochastic pendant  $r_0$  via  $r_0 = N_A V k_0$ .  $r_0$  is equal to the probability per unit time that this synthesis happens, the so-called propensity. For a monomolecular reaction  $A \rightarrow \dots$  the concentration reduction per time is given by the product of the rate constant  $k_1$  and the current concentration of  $A$ . In this case, the stochastic rate is given by the mass-action rate  $r_1 = k_1$ . The propensity that any of the  $n_A$  molecules of type  $A$  undergoes this first-order reaction is given by  $a = n_A r_1$ . Analogously, the conversion for a bimolecular reaction  $A + B \rightarrow \dots$  is given by  $r_2 = k_2/(N_A V)$ . For different molecular species  $A$  and  $B$ , the propensity results



as  $a = n_A n_B r_2$ , because the number of pairs that may collide is  $n_A n_B$ . Note that for a bimolecular reaction  $2A \rightarrow \dots$ , the number of reactant pairs needs to be reduced, see [190]. In summary, the stochastic rate  $r_i$  describes the number of reaction events per unit time for a single reactant or reactant pair in a well-mixed environment. In order to obtain the reaction propensity, this constant needs to be multiplied with a statistical factor  $h_i$  that encapsulates the number of reactants or reactant pairs that are available for the corresponding reaction,  $a_i = h_i r_i$ .

## A.2.2 Chemical master equation

The chemical master equation describes the time evolution of one or multiple molecular species that undergo certain reactions in a Markov process. The state of the system is given by the number of molecules  $n_i \in \mathbb{N}$  for each species  $i \in [1, \dots, k]$  at a time  $t$ . Let  $\mathbf{n}(t) = (n_1(t), \dots, n_k(t))$  denote the state vector at time  $t$ . The time span is continuous, but the state changes only when an elementary reaction  $r_j$ ,  $j \in [1, \dots, m]$  occurs. The state change due to  $r_j$  is given by the vector  $\mathbf{v}_j$ . The probability, that one reaction  $r_j$  happens in the infinitesimal time interval  $[t, t + dt)$  is given by the propensity  $a_j(\mathbf{n}) dt + \mathcal{O}(dt)$ , where  $\mathcal{O}(dt)/dt \rightarrow 0$  for  $dt \rightarrow 0$ . Two or more reactions are assumed to happen within  $dt$  with a negligible probability  $\mathcal{O}(dt)$ . Consequently, the probability that the system stays in its current state  $\mathbf{n}(t)$  during  $dt$  and no reaction occurs is given by  $1 - \sum_{j=1}^m a_j(\mathbf{n}) dt + \mathcal{O}(dt)$ . The conditional probability to be in state  $\mathbf{n}$  at  $t + dt$ , given an initial state  $\mathbf{n}_0$  at  $t_0$  is thus given by

$$p(\mathbf{n}, t + dt | \mathbf{n}_0, t_0) = \left( 1 - \sum_{j=1}^m a_j(\mathbf{n}) dt \right) p(\mathbf{n}, t | \mathbf{n}_0, t_0) + \sum_{j=1}^m a_j(\mathbf{n} - \mathbf{v}_j) dt p(\mathbf{n} - \mathbf{v}_j, t | \mathbf{n}_0, t_0) + \mathcal{O}(dt). \quad (\text{A.21})$$

Subtraction of  $p(\mathbf{n}, t | \mathbf{n}_0, t_0)$ , division by  $dt$ , and taking the limit  $dt \rightarrow 0$  leads to the chemical master equation

$$\frac{\partial}{\partial t} p(\mathbf{n}, t | \mathbf{n}_0, t_0) = - \sum_{j=1}^m a_j(\mathbf{n}) p(\mathbf{n}, t | \mathbf{n}_0, t_0) + \sum_{j=1}^m a_j(\mathbf{n} - \mathbf{v}_j) p(\mathbf{n} - \mathbf{v}_j, t | \mathbf{n}_0, t_0). \quad (\text{A.22})$$

It defines a set of in general coupled differential equations that needs to be solved with the initial condition  $p(\mathbf{n}, t_0 | \mathbf{n}_0, t_0) = \delta_{\mathbf{n}, \mathbf{n}_0}$ . Analytical solutions of the chemical master equation are often unfeasible, even for few species and a limited number of molecules. In these cases, numerical approaches are the method of choice.

## A.2.3 Gillespie algorithm

The use of random numbers in computational methods dates back to the late 1940s when the Monte Carlo method was developed by Ulam, von Neumann, Metropolis and

coworkers [236]. This development is closely connected to the birth of electronic computers and the new potential and possibilities they provided [3]. Random sampling allowed to approximate values that were not or only under high effort obtainable with deterministic approaches. One example with many applications in statistical physics is the Metropolis-Hastings algorithm, a sampling method that allows to simulate Markov chains with a desired stationary distribution, even if the probability distribution itself cannot be sampled directly [154, 237].

From the 1960s on, the Kinetic Monte Carlo (KMC) method was introduced, which expanded the field to time-dependent and non-equilibrium processes, such as diffusion and reaction kinetics [35, 62, 355]. Gillespie introduced two rejection-free KMC algorithms for well-mixed systems of discrete chemical reactants [137, 138], which paved the way for numerous applications and extensions [190]. The so-called “Direct method” and “First reaction method” of the Gillespie algorithm belong to the exact stochastic algorithms, i.e. they produce statistically correct trajectories of the underlying system of master equations. A large number of these trajectories is required to approximate the solution of the master equation, the set of probability distributions  $p(\mathbf{n}, t)$ , and to obtain statistical quantities such as expected values and variances. For few reaction channels, the two algorithms introduced by Gillespie are not only statistically correct, but also efficient. While traditional algorithms proceed in time with constant, small time steps  $\Delta t$  to check whether a reaction happens or not, the Gillespie algorithm decides at once, when the next reaction happens and which type of reaction it is going to be. Thus, both algorithms “jump” from one reaction to the next one. They differ in their way of choosing the time and type of the next reaction.

As every reaction is explicitly simulated, especially the stochastic nature of discrete, small systems can be represented. However, there are certain limitations for the two exact methods of the algorithm. The computational costs increase strongly when the number of reaction channels or species grows, or when reaction rates often need to be recalculated. Additionally, the precision of the method is premised on the assumption of a thermally equilibrated and spatially homogeneous system. Adaptations and extensions, such as an accelerated, but only approximate version of the Gillespie algorithm, broadened the scope of its applications [139, 190].

### “Direct method” and “First reaction method”

The algorithm is originally intended for a mixture of  $k$  molecular species with  $m$  independent reaction channels. The state of the system  $\mathbf{n}(t) = (X_1, \dots, X_k)(t)$  is described by the molecule numbers  $n_i$ ,  $i \in \{1, \dots, k\}$  at a time  $t$ . Each reaction channel  $r_j$  is defined by the change in the number of species it causes, denoted by  $\mathbf{v}_j$  and its propensity  $a_j(\mathbf{n})$ . The fundamental hypothesis is the same that is used for the derivation of the chemical master equation itself. It states that  $a_j(\mathbf{n})dt$  defines the probability for one reaction  $j$  occurs in

the infinitesimal interval  $[t, t + dt]$ , given the system is in state  $\mathbf{n}$  at time  $t$ . From this assumption, the probability  $p(\tau, x|\mathbf{n}, t)$  can be derived [137]:

$$p(\tau, x|\mathbf{n}, t) = a_x \exp(-a\tau), \quad (\text{A.23})$$

where  $a = \sum_{j=1}^m a_j$ . It describes the conditional probability that the next reaction will happen after a waiting time  $0 \leq \tau < \infty$  and that it is a reaction with channel index  $x \in [1, \dots, m]$ , given the system is at  $\mathbf{n}$  at time  $t$ . Both exact algorithms create stochastic trajectories by determining  $\tau$  and  $x$  repeatedly.

The system is initialized by setting the number of each species at time  $t_0$ . For the “Direct method” two random numbers  $u_1$  and  $u_2$  are drawn from a uniform distribution in  $[0, 1)$  in each step to decide when the next reaction occurs and which reaction it will be. The waiting time for the next reaction follows an exponential distribution with parameter  $a = \sum_{j=1}^m a_j$ :

$$\tau = -\ln(u_1)/a. \quad (\text{A.24})$$

The reaction channel index  $x$  is determined by the smallest integer that fulfills

$$u_2 < \sum_{j=1}^x a_j/a. \quad (\text{A.25})$$

Thus, the integer  $k$  follows the density function  $a_k/a$ . The product of the exponential waiting time distribution  $p(\tau) = a \exp(-a\tau)$  and  $a_k/a$  gives the correct conditional probability  $p(\tau, x|\mathbf{n}, t)$ .

In the “First reaction method”,  $m$  random variables  $u_j$  are drawn that follow a uniform distribution in  $[0, 1)$ . They are used to create  $m$  waiting times  $\tau_j = -\ln(u_j)/a_j$  with  $j = 1, \dots, m$ , i.e. one time for each reaction channel. The channel index with the minimal waiting time  $\tau_x = \min(\tau_1, \dots, \tau_m)$  is chosen, because the corresponding reaction happens first. The “First reaction method” also generates pairs  $(\tau, x)$  according to  $p(\tau, x|\mathbf{n}, t)$ , but uses  $m$  random variables instead of two.

When the waiting time and the reaction type are calculated, time and state of the system can be updated accordingly. The simulation is stopped, when the desired duration time or number of reactions is reached. Both algorithm methods are summarized in Fig. 1.2. For the adhesion cluster models presented in this thesis, the “Direct method” is used.

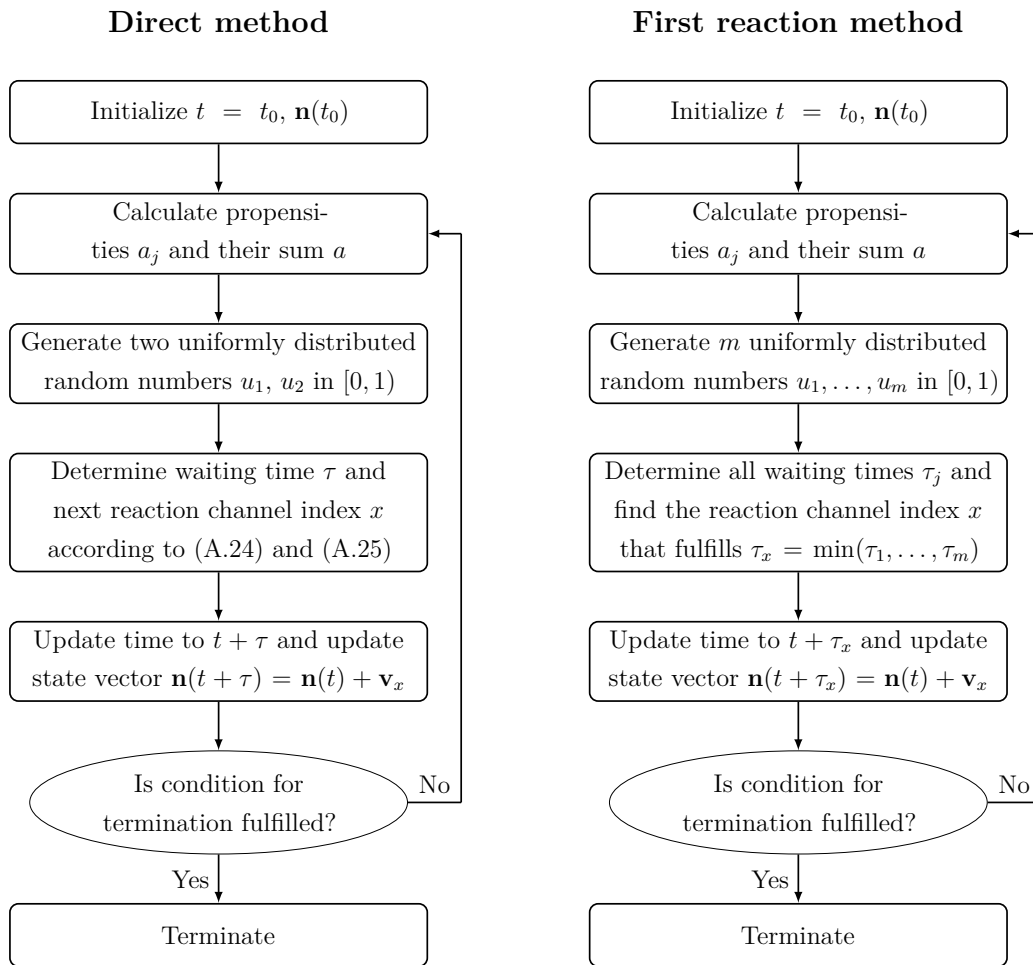


Figure 1.2. Flowcharts of the two exact Gillespie algorithm methods.

# Acknowledgements

First and foremost I would like to thank the two reviewers, Prof. Gerhard Gompper and Prof. Johannes Berg. I very much appreciate the effort you provide for reading this thesis. I would like to extend my sincere thanks to Prof. Markus Braden for chairing the thesis defense committee and to Prof. Benedikt Sabaß for joining the committee as minutes taker.

This project and thesis would not have been possible without my Doktorvater, Prof. Gerhard Gompper, or my supervisor, Prof. Benedikt Sabaß. Gerhard, thank you for this opportunity and your scientific advice. Your comments have always been extremely valuable. Benedikt, thank you for offering me this project and for your guidance. I am very grateful for all the time you invested in our discussions and for your inspiring ideas.

I would like to thank Dr. Thorsten Auth for letting me join the IHRS BioSoft Guest Student Programme. Furthermore, I also wish to thank Prof. Jan Kierfeld for supervising me during my studies at TU Dortmund and for drawing my attention to the field of Biophysics and Soft Matter.

Next, I wish to thank all the great colleagues in ICS-2, now IBI-5, and IAS-2 at Forschungszentrum Jülich for the many discussions and encouraging words. Our yearly hike, the Christmas parties and numerous cakes will remain in good memory. I would like to extend my thanks to Judit, Sergi and Ahmet for the refreshing coffee breaks with so many fun conversations. Kai and Ahmet, you were both wonderful office mates. Thank you very much for your help and the great times.

I am also grateful to my friends at home and in Jülich. Katarina, we started together and we will finish it together. Thank you for being there for me during all this time. Finally, I would like to thank my sister, my mother, my grandmother, the rest of my family, and Lukas for their unconditional support and profound belief in my abilities.



# Erklärung

Hiermit versichere ich an Eides statt, dass ich die vorliegende Dissertation selbstständig und ohne die Benutzung anderer als der angegebenen Hilfsmittel und Literatur angefertigt habe. Alle Stellen, die wörtlich oder sinngemäß aus veröffentlichten und nicht veröffentlichten Werken dem Wortlaut oder dem Sinn nach entnommen wurden, sind als solche kenntlich gemacht. Ich versichere an Eides statt, dass diese Dissertation noch keiner anderen Fakultät oder Universität zur Prüfung vorgelegen hat; dass sie - abgesehen von unten angegebenen Teilpublikationen und eingebundenen Artikeln und Manuskripten - noch nicht veröffentlicht worden ist sowie, dass ich eine Veröffentlichung der Dissertation vor Abschluss der Promotion nicht ohne Genehmigung des Promotionsausschusses vornehmen werde. Die Bestimmungen dieser Ordnung sind mir bekannt. Darüber hinaus erkläre ich hiermit, dass ich die Ordnung zur Sicherung guter wissenschaftlicher Praxis und zum Umgang mit wissenschaftlichem Fehlverhalten der Universität zu Köln gelesen und sie bei der Durchführung der Dissertation zugrundeliegenden Arbeiten und der schriftlich verfassten Dissertation beachtet habe und verpflichte mich hiermit, die dort genannten Vorgaben bei allen wissenschaftlichen Tätigkeiten zu beachten und umzusetzen. Ich versichere, dass die eingereichte elektronische Fassung der eingereichten Druckfassung vollständig entspricht.

Teilpublikationen:

Braeutigam, A., Simsek, A.N., Gompper, G. et al. Generic self-stabilization mechanism for biomolecular adhesions under load. Nat Commun 13, 2197 (2022). <https://doi.org/10.1038/s41467-022-29823-2>

25.04.2022

Datum

Andrea Bräutigam

Andrea Bräutigam





# Andrea Bräutigam

## *Curriculum Vitae*

---

### Personal Information

Name Andrea Bräutigam  
Born 1993 in Arnsberg  
Nationality German

---

### Education

- 2018–Present **PhD Candidate in Physics**  
Universität zu Köln  
PhD Thesis: “Response of stochastic adhesion clusters to pulling and shearing forces”  
under the supervision of Prof. Benedikt Sabaß and Prof. Gerhard Gompper
- 2015–2017 **Master of Science in Physics**  
Technische Universität Dortmund, GPA 1,0  
Master Thesis: „Formen lokaler Membranablösungen in zylindrischer Geometrie“  
(“*Shapes of local membrane detachments in cylindrical geometry*”) under the supervision  
of Prof. Jan Kierfeld
- 2012–2015 **Bachelor of Science in Physics**  
Technische Universität Dortmund, GPA 1.5  
Bachelor Thesis: „Monte-Carlo-Simulation der Verarmungswechselwirkung harter  
Scheiben“ (“*Monte Carlo Simulation of depletion interaction in a hard disk system*”)  
under the supervision of Prof. Jan Kierfeld
- 2003–2012 **Abitur** (*general qualification for university entrance*)  
Städt. Gymnasium Laurentianum Arnsberg, GPA 1.0